9-15-2011

Non-Adiabatic Atomic Transitions: Computational Cross Section Calculations of Alkali Metal-Noble Gas Collisions

Charlton D. Lewis II

NON-ADIABATIC ATOMIC TRANSITIONS: COMPUTATIONAL CROSS SECTION CALCULATIONS OF ALKALI METAL - NOBLE GAS COLLISIONS

DISSERTATION

Charlton D. Lewis, II, Captain, USAF

AFIT/DS/ENP/11-S04

DEPARTMENT OF THE AIR FORCE
AIR UNIVERSITY

AIR FORCE INSTITUTE OF TECHNOLOGY

Wright-Patterson Air Force Base, Ohio

AFIT/DS/ENP/11-S04

NON-ADIABATIC ATOMIC TRANSITIONS: COMPUTATIONAL CROSS SECTION CALCULATIONS OF ALKALI METAL - NOBLE GAS COLLISIONS

DISSERTATION

Presented to the Faculty

Graduate School of Engineering and Management

Air Force Institute of Technology

Air University

Air Education and Training Command

in Partial Fulfillment of the Requirements for the

Degree of Doctor of Philosophy

Charlton D. Lewis, II, BS, MS

Captain, USAF

September 2011

AFIT/DS/ENP/11-S04

NON-ADIABATIC ATOMIC TRANSITIONS: COMPUTATIONAL CROSS SECTION CALCULATIONS OF ALKALI METAL - NOBLE GAS COLLISIONS

Charlton D. Lewis, II, BS, MS
Captain, USAF

Approved:

//signed//	September 2011
David E. Weeks, PhD (Chairman)	Date
//signed//	September 2011
Mark E. Oxley, PhD (Member)	Date
//signed//	September 2011
Larry W. Burggraf, PhD (Member)	Date

Accepted:

//signed//	September 2011
Marlin U. Thomas Dean, Graduate School of Engineering and Management	Date

Abstract

Diode Pumped Alkali Lasers operate by exciting a gaseous cell of alkali metal to its $P_{3/2}$ excited energy state. A noble gas, present in the cell, collisionally de-excites the alkali metal to its $P_{1/2}$ state. The alkali atoms then relax to their $S_{1/2}$ ground state by emitting photons. These photons are used to produce laser light. The de-excitation due to collisions with inert gas molecules represents an interesting juncture for DPALs operation. This process must be faster than the relaxation back to the $S_{1/2}$ state or the laser will not work. The rate of de-excitation is related to the collisional cross section and the cross section to the $\widehat{\mathbf{S}}$-Matrix.

A time-dependent numerical algorithm was developed using FORTRAN 90 to predict $\widehat{\mathbf{S}}$-Matrix elements for alkali metal - noble gas (MNg) collisions. The split operator method was used to propagate nuclear Moller reactant states along dynamic spin-orbit split molecular potential energy surfaces. Correlation functions were then calculated between nuclear Moller reactant and product states so that the Channel Packet Method[46][41] could be implemented for $\widehat{\mathbf{S}}$-Matrix calculations.

The $\widehat{\mathbf{S}}$-Matrix contains the close-coupled Hamiltonian of the MNg system. This Hamiltonian was derived in a body-fixed coordinate system and represented in the P-manifold Born-Oppenheimer molecular basis. We found that there were two major state to state coupling phenomenon: spin-orbit coupling and Coriolis coupling. These two phenomena were responsible for the intramultiplet mixing of the alkali metal.

A total of nine collisions were computationally simulated. The alkali metals were potassium, rubidium, and cesium and the noble gas partners were helium, neon, and argon. Lastly, temperature averaged cross sections were calculated for the $^2P_{3/2} \leftarrow {}^2P_{1/2}$ transition and compared to experimental observations.

Acknowledgements

I would like to thank Dr. Weeks for the many engaging conversations both scientific and philosophical that we had over the course of this work. With his guidance I was able to take my first professional step on the path to understanding the physical universe. Also I'd like to thank my committee and the physics department for their time and effort to see me through the completion of my doctorate degree.

Charlton D. Lewis, II

Table of Contents

Page

Page

List of Figures

Figure Page

List of Tables

Table Page

List of Abbreviations

NON-ADIABATIC ATOMIC TRANSITIONS: COMPUTATIONAL CROSS SECTION CALCULATIONS OF ALKALI METAL - NOBLE GAS COLLISIONS

I. Introduction

1.1 Diode Pumped Alkali Lasers

The purpose of this work is to explore the non-radiative intramultiplet transfer of excited state atoms in a class of gas-electric hybrid lasers known as a Diode Pumped Alkali Laser (DPAL). The lasing medium is a gaseous cell composed of an alkali metal typically Rubidium[26, 37] or Cesium[5, 18]. The unique character of the alkali atoms, having a single valence electron in the $S_{1/2}$ ground state, allows its first two excited states to be exploited.

An electric diode laser is used to pump or excite the alkali atoms to their $P_{3/2}$ excited state. Then an inert gas, typically Helium, Neon, or Argon for the lighter alkali metals or methane or ethane for the heavier alkali metals, is used to collisionally de-excite the alkali to its $P_{1/2}$ excited state. The alkali once it is in its $P_{1/2}$ undergoes amplified spontaneous emission. This emission is then utilized to create laser light. Figure 1 graphically depicts the DPAL system.

The non-radiative de-excitation obviously represents an interesting juncture for the DPAL mechanism. If this process is slow or negligible compared to the depopulation of the $P_{1/2}$ level then the laser will not operate effectively[5, 24, 26].

The atomic collisions involved in the non-radiative process will therefore be studied intensely. Quantum scattering theory is used to characterize and determine the collisional cross sections between the alkali atom and the inert atom. These collisional

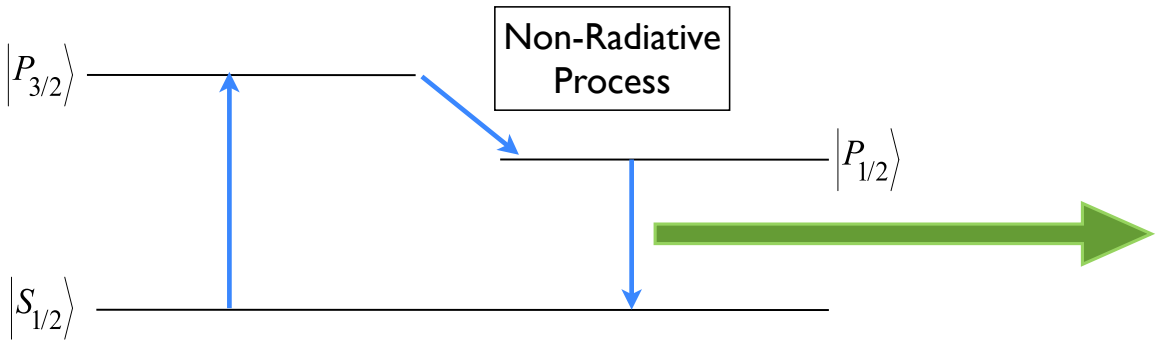

Figure 1. DPAL System Diagram.

cross sections are related to the rate of non-radiative population transfer[6][19][25]. With this knowledge we can predict at what energies the cross sections are maximized.

Nine pairs of alkali-noble gas systems, M + Ng, were studied where M = K, Rb, Cs and N = He, Ne, and Ar. The Potential Energy Surfaces (PES) governing the dynamics of these systems are calculated using numerical *ab initio* calculations such as Hartree-Fock, Multi-Configuration Self-Consistent Field (MCSCF) Interactions, or Perturbation Theories[40].

We will find that due to the dynamic processes involved, coupling between excited energy state levels of the collision diatom will exist. These couplings, spin-orbit, Coriolis, and radial derivative, are involved in determining the cross section of collision at various system energies. Comparing experimental cross sections with numerically derived ones will provide insight in to how the individual physical processes contribute to the total cross section.

At the basic level the theory generated throughout this paper has applicability to not just DPAL systems, but any system which involves atomic and molecular collisions at non-relativistic velocities.

1.2 Computational Methods

At the heart of many quantum mechanical descriptions of matter are differential equations. Simple models are typically employed for ease of use in understanding basic phenomenon as well as for their mathematical simplicity in solving their equations. However when modeling real world systems it is often the case, unless approximations are used, that solutions to dynamical equations are not analytic or easily solvable by hand.

Many programming languages exist to help solve some of the most complicated quantum mechanical problems. In particular this research will make use of FORTRAN, a programming language that has been in use by many scientists since its inception by IBM in the 1950's. One of the most appealing aspects of FORTRAN is its portability. Code can be developed in a personal computing environment and then that source code can be ported and compiled on massive parallel computing clusters. With such resources, very high resolution and detailed solutions to collisional phenomenon can be computed and compared with experiment.

Another important element and advantage to using a low level code like FORTRAN are the freely available numerical libraries. Two in particular which will be used numerous times for this work are the Fast Fourier Transform (FFT) and matrix diagonalization routines. The computer science community has spent many decades in the optimization of both mentioned routines and fortunately we get to benefit from their success.

1.3 Dissertation Outline

This work is divided in to three major sections. Chapters II, III, and IV comprise the theoretical ideas that will enable us to understand the basic quantum mechanical description of the Alkali-Noble gas system, how it is represented, and how it evolves

in time. Chapter V is devoted to the second major section, the development of the computational tools and techniques used to simulate these atomic collisions. In this section we present two model systems to test the computational algorithms. The last section, Chapters VI and VII, combine the theory and computational tools to model alkali metal-noble gas collisions. The results of the simulation, the temperature averaged cross sections, are then compared to experimental observations.

II. Basic Theory

2.1 Introduction

The theoretical foundations of this work start with the basic mathematical principles of quantum mechanics and move to the more complicated theories of quantum molecular scattering. Once the basic mathematics are established, we begin at the electronic level of a single atom. At this level of theory the geometry of the system plays an important role in how the atomic Hamiltonian is manifested. Then, a second atom is introduced, ultimately the noble gas collision partner, to the geometry of the atomic system and a molecular Hamiltonian is derived. Again how one decides to specify the molecule plays a major role in how the Hamiltonian is expressed. In particular this study will work in body-fixed coordinates for all computational calculations. Having established the molecular Hamiltonian two distinct types of motion can be observed, the motion of the nuclei and the motion of the electrons. Born-Oppenheimer theory will be used to help aid in solving the dynamics of the system. The dynamics then are governed by the time-dependent Schrödinger equation. From these dynamical equations a theory of time dependent quantum mechanical scattering will be introduced and the S-Matrix derived. The S-Matrix will relate the state of the interacting system before and after collision. The scattering cross sections are directly calculable from this S-matrix.

2.2 State Space

The mathematical foundations of quantum mechanics can be found in many textbook references[36][12][29]. This section follows Shankar[36]. In order to understand quantum scattering we must first understand how to describe, mathematically, a quantum mechanical system. Traditionally, the first postulate of quantum mechanics

states that every physically real quantum system is described by the abstract ket $|\psi\rangle$. This vector contains all the information needed to describe the system, i.e., its center of mass in space, internal spin states, vibrational modes, etc. Topologically speaking these vectors form a complete separable complex Hilbert Space, $\mathbb{H}$, with an inner product, $\langle\cdot|\cdot\rangle$, that has the following properties[31]. For every $|\phi\rangle$, $|\psi_1\rangle$, $|\psi_2\rangle \in \mathbb{H}$,

1. $\langle\phi|\psi_1 + \psi_2\rangle = \langle\phi|\psi_1\rangle + \langle\phi|\psi_2\rangle$
2. $\langle\phi|\alpha \cdot \psi\rangle = \alpha \cdot \langle\phi|\psi\rangle$, $\forall\alpha \in \mathbb{C}$
3. $\langle\phi|\psi\rangle = \langle\psi|\phi\rangle^*$
4. $\langle\psi|\psi\rangle > 0$, if and only if $\psi \neq 0$

Note that in this bra-ket notation, the ket, $|\psi\rangle$, is an element of the vector space $\mathbb{H}$, where as the bra, $\langle\psi|$, is an element of the dual space, $\mathbb{H}^*$. In this sense the bras are linear functionals on the Hilbert Space.

It is enough to observe a countable number of properties, such as spin, orbital momentum, etc., to specify a quantum state. The Hilbert Space can be built by taking the tensor product, $\bigotimes$, of separate Hilbert Spaces that correspond to observable properties. For example a particle's state with a specific location and spin would be an element of the Hilbert Space $\mathbb{H} = \mathbb{H}_{space} \bigotimes \mathbb{H}_{spin}$. If a diatom were to be described one might specify its center of mass, angular momentum, and vibrational state instead. This Hilbert space would be described as $\mathbb{H} = \mathbb{H}_{CM} \bigotimes \mathbb{H}_{ang.mom.} \bigotimes \mathbb{H}_{vib}$.

As with any linear vector space there exists a set, $\mathcal{B}$, of independent basis vectors, $\{e_i\}$ where $i \in I$, that span the entire space. These basis vectors can be used to expand any member of the vector space:

$$|\psi\rangle = \sum_{i \in I} \psi_i \, |e_i\rangle \tag{1}$$

where $\psi_i \in \mathbb{C}$. The same is also true for the dual vector space:

$$\langle\psi| = \sum_{i\in I} \psi_i^* \langle e_i| \tag{2}$$

where $\psi_i^* \in \mathbb{C}$ as well. The ψ_i (ψ_i^*) are called the expansion coefficients or components of the vector (functional). In order to find the j^{th} component of a particular vector we need to take the inner product of $|\psi\rangle$ with $\langle e_j|$ such that (assuming the basis set is orthonormal):

$$\begin{aligned}\langle e_j|\psi\rangle &= \sum_{i=1}^{\infty} \psi_i \langle e_j|e_i\rangle \\ &= \sum_{i=1}^{\infty} \psi_i \delta_{ij} \\ &= \psi_j \end{aligned} \tag{3}$$

With this result the vector can be re-written as:

$$|\psi\rangle = \sum_{i=1}^{\infty} |e_i\rangle \langle e_i|\psi\rangle \tag{4}$$

This process is how one represents an abstract ket. The number of basis vectors need not be countable however. For instance if we wanted to represent a vector in coordinate space we would use the $|x\rangle$ basis where $x \in \mathbb{R}^N$. This coordinate representation uses as a label each point in $\mathbb{R}^N$ space for its basis vectors. As such the basis is uncountably infinite and linearly independent. The expansions (1) and (2) then become:

$$|\psi\rangle = \int_{\mathbb{R}^N} dx \psi(x) |x\rangle \tag{5}$$

$$\langle\psi| = \int_{\mathbb{R}^N} dx \psi(x) \langle x| \tag{6}$$

The orthonormalization condition for this coordinate basis is:

$$\langle x'|x\rangle = \delta(x - x') \tag{7}$$

Using this fact, the expansion coefficients become a function that will be the representation of $|\psi\rangle$ in the $|x\rangle$ basis:

$$\langle x|\psi\rangle = \int_{\mathbb{R}^N} dx\psi(x')\langle x|x'\rangle = \int_{\mathbb{R}^N} dx\psi(x')\delta(x' - x) = \psi(x) \tag{8}$$

We can examine the inner product of $|\psi\rangle$ with itself we demand that this operation does not diverge. With assistance of the closure relation,

$$\int_{\mathbb{R}^N} dx\,|x\rangle\,\langle x| = \mathbb{I} \tag{9}$$

where $\mathbb{I}$ is the identity operator on $\mathbb{H}$, the inner product is computed such that:

$$\begin{aligned}\langle\psi|\psi\rangle &= \langle\psi|\,\mathbb{I}\,|\psi\rangle \\ &= \int_{\mathbb{R}^N} dx\langle\psi|x\rangle\langle x|\psi\rangle \\ &= \int_{\mathbb{R}^N} dx\psi^*(x)\psi(x) \\ &< \infty\end{aligned} \tag{10}$$

This tells us that not any arbitrary function of a continuous variable can be admitted to represent the state vector. The class of functions that do fit the above criteria are known as *Lebesgue Square Integrable Functions*. For three-dimensional wave functions this set would be denoted as $\mathcal{L}^2(\mathbb{C}^3)$.

We are not confined to representing the state vector in coordinates only. Other valid representations include energy and momentum. Also not every representation

has to be infinite dimensional either. For spin 1/2 particles only two choices are available, spin up or spin down. For this observable the corresponding separable Hilbert space contains only two basis vectors $|\alpha\rangle$ for spin up and $|\beta\rangle$ for spin down.

2.3 Observables, Operators, and Measurement

For every classical observable, $q \in \mathbb{R}$, there exists a self-adjoint operator, $\widehat{Q}$ in quantum mechanics which when operating on a particular state will return the observable value multiplied by the same state, that is:

$$\widehat{Q}\,|\psi\rangle = q\,|\psi\rangle \tag{11}$$

Due to the wave nature of quantum mechanics, we must take a probabilistic view of observing a classical observable. Upon measurement of $\widehat{Q}$ on $|\psi\rangle$ the eigenvalue of that operator is returned with a probability defined as:

$$\mathcal{P}(q) = |\langle q|\psi\rangle|^2 = |\psi(q)|^2 \tag{12}$$

Since the number of possible values that q could take on is uncountably infinite $\mathcal{P}(q)$ is interpreted to be the probability density at q. So, the probability of finding a state between q+dq is $\mathcal{P}(q)dq$ where $\mathcal{P}(q) \in [0, 1]$.

If one is only interested in the average or mean value of q, then one calculates the

expectation value, $\langle \widehat{Q} \rangle$:

$$\begin{aligned}
\langle \widehat{Q} \rangle &= \int_{\mathbb{R}} dq \mathcal{P}(q) q = \int_{\mathbb{R}} dq |\langle q|\psi\rangle|^2 q \\
&= \int_{\mathbb{R}} dq \langle \psi|q\rangle \langle q|\psi\rangle q \\
&= \int_{\mathbb{R}} dq \, \langle \psi| \, \widehat{Q} \, |q\rangle \, \langle q|\psi\rangle \\
&= \langle \psi| \, \widehat{Q} \, |\psi\rangle
\end{aligned} \tag{13}$$

where we have made use of equation (11) and completeness.

Chief among observable operators are the coordinate and momentum operators. Other observable operators do exist, but are typically fashioned out of some mathematic combination of the aforementioned two operators. We are now equipped to describe an atom.

2.4 Quantum Description of an Atom

Consider an atom whose nucleus is labeled A to be in a region that is free of all external forces. This nucleus with respect to a space-fixed coordinate system is at a position $\vec{R}'_A$ and the atom's i-electrons are at a position $\vec{r'}_i$. This situation is depicted in Figure 2.

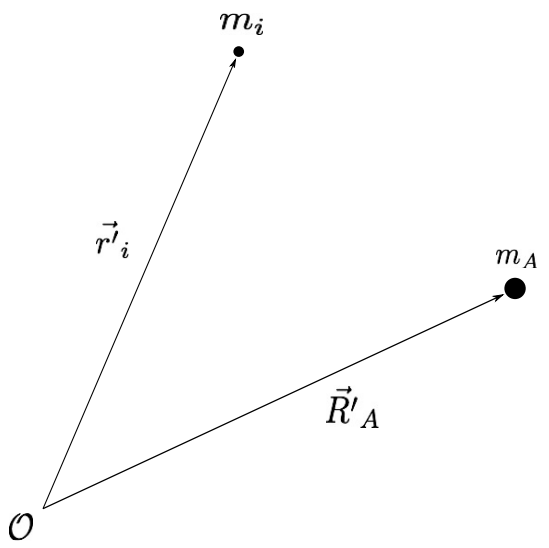

Figure 2. Geometry of an Atom in Space Fixed Coordinates.

The Hamiltonian for this atomic system is written as follows:

$$\widehat{\mathbf{H}} = -\frac{1}{2m_A}\vec{\nabla}^2_{\vec{R'}_A} - \sum_{i=1}^{n}\frac{1}{2m_i}\vec{\nabla}^2_{\vec{r'}_i} - \sum_{i=1}^{n}\frac{Z_A Z_i}{|\vec{R'}_A - \vec{r'}_i|} + \sum_{i>j}^{n}\frac{Z_i Z_i}{|\vec{r'}_i - \vec{r'}_j|} + \widehat{\mathbf{V}}_{ls}(|\vec{R'}_A - \vec{r'}_i|) \quad (14)$$

where Z_A and Z_i are the charge of the nucleus and the electrons, m_A the mass of the nucleus, m_i the mass of the electrons, and n is the total number of electrons. The first two terms are the kinetic energies of the nucleus and the n-electrons respectively. The next two terms are the electrostatic interactions and the last term, $\widehat{\mathbf{V}}_{ls}$, is the spin orbit potential. It will be beneficial to refer all coordinates to the center of mass of the atom. In order to do so the following transformation must take place:

$$\vec{r'}_i \rightarrow \vec{r}_i = \vec{r'}_i - \vec{R}_{CM}$$
$$\vec{R'}_A \rightarrow \vec{R}_{CM} = \frac{m_A\vec{R'}_A + \sum_{i=1}^{n} m_i\vec{r'}_i}{M}; M = m_A + \sum_{i=1}^{n} m_i$$

For the sake of derivation the two electron case will be considered. The extension

to n-electrons follows easily. The transformation can be written in a vector/matrix form:

$$\begin{pmatrix} \vec{r}_1 \\ \vec{r}_2 \\ \vec{R}_{CM} \end{pmatrix} = \begin{pmatrix} \frac{M-m_1}{M} & \frac{-m_2}{M} & \frac{m_A}{M} \\ \frac{-m_1}{M} & \frac{M-m_2}{M} & \frac{-m_A}{M} \\ \frac{m_1}{M} & \frac{m_2}{M} & \frac{m_A}{M} \end{pmatrix} \begin{pmatrix} \vec{r'}_1 \\ \vec{r'}_2 \\ \vec{R'}_A \end{pmatrix} \tag{15}$$

To see how this transformation affects the atomic Hamiltonian first start with the Lagrangian of the system. Temporarily suppressing the functional form of the electrostatic and spin-orbit potential, the kinetic energy, $\widehat{\mathbf{T}}$, minus the potential energy, $\widehat{\mathbf{T}}$, are written down as the Lagrangian:

$$\begin{aligned} \widehat{\mathbf{L}} &= \widehat{\mathbf{T}} - \widehat{\mathbf{V}}(|\vec{R'}_A - \vec{r'}_1|, |\vec{R'}_A - \vec{r'}_2|, |\vec{r'}_2 - \vec{r'}_1|) \\ &= \frac{1}{2} \begin{pmatrix} \dot{\vec{r}}_1{}' & \dot{\vec{r}}_2{}' & \dot{\vec{R}}_A{}' \end{pmatrix} \begin{pmatrix} m_1 & 0 & 0 \\ 0 & m_2 & 0 \\ 0 & 0 & m_A \end{pmatrix} \begin{pmatrix} \dot{\vec{r}}_1{}' \\ \dot{\vec{r}}_2{}' \\ \dot{\vec{R}}_A{}' \end{pmatrix} - \widehat{\mathbf{V}}(|\vec{R'}_A - \vec{r'}_1|, |\vec{R'}_A - \vec{r'}_2|, |\vec{r'}_2 - \vec{r'}_1|). \end{aligned} \tag{16}$$

Inverting the coordinate transformation, Equation (15), and taking a time derivative, we have that

$$\begin{pmatrix} \dot{\vec{r}}_1{}' \\ \dot{\vec{r}}_2{}' \\ \dot{\vec{R}}_A{}' \end{pmatrix} = \begin{pmatrix} 1 & 0 & 1 \\ 0 & 1 & 1 \\ -\frac{m_1}{m_A} & -\frac{m_2}{m_A} & 1 \end{pmatrix} \begin{pmatrix} \dot{\vec{r}}_1 \\ \dot{\vec{r}}_2 \\ \dot{\vec{R}}_{CM} \end{pmatrix} \tag{17}$$

$$\begin{pmatrix} \dot{\vec{r}}_1{}' & \dot{\vec{r}}_2{}' & \dot{\vec{R}}_A{}' \end{pmatrix} = \begin{pmatrix} \dot{\vec{r}}_1 & \dot{\vec{r}}_2 & \dot{\vec{R}}_{CM} \end{pmatrix} \begin{pmatrix} m_1 & 0 & -\frac{m_1}{m_A} \\ 0 & 1 & -\frac{m_2}{m_A} \\ 1 & 1 & 1 \end{pmatrix} \tag{18}$$

and the Lagrangian becomes the following:

$$\begin{aligned}\widehat{\mathbf{L}} &= \frac{1}{2}\begin{pmatrix}\dot{\vec{r}}_1 & \dot{\vec{r}}_2 & \dot{\vec{R}}_{CM}\end{pmatrix}\begin{pmatrix}1 & 0 & 1\\ 0 & 1 & 1\\ -\frac{m_1}{m_A} & -\frac{m_2}{m_A} & 1\end{pmatrix}\begin{pmatrix}m_1 & 0 & 0\\ 0 & m_2 & 0\\ 0 & 0 & m_A\end{pmatrix}\begin{pmatrix}m_1 & 0 & -\frac{m_1}{m_A}\\ 0 & 1 & -\frac{m_2}{m_A}\\ 1 & 1 & 1\end{pmatrix}\begin{pmatrix}\dot{\vec{r}}_1\\ \dot{\vec{r}}_2\\ \dot{\vec{R}}_{CM}\end{pmatrix}\\ &\quad - \widehat{\mathbf{V}}(|\vec{R'}_A - \vec{r'}_1|, |\vec{R'}_A - \vec{r'}_2|, |\vec{r'}_2 - \vec{r'}_1|)\\ &= \frac{1}{2}\left[\frac{m_1(m_1+m_A)}{m_A}\,\dot{\vec{r}}_1^{\,2} + \frac{m_2(m_2+m_A)}{m_A}\,\dot{\vec{r}}_2^{\,2} + M\dot{\vec{R}}_{CM}^{\,2} + 2\frac{m_1 m_2}{m_A}\dot{\vec{r}_1}\cdot\dot{\vec{r}_2}\right]\\ &\quad - \widehat{\mathbf{V}}(|\vec{R'}_A - \vec{r'}_1|, |\vec{R'}_A - \vec{r'}_2|, |\vec{r'}_2 - \vec{r'}_1|). \end{aligned} \tag{19}$$

Using atomic units we set $m_1 = m_2 = 1$ and since the mass of the nucleus is much greater than an election, $\frac{1+m_A}{m_A} \approx 1$, and the Lagrangian is approximately,

$$\widehat{\mathbf{L}} \approx \frac{1}{2}\left[\dot{\vec{r}}_1^{\,2} + \dot{\vec{r}}_2^{\,2} + M\dot{\vec{R}}_{CM}^{\,2} + 2\frac{m_1 m_2}{m_A}\dot{\vec{r}_1}\cdot\dot{\vec{r}_2}\right] - \widehat{\mathbf{V}}(\vec{r'_1}, \vec{r'_2}, \vec{R'_A}). \tag{20}$$

By performing a Legendre transformation, $\widehat{\mathbf{H}} = \dot{q}_i p_i - \widehat{\mathbf{L}}$ where $p_i = \frac{\partial \widehat{\mathbf{L}}}{\partial \dot{q}_i}$, the Hamiltonian in atomic center of mass coordinates is revealed. The generalized momenta are,

$$\vec{p}_1 = \frac{\partial \widehat{\mathbf{L}}}{\partial \dot{\vec{r}}_1} = \dot{\vec{r}}_1 + \frac{\dot{\vec{r}}_2}{m_A} \tag{21}$$

$$\vec{p}_2 = \frac{\partial \widehat{\mathbf{L}}}{\partial \dot{\vec{r}}_2} = \dot{\vec{r}}_2 + \frac{\dot{\vec{r}}_1}{m_A} \tag{22}$$

$$\vec{P}_{CM} = \frac{\partial \widehat{\mathbf{L}}}{\partial \dot{\vec{R}}_{CM}} = M\dot{\vec{R}}_{CM} \tag{23}$$

and upon inversion of the coordinates and taking their squares we have:

$$\dot{\vec{r}}_1 = \vec{p_1} - \frac{\vec{p_2}}{M}$$
$$\dot{\vec{r}}_1^{\,2} = \vec{p_1}^{\,2} + \frac{\vec{p_2}^{\,2}}{m_A^2} - \frac{2\vec{p_1}\cdot\vec{p_2}}{m_A} \tag{24}$$
$$\dot{\vec{r}}_2 = \vec{p_2} - \frac{\vec{p_1}}{M}$$
$$\dot{\vec{r}}_2^{\,2} = \vec{p_2}^{\,2} + \frac{\vec{p_1}^{\,2}}{m_A^2} - \frac{2\vec{p_1}\cdot\vec{p_2}}{m_A} \tag{25}$$
$$\dot{\vec{R}}_{CM} = \frac{\vec{P}_{CM}}{M}$$
$$\dot{\vec{R}}_{CM}^{\,2} = \frac{\vec{P}_{CM}^2}{M^2} \tag{26}$$

Substituting these momenta and coordinates into the Legendre transformation the kinetic portion of the Hamiltonian becomes:

$$\begin{aligned}\widehat{\mathbf{T}} &= \frac{1}{2}\vec{p_1}^{\,2} + \frac{1}{2}\vec{p_2}^{\,2} + \frac{1}{2}\frac{\vec{P}_{CM}^2}{M} + \frac{\vec{p_1}\cdot\vec{p_2}}{m_A} + \frac{1}{2m_A^2}(\vec{p_1}^{\,2} + \vec{p_2}^{\,2}) - \frac{\vec{p_1}\cdot\vec{p_2}}{m_A^3} \\ &\approx \frac{1}{2}\vec{p_1}^{\,2} + \frac{1}{2}\vec{p_2}^{\,2} + \frac{1}{2}\frac{\vec{P}_{CM}^2}{M} + \frac{\vec{p_1}\cdot\vec{p_2}}{m_A}\end{aligned} \tag{27}$$

The last term of this transformed kinetic energy operator is the mass polarization operator. It represents how much the center of mass polarizes from the center of the nucleus. Typically, this term is small, owing to the differences in masses between the electrons and nucleus, and thus, is usually neglected or treated in a perturbative manner.

The transformation of the potential can be accomplished by direct substitution of space-fixed coordinates to center of mass coordinates. Setting the charge of the electron equal to one, $Z_i = 1$, and using the same approximation as in Equation 20

the potential terms are:

$$|\vec{r_2'} - \vec{r_1'}|^{-1} = |\vec{r_2} + \vec{R}_{CM} - \vec{r_1} - \vec{R}_{CM}|^{-1}$$
$$= |\vec{r_2} - \vec{r_1}|^{-1} \tag{28}$$

$$\begin{aligned}
&- Z_A|\vec{R_A'} - \vec{r_1'}|^{-1} \\
&= -Z_A \left| \left(\frac{M}{m_A}\right) \vec{R}_{CM} - \left(\frac{1}{m_A}\right)(\vec{r_1} + \vec{R}_{CM}) - \left(\frac{1}{m_A}\right)(\vec{r_2} + \vec{R}_{CM}) - (\vec{r_1} + \vec{R}_{CM}) \right|^{-1} \\
&= -Z_A \left| \left(\frac{M}{m_A} - \frac{1}{m_A} - \frac{1}{m_A} - 1\right) \vec{R}_{CM} + \left(-\frac{1}{m_A} - 1\right) \vec{r_1} + \left(-\frac{1}{m_A}\right) \vec{r_2} \right|^{-1} \\
&= -Z_A \left| -\left(\frac{1+m_A}{m_A}\right) \vec{r_1} - \left(\frac{1}{m_A}\right) \vec{r_2} \right|^{-1} \\
&\approx -Z_A \left| \vec{r_1} + \frac{1}{m_A} \vec{r_2} \right|^{-1}
\end{aligned} \tag{29}$$

$$-Z_A|\vec{R_A'} - \vec{r_2'}|^{-1} = -Z_A \left| \vec{r_2} + \frac{1}{m_A} \vec{r_1} \right|^{-1} \tag{30}$$

The spin-orbit potential depends only on the distance between the nucleus and the electron and in the center of mass coordinate system remains approximately the same:

$$\begin{aligned}
\widehat{\mathbf{V}}_{ls} &= f_1(|\vec{R_A'} - \vec{r_1'}|)\widehat{\mathbf{l}}_1 \cdot \widehat{\mathbf{s}}_1 + f_2(|\vec{R_A'} - \vec{r_2'}|)\widehat{\mathbf{l}}_2 \cdot \widehat{\mathbf{s}}_2 \\
&= f_1\left(\left|\vec{r_1} + \frac{1}{m_A}\vec{r_2}\right|\right)\widehat{\mathbf{l}}_1 \cdot \widehat{\mathbf{s}}_1 + f_2\left(\left|\vec{r_2} + \frac{1}{m_A}\vec{r_1}\right|\right)\widehat{\mathbf{l}}_2 \cdot \widehat{\mathbf{s}}_2 \\
&\approx f_1\left(|\vec{r_1}|\right)\widehat{\mathbf{l}}_1 \cdot \widehat{\mathbf{s}}_1 + f_2\left(|\vec{r_2}|\right)\widehat{\mathbf{l}}_2 \cdot \widehat{\mathbf{s}}_2.
\end{aligned} \tag{31}$$

The operators $\widehat{\mathbf{l}}_1$, $\widehat{\mathbf{l}}_2$, $\widehat{\mathbf{s}}_1$, and $\widehat{\mathbf{s}}_2$ represent the respective electron's orbital angular momentum, $\widehat{\mathbf{l}}$, and spin angular momentum, $\widehat{\mathbf{s}}$. The $f_1, f_2 \in \mathbb{R}$ functions represent the spin-orbit parameters.

The atomic Hamiltonian transformed to center of mass coordinates is

$$\begin{aligned}\widehat{\mathbf{H}} &= \frac{1}{2}\frac{\vec{P}_{CM}^2}{M} + \frac{1}{2}\vec{p_1}^2 + \frac{1}{2}\vec{p_2}^2 + \frac{\vec{p_1}\cdot\vec{p_2}}{m_A} - Z_A\left|\vec{r_1} + \frac{1}{m_A}\vec{r_2}\right|^{-1} - Z_A\left|\vec{r_2} + \frac{1}{m_A}\vec{r_1}\right|^{-1} \\ &\quad + |\vec{r_2} - \vec{r_1}|^{-1} + \widehat{\mathbf{V}}_{LS} \\ &= \frac{1}{2M}\vec{P}_{CM}^2 + \widehat{\mathbf{H}}_A^0(\vec{r_1}, \vec{r_2}) + \widehat{\mathbf{V}}_{ls}(\vec{r_1}, \vec{r_2}) \end{aligned} \tag{32}$$

where we have grouped together the electron kinetic energy, the mass polarization terms, and all electrostatic terms under the electronic Hamiltonian, $\widehat{\mathbf{H}}_A^0(\vec{r_1}, \vec{r_2})$. The geometry is depicted in the Figure 3.

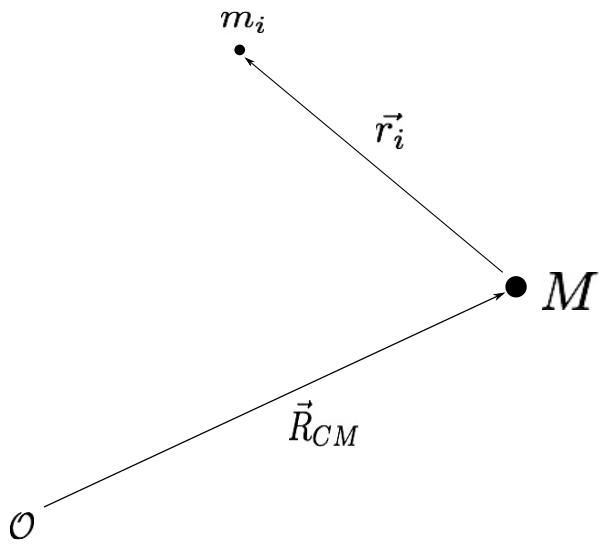

Figure 3. Geometry of an Atom in Space-Fixed Center of Mass Coordinates.

The electronic Hamiltonian, $\widehat{\mathbf{H}}_A^0$ commutes with both the electronic angular momentum operator, $\widehat{\mathbf{l}}$, as well as the electronic spin operator, $\widehat{\mathbf{s}}$. Thus, to completely specify the state of the atom one has to specify the quantum numbers n, l, s, and

the projections onto the z-axis of the electronic angular and electronic spin momentum, m_l and m_s. The state space for this atom is spanned by the vectors $\left|n^{l\ \ s}_{m_l m_s}\right\rangle$. The electronic Hamiltonian acts in the usual way on these basis vectors revealing the electronic energy, $\mathcal{E}^{n,l,s} \in \mathbb{R}$, of the system:

$$\widehat{\mathbf{H}}^0_A \left|n^{l\ \ s}_{m_l m_s}\right\rangle = \mathcal{E}^{n,l,s} \left|n^{l\ \ s}_{m_l m_s}\right\rangle \tag{33}$$

For this work we choose to work in the total electronic angular momentum basis $\left|{}^{j}_{m_j}\right\rangle$ because the spin-orbit potential is diagonal in this basis. This can be accomplished by taking the direct sum of the electronic orbital angular momentum and the electronic spin angular momentum such that $j = l \bigoplus s$. The basis vectors in the l,s set are related to the basis vectors in the j set through the Clebsch-Gordon coefficients:

$$\left|{}^{j}_{m_j}\right\rangle = \sum_{m_l} \sum_{m_s} (l m_l, s m_s | j m_j, l s) \left|{}^{l\ \ s}_{m_l m_s}\right\rangle \tag{34}$$

In this angular momentum basis the kets $\left|{}^{j}_{m_j}\right\rangle$ are still eigenfunctions of the $\widehat{\mathbf{l}}^2$ and $\widehat{\mathbf{s}}^2$ operators. The electronic operators act on these basis vectors in the following way:

$$\widehat{\mathbf{H}}^0_A \left|{}^{j}_{m_j}\right\rangle = \mathcal{E}^{n,j} \left|{}^{j}_{m_j}\right\rangle \tag{35}$$

$$\widehat{\mathbf{j}}^2 \left|{}^{j}_{m_j}\right\rangle = j(j+1) \left|{}^{j}_{m_j}\right\rangle \tag{36}$$

$$\widehat{\mathbf{j}}_z \left|{}^{j}_{m_j}\right\rangle = m_j \left|{}^{j}_{m_j}\right\rangle \tag{37}$$

$$\widehat{\mathbf{j}}_\pm \left|{}^{j}_{m_j}\right\rangle = [(j \mp m)(j \pm m + 1)]^{1/2} \left|{}^{j}_{m_j \pm 1}\right\rangle \tag{38}$$

The spin orbit operator acts on the same basis such that

$$\widehat{\mathbf{V}}_{ls} \left|{}^{j}_{m_j}\right\rangle = a(\widehat{\mathbf{j}}^2 - \widehat{\mathbf{l}}^2 - \widehat{\mathbf{s}}^2) \left|{}^{j}_{m_j}\right\rangle \tag{39}$$

where a is the spin-orbit splitting parameter of the atom that leads to its fine structure. Now consider an interaction where two atoms come together forming a molecule.

2.5 Quantum Description of a Diatomic Molecule

The Hamiltonian of the diatomic system in space-fixed coordinates is similar to equation (14) except now we include similar terms for atom B. There is also a new and extremely important potential term added called the interaction potential. As the atoms approach each other, the electrostatic interactions between the nucleus and electrons of atom A with those of atom B become important. This potential will then be a function of the distance between atoms A and B. As this distance goes to infinity the molecule dissociates into two separate atoms and the interaction potential goes to zero.

The spin-orbit potential of atom A is also affected by the electromagnetic interactions due to atom B and vice versa. Therefore the spin-orbit potentials also become a function of the distance between the two atoms. The molecular Hamiltonian of atom A interacting with atom B in space-fixed coordinates is

$$\begin{aligned}\widehat{\mathbf{H}} = &-\frac{1}{2m_A}\vec{\nabla}^2_{\vec{R}'_A} - \sum_{i=1}^{N_A}\frac{1}{2m_i}\vec{\nabla}^2_{\vec{r}'_i} - \sum_{i=1}^{N_A}\frac{Z_A Z_i}{|\vec{R}'_A - \vec{r}'_i|} + \sum_{i>j}^{N_A}\frac{Z_i Z_i}{|\vec{r}'_i - \vec{r}'_j|} \\ &-\frac{1}{2m_B}\vec{\nabla}^2_{\vec{R}'_B} - \sum_{i=1}^{N_B}\frac{1}{2m_i}\vec{\nabla}^2_{\vec{r}'_i} - \sum_{i=1}^{N_B}\frac{Z_A Z_i}{|\vec{R}'_B - \vec{r}'_i|} + \sum_{i>j}^{N_B}\frac{Z_i Z_i}{|\vec{r}'_i - \vec{r}'_j|} \\ &+\widehat{\mathbf{V}}^A_{ls}(\vec{r}'_1, ..., \vec{r}'_{N_A}, |\vec{R}'_A - \vec{R}'_B|) + \widehat{\mathbf{V}}^B_{ls}(\vec{r}'_1, ..., \vec{r}'_{N_B}, |\vec{R}'_B - \vec{R}'_A|) \\ &+\widehat{\mathbf{V}}_{AB}(\vec{r}'_1, ..., \vec{r}'_{N_A}, \vec{r}'_{N_A+1}, ..., \vec{r}'_{N_A+N_B}, |\vec{R}'_A - \vec{R}'_B|). \end{aligned} \tag{40}$$

The first line of Equation (40) refers to the kinetic energies and electrostatic potentials of atom A with a mass of m_A and N_A electrons. The second line refers to the kinetic and electrostatic potentials of atom B with a mass of m_B and N_B electrons. The third

line contains the spin orbit potential terms of atom A and atom B, respectively, now a function of, not only their respective electrons, but also on the distance between atoms. The last line, is the electrostatic interaction potential. As the distance $|\vec{R}'_B - \vec{R}'_A| \to \infty$ the spin orbit potential terms loose their dependence on the internuclear distance and the electrostatic interaction potential goes to zero.

The geometry of the situation is depicted in Figure 4. Following the same

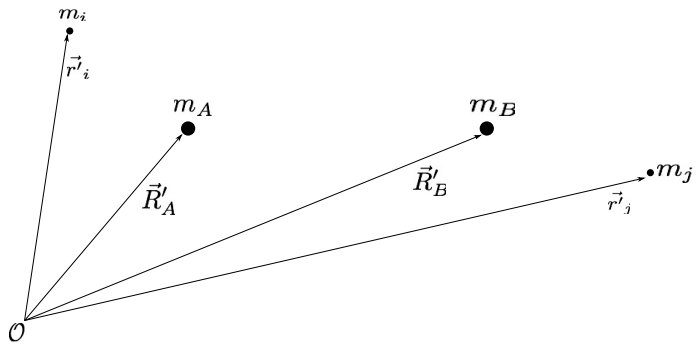

Figure 4. Geometry of a diatom in Space-Fixed Coordinates.

prescription as before we can move into a coordinate system where the positions of the electrons are referred to as their respective centers of mass. This is shown in Figure 5. The molecular Hamiltonian in center of mass coordinates is

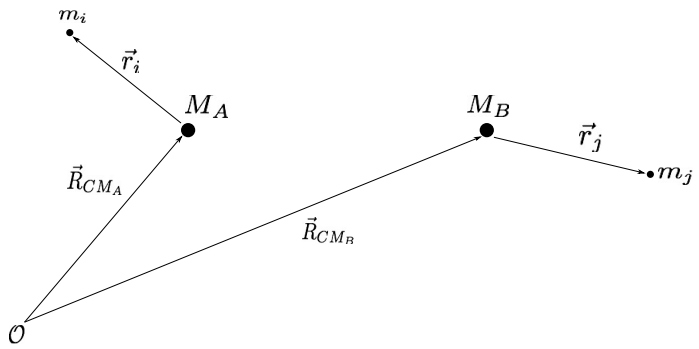

Figure 5. Geometry of a diatom in Space-Fixed Coordinates.

$$\begin{aligned}\widehat{\mathbf{H}} =& \frac{1}{2M_A}\vec{\nabla}^2_{\vec{R}_A} + \frac{1}{2M_B}\vec{\nabla}^2_{\vec{R}_B} + \widehat{\mathbf{H}}^0_A(\vec{r_i}) + \widehat{\mathbf{H}}^0_B(\vec{r_j}) \\ &+ \widehat{\mathbf{V}}^A_{ls}(\vec{r}_1, ..., \vec{r}_{N_A}, |\vec{R}_{CM_A} - \vec{R}_{CM_B}|) + \widehat{\mathbf{V}}^B_{ls}(\vec{r}_1, ..., \vec{r}_{N_B}, |\vec{R}_{CM_A} - \vec{R}_{CM_B}|) \\ &+ \widehat{\mathbf{V}}_{AB}(\vec{r}_1, ..., \vec{r}_{N_A}, \vec{r}_{N_A+1}, ..., \vec{r}_{N_A+N_B}, |\vec{R}_{CM_A} - \vec{R}_{CM_B}|). \end{aligned} \tag{41}$$

where $\widehat{\mathbf{H}}^0_A$ and $\widehat{\mathbf{H}}^0_B$ were defined in Equation (32). To further simplify this molecular Hamiltonian we can treat the two nuclei as a two body problem and move to a coordinate system that is referenced to the nuclear center of mass. However we leave the electron coordinates referenced to their respective nuclei. The new set of nuclear coordinates become:

$$\begin{aligned}\vec{R}_\mu &= \frac{M_A\vec{R}_{CM_A} + M_B\vec{R}_{CM_B}}{M_A + M_B} \\ \vec{R} &= \vec{R}_{CM_A} - \vec{R}_{CM_B}\end{aligned} \tag{42}$$

Lastly, we move the origin of the coordinate system to the center of mass effectively setting $\vec{R}_\mu = 0$. The final geometric configuration of the system, Figure 6, and the molecular Hamiltonian in space fixed coordinates are

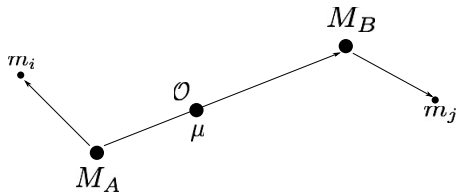

Figure 6. Geometry of a diatom in Space-Fixed Center of Mass Coordinates, $\vec{R}_\mu = 0$.

$$\widehat{\mathbf{H}} = \frac{1}{2\mu}\vec{P}^2_{\vec{R}_\mu} + \widehat{\mathbf{H}}^0_A(\vec{r}_{N_A}) + \widehat{\mathbf{H}}^0_B(\vec{r}_{N_B}) + \widehat{\mathbf{V}}^A_{ls}(\vec{r}_{N_A}, \vec{R}) + \widehat{\mathbf{V}}^B_{ls}(\vec{r}_{N_B}, \vec{R}) + \widehat{\mathbf{V}}_{AB}(\vec{r}_{N_A}, \vec{r}_{N_B}, \vec{R}). \tag{43}$$

When atom A is an alkali metal, M, and atom B is a noble gas, Ng the spin orbit potential of the noble gas is zero because in its ground state the electronic angular momentum is zero. Dropping this potential term the molecular Hamiltonian for atomic-noble gas collisions becomes

$$\begin{aligned}\widehat{\mathbf{H}} &= \frac{1}{2\mu}\vec{P}^2_{\vec{R}_\mu} + \widehat{\mathbf{H}}^0_M(\vec{r}_{N_M}) + \widehat{\mathbf{H}}^0_{Ng}(\vec{r}_{N_{Ng}}) + \widehat{\mathbf{V}}^M_{ls}(\vec{r}_{N_M}, \vec{R}) + \widehat{\mathbf{V}}_{MNg}(\vec{r}_{N_M}, \vec{r}_{N_Ng}, \vec{R}) \\ &= \frac{1}{2\mu}\vec{P}^2_{\vec{R}_\mu} + \widehat{\mathbf{H}}^0_{MNg}(\vec{r}_{N_M}, \vec{r}_{N_{Ng}}, \vec{R}) + \widehat{\mathbf{V}}^M_{ls}(\vec{r}_{N_M}, \vec{R})\end{aligned} \tag{44}$$

where $\widehat{\mathbf{H}}^0_{MNg}(\vec{r}_{N_M}, \vec{r}_{N_{Ng}}, \vec{R}) = \widehat{\mathbf{H}}^0_M(\vec{r}_{N_M}) + \widehat{\mathbf{H}}^0_{Ng}(\vec{r}_{N_{Ng}}) + \widehat{\mathbf{V}}_{MNg}(\vec{r}_{N_M}, \vec{r}_{N_Ng}, \vec{R})$.

This is the starting point for many such diatomic collision studies[1, 23, 30]. We grouped the electronic Hamiltonians and the electrostatic interaction potential terms in to an operator labeled $\widehat{\mathbf{H}}^0_{MNg}$ and now invoke the Born-Oppenheimer Expansion. By doing so we demote the continuous coordinate $\vec{R}$ to a parametric coordinate. We do this because as it stands the Hamiltonian in equation (44) is not separable due to the interaction potential $\widehat{\mathbf{V}}_{MNg}$. This problem is resolved by the Born-Oppenheimer Expansion.

2.6 The Born-Oppenheimer Expansion

One can envision taking two atomic species at a constant nuclear separation $\vec{R}$ and calculating the eigenvalues of the electronic Hamiltonian, $\widehat{\mathbf{H}}^0_{MNg}$, for this configuration. Now perform the same calculation, but bring the nuclear positions slightly closer. This process is repeated for all parametric values of $\vec{R}$. What is realized is a plot or surface of potential energy values required for specific nuclear configurations.

These surfaces are termed the adiabatic potential energy surfaces with respect to the interaction potential. The justification for this process lies in the fact that the nuclei are much more massive than the electrons. The electrons with their higher kinetic energy can settle in an eigenstate before the nuclear positions are perturbed again. The adiabatic potential energy surfaces become the potentials that the nuclei are subjected to during collision. The collision process then becomes a problem of determining nuclear dynamics, rather than electronic and nuclear dynamics.

The Hamiltonian for an alkali metal-noble gas (M-Ng) system is

$$\widehat{\mathbf{H}} = \widehat{\mathbf{T}}_N(\vec{R}) + \widehat{\mathbf{H}}^0_{MNg}(\vec{r}_{N_M}, \vec{r}_{N_{Ng}}, \vec{R}) + \widehat{\mathbf{V}}^M_{ls}(\vec{r}_{N_M}, \vec{R}). \tag{45}$$

where we have written the nuclear kinetic energy as an operator, $\widehat{T}_N(\vec{R}) = \frac{1}{2\mu}\vec{P}^2_{\vec{R}_\mu}$, N_M are the N electrons of the metal atom, and N_{Ng} are the N electrons of the noble gas. Determining these adiabatic surfaces is handled by solving the electronic Hamiltonian as a function of the parameter $\vec{R}$. This parameterization is denoted by the use of a semicolon in the interaction potential:

$$\widehat{\mathbf{H}}^0_{MNg}(\vec{r}_{N_M}, \vec{r}_{N_{Ng}}; \vec{R}) = \widehat{\mathbf{H}}^0_M(\vec{r}_{N_M}) + \widehat{\mathbf{H}}^0_{Ng}(\vec{r}_{N_{Ng}}) + \widehat{\mathbf{V}}_{MNg}(\vec{r}_{N_M}, \vec{r}_{N_{Ng}}; \vec{R}) \tag{46}$$

This Hamiltonian operates on the electronic Hilbert space such that

$$\widehat{\mathbf{H}}^0_{MNg}\Phi_i(\vec{r}; \vec{R}) = E_i(\vec{R})\Phi_i(\vec{r}; \vec{R}). \tag{47}$$

We have dropped the M and Ng labels on the electron coordinates and now refer all electron coordinate labels to the coordinate label $\vec{r}$. The Φ_i are molecular orbitals

that form a complete orthonormal basis set in the electronic space at every point $\vec{R}$.

$$\sum_{i=1}^{\infty} \Phi_i^*(\vec{r'};\vec{R})\Phi_i(\vec{r};\vec{R}) = \delta(\vec{r'}-\vec{r}) \tag{48}$$

$$\int_{\mathbb{R}^3} d\vec{r}\Phi_i^*(\vec{r};\vec{R})\Phi_j(\vec{r};\vec{R}) = \delta_{ij} \tag{49}$$

This basis is known as the Born-Oppenheimer molecular basis[30].

The solution to the total Hamiltonian, nuclear plus electronic, can be fashioned out of the Φ_i in a linear combination. This is known as the Born-Oppenheimer expansion[3]:

$$\Psi(\vec{r};\vec{R}) = \sum_i \chi_i(\vec{R})\Phi_i(\vec{r};\vec{R}) \tag{50}$$

$$\widehat{\mathbf{H}}\Psi(\vec{r};\vec{R}) = E\Psi(\vec{r};\vec{R}) \tag{51}$$

The total wave function is $\Psi(\vec{r};\vec{R})$, the expansion coefficients, $\chi_i(\vec{R})$, are the nuclear-centered wave functions, and E is the total energy of the system. These nuclear wave functions are what we wish to propagate for collisional studies, and therefore, we must understand how the total Hamiltonian acts on them in order to resolve their time evolution. In order to accomplish this insert Equation (50) into Equation (51), multiply from the left with $\Phi_j^*(\vec{r};\vec{R})$, and integrate over $\vec{r}$ utilizing the electronic orthogonality relations. Schrödinger's time independent Equation (51) becomes,

$$E\chi_i(\vec{R}) = \int d\vec{r}\Phi_j^*(\vec{r};\vec{R})[\widehat{\mathbf{T}}_N + \widehat{\mathbf{H}}^0_{MNg} + \widehat{\mathbf{V}}^M_{ls}]\sum_i \Phi_i(\vec{r};\vec{R})\chi_i(\vec{R}) \tag{52}$$

where we have separated the total Hamiltonian into the sum of its parts.

The first term of Equation (52) requires the use of the product rule for differentiation. Using the definition of the nuclear kinetic energy operator, $\widehat{\mathbf{T}}_N = -\frac{1}{2\mu}\vec{\nabla}_{\vec{R}}\cdot\vec{\nabla}_{\vec{R}}$,

the first term becomes (suppressing $(\vec{r};\vec{R})$ for notational brevity):

$$\begin{aligned}
&\int d\vec{r}\Phi_j^*(\vec{r};\vec{R})\widehat{\mathbf{T}}_N\Phi_i(\vec{r};\vec{R})\chi_i(\vec{R}) \\
&= -\int d\vec{r}\sum_i \frac{1}{2\mu}[\Phi_j^*\vec{\nabla}\cdot\vec{\nabla}(\Phi_i\chi_i)] \\
&= -\int d\vec{r}\sum_i \frac{1}{2\mu}[\Phi_j^*\vec{\nabla}\cdot(\Phi_i\vec{\nabla}\chi_i+\chi_i\vec{\nabla}\Phi_i)] \\
&= -\int d\vec{r}\sum_i \frac{1}{2\mu}[\Phi_j^*(\Phi_i\vec{\nabla}^2\chi_i+\vec{\nabla}\chi_i\cdot\vec{\nabla}\Phi_i+\chi_i\vec{\nabla}^2\Phi_i+\vec{\nabla}\Phi_i\cdot\vec{\nabla}\chi_i)] \\
&= -\int d\vec{r}\sum_i \frac{1}{2\mu}[\Phi_j^*(\Phi_i\vec{\nabla}^2\chi_i+2\vec{\nabla}\Phi_i\cdot\vec{\nabla}\chi_i+\vec{\nabla}^2\Phi_i\chi_i)] \\
&= -\int d\vec{r}\sum_i \frac{1}{2\mu}[\Phi_j^*(\Phi_i\vec{\nabla}^2+2\vec{\nabla}\Phi_i\cdot\vec{\nabla}+\vec{\nabla}^2\Phi_i)\chi_i] \qquad (53)
\end{aligned}$$

Making the association of $\Phi_i(\vec{r};\vec{R}) \rightarrow \left|\Phi_i(\vec{r};\vec{R})\right\rangle \rightarrow |i\rangle$, we can arrive at a compact form of Equation (53):

$$\begin{aligned}
\int d\vec{r}\Phi_j^*(\vec{r};\vec{R})\widehat{\mathbf{T}}_N\Phi_i(\vec{r};\vec{R})\chi_i(\vec{R}) &= -\sum_j \frac{1}{2\mu}[\delta_{ij}\vec{\nabla}^2_{\vec{R}}+2F_{ji}\cdot\vec{\nabla}_{\vec{R}}+G_{ji}]\chi_i(\vec{R}) \\
&= -\sum_j \frac{1}{2\mu}[\delta_{ij}\vec{\nabla}^2_{\vec{R}}+\Lambda_{ji}]\chi_i(\vec{R}) \qquad (54)
\end{aligned}$$

where, $F_{ji} = \langle j|\,\vec{\nabla}_{\vec{R}}\,|i\rangle$, $G_{ji} = \langle j|\,\vec{\nabla}^2_{\vec{R}}\,|i\rangle$ and $\Lambda_{ji} = 2F_{ji}\cdot\vec{\nabla}_A + G_{ji}$.

The **F** matrix vector in Equation (54) is known as the derivative coupling matrix vector. These non-diagonal matrix elements in the nuclear kinetic energy couple eigenstates of the electronic Hamiltonian. The **G** matrix is known as the scalar coupling matrix and is of second order compared to the derivative couplings.

The second term of Equation (52) is easiest to handle by use of Equations (47) and (49):

$$\int d\vec{r}\Phi_j^*(\vec{r};\vec{R})\widehat{\mathbf{H}}^0_{MNg}\sum_i \Phi_i(\vec{r};\vec{R})\chi_i(\vec{R}) = E_j\chi_j(\vec{R}) \qquad (55)$$

The third and last term, the spin-orbit potential, is simply left as is to be evaluated properly in the next chapter.

When combined with Equation (52) and then inserted in to Equation (51) the Born-Oppenheimer expansion takes the following form:

$$[\widehat{\mathbf{T}}_N + E_j(\vec{R})]\chi_j(\vec{R}) + \langle j|\, \widehat{\mathbf{V}}^M_{ls}\, |i\rangle\, \chi_i(\vec{R}) - \sum_i \Lambda_{ji}\chi_i(\vec{R}) = E\chi_j(\vec{R}) \tag{56}$$

We will see in the sSection 2.8 that states where the electronic adiabatic energies approach each other will couple strongly. If we only include the coupled states in Equation (56) and neglect the non-coupled states then we enter a regime known as the group Born-Oppenheimer approximation. The dimension of Λ_{ji} is the number of coupled states. In the limit that the set of coupled states contain a single state then we are in what is known as the Born-Oppenheimer approximation[47].

2.7 Two State Born-Oppenheimer Expansion Derivation

To understand the implications of the derivative coupling matrix on the molecular Hamiltonian we derive the effect upon a simple two level system. We start the two-state Born-Oppenheimer expansion by first assuming that only a group of two molecular states are energetically coupled. In doing so we have two molecular orbitals that when acted upon by the electronic Hamiltonian produce two adiabatic potential surfaces labeled A_1 and A_2:

$$\widehat{\mathbf{H}}_e(\vec{r};\vec{R})\Phi_1(\vec{r};\vec{R}) = A_1(\vec{R})\Phi_1(\vec{r};\vec{R}) \tag{57}$$

$$\widehat{\mathbf{H}}_e(\vec{r};\vec{R})\Phi_2(\vec{r};\vec{R}) = A_2(\vec{R})\Phi_2(\vec{r};\vec{R}) \tag{58}$$

where,

$$\langle \Phi_1 | \Phi_1 \rangle = \langle \Phi_2 | \Phi_2 \rangle = 1$$

$$\langle \Phi_1 | \Phi_2 \rangle = 0$$

The total wave function is expanded using a combination of the molecular orbitals with the nuclear wave functions as the expansion coefficients:

$$\Psi = \chi_1(\vec{R})\Phi_1(\vec{r};\vec{R}) + \chi_2(\vec{R})\Phi_2(\vec{r};\vec{R}) \tag{59}$$

Now take the full Hamiltonian, nuclear kinetic plus electronic energy, and solve for the nuclear wave functions.

$$\widehat{\mathbf{H}}\Psi = E\Psi$$

$$(\widehat{\mathbf{T}}_N + \widehat{\mathbf{H}}_e)\{\chi_1\Phi_1 + \chi_2\Phi_2\} = E\{\chi_1\Phi_1 + \chi_2\Phi_2\}$$

Using the electronic Hamiltonian eigen-equations come in from the left with Φ_1^*.

$$\begin{aligned} E\chi_1 &= \int d\vec{r}\Phi_1^*(\widehat{\mathbf{T}}_N + \widehat{\mathbf{H}}_e)\{\chi_1\Phi_1 + \chi_2\Phi_2\} \\ &= \int d\vec{r}\Phi_1^*\widehat{\mathbf{T}}_N(\chi_1\Phi_1 + \chi_2\Phi_2) + \int d\vec{r}\Phi_1^* A_1\chi_1\Phi_1 + \int d\vec{r}\Phi_1^* A_1\chi_1\Phi_2 \end{aligned}$$

The third term becomes zero by the molecular orbital orthogonality relations and we continue by specifying the nuclear operator as $\widehat{\mathbf{T}}_N = -\frac{1}{2\mu}\vec{\nabla}\cdot\vec{\nabla}$.

$$\begin{aligned}(E-A_1)\chi_1 &= -\frac{1}{2\mu}\int d\vec{r}\Phi_1^*\vec{\nabla}\cdot\vec{\nabla}(\chi_1\Phi_1+\chi_2\Phi_2)\\ &= -\frac{1}{2\mu}\int d\vec{r}\Phi_1^*\vec{\nabla}\cdot\{\vec{\nabla}\chi_1\Phi_1+\chi_1\vec{\nabla}\Phi_1+\vec{\nabla}\chi_2\Phi_2+\chi_2\vec{\nabla}\Phi_2\}\\ &= -\frac{1}{2\mu}\int d\vec{r}\Phi_1^*\{\vec{\nabla}^2\chi_1\Phi_1+\vec{\nabla}\chi_1\vec{\nabla}\Phi_1+\vec{\nabla}\chi_1\vec{\nabla}\Phi_1+\chi_1\vec{\nabla}^2\Phi_1\\ &+\vec{\nabla}^2\chi_2\Phi_2+\vec{\nabla}\chi_2\vec{\nabla}\Phi_2+\vec{\nabla}\chi_2\vec{\nabla}\Phi_2+\chi_2\vec{\nabla}^2\Phi_2\}\end{aligned}$$

Continue by collecting terms and factoring:

$$\begin{aligned}(E-A_1)\chi_1 &= -\frac{1}{2\mu}\vec{\nabla}^2\chi_1-\frac{1}{2\mu}\int d\vec{r}\{2\Phi_1^*\vec{\nabla}\Phi_1\vec{\nabla}+\Phi_1^*\vec{\nabla}^2\Phi_1\}\chi_1\\ &-\frac{1}{2\mu}\int d\vec{r}\{2\Phi_1^*\vec{\nabla}\Phi_2\vec{\nabla}+\Phi_1^*\vec{\nabla}^2\Phi_2\}\chi_2\\ &= \widehat{\mathbf{T}}_N\chi_1-\frac{1}{2\mu}\{2\langle\Phi_1|\vec{\nabla}\Phi_1\rangle\cdot\vec{\nabla}+\langle\Phi_1|\vec{\nabla}^2\Phi_1\rangle\}\chi_1\\ &-\frac{1}{2\mu}\{2\langle\Phi_1|\vec{\nabla}\Phi_2\rangle\cdot\vec{\nabla}+\langle\Phi_1|\vec{\nabla}^2\Phi_2\rangle\}\chi_2\end{aligned}$$

The same analysis is repeated to the full Hamiltonian except we come in from the left with Φ_2^* instead of Φ_1^*.

$$\begin{aligned}(E-A_2)\chi_2 &= \widehat{\mathbf{T}}_N\chi_2-\frac{1}{2\mu}\{2\langle\Phi_2|\vec{\nabla}\Phi_1\rangle\cdot\vec{\nabla}+\langle\Phi_2|\vec{\nabla}^2\Phi_1\rangle\}\chi_1\\ &-\frac{1}{2\mu}\{2\langle\Phi_2|\vec{\nabla}\Phi_2\rangle\cdot\vec{\nabla}+\langle\Phi_2|\vec{\nabla}^2\Phi_2\rangle\}\chi_2\end{aligned}$$

Labeling $F_{ji} = \langle\Phi_j|\vec{\nabla}\Phi_i\rangle$ and $G_{ji} = \langle\Phi_j|\vec{\nabla}^2\Phi_i\rangle$, $i,j = 1,2$, the final two results can be combined into a matrix equation with $\mathbf{A}$ being the diagonal matrix of adiabatic

energies and $\mathbb{I}$ the identity matrix:

$$\widehat{\mathbf{T}}_N\Psi - \frac{1}{2\mu}(2\mathbf{F}\cdot\vec{\nabla} + \mathbf{G})\Psi + (\mathbf{A} - E\mathbb{I})\Psi = 0. \tag{60}$$

This can be more succinctly written as[47],

$$\left[-\frac{1}{2\mu}(\vec{\nabla} + \mathbf{F})^2 + (\mathbf{A} - E\mathbb{I})\right]\Psi = 0 \tag{61}$$

The dressed kinetic energy operator $(\vec{\nabla} + \mathbf{F})^2$ has many analogies with gauge theory and this is a useful starting point for investigation.

At this point we need to get rid of the derivative coupling term in Equation (61) for reasons necessitated by computational considerations (see section 5.2) . This can be accomplished for the two state system by rotating the nuclear wave function using a 2x2 unitary rotation matrix. Denote this rotation matrix $\mathbf{U}$ such that the new nuclear wave function is:

$$\Psi = \mathbf{U}\xi \tag{62}$$

Inserting this in to equation (61) we can derive a condition that $\mathbf{U}$ must satisfy such that the dressed kinetic energy term $(\vec{\nabla} + \mathbf{F})^2$ becomes diagonal[3].

$$\begin{aligned}
(\vec{\nabla} + \mathbf{F})^2\mathbf{U}\xi &= (\vec{\nabla} + \mathbf{F})(\vec{\nabla} + \mathbf{F})U\xi = (\vec{\nabla} + \mathbf{F})[\vec{\nabla}(\mathbf{U}\xi) + \mathbf{F}\mathbf{U}\xi] \\
&= (\vec{\nabla} + \mathbf{F})[\mathbf{U}(\vec{\nabla}\xi) + \xi(\vec{\nabla}\mathbf{U}) + \mathbf{F}\mathbf{U}\xi] \\
&= [\vec{\nabla}(\mathbf{U}(\vec{\nabla}\xi)) + \vec{\nabla}(\xi(\vec{\nabla}\mathbf{U})) + \vec{\nabla}(\mathbf{F}\mathbf{U}\xi)] + [\mathbf{F}\mathbf{U}(\vec{\nabla}\xi) + \mathbf{F}\xi(\vec{\nabla}\mathbf{U}) + \mathbf{F}^2\mathbf{U}\xi] \\
&= \mathbf{U}\vec{\nabla}^2\xi + \vec{\nabla}\xi\vec{\nabla}\mathbf{U} + \xi\vec{\nabla}^2\mathbf{U} + \vec{\nabla}\mathbf{U}\vec{\nabla}\xi + \mathbf{F}\vec{\nabla}(\mathbf{U}\xi) + \mathbf{U}\xi\vec{\nabla}(\mathbf{F}) \\
&+ [\mathbf{F}\mathbf{U}(\vec{\nabla}\xi) + \mathbf{F}\xi(\vec{\nabla}\mathbf{U}) + \mathbf{F}^2\mathbf{U}\xi] \\
&= 2(\vec{\nabla}\mathbf{U})\cdot\vec{\nabla}\xi + \mathbf{U}\vec{\nabla}^2\xi + (\vec{\nabla}^2\mathbf{U})\xi + (\vec{\nabla}\mathbf{F})\mathbf{U}\xi + 2\mathbf{F}(\vec{\nabla}\mathbf{U})\xi + 2\mathbf{F}\mathbf{U}(\vec{\nabla}\xi) + \mathbf{F}^2\mathbf{U}\xi
\end{aligned}$$

Upon using the product rule to shorten this expression we finally arrive at the following equation:

$$(\vec{\nabla} + \mathbf{F})^2 \mathbf{U}\xi = \mathbf{U}\vec{\nabla}^2\xi + 2(\vec{\nabla}\mathbf{U} + \mathbf{F}\mathbf{U}) \cdot \vec{\nabla}\xi + \{(\mathbf{F} + \vec{\nabla}) \cdot (\vec{\nabla}\mathbf{U} + \mathbf{F}\mathbf{U})\}\xi \tag{63}$$

By constraining the rotation matrix $\mathbf{U}$ to be the solution to the following differential equation,

$$\vec{\nabla}\mathbf{U} + \mathbf{F}\mathbf{U} = 0, \tag{64}$$

the dressed kinetic energy operator becomes diagonal once again. This is the local gauge for Equation (61)[47].

$$(\vec{\nabla} + \mathbf{F})^2 \mathbf{U}\xi = \mathbf{U}\vec{\nabla}^2\xi \tag{65}$$

Inserting this result back in to equation (61) we find that:

$$-\frac{1}{2\mu}\mathbf{U}\vec{\nabla}^2\xi + (\mathbf{A} - E\mathbb{I})\mathbf{U}\xi = 0 \tag{66}$$

Since the 2x2 rotation matrix is unitary we can come in from the left with $\mathbf{U}^\dagger$ to realize that

$$-\frac{1}{2\mu}\vec{\nabla}^2\xi + (\mathbf{U}^\dagger A\mathbf{U} - E\mathbb{I})\xi = 0. \tag{67}$$

The kinetic energy operator now contains zero off diagonal terms, but at the same time to keep the integrity of Schrodinger's Equation the adiabatic potential energy surfaces are no longer diagonal and we have created the strictly diabatic representation of the potential energy surfaces:

$$D = \mathbf{U}^\dagger A\mathbf{U} \tag{68}$$

For the two state example used in this scenario, if the molecular wave functions are real then the **F** matrix becomes an anti-symmetric matrix. Also, given that the Adiabatic to Diabatic Transformation (ADT) matrix, **U**, is a 2x2 rotation matrix, it only has one degree of freedom the rotation angle, $\alpha(\vec{R})$. Equation (64) is now expanded to solve for **U**:

$$\vec{\nabla}\begin{pmatrix} cos(\alpha(\vec{R})) & -sin(\alpha(\vec{R})) \\ sin(\alpha(\vec{R})) & cos(\alpha(\vec{R})) \end{pmatrix} + \begin{pmatrix} F_{11} & F_{12} \\ F_{21} & F_{22} \end{pmatrix}\begin{pmatrix} cos(\alpha(\vec{R})) & -sin(\alpha(\vec{R})) \\ sin(\alpha(\vec{R})) & cos(\alpha(\vec{R})) \end{pmatrix} = 0 \quad (69)$$

The four equations that follow are:

$$\frac{\partial}{\partial R}\alpha = F_{11}cot(\alpha) + F_{12} \quad (70)$$

$$\frac{\partial}{\partial R}\alpha = F_{11}tan(\alpha) + F_{12} \quad (71)$$

$$\frac{\partial}{\partial R}\alpha = -F_{21} + F_{22}tan(\alpha) = F_{12} + F_{22}tan(\alpha) \quad (72)$$

$$\frac{\partial}{\partial R}\alpha = -F_{21} + F_{22}cot(\alpha) = F_{12} + F_{22}cot(\alpha) \quad (73)$$

The angular derivatives of the $\vec{\nabla}$ operator are handled by the angular momentum calculus in Section 3.4.

The diagonal elements F_{11} and F_{22} typically are equal to zero[47] as the result of symmetry and we are left with one equation relating the rotation angle with the off

diagonal coupling term. Its solution is the following:

$$\begin{aligned}
\frac{\partial}{\partial R}\alpha &= F_{12} \\
\frac{\partial}{\partial R}\alpha(\vec{R}) &= \int dr \Phi_1^*(\vec{r};\vec{R})\frac{\partial}{\partial R}\Phi_2^*(\vec{r};\vec{R}) \\
\int_{R_0}^{R}\frac{\partial}{\partial R}\alpha(\vec{R}) &= \int_{R_0}^{R} dR \int dr \Phi_1^*(\vec{r};\vec{R})\frac{\partial}{\partial R}\Phi_2^*(\vec{r};\vec{R}) \\
\alpha(\vec{R}) &= \alpha(\vec{R_0}) + \int_{R_0}^{R} dR \int dr \Phi_1^*(\vec{r};\vec{R})\frac{\partial}{\partial R}\Phi_2^*(\vec{r};\vec{R})
\end{aligned} \tag{74}$$

The contour integral in this case happens to be a simple line integral along one direction. Therefore in the two atom collision case strictly diabatic potential energy surfaces can be calculated. If more than one degree of freedom existed, say for instance collisions between three atoms or an atom and a diatom, then the contour integral is used to minimize the effect the derivative coupling terms. When this is the case the surfaces are called quasi-diabatic potential energy surfaces[47].

2.8 Adiabatic Approximation

The derivative coupling and scalar coupling terms in equation (54) pose a problem. In order to properly propagate a collision event using a time dependent computational technique the kinetic energy operator must be diagonal in the the momentum representation so the exponential of the kinetic energy becomes a simple multiplication operation (sec 5.2). There are two solutions.

The first solution involves simply disregarding the kinetic energy coupling terms in what is known as the Adiabatic Approximation:

$$[\widehat{\mathbf{T}}_N + E_j(\vec{R}) - E]\chi_j = 0 \tag{75}$$

Only when the derivative coupling terms are small will this approximation be valid.

The coupling terms can also approach zero if the nuclear masses tend to infinity so that $\frac{1}{2\mu}F_{ji} \approx 0$. It is possible though that even in the scenario where the nuclear masses are large the coupling terms can still tend toward infinity.

One can explore the commutation between the nuclear momentum operator and the electronic Hamiltonian to understand when this approximation is valid.

$$\begin{aligned}\langle i|\left[\widehat{P}_A, \widehat{H}_e\right]|j\rangle &= \langle i|\,\widehat{P}_A\widehat{H}_e\,|j\rangle - \langle i|\,\widehat{H}_e\widehat{P}_A]\,|j\rangle \\ &= E_j\,\langle i|\,\widehat{P}_A\,|j\rangle - E_i\,\langle i|\,\widehat{P}_A\,|j\rangle \\ &= (E_j - E_i)\,\langle i|\,\widehat{P}_A\,|j\rangle \end{aligned} \tag{76}$$

and so,

$$\langle i|\,\widehat{P}_A\,|j\rangle = -iF_{ij} = \frac{\langle i|\left[\widehat{P}_A, \widehat{H}_e\right]|j\rangle}{(E_j - E_i)} \tag{77}$$

If the adiabatic electronic energy levels, E_j and E_i, at a particular nuclear separation distance, R, approach each other then these coupling terms cannot be ignored and can tend toward infinity. However if the levels never approach each other then one can simply evoke this approximation without any consequence.

The second solution is of course to follow the outline of the two-state example and compute the gauge that transforms the dressed kinetic energy operator in to a diagonal kinetic energy operator. As the number of coupled states increase so does the size of the rotation matrix required to accomplish this transformation. This solution will be pursued.

2.9 Summary

The description of a molecule first includes choosing a coordinate system to describe the positions of the nuclei and the electrons. In particular we have shown the transformation from space-fixed coordinates to center of mass space-fixed coordinates.

This however isn't the only choice that can be made. Some authors have shown the geometrical center of nuclei coordinate system to be useful[33]. No description is right or wrong and ultimately the coordinate system choice that makes the Hamiltonian simplest to solve is chosen.

The effect of the interaction potential is to make the molecular Hamiltonian inseparable. Fortunately the differences in mass between the electrons and nuclei allow the electronic portion of the problem to be solved first via the Born-Oppenheimer expansion. What remains is to solve the nuclear portion of the problem, $\chi_i(\vec{R})$.

The $\chi_i(\vec{R})$ to be solved are subjected to equations (56). For reasons that will be explained in the next chapter we only need to concern ourselves with solving six coupled nuclear wave functions for alkali-noble gas collisions. Though not yet obvious in equation (56) the chief state to state coupling mechanisms are spin-orbit, Coriolis, and radial derivative. Radial derivative coupling has already been hinted at in equation (54) via the F_{ji} and G_{ji} matrix elements. These three couplings account for the majority non-radiative of state to state transitions.

III. Close-Coupled Equations

3.1 Introduction

In order to fully express the molecular Hamiltonian in space-fixed center of mass coordinates a basis must be chosen. This was done with an atom in section 2.4, but now it must be done with a molecule. First, we list the meanings of all the relative quantum numbers and their respective space-fixed z-axis and body-fixed projections:

s, m_s, σ - electron spin angular momentum

l, m_l, λ - electron orbital angular momentum

j, m_j, ω - total electron angular momentum

L, K, Λ - nuclear molecular angular momentum

J, M, Ω - total molecular angular momentum

By virtue of being inert the noble gas atom has no spin-orbital angular momentum and so does not contribute to the molecular electronic angular momentum. All electronic angular momentum is due to the alkali atom. Therefore as shown in the atomic description of an atom we use the method of addition of angular momentum to express the Born-Oppenheimer molecular basis vectors as $\left|\vec{R}, {}^{j}_{m_j}\right\rangle = \sum_{m_l}\sum_{m_s}\langle lm_l, sm_s|jm_j, ls\rangle \left|\vec{R}, {}^{l\ s}_{m_l m_s}\right\rangle$. However these state vectors are now dependent on the distance, $\vec{R}$, between the nuclei.

Semi-classically the nuclear angular momentum is varied by examining different values of the impact parameter. For the full quantum mechanical treatment this is accomplished by utilizing a complete set of angular wave functions. In particular we will use the angular harmonics labeled $\Theta^L_{K\Lambda}$. The total molecular wave function via

the Born-Oppenheimer expansion is written down as

$$\Psi(\vec{r};\vec{R}) = \sum_{L,K} \Theta^{L}_{K\Lambda} \frac{\chi_{L,K}(R)}{R} \Phi_{j,m_j}(\vec{r};\vec{R}). \tag{78}$$

where $\Phi_{j,m_j}(\vec{r};\vec{R}) = \langle \vec{r} \,|\vec{R},\, {}^{j}_{m_j}\rangle$ are eigenstates of $\widehat{\mathbf{H}}^{0}_{MNg}$ and $\vec{R}$ behaves as a parameter.

To solve for the nuclear wave functions insert the molecular wave function in to the molecular Hamiltonian and come in from the left with $\left\langle \vec{R},\, {}^{j'}_{m'_j} \right|$:

$$\widehat{\mathbf{H}}\Psi = E\Psi \tag{79}$$

$$\left\langle \vec{R},\, {}^{j'}_{m'_j} \right| (\widehat{\mathbf{T}}_N + \widehat{\mathbf{H}}^{0}_{MNg} + \widehat{\mathbf{V}}^{M}_{ls}) \sum_{L,K} \Theta^{L}_{K\Lambda}(\theta,\phi) \frac{\chi_{L,K}(R)}{R} \left| \vec{R},\, {}^{j}_{m_j} \right\rangle = \left\langle \vec{R},\, {}^{j'}_{m'_j} \right| E \sum_{L,K} \Theta^{L}_{K\Lambda} \frac{\chi_{L,K}(R)}{R} \left| \vec{R},\, {}^{j}_{m_j} \right\rangle. \tag{80}$$

The matrix elements in the Born-Oppenheimer bases are,

$$\sum_{L,K} \left\langle \vec{R},\, {}^{j'}_{m'_j} \right| \widehat{\mathbf{T}}_N \left| \vec{R},\, {}^{j}_{m_j} \right\rangle \Theta^{L}_{K\Lambda} \frac{\chi_{L,K}(R)}{R} \tag{81}$$

$$+ \sum_{L,K} \left\langle \vec{R},\, {}^{j'}_{m'_j} \right| \widehat{\mathbf{H}}^{0}_{MNg} \left| \vec{R},\, {}^{j}_{m_j} \right\rangle \Theta^{L}_{K\Lambda} \frac{\chi_{L,K}(R)}{R} \tag{82}$$

$$+ \sum_{L,K} \left\langle \vec{R},\, {}^{j'}_{m'_j} \right| \widehat{\mathbf{V}}^{M}_{ls} \left| \vec{R},\, {}^{j}_{m_j} \right\rangle \Theta^{L}_{K\Lambda} \frac{\chi_{L,K}(R)}{R} \tag{83}$$

$$= \sum_{L,K} \left\langle \vec{R},\, {}^{j'}_{m'_j} \right| E \left| \vec{R},\, {}^{j}_{m_j} \right\rangle \Theta^{L}_{K\Lambda} \frac{\chi_{L,K}(R)}{R}. \tag{84}$$

For the M-Ng system at the energies of interest to DPALs operation we only need to consider the group of molecular states in the P-manifold. That is we only need to concern ourselves with a maximum electronic orbital angular momentum of one, $l = 1$, and an electronic spin angular momentum of one half, $s = 1/2$. This means that there are only a total of six electronic molecular states to consider. These states are labeled as $\left|\vec{R},\, {}^{j}_{m_j}\right\rangle$: $\left|{}^{3/2}_{3/2}\right\rangle$, $\left|{}^{3/2}_{1/2}\right\rangle$, $\left|{}^{1/2}_{1/2}\right\rangle$, $\left|{}^{3/2}_{-3/2}\right\rangle$, $\left|{}^{3/2}_{-1/2}\right\rangle$, $\left|{}^{1/2}_{-1/2}\right\rangle$ where the dependence

on $\vec{R}$ is given, but dropped for notational sake. As such we expect for each L, K label, equations (81) - (84) will be at most a set of 6x6 matrices.

Before the nuclear wave functions are subjected to Schrödinger's Time Dependent Equation and the S-Matrix formulation we now explicitly determine the functional form of the Hamiltonian and explain mechanistically each coupling phenomenon. This will be greatly aided by moving in to yet another coordinate system, one that rotates with the internuclear vector, $\vec{R}$. This coordinate system is known as the body-fixed coordinate system.

Both the Hamiltonian and total wave function are subjected to these rotations.

3.2 Rotating Coordinate System

Up till now all geometrical inquiries have taken place in space-fixed coordinates. There is one last transformation to be made, the transformation to body-fixed coordinates. This will essentially turn the two body problem in to a one dimensional problem involving only the nuclear coordinate R. The nuclear coordinates θ and ϕ will then be handled by the angular momentum calculus.

The space-fixed coordinate system is rotated such that the new z-axis, the z-axis of the body-fixed coordinate system, always moves with the internuclear vector $\vec{R}$. The process to bring about this change is described in Figure 7.

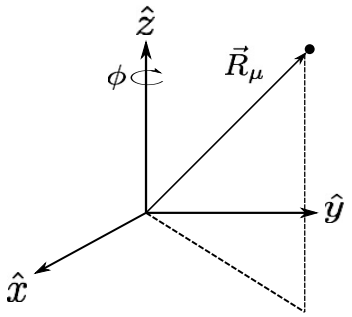

(a) First, rotate ϕ about the $\hat{z}$-axis such that $\hat{x}$ lies anti-parallel to the projection of $\vec{R}_\mu$ in the $\hat{x}$-$\hat{y}$ plane.

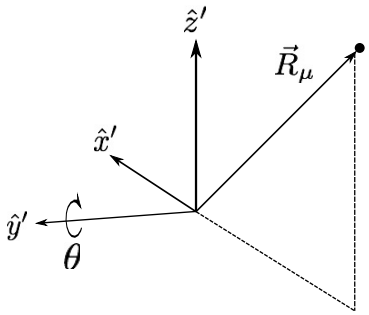

(b) Next, rotate θ about the $\hat{y}'$-axis such that $\hat{z}'$ lies along $\vec{R}_\mu$.

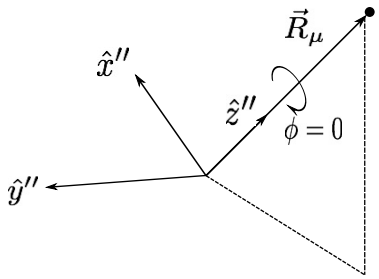

(c) Lastly, rotate $\phi = 0$ about the $\hat{z}''$-axis

Figure 7. Euler rotations that produce body-fixed coordinates.

This rotation operator, $\mathcal{R}$, is represented by the matrix $\mathbb{R}(\phi, \theta, 0)$:

$$\begin{pmatrix} \hat{x}'' \\ \hat{y}'' \\ \hat{z}'' \end{pmatrix} = \mathbb{R}(\phi, \theta, 0) \begin{pmatrix} \hat{x} \\ \hat{y} \\ \hat{z} \end{pmatrix}$$
$$= \begin{pmatrix} cos(\theta)cos(\phi) & cos(\theta)sin(\phi) & -sin(\theta) \\ -sin(\phi) & cos(\phi) & 0 \\ sin(\theta)cos(\phi) & sin(\theta)sin(\phi) & cos(\theta) \end{pmatrix} \begin{pmatrix} \hat{x} \\ \hat{y} \\ \hat{z} \end{pmatrix} \tag{85}$$

where the double primed vector represent the body fixed coordinates. In relation to the space-fixed coordinate system, the body-fixed coordinates follow the spherical-polar representation of $\vec{R}$. This means the body-fixed basis vectors point in the same direction as spherical-polar space-fixed basis vectors: $\hat{x}'' = \hat{\theta}$, $\hat{y}'' = \hat{\phi}$, $\hat{z}'' = \hat{R}$. This fact will be useful in Section 3.4.

These rotations are now applied to both the space-fixed Hamiltonian and its wave function. This is accomplished first by inserting $\mathbb{I} = \mathcal{R}\mathcal{R}^{-1}$ in Hamilton's equation,

$$\widehat{\mathbf{H}}(\vec{r}, \vec{R})\mathcal{R}\mathcal{R}^{-1}\Psi(\vec{r}; \vec{R}) = E\Psi(\vec{r}; \vec{R}) \tag{86}$$

and then multiplying on the left by $\mathcal{R}^{-1}$,

$$\mathcal{R}^{-1}\widehat{\mathbf{H}}(\vec{r}, \vec{R})\mathcal{R}\mathcal{R}^{-1}\Psi(\vec{r}; \vec{R}) = E\mathcal{R}^{-1}\Psi(\vec{r}; \vec{R}) \tag{87}$$

$$\widehat{\mathbf{H}}(\vec{\mathfrak{r}}, R)\Psi(\vec{\mathfrak{r}}, R) = E\Psi(\vec{\mathfrak{r}}, R) \tag{88}$$

where $\widehat{\mathbf{H}}(\vec{\mathfrak{r}}, R) = \mathcal{R}^{-1}\widehat{\mathbf{H}}(\vec{r}, \vec{R})\mathcal{R}$ and $\Psi(\vec{\mathfrak{r}}, R) = \mathcal{R}^{-1}\Psi(\vec{r}; \vec{R})$ are the body-fixed Hamiltonian and wave function.

Notice now that the new nuclear coordinate is simply R. This has a couple implications. First, traveling with the body causes all information concerning nuclear

θ and nuclear ϕ orientation to be lost. This makes $\mathbf{L}$ and $\mathbf{K}$ poor quantum numbers to keep track of. However we can always rely on the conserved quantity $\mathbf{J}$ and its projection, Ω, along the $\hat{z}''$ or R direction. The body-fixed nuclear wave functions read $\Theta^J_{M\Omega}\frac{\chi_{J,\Omega}(R)}{R}$ compared to the space-fixed nuclear wave functions $\Theta^L_{K\Lambda}\frac{\chi_{L,K}(R)}{R}$. Second, the rotation $\mathcal{R}$ only depends on θ and ϕ so if an operator or constant of motion does not depend on these nuclear coordinates then that operator or constant is unaffected by the transition from space-fixed to body-fixed coordinates. So, $\widehat{\mathbf{H}}^0_{MNg}$, $\widehat{\mathbf{V}}^M_{ls}$, and E are then unaffected because they depend on rotationally invariant distances and scalar products that are independent of θ and ϕ. $\widehat{\mathbf{T}}_N$ however is affected.

Equations (81) - (84) take on a new form in body-fixed coordinates:

$$\sum_{J,\Omega}\left\langle R,\, {}^{j'}_{\omega'}\right| \mathcal{R}^{-1}\widehat{\mathbf{T}}_N\mathcal{R}\left|R,\, {}^{j}_{\omega}\right\rangle \Theta^J_{M\Omega}\frac{\chi_{J,\Omega}(R)}{R} \tag{89}$$

$$+\sum_{J,\Omega}\left\langle R,\, {}^{j'}_{\omega'}\right| \widehat{\mathbf{H}}^0_{MNg}\left|R,\, {}^{j}_{\omega}\right\rangle \Theta^J_{M\Omega}\frac{\chi_{J,\Omega}(R)}{R} \tag{90}$$

$$+\sum_{J,\Omega}\left\langle R,\, {}^{j'}_{\omega'}\right| \widehat{\mathbf{V}}^M_{ls}\left|R,\, {}^{j}_{\omega}\right\rangle \Theta^J_{M\Omega}\frac{\chi_{J,\Omega}(R)}{R} \tag{91}$$

$$=\sum_{J,\Omega}\left\langle R,\, {}^{j'}_{\omega'}\right| E\left|\vec{R},\, {}^{j}_{\omega}\right\rangle \Theta^J_{M\Omega}\frac{\chi_{J,\Omega}(R)}{R}. \tag{92}$$

The next three sections will be devoted to expanding the body-fixed molecular Hamiltonian in the P-manifold group of coupled states: $\left|\vec{R},\, {}^{J\,j}_{\Omega m_j}\right\rangle$: $\left|{}^{J\,3/2}_{\Omega 3/2}\right\rangle$, $\left|{}^{J\,3/2}_{\Omega 1/2}\right\rangle$, $\left|{}^{J\,1/2}_{\Omega 1/2}\right\rangle$, $\left|{}^{J\,3/2}_{\Omega -3/2}\right\rangle$, $\left|{}^{J\,3/2}_{\Omega -1/2}\right\rangle$, $\left|{}^{J\,1/2}_{\Omega -1/2}\right\rangle$. We insert in to the six state vectors the quantum numbers $\mathbf{J}$ and $\mathbf{\Omega}$ to help elucidate all coupling details. In the final set of coupled equations we recognize that any operator acting on J, Ω act on the angular harmonics. First, equations (90) and (91) will be expanded to show the effect of Spin-Orbit Coupling. Then equation (89) will be expanded to show the effects of both Coriolis and radial coupling.

3.3 Spin-Orbit Coupling

Within the Born-Oppenheimer regime the electronic eigenfunctions of the electronic Hamiltonian, $\widehat{\mathbf{H}}^0_{MNg}$, are traditionally designated by the quantum numbers λ, L, σ, and s[1]. The eigen energies of $\widehat{\mathbf{H}}^0_{MNg}$ are the adiabatic PES with respect to the interaction potential and are calculated by *ab initio* techniques. The eigen equation of ths M-Ng system reads

$$\widehat{\mathbf{H}}^0_{MNg} \left| R, n \, {}^{l\ s}_{\lambda\sigma} \right\rangle = W_{\lambda,\sigma,l,s}(R) \left| R, n \, {}^{l\ s}_{\lambda\sigma} \right\rangle . \tag{93}$$

Using the group Born-Oppenheimer approximation only states with L=0,1 and s=$\pm$1/2 are of concern. Molecularly speaking then at this level of theory we expect only two adiabatic electronic energy surfaces labeled W_Π an W_Σ which will be written as Π and Σ. In it's 6x6 matrix form, suppressing the R notational dependence, the electronic Hamiltonian in the $\left| {}^{l\ s}_{\lambda\sigma} \right\rangle$ basis appears as,

$$\widehat{\mathbf{H}}^0_{MNg} = \begin{array}{c} \begin{array}{ccc} \left| {}^{1\ \frac{1}{2}}_{1\pm\frac{1}{2}} \right\rangle & \left| {}^{1\ \ 1/2}_{-1\pm 1/2} \right\rangle & \left| {}^{1 1/2}_{0\pm 1/2} \right\rangle \end{array} \\ \begin{pmatrix} \Pi & 0 & 0 \\ 0 & \Pi & 0 \\ 0 & 0 & \Sigma \end{pmatrix} \end{array} \tag{94}$$

The spin-orbit operator, $\widehat{\mathbf{V}}^M_{ls} = a(R)\widehat{l} \cdot \widehat{s}$, could be written down in this basis. However it is not diagonal in the $\left| {}^{l\ s}_{\lambda\sigma} \right\rangle$ basis and would lead to non-diagonal coupling elements. Instead though with the aid of the Clebsch-Gordon coefficients we express $\widehat{\mathbf{H}}^0_{MNg}$ and $\widehat{\mathbf{V}}^M_{ls}$ in the total electronic momentum Born-Oppenheimer basis. This is done because the spin-orbit operator is diagonal in this basis. The electronic and

magnetic terms in the $\left|{}^{j}_{\omega}\right\rangle$ basis are,

$$\begin{aligned}\left\langle {}^{j'}_{\omega'}\right| \widehat{\mathbf{H}}^0_{MNg} + \widehat{\mathbf{V}}^M_{ls} \left|{}^{j}_{\omega}\right\rangle &= \left\langle {}^{j'}_{\omega'}\right| \widehat{\mathbf{H}}^0_{MNg} \left|{}^{j}_{\omega}\right\rangle + \left\langle {}^{j'}_{\omega'}\right| \widehat{\mathbf{V}}^M_{ls} \left|{}^{j}_{\omega}\right\rangle \\ &= \sum_{\lambda',\sigma',\lambda,\sigma} (l\lambda' s\sigma'|lsj'\omega')(l\lambda s\sigma|lsj\omega) \left\langle {}^{l\ s}_{\lambda'\sigma'}\right| \widehat{\mathbf{H}}^0_{MNg} \left|{}^{l\ s}_{\lambda\sigma}\right\rangle \\ &+ \left\langle {}^{j'}_{\omega'}\right| \widehat{\mathbf{V}}^M_{ls} \left|{}^{j}_{\omega}\right\rangle . \end{aligned} \tag{95}$$

Recognizing that $\hat{j}^2 = (\hat{l}+\hat{s})(\hat{l}+\hat{s}) = \hat{l}^2 + \hat{s}^2 + 2\hat{l}\cdot\hat{s}$, we can substitute $\hat{l}\cdot\hat{s}$ into $\widehat{\mathbf{V}}^M_{ls}$,

$$\widehat{\mathbf{V}}^M_{ls} = \frac{a(R)}{2}(\hat{j}^2 - \hat{l}^2 - \hat{s}^2) \tag{96}$$

This form is beneficial because $\hat{j}^2$, $\hat{l}^2$, and $\hat{s}^2$ are eigen operators of $\left|{}^{j}_{\omega}\right\rangle$. Matrix elements of the spin-orbit operator become,

$$\left\langle {}^{j'}_{\omega'}\right| \widehat{\mathbf{V}}^M_{ls} \left|{}^{j}_{\omega}\right\rangle = \delta_{j',j}\delta_{\omega',\omega} \left[\frac{a(R)}{2}(j(j+1) - l(l+1) - s(s+1))\right]. \tag{97}$$

With the help of equation (93) the matrix elements of the electronic Hamiltonian are,

$$\begin{aligned}\left\langle {}^{j'}_{\omega'}\right| \widehat{\mathbf{H}}^0_{MNg} \left|{}^{j}_{\omega}\right\rangle &= \sum_{\lambda',\sigma',\lambda,\sigma} (l\lambda' s\sigma'|lsj'\omega')(l\lambda s\sigma|lsj\omega) \left\langle {}^{l\ s}_{\lambda'\sigma'}\right| \widehat{\mathbf{H}}^0_{MNg} \left|{}^{l\ s}_{\lambda\sigma}\right\rangle \\ &= \sum_{\lambda',\sigma',\lambda,\sigma} (l\lambda' s\sigma'|lsj'\omega')(l\lambda s\sigma|lsj\omega) W_{\lambda,\sigma}(R)\delta_{\lambda',\lambda}\delta_{\sigma',\sigma} \\ &= \delta_{\omega',\omega} \sum_{\lambda,\sigma} (l\lambda' s\sigma'|lsj'\omega')(l\lambda s\sigma|lsj\omega) W_{\lambda,\sigma} \end{aligned} \tag{98}$$

where in the last line it is noted that $\lambda + \sigma = \omega$ and so $\delta_{\lambda',\lambda}\delta_{\sigma',\sigma} = \delta_{\omega',\omega}$. This expression is re-written replacing the Clebsch-Gordon coefficients with the Wigner-3j

symbols,

$$\left\langle \begin{matrix} j' \\ \omega' \end{matrix} \right| \widehat{\mathbf{H}}^0_{MNg} \left| \begin{matrix} j \\ \omega \end{matrix} \right\rangle = \delta_{\omega',\omega}[(2j'+1)(2j+1)]^{1/2} \sum_{\lambda,\sigma} \begin{pmatrix} l & s & j' \\ \lambda & \sigma & -\omega \end{pmatrix} \begin{pmatrix} l & s & j \\ \lambda & \sigma & -\omega \end{pmatrix} W_{\lambda,\sigma}. \quad (99)$$

The Wigner-3j symbols have useful orthogonality relationships and they are:

$$\sum_{\lambda,\sigma} \begin{pmatrix} l & s & j' \\ \lambda & \sigma & -\omega' \end{pmatrix} \begin{pmatrix} l & s & j \\ \lambda & \sigma & -\omega \end{pmatrix} = \frac{\delta_{j',j}\delta_{\omega',\omega}}{2j+1}. \quad (100)$$

Expanding l within the p-manifold group of states the matrix elements become

$$\left\langle \begin{matrix} j' \\ \omega' \end{matrix} \right| \widehat{\mathbf{H}}^0_{MNg} \left| \begin{matrix} j \\ \omega \end{matrix} \right\rangle = \delta_{\omega',\omega}[(2j'+1)(2j+1)]^{1/2} \sum_{\sigma} \begin{pmatrix} 1 & s & j' \\ 1 & \sigma & -\omega \end{pmatrix} \begin{pmatrix} 1 & s & j \\ 1 & \sigma & -\omega \end{pmatrix} \Pi \quad (101a)$$

$$+ \begin{pmatrix} 1 & s & j' \\ -1 & \sigma & -\omega \end{pmatrix} \begin{pmatrix} 1 & s & j \\ -1 & \sigma & -\omega \end{pmatrix} \Pi \quad (101b)$$

$$+ \begin{pmatrix} 1 & s & j' \\ 0 & \omega & -\omega \end{pmatrix} \begin{pmatrix} 1 & s & j \\ 0 & \omega & -\omega \end{pmatrix} \Sigma \quad (101c)$$

$$+ \begin{pmatrix} 1 & s & j' \\ 0 & \omega & -\omega \end{pmatrix} \begin{pmatrix} 1 & s & j \\ 0 & \omega & -\omega \end{pmatrix} \Pi \quad (101d)$$

$$- \begin{pmatrix} 1 & s & j' \\ 0 & \omega & -\omega \end{pmatrix} \begin{pmatrix} 1 & s & j \\ 0 & \omega & -\omega \end{pmatrix} \Pi. \quad (101e)$$

A number of manipulations have taken place. First in equations 101a, 101b, and 101c W_λ has been replaced with Π and Σ based on the quantum value of l, 1 or 0,

respectively. Second, in equation 101c, $\lambda = 0$ so in this block we can set $\sigma = \omega$. Third, we add zero by adding and subtracting the same term through equations 101d and 101e. This will allow the use of the 3j orthogonality relations. Equations (101)a, (101)b, and (101)d combine to yield the following form of the electronic Hamiltonian matrix elements,

$$\begin{aligned}
&\left\langle {j' \atop \omega'} \right| \widehat{\mathbf{H}}^0_{MNg} \left| {j \atop \omega} \right\rangle \\
&= \delta_{\omega',\omega}[(2j'+1)(2j+1)]^{1/2} \left[\delta_{j',j}\delta_{\omega',\omega} \frac{\Pi}{2j+1} + (\Sigma - \Pi) \begin{pmatrix} 1 & s & j' \\ 0 & \omega & -\omega \end{pmatrix} \begin{pmatrix} 1 & s & j \\ 0 & \omega & -\omega \end{pmatrix} \right] \\
&= \delta_{\omega',\omega} \left[\delta_{j',j}\Pi + [(2j'+1)(2j+1)]^{1/2} (\Sigma - \Pi) \begin{pmatrix} 1 & s & j' \\ 0 & \omega & -\omega \end{pmatrix} \begin{pmatrix} 1 & s & j \\ 0 & \omega & -\omega \end{pmatrix} \right] \qquad (102)
\end{aligned}$$

Now it is obvious since there is no $\delta_{j',j}$ in the second term that $\widehat{\mathbf{H}}^0_{MNg}$ is not diagonal in the total electronic j basis.

Equations (97) and (102) reveal the $\left\langle {j' \atop \omega'} \right| \widehat{\mathbf{H}}^0_{MNg} + \widehat{\mathbf{V}}^M_{ls} \left| {j \atop \omega} \right\rangle$ matrix elements in a calculable form. For $l = 1$ and $s = 1/2$ we have,

$$\begin{aligned}
&\left\langle {j' \atop \omega'} \right| \widehat{\mathbf{H}}^0_{MNg} + \widehat{\mathbf{V}}^M_{ls} \left| {j \atop \omega} \right\rangle = \\
&\delta_{\omega',\omega}\delta_{j',j} \left[\Pi + \frac{a(R)}{2} \left(j(j+1) - \frac{11}{4} \right) \right] \\
&+ \delta_{\omega',\omega}[(2j'+1)(2j+1)]^{1/2} (\Sigma - \Pi) \begin{pmatrix} 1 & 1/2 & j' \\ 0 & \omega & -\omega \end{pmatrix} \begin{pmatrix} 1 & 1/2 & j \\ 0 & \omega & -\omega \end{pmatrix}. \qquad (103)
\end{aligned}$$

Correctly computing the 3j symbols the matrix elements of $\widehat{\mathbf{H}}^0_{MNg} + \widehat{\mathbf{V}}^M_{ls}$ in our group

of six states are,

$$\widehat{\mathbf{H}}^0_{MNg} + \widehat{\mathbf{V}}^M_{ls} = \begin{array}{c} \left|{}^{J\ \ 3/2}_{\pm 3/2\ \pm 3/2}\right\rangle \quad \left|{}^{J\ \ 3/2}_{\pm 1/2\ \pm 1/2}\right\rangle \quad \left|{}^{J\ \ 1/2}_{\pm 1/2\ \pm 1/2}\right\rangle \\ \begin{pmatrix} \Pi + \frac{a(R)}{2} & 0 & 0 \\ 0 & \frac{(2\Sigma+\Pi)}{3} + \frac{a(R)}{2} & \mp\frac{\sqrt{2}}{3}(\Sigma - \Pi) \\ 0 & \mp\frac{\sqrt{2}}{3}(\Sigma - \Pi) & \frac{(\Sigma+2\Pi)}{3} - a(R) \end{pmatrix} \end{array} \tag{104}$$

3.4 Coriolis Coupling

The next portion of the total Hamiltonian that must be transformed to body-fixed coordinates is the nuclear kinetic energy

$$\sum_{J,\Omega} \left\langle R, {}^{j'}_{\omega'} \right| \mathcal{R}^{-1} \widehat{\mathbf{T}}_N \mathcal{R} \left| R, {}^{j}_{\omega} \right\rangle \Theta^J_{M\Omega} \frac{\chi_{J,\Omega}(R)}{R} = \sum_{J,\Omega} \left\langle R, {}^{j'}_{\omega'} \right| \mathcal{R}^{-1} \frac{\widehat{P}^2_{\vec{R}}}{2\mu} \mathcal{R} \left| R, {}^{j}_{\omega} \right\rangle \Theta^J_{M\Omega} \frac{\chi_{J,\Omega}(R)}{R}. \tag{105}$$

One can compute this tranformation like various other authors[21][16][38] by transforming the space-fixed derivatives contained in $\widehat{P}^2_{\vec{R}}$ to body-fixed derivatives. Labeling the spherical coordinates for the space-fixed vector $\vec{R}$ as R, θ, and ϕ the kinetic energy is

$$\frac{\widehat{P}^2_{\vec{R}}}{2\mu} = -\frac{1}{2\mu}\vec{\nabla}^2_{\vec{R}}|_s = -\frac{1}{2\mu}\frac{d^2}{dR^2} - \frac{1}{2\mu R^2 sin^2\theta}\left[\left(sin\theta\frac{d}{d\theta}\right)^2_s + \left(\frac{d}{d\phi}\right)^2_s\right] \tag{106}$$

where s denotes a derivative with respect to space-fixed coordinates. Applying the transformation $\mathcal{R}$ to this equation only effects the angular components. The deriva-

tives transform as

$$\left(\frac{d}{d\theta}\right)_s = \left(\frac{d}{d\theta}\right)_b - ij_y \tag{107}$$

$$\left(\frac{d}{d\phi}\right)_s = \left(\frac{d}{d\phi}\right)_b + isin\theta j_x - icos\theta j_z \tag{108}$$

where b denotes a derivative with respect to body-fixed coordinates and j_x, j_y, and j_z are the components of $\vec{j}$.

We however take a different approach that takes advantage of the angular momentum calculus. In the body-fixed frame we can write down the nuclear angular momentum as,

$$\vec{L}_R = \vec{R} \times \vec{P}_R = R\hat{z}'' \times \vec{P}_R = R[\hat{y}''(P_R)_{\hat{x}''} - \hat{x}''(P_R)_{\hat{y}''}] \tag{109}$$

or written by components,

$$(L_R)_{x''} = -R(P_R)_{\hat{x}''} \tag{110}$$

$$(L_R)_{y''} = R(P_R)_{\hat{x}''} \tag{111}$$

$$(L_R)_{z''} = 0. \tag{112}$$

Since the body-fixed axes are the spherical polar axes of $\vec{R}$ we have that $\hat{x}'' = \hat{\theta}$, $\hat{y}'' = \hat{\phi}$, $\hat{z}'' = \hat{R}$ so that $(P_R)_{\hat{z}''}$ becomes the radial momentum

$$(P_R)_{\hat{z}''} = P_R = -i\frac{1}{R}\left(\frac{d}{dR}\right)R. \tag{113}$$

Inverting equations (110) and (111) yields the other two components of the nuclear

momentum:

$$(P_R)_{\hat{x}''} = \frac{(L_R)_{y''}}{R} \tag{114}$$

$$(P_R)_{\hat{y}''} = -\frac{(L_R)_{x''}}{R}. \tag{115}$$

The square of the momentum can now be derived,

$$\vec{P}_R \cdot \vec{P}_R = (P_R)^2_{\hat{x}''} + (P_R)^2_{\hat{y}''} + (P_R)^2_{\hat{z}''} \tag{116}$$

$$= P_R^2 + \frac{(L_R)^2_{x''}}{R^2} + \frac{(L_R)^2_{y''}}{R^2} \tag{117}$$

$$= P_R^2 + \frac{\vec{L}_R^2}{R^2}. \tag{118}$$

As explained before the nuclear wave function in the body-fixed system has no θ or ϕ coordinate therefore we use the total angular momentum $\vec{J} = \vec{L}_R + \vec{j}$. Upon solving for the nuclear angular momentum, inserting $\vec{L}_R$ in to the kinetic energy, and taking the dot product, the kinetic energy operator in body-fixed coordinates is revealed:

$$\mathcal{R}^{-1}\widehat{\mathbf{T}}_N\mathcal{R} = \frac{P_R^2}{2\mu} + \frac{\vec{L}_R^2}{2\mu R^2} \tag{119}$$

$$= \frac{\hat{P}_R^2}{2\mu} + \frac{(\vec{J} - \vec{j})^2}{2\mu R^2} \tag{120}$$

$$= \frac{\hat{P}_R^2}{2\mu} + \frac{J^2 + j^2 - \vec{j}\cdot\vec{J} - \vec{J}\cdot\vec{j}}{2\mu R^2} \tag{121}$$

It is evident through the $-\vec{j}\cdot\vec{J} - \vec{J}\cdot\vec{j}$ terms that the total electronic momentum couples to the nuclear angular momentum. This is called Coriolis coupling and only appears in this way when considering a body-fixed representation. Mechanistically speaking this is a completely dynamical effect and it is a measure of whether or not the molecular wave function will rotate with the nuclear axis during collision or lag behind it. If the molecular wave function rotates with the nuclear axis then L_R

behaves as an adiabatic parameter and no transition will take place. However when energies are high enough the nuclear angular momentum changes at a rate that is comparable to or faster than electron relaxation. In this case the nuclear angular momentum can no longer be considered an adiabatic parameter with respect to the molecular wave function. Therefore as the nuclei scatter in to the asymptotic limit a non-adiabatic transition of the electronic state has occurred.

Now what remains is to express the matrix elements of $J^2 + j^2 - \vec{j} \cdot \vec{J} - \vec{J} \cdot \vec{j}$. The action of $J^2 + j^2$ is known since they are immediately eigen operators of the total molecular wave function,

$$\sum_{J,\Omega} \left\langle \begin{smallmatrix} J' j' \\ \Omega' \omega' \end{smallmatrix} \right| \frac{J^2 + j^2}{2\mu R^2} \left| \begin{smallmatrix} J j \\ \Omega \omega \end{smallmatrix} \right\rangle = \delta_{J',J} \delta_{\Omega',\Omega} \delta_{j',j} \delta_{\omega',\omega} \frac{[J(J+1) + j(j+1)]}{2\mu R^2} \tag{122}$$

To compute the coupling elements first express them in their component form:

$$\vec{J} = (J_x, J_y, J_z) \tag{123}$$

$$\vec{j} = (j_x, j_y, j_z). \tag{124}$$

In the body-fixed system there is no component of nuclear angular momentum along the radial direction. So the radial component of total angular momentum is simply, $J_z = L_z + j_z = j_z$. The dot products become

$$-\vec{j} \cdot \vec{J} - \vec{J} \cdot \vec{j} = - \begin{pmatrix} j_x & j_y & j_z \end{pmatrix} \cdot \begin{pmatrix} J_x \\ J_y \\ j_z \end{pmatrix} - \begin{pmatrix} J_x & J_y & j_z \end{pmatrix} \cdot \begin{pmatrix} j_x \\ j_y \\ j_z \end{pmatrix} \tag{125}$$

$$= -(2j_z^2) - (j_x J_x + j_y J_y + J_x j_x + J_y j_y) \tag{126}$$

Once again, the action of j_z^2 is immediately known:

$$\sum_{J,\Omega} \left\langle {}^{J'\,j'}_{\Omega'\omega'} \right| \frac{-2j_z^2}{2\mu R^2} \left| {}^{J\,j}_{\Omega\omega} \right\rangle = \delta_{J',J}\delta_{\Omega',\Omega}\delta_{j',j}\delta_{\omega',\omega}\frac{-2\omega^2}{2\mu R^2}. \tag{127}$$

Utilizing the raising and lowering operators of the body-fixed total angular momentum, $J^{\pm} = J_x \pm iJ_y$, and the total electronic angular momentum, $j_{\pm} = j_x \pm ij_y$, we can show that

$$j_-J^+ + j_+J^- = (j_xJ_x + j_yJ_y + J_xj_x + J_yj_y). \tag{128}$$

Substituting this relation in to equation (126) the remaining matrix element left to be computed is

$$\sum_{J,\Omega} \left\langle {}^{J'\,j'}_{\Omega'\omega'} \right| - \frac{j_-J^+ + j_+J^-}{2\mu R^2} \left| {}^{J\,j}_{\Omega\omega} \right\rangle. \tag{129}$$

Since in body-fixed coordinates the commutation rules are reversed [45],

$$[J_x, J_y] = -iJ_z$$
$$[J_y, J_z] = -iJ_x$$
$$[J_z, J_x] = -iJ_y,$$

the action of the total angular momentum ladder operators are reversed (denoted by the superscript $\pm$),

$$J^{\pm} \left| {}^{J\,j}_{\Omega\omega} \right\rangle = [(J \pm \Omega)(J \mp \Omega + 1)]^{1/2} \left| {}^{J\;\;j}_{\Omega\mp1\;\omega} \right\rangle \tag{130}$$
$$= C^{\pm}(J,\Omega) \left| {}^{J\;\;j}_{\Omega\mp1\;\omega} \right\rangle \tag{131}$$

while the total electronic angular momentum operators remain unchanged,

$$j_{\pm} \left|{}^{J\,j}_{\Omega\omega}\right\rangle = [(j \mp \omega)(j \pm \omega + 1)]^{1/2} \left|{}^{J\,j}_{\Omega\omega\pm1}\right\rangle \tag{132}$$

$$= c_{\pm}(j,\omega) \left|{}^{J\,j}_{\Omega\omega\pm1}\right\rangle . \tag{133}$$

Combining these relationships the Coriolis coupling elements are

$$\sum_{J,\Omega} \left\langle {}^{J'\,j'}_{\Omega'\omega'}\right| - \frac{j_- J^+ + j_+ J^-}{2\mu R^2} \left|{}^{J\,j}_{\Omega\omega}\right\rangle =$$
$$- \frac{C^+(J,\Omega)c_-(j,\omega)}{2\mu R^2}\delta_{J',J}\delta_{\Omega',\Omega-1}\delta_{j',j}\delta_{\omega',\omega-1} - \frac{C^-(J,\Omega)c_+(j,\omega)}{2\mu R^2}\delta_{J',J}\delta_{\Omega',\Omega+1}\delta_{j',j}\delta_{\omega',\omega+1}. \tag{134}$$

In the case of diatomic collisions in body-fixed coordinates the nuclear momentum is completely perpendicular to the internuclear axis R. So the only value that the projection of $\vec{J}$ can take is that of $\vec{j}$ since $\vec{J} = \vec{L}_R + \vec{j}$. For the group of states considered in this work Ω can only take the value of $\pm 3/2$ for the $\left|{}^{3/2}_{\pm3/2}\right\rangle$ state and $\pm 1/2$ for the $\left|{}^{3/2}_{\pm1/2}\right\rangle$ and $\left|{}^{1/2}_{\pm1/2}\right\rangle$ states. Expressing the angular portion of nuclear kinetic energy in the total angular momentum Born-Oppenheimer basis the 6x6 matrix is as follows:

$$
\sum_{J,\Omega}\left\langle {}^{J'\,j'}_{\Omega'\omega'}\right|\frac{\hat{J}^2+\hat{j}^2-\hat{j}_z^2-(j_-J^++j_+J^-)}{2\mu R^2}\left|{}^{J\,j}_{\Omega\omega}\right\rangle =
$$

$$
\begin{array}{c}
\left|{}^{J\ \ 3/2}_{3/2\,3/2}\right\rangle \\
\left(\begin{array}{cccccc}
\frac{J(J+1)-\frac{3}{4}}{2\mu R^2} & -\frac{[3(J-\frac{1}{2})(J+\frac{3}{2})]^{1/2}}{2\mu R^2} & 0 & 0 & 0 & 0 \\
-\frac{[3(J-\frac{1}{2})(J+\frac{3}{2})]^{1/2}}{2\mu R^2} & \frac{J(J+1)+\frac{13}{4}}{2\mu R^2} & 0 & 0 & -\frac{2(J+1)}{2\mu R^2} & 0 \\
0 & 0 & \frac{J(J+1)+\frac{3}{4}}{2\mu R^2} & 0 & 0 & -\frac{J+1}{2\mu R^2} \\
0 & 0 & 0 & \frac{J(J+1)-\frac{3}{4}}{2\mu R^2} & -\frac{[3(J-\frac{1}{2})(J+\frac{3}{2})]^{1/2}}{2\mu R^2} & 0 \\
0 & -\frac{2(J+1)}{2\mu R^2} & 0 & -\frac{[3(J-\frac{1}{2})(J+\frac{3}{2})]^{1/2}}{2\mu R^2} & \frac{J(J+1)+\frac{13}{4}}{2\mu R^2} & 0 \\
0 & 0 & -\frac{J+1}{2\mu R^2} & 0 & 0 & \frac{J(J+1)+\frac{3}{4}}{2\mu R^2}
\end{array}\right)
\end{array}
\begin{array}{c}
\left|{}^{J\ \ 1/2}_{1/2\,1/2}\right\rangle \\
\left|{}^{J\ \ 3/2}_{1/2\,1/2}\right\rangle \\
\left|{}^{J\ \ 3/2}_{-3/2\,-3/2}\right\rangle \\
\left|{}^{J\ \ 3/2}_{-1/2\,-1/2}\right\rangle \\
\left|{}^{J\ \ 1/2}_{-1/2\,-1/2}\right\rangle
\end{array}
\tag{135}
$$

Due to the $\delta_{j',j}$ term only states that originate from the same asymptotic spin orbit Born-Oppenheimer state will couple through Coriolis coupling. Coriolis coupling can not change total electronic angular momentum, but it can change the projection of $\vec{j}$ along the internuclear axis. The diagonal elements represent the centrifugal potential written in body-fixed coordinates which closely resembles the form of the centripetal potential in space-fixed coordinates, $\frac{L(L+1)}{2\mu R^2}$.

The radial portion of the kinetic energy operator will be discussed in the next section.

3.5 Radial Derivative Coupling

By rotating to the body-fixed coordinate system we were able to separate out the radial components, R, from the angular components, θ and ϕ. What remains left is to analyze the matrix elements of P_R^2. The functional form of P_R^2 reads as $-\frac{1}{2\mu}(\frac{d}{dR} \cdot \frac{d}{dR})$ because we chose the radial functions to be of the form $\frac{\chi_{J,\Omega}(R)}{R}$ rather than just $\chi_{J,\Omega}(R)$. We now follow the derivation of equation (53), but replace the

$\vec{\nabla}_{\vec{R}} \cdot \vec{\nabla}_{\vec{R}}$ with $\frac{d}{dR} \cdot \frac{d}{dR}$ and express the electronic kets in their coordinate form:

$$
\begin{aligned}
&\sum_{J,\omega} \Theta^J_{M\omega} \int d\vec{r} \Phi^*_{j',\omega'}(\vec{r};\vec{R}) \widehat{\mathbf{T}}_N \Phi_{j,\omega}(\vec{r};\vec{R}) \chi_{J,\omega}(\vec{R}) \\
&= -\sum_{J,\omega} \Theta^J_{M\omega} \int d\vec{r} \sum_j \frac{1}{2\mu} \left[\Phi^*_{j',\omega'} \frac{d}{dR} \cdot \frac{d(\Phi_{j,\omega}\chi_{J,\omega})}{dR} \right] \\
&= -\sum_{J,\omega} \Theta^J_{M\omega} \int d\vec{r} \sum_j \frac{1}{2\mu} \left[\Phi^*_{j',\omega'} \frac{d}{dR} \cdot \left(\Phi_{j,\omega} \frac{d\chi_{J,\omega}}{dR} + \chi_{J,\omega} \frac{d\Phi_{j,\omega}}{dR} \right) \right] \\
&= -\sum_{J,\omega} \Theta^J_{M\omega} \int d\vec{r} \sum_j \frac{1}{2\mu} \left[\Phi^*_{j',\omega'} \left(\Phi_{j,\omega} \frac{d^2\chi_{J,\omega}}{dR^2} + \frac{d\chi_{J,\omega}}{dR} \cdot \frac{d\Phi_{j,\omega}}{dR} + \chi_{J,\omega} \frac{d^2\Phi_{j,\omega}}{dR^2} + \frac{d\Phi_{j,\omega}}{dR} \cdot \frac{d\chi_{J,\omega}}{dR} \right) \right] \\
&= -\sum_{J,\omega} \Theta^J_{M\omega} \int d\vec{r} \sum_j \frac{1}{2\mu} \left[\Phi^*_{j',\omega'} \left(\Phi_{j,\omega} \frac{d^2\chi_{J,\omega}}{dR^2} + 2\frac{d\Phi_{j,\omega}}{dR} \cdot \frac{d\chi_{J,\omega}}{dR} + \frac{d^2\Phi_{j,\omega}}{dR^2} \chi_{J,\omega} \right) \right] \\
&= -\sum_{J,\omega} \Theta^J_{M\omega} \int d\vec{r} \sum_j \frac{1}{2\mu} \left[\Phi^*_{j',\omega'} \left(\Phi_{j,\omega} \frac{d^2}{dR^2} + 2\frac{d}{dR}\Phi_{j,\omega} \cdot \frac{d}{dR} + \frac{d^2}{dR^2}\Phi_{j,\omega} \right) \chi_{J,\omega} \right].
\end{aligned}
\tag{136}
$$

Moving back in to a matrix vector form we have,

$$
\begin{aligned}
&\sum_{J,\omega} \left\langle R, \begin{smallmatrix} j' \\ \omega' \end{smallmatrix} \right| -\frac{1}{2\mu} \left(\frac{d}{dR} \cdot \frac{d}{dR} \right) \left| R, \begin{smallmatrix} j \\ \omega \end{smallmatrix} \right\rangle \Theta^J_{M\omega} \chi_{J,\omega}(R) = \\
&-\sum_{J,\omega} \Theta^J_{M\omega} \sum_j \frac{1}{2\mu} [\delta_{j'j}\delta_{\omega'\omega} \frac{d^2}{dR^2} + 2F_{j'\omega'j\omega} \cdot \frac{d}{dR} + G_{j'\omega'j\omega}] \chi_{J,\omega}(R)
\end{aligned}
\tag{137}
$$

where, $F_{j'\omega'j\omega} = \left\langle \begin{smallmatrix} j' \\ \omega' \end{smallmatrix} \right| \frac{d}{dR} \left| \begin{smallmatrix} j \\ \omega \end{smallmatrix} \right\rangle$ and $G_{j'\omega'j\omega} = \left\langle \begin{smallmatrix} j' \\ \omega' \end{smallmatrix} \right| \frac{d^2}{dR^2} \left| \begin{smallmatrix} j \\ \omega \end{smallmatrix} \right\rangle$.

Using an identity which is valid for a complete set[16],

$$
\mathbf{G} = -i\frac{d}{dR} \cdot \mathbf{F} + \mathbf{F} \cdot \mathbf{F} \tag{138}
$$

we can recast the matrix elements in favor of $\mathbf{F}$ and they finally become:

$$
\sum_{J,\omega} \left\langle R, \begin{smallmatrix} j' \\ \omega' \end{smallmatrix} \right| -\frac{1}{2\mu} \left(\frac{d}{dR} \cdot \frac{d}{dR} \right) \left| R, \begin{smallmatrix} j \\ \omega \end{smallmatrix} \right\rangle \Theta^J_{M\omega} \chi_{J,\omega}(R) = -\frac{1}{2\mu} \left(\mathbb{I}\frac{d}{dR} + \mathbf{F} \right)^2 \chi. \tag{139}
$$

Since equation (138) is valid only for a complete set of electronic eigen vectors, choosing to invoke the group Born-Oppenheimer approximation must be done with care. Depending on the system under study and level of accuracy needed the group Born-Oppenheimer approximation could introduce an error when using this compact form.

As done in section 2.7 the nuclear wave function is rotated in such a way to minimize the derivative couplings. This rotation creates a representation that is termed diabatic with respect to derivative couplings. We will append to this transformation matrix the subscript F signifying that it comes from a rotation that minimizes the derivative couplings. For the case of diatomic scattering these couplings can be completely transformed away[28].

For our group of six states Belcher showed that because of symmetry considerations only the $\left|{}^{3/2}_{\pm 1/2}\right\rangle$ and $\left|{}^{1/2}_{\pm 1/2}\right\rangle$ states are coupled through the derivative couplings. In our 6x6 matrix form the dressed kinetic energy operator in the body-fixed coordinate system is as follows:

$$
\begin{aligned}
&-\frac{1}{2\mu}\left(\mathbb{I}\frac{d}{dR}+\mathbf{F}\right)^2 = \\
&-\frac{1}{2\mu}\begin{array}{c}
\begin{array}{ccc}
\left|{}^{J\ \ 3/2}_{\pm 3/2\ \pm 3/2}\right\rangle & \left|{}^{J\ \ 3/2}_{\pm 1/2\ \pm 1/2}\right\rangle & \left|{}^{J\ \ 1/2}_{\pm 1/2\ \pm 1/2}\right\rangle
\end{array}{}^{2} \\
\begin{pmatrix}
\frac{d}{dR} & 0 & 0 \\
0 & \frac{d}{dR} & F \\
0 & F & \frac{d}{dR}
\end{pmatrix}
\end{array}
\end{aligned}
\tag{140}
$$

Since the derivative couplings only couple two states we expect the rotation matrix,

$\mathbf{U}_F$, to be contained in a 2x2 subspace with only one degree of freedom, $\alpha(R)$.

$$\mathbf{U}_F = \begin{pmatrix} 1 & 0 & 0 \\ 0 & cos(\alpha(R)) & -sin(\alpha(R)) \\ 0 & sin(\alpha(R)) & cos(\alpha(R)) \end{pmatrix} \tag{141}$$

The rotation angle α as a function of R was calculated by Belcher and will be compared with an alternative formulation later in the computational section of this work.

Mechanistically this result tells us that radial derivative coupling mixes eigenstates of the electronic Hamiltonian.

3.6 Close-Coupled Hamiltonian

The close-coupled Hamiltonian written in body-fixed coordinates is as follows:

$$\widehat{\mathbf{H}} = -\frac{1}{2\mu}\left(\mathbb{I}\frac{d}{dR} + \mathbf{F}\right)^2 + \frac{\hat{\mathbf{J}}^2 + \hat{\mathbf{j}}^2 - \hat{\mathbf{j}}_z^2}{2\mu R^2} + \frac{-(\mathbf{j}_-\mathbf{J}^+ + \mathbf{j}_+\mathbf{J}^-)}{2\mu R^2} + \widehat{\mathbf{H}}^0_{MNg} + \widehat{\mathbf{V}}^M_{ls} \tag{142}$$

where the first term is the radial nuclear dressed kinetic energy with radial derivative couplings, the second term is the centrifugal potential, the third term is the Coriolis coupling "potential", the fourth term is the electronic Hamiltonian which includes the interaction potential, and the fifth term is the electronic magnetic term or spin-orbit potential with spin-orbit coupling terms. Of course the Coriolis coupling is not a potential, but rather a dynamical phenomenon. It is a coordinate dependent term in the kinetic energy. Since it depends on coordinates it can be included with the potential energy to yield an "effective potential".

When written out in terms of matrix elements the form is exactly the same as Grosser[21] who transformed the angular derivatives from space-fixed to body-fixed rather than taking advantage of the angular momentum calculus. For P-Manifold

states the matrix elements in the Born-Oppenheimer molecular basis become:

$$H = \begin{array}{c} \left|\begin{smallmatrix} J & 3/2 \\ 3/2 & 3/2 \end{smallmatrix}\right\rangle \quad \left|\begin{smallmatrix} J & 3/2 \\ 1/2 & 1/2 \end{smallmatrix}\right\rangle \quad \left|\begin{smallmatrix} J & 1/2 \\ 1/2 & 1/2 \end{smallmatrix}\right\rangle \quad \left|\begin{smallmatrix} J & 3/2 \\ -3/2 & -3/2 \end{smallmatrix}\right\rangle \quad \left|\begin{smallmatrix} J & 3/2 \\ -1/2 & -1/2 \end{smallmatrix}\right\rangle \quad \left|\begin{smallmatrix} J & 1/2 \\ -1/2 & -1/2 \end{smallmatrix}\right\rangle \end{array}^{2}$$

$$-\frac{1}{2\mu}\begin{pmatrix} \frac{d}{dR} & 0 & 0 & 0 & 0 & 0 \\ 0 & \frac{d}{dR} & F & 0 & 0 & 0 \\ 0 & F & \frac{d}{dR} & 0 & 0 & 0 \\ 0 & 0 & 0 & \frac{d}{dR} & 0 & 0 \\ 0 & 0 & 0 & 0 & \frac{d}{dR} & F \\ 0 & 0 & 0 & 0 & F & \frac{d}{dR} \end{pmatrix} + \tag{143}$$

$$
\begin{array}{c}
\left|\begin{smallmatrix} J & 3/2 \\ 3/2 & 3/2 \end{smallmatrix}\right\rangle \\
\left(\begin{array}{c}
\Pi + \frac{a(R)}{2} \\
0 \\
0 \\
0 \\
0 \\
0
\end{array}\right.
\end{array}
\begin{array}{c}
\left|\begin{smallmatrix} J & 3/2 \\ 1/2 & 1/2 \end{smallmatrix}\right\rangle \\
\left(\begin{array}{c}
0 \\
\frac{(2\Sigma+\Pi)}{3} + \frac{a(R)}{2} \\
-\frac{\sqrt{2}}{3}(\Sigma - \Pi) \\
0 \\
0 \\
0
\end{array}\right.
\end{array}
\begin{array}{c}
\left|\begin{smallmatrix} J & 1/2 \\ 1/2 & 1/2 \end{smallmatrix}\right\rangle \\
\left(\begin{array}{c}
0 \\
-\frac{\sqrt{2}}{3}(\Sigma - \Pi) \\
\frac{(\Sigma+2\Pi)}{3} - a(R) \\
0 \\
0 \\
0
\end{array}\right.
\end{array}
\begin{array}{c}
\left|\begin{smallmatrix} J & 3/2 \\ -3/2 & -3/2 \end{smallmatrix}\right\rangle \\
\left(\begin{array}{c}
0 \\
0 \\
0 \\
\Pi + \frac{a(R)}{2} \\
0 \\
0
\end{array}\right.
\end{array}
\begin{array}{c}
\left|\begin{smallmatrix} J & 3/2 \\ -1/2 & -1/2 \end{smallmatrix}\right\rangle \\
\left(\begin{array}{c}
0 \\
0 \\
0 \\
0 \\
\frac{(2\Sigma+\Pi)}{3} + \frac{a(R)}{2} \\
\frac{\sqrt{2}}{3}(\Sigma - \Pi)
\end{array}\right.
\end{array}
\begin{array}{c}
\left|\begin{smallmatrix} J & 1/2 \\ -1/2 & -1/2 \end{smallmatrix}\right\rangle \\
\left(\begin{array}{c}
0 \\
0 \\
0 \\
0 \\
\frac{\sqrt{2}}{3}(\Sigma - \Pi) \\
\frac{(\Sigma+2\Pi)}{3} - a(R)
\end{array}\right)
\end{array}
\tag{144}
$$

$$
\begin{array}{c}
\left|\begin{smallmatrix} J & 3/2 \\ 3/2 & 3/2 \end{smallmatrix}\right\rangle \\
\left(\begin{array}{c}
\frac{J(J+1)-\frac{3}{4}}{2\mu R^2} \\
-\frac{[3(J-\frac{1}{2})(J+\frac{3}{2})]^{1/2}}{2\mu R^2} \\
0 \\
0 \\
0 \\
0
\end{array}\right.
\end{array}
\begin{array}{c}
\left|\begin{smallmatrix} J & 3/2 \\ 1/2 & 1/2 \end{smallmatrix}\right\rangle \\
\left(\begin{array}{c}
-\frac{[3(J-\frac{1}{2})(J+\frac{3}{2})]^{1/2}}{2\mu R^2} \\
\frac{J(J+1)+\frac{13}{4}}{2\mu R^2} \\
0 \\
0 \\
-\frac{2(J+1)}{2\mu R^2} \\
0
\end{array}\right.
\end{array}
\begin{array}{c}
\left|\begin{smallmatrix} J & 1/2 \\ 1/2 & 1/2 \end{smallmatrix}\right\rangle \\
\left(\begin{array}{c}
0 \\
0 \\
\frac{J(J+1)+\frac{3}{4}}{2\mu R^2} \\
0 \\
-\frac{[3(J-\frac{1}{2})(J+\frac{3}{2})]^{1/2}}{2\mu R^2} \\
-\frac{J+1}{2\mu R^2}
\end{array}\right.
\end{array}
\begin{array}{c}
\left|\begin{smallmatrix} J & 3/2 \\ -3/2 & -3/2 \end{smallmatrix}\right\rangle \\
\left(\begin{array}{c}
0 \\
0 \\
0 \\
\frac{J(J+1)-\frac{3}{4}}{2\mu R^2} \\
0 \\
0
\end{array}\right.
\end{array}
\begin{array}{c}
\left|\begin{smallmatrix} J & 3/2 \\ -1/2 & -1/2 \end{smallmatrix}\right\rangle \\
\left(\begin{array}{c}
0 \\
-\frac{2(J+1)}{2\mu R^2} \\
0 \\
-\frac{[3(J-\frac{1}{2})(J+\frac{3}{2})]^{1/2}}{2\mu R^2} \\
\frac{J(J+1)+\frac{13}{4}}{2\mu R^2} \\
0
\end{array}\right.
\end{array}
\begin{array}{c}
\left|\begin{smallmatrix} J & 1/2 \\ -1/2 & -1/2 \end{smallmatrix}\right\rangle \\
\left(\begin{array}{c}
0 \\
0 \\
-\frac{J+1}{2\mu R^2} \\
0 \\
0 \\
\frac{J(J+1)+\frac{3}{4}}{2\mu R^2}
\end{array}\right)
\end{array}
\tag{145}
$$

3.7 Adiabatic vs. Diabatic Representations

The terms adiabatic and diabatic can become misleading if not sufficiently described with respect to the representations they are referring to. So to be clear with in the frame work of the close-coupled equations and for the rest of this work we turn to Smith[38] who says, "The distinction between adiabatic and diabatic states is clarified when one examines the radial momentum matrix as well as the electronic energy matrix. The adiabatic representation is defined by diagonalizing the electronic energy, but if this is done the off-diagonal terms in the radial momentum matrix become large. On the other hand, the radial momentum matrix may itself be diagonalized, in which case the electronic energy matrix is no longer diagonal. It will be shown that it is possible to diagonalize the radial momentum everywhere, and this seems to be the basis for a satisfactory diabatic representation." In essence one must look at both the kinetic energy matrix and the potential energy matrix to determine whether or not one is looking at an adiabatic or diabatic representation.

For example we can take the original Born-Oppenheimer formulation, equation (93), and look at both the kinetic energy and potential energy matrices:

$$\begin{aligned}\widehat{\mathbf{H}} &= -\frac{1}{2\mu}\left(\mathbb{I}\vec{\nabla}+\vec{\mathbf{F}}\right)^2+\widehat{\mathbf{H}}^0_{MNg}\\ &= -\frac{1}{2\mu}\begin{array}{c}\begin{matrix}\left|1\,{}^{\frac{1}{2}}_{1\pm\frac{1}{2}}\right\rangle & \left|1\;{}^{1/2}_{-1\pm1/2}\right\rangle & \left|1{}^{1/2}_{0\pm1/2}\right\rangle\end{matrix}\\ \begin{pmatrix}\vec{\nabla} & 0 & 0\\ 0 & \vec{\nabla} & \vec{F}\\ 0 & \vec{F} & \vec{\nabla}\end{pmatrix}\end{array}^2+\begin{array}{c}\begin{matrix}\left|1\,{}^{\frac{1}{2}}_{1\pm\frac{1}{2}}\right\rangle & \left|1\;{}^{1/2}_{-1\pm1/2}\right\rangle & \left|1{}^{1/2}_{0\pm1/2}\right\rangle\end{matrix}\\ \begin{pmatrix}\Pi & 0 & 0\\ 0 & \Pi & 0\\ 0 & 0 & \Sigma\end{pmatrix}\end{array}\end{aligned} \tag{146}$$

In this example we would say that this is the *adiabatic* representation with respect to the electronic Hamiltonian. We see that the nuclear kinetic energy matrix is not diagonal (for the sake of discussion we do not separate the radial and rotational

portions) and that the potential energy matrix is diagonal. Of course at this particular level of theory and depending on the physical system under inspection the derivative couplings in this manner may or may not be a significant factor.

Now let us take the *diabatic* picture of the original Born-Oppenheimer formulation. We would seek a particular rotation, $\mathbf{U}_F(\vec{R})$, that would completely rid of or minimize the derivative couplings, $\vec{F}$. This rotation is applied not only to the dressed kinetic energy operator, but also to the adiabatic electronic Hamiltonian potential.

$$\begin{aligned}\widehat{\mathbf{H}} &= -\frac{1}{2\mu}\mathbf{U}_F^{\dagger}\left(\mathbb{I}\vec{\nabla}+\vec{\mathbf{F}}\right)^2\mathbf{U}_F + \mathbf{U}_F^{\dagger}\widehat{\mathbf{H}}^0_{MNg}\mathbf{U}_F \\ &= -\frac{1}{2\mu}\vec{\nabla}^2 + \mathbf{U}_F^{\dagger}\widehat{\mathbf{H}}^0_{MNg}\mathbf{U}_F \end{aligned} \tag{147}$$

This representation is *strictly* diabatic with respect to the electronic Hamiltonian potential. The radial kinetic energy is diagonal and the electronic potential energy is undiagonalized. Sometimes $\mathbf{U}_F^{\dagger}\widehat{\mathbf{H}}^0_{MNg}\mathbf{U}_F$ is stated to be the strictly diabatic potential, but this is truly only the case when the radial kinetic energy is presented as diagonal. Otherwise without knowing if the radial kinetic energy is diagonal $\mathbf{U}_F^{\dagger}\widehat{\mathbf{H}}^0_{MNg}\mathbf{U}_F$ should simply be called diabatic.

For the second example we add to (146) the magnetic or spin-orbit potential:

$$
\begin{aligned}
\widehat{\mathbf{H}} &= -\frac{1}{2\mu}\left(\mathbb{I}\vec{\nabla}+\vec{\mathbf{F}}\right)^2+\widehat{\mathbf{H}}^0_{MNg}+\widehat{\mathbf{V}}^M_{ls} \\
&= -\frac{1}{2\mu}\begin{array}{c}\begin{matrix}\left|1\,{}^{1}_{1\pm\frac{1}{2}}\right\rangle & \left|1\;{}^{1/2}_{-1\pm1/2}\right\rangle & \left|1\,{}^{1/2}_{0\pm1/2}\right\rangle\end{matrix}\\ \begin{pmatrix}\vec{\nabla} & 0 & 0\\ 0 & \vec{\nabla} & \vec{F}\\ 0 & \vec{F} & \vec{\nabla}\end{pmatrix}\end{array}^2+\begin{array}{c}\begin{matrix}\left|1\,{}^{1}_{1\pm\frac{1}{2}}\right\rangle & \left|1\;{}^{1/2}_{-1\pm1/2}\right\rangle & \left|1\,{}^{1/2}_{0\pm1/2}\right\rangle\end{matrix}\\ \begin{pmatrix}\Pi & 0 & 0\\ 0 & \Pi & 0\\ 0 & 0 & \Sigma\end{pmatrix}\end{array} \\
&\quad+\begin{array}{c}\begin{matrix}\left|1\,{}^{1}_{1\pm\frac{1}{2}}\right\rangle & \left|1\;{}^{1/2}_{-1\pm1/2}\right\rangle & \left|1\,{}^{1/2}_{0\pm1/2}\right\rangle\end{matrix}\\ \begin{pmatrix}S & 0 & S\\ 0 & S & S\\ S & S & S\end{pmatrix}\end{array} \\
&= -\frac{1}{2\mu}\begin{array}{c}\begin{matrix}\left|1\,{}^{1}_{1\pm\frac{1}{2}}\right\rangle & \left|1\;{}^{1/2}_{-1\pm1/2}\right\rangle & \left|1\,{}^{1/2}_{0\pm1/2}\right\rangle\end{matrix}\\ \begin{pmatrix}\vec{\nabla} & 0 & 0\\ 0 & \vec{\nabla} & \vec{F}\\ 0 & \vec{F} & \vec{\nabla}\end{pmatrix}\end{array}^2+\begin{array}{c}\begin{matrix}\left|1\,{}^{1}_{1\pm\frac{1}{2}}\right\rangle & \left|1\;{}^{1/2}_{-1\pm1/2}\right\rangle & \left|1\,{}^{1/2}_{0\pm1/2}\right\rangle\end{matrix}\\ \begin{pmatrix}\Pi+S & 0 & S\\ 0 & \Pi+S & S\\ S & S & \Sigma+S\end{pmatrix}\end{array}
\end{aligned}
\tag{148}
$$

The spin-orbit operator in the $\left|{}^{l\ s}_{\lambda\sigma}\right\rangle$ basis connects states with $\Delta S=\pm1,0$ and $\Delta L=\pm1,0$. We generically label these elements S noting that their functional form is a function of $a(\vec{R})$.

In its present form equation (148) is neither in an adiabatic or strictly diabatic form. We can choose to use $\mathbf{U}_F$ and transform away the derivative couplings leaving a strictly diabatic form with respect to the electronic and spin-orbit Hamiltonian or we can choose to diagonalize the potentials with $\mathbf{U}_{SO}$ creating an adiabatic form with

respect to the electronic and spin-orbit Hamiltonian. The strictly diabatic representation would be,

$$\begin{aligned}\widehat{\mathbf{H}} &= -\frac{1}{2\mu}\mathbf{U}_F^{\dagger}\left(\mathbb{I}\vec{\nabla}+\vec{\mathbf{F}}\right)^2\mathbf{U}_F + \mathbf{U}_F^{\dagger}(\widehat{\mathbf{H}}^0_{MNg}+\widehat{\mathbf{V}}^M_{ls})\mathbf{U}_F \\ &= -\frac{1}{2\mu}\vec{\nabla}^2 + \mathbf{U}_F^{\dagger}(\widehat{\mathbf{H}}^0_{MNg}+\widehat{\mathbf{V}}^M_{ls})\mathbf{U}_F \end{aligned} \tag{149}$$

and the adiabatic representation would be,

$$\begin{aligned}\widehat{\mathbf{H}} &= \mathbf{U}_{SO}^{\dagger}\mathbf{T}_N\mathbf{U}_{SO} + \mathbf{U}_{SO}^{\dagger}(\widehat{\mathbf{H}}^0_{MNg}+\widehat{\mathbf{V}}^M_{ls})\mathbf{U}_{SO} \\ &= \mathbf{U}_{SO}^{\dagger}\mathbf{T}_N\mathbf{U}_{SO} + (\widehat{\mathbf{H}}^0_{MNg}+\widehat{\mathbf{V}}^M_{ls})_{\mathfrak{so}}. \end{aligned} \tag{150}$$

where the subscript $\mathfrak{so}$ denotes that we are in an adiabatic diagonal form with respect to electronic and magnetic potentials. In the case of adding the spin-orbit coupling we can see why sometimes it is referred to as radial coupling. Upon placing the Hamiltonian into an adiabatic form with respect to the electronic and adiabatic potential the nuclear kinetic energy matrix is rotated introducing coupling terms that were not present before. This is further compounded by the fact that $\mathbf{U}_{SO}$ is a function of $\vec{R}$. However these "new" couplings should not be thought of as a new phenomenon, they are simply the spin-orbit couplings in a different representation. In fact to see the full implication on the kinetic energy one would need to insert $\mathbf{U}_{SO}$ in to equation (53) as $\int d\vec{r}\Phi_j^*(\vec{r};\vec{R})\mathbf{U}_{SO}^{\dagger}(\vec{R})\widehat{\mathbf{T}}_N\mathbf{U}_{SO}(\vec{R})\Phi_i(\vec{r};\vec{R})\chi_i(\vec{R})$ and then carry out its derivation as prescribed.

Its also correct to refer to representations such as equation (148) as just simply diabatic. In this discussion we have followed Mead and Truhlar[28] to say that a representation is *strictly* diabatic with respect to a given set of potentials if and only if the kinetic energy of the full Hamiltonian is diagonal. Otherwise we drop the *strictly* and simply say diabatic. As it stands now the close coupled equations derived

in equation (143) are in a diabatic form.

3.8 Summary

The space-fixed molecular Hamiltonian derived in section 2.5 was transformed to body-fixed coordinates. This essentially enabled the problem to be described as a one dimensional radial problem where the angular portions are handled by the angular momentum calculus. Upon rotating the Hamiltonian and its wave functions to body-fixed coordinates we found that the electronic and magnetic Hamiltonians were unaffected, but the kinetic energy was affected. Equation (143) will be the close-coupled Hamiltonian that will be subjected to a time-dependent analysis to determine S-Matrix elements as a function of energy.

Sometimes these equations are written in a form known as the Closed State equations[1]. Here the nuclear angular momentum is replaced with an average value. This has the added effect of also getting rid of all Coriolis coupling. Other times the radial derivative couplings are completely neglected. This can be a valid approximation especially if the adiabatic energies do not approach each other. However if they do approach each other at what is known as an avoided crossing, the derivative couplings via equation (77) become significant.

The advantage of deriving these close coupled equations as (143) is that with out decreasing or approximating the level of theory we can artificially set the various coupling terms to zero by simply replacing their matrix element with zero and re-simulate the system. The coupling phenomenon can then be compared and their effects on the collisional cross section will be clear.

IV. Quantum Dynamics

4.1 Introduction

All quantum mechanical systems evolve in time according to the time dependent Schrödinger equation. The solution at any time t is relatively simple so long as the Hamiltonian is a conservative system. A scattering event is by its very nature a time dependent phenomenon. By appealing to classical scattering theory and imposing on it the quantum theory we can develop a quantum scattering theory. The development of this theory presents us with what is known as the $\widehat{\mathbf{S}}$-operator. This operator contains all the detailed information about the scattering event. It relates the incoming state of the system with the outgoing state of the system. This information is then used to calculate the collisional cross section for the scattering event.

4.2 Time Evolution: Schrödinger Equation

The time evolution of any quantum mechanical system is governed by the *Schrödinger Equation*:

$$i\hbar\frac{d}{dt}\left|\psi(t)\right\rangle = \widehat{\mathbf{H}}\left|\psi(t)\right\rangle \tag{151}$$

where the Hamiltonian, $\widehat{\mathbf{H}}$, is defined to be the total energy of the system, kinetic energy plus potential energy, $\widehat{\mathbf{T}} + \widehat{\mathbf{V}}$. Since this is a first order ordinary differential equation the solution at any time, t, is determined by its initial state at time, $t = t_0$. As long as conservative systems are the only ones considered, those systems where the Hamiltonian does not change with time, then the solution to (151) is

$$\left|\psi(t)\right\rangle = \widehat{\mathbf{U}}(t, t_0)\left|\psi(t_0)\right\rangle \tag{152}$$

where,

$$\widehat{\mathbf{U}}(t, t_0) = e^{-\frac{i}{\hbar}\widehat{\mathbf{H}}(t-t_0)} \tag{153}$$

is known as the propagator or the semigroup of operators.

4.3 Quantum Scattering and the $\widehat{\mathbf{S}}$-Operator

In order to understand the complexity involved in quantum scattering it will be quite useful to appeal first to classical scattering via Taylor[42]. Suppose we think classically of an electron scattering off of a target atom. We can think spatially of its trajectory, x(t), being divided into three regions. The first region we will call the in-asymptotic region. This is where the electron approaches the atom in an almost straight line orbit. The second region is called the interaction region where the electron might orbit the atom in a complicated way due to some interaction potential. Lastly, the third region is similar to the first and we will call it the out-asymptotic region. This is the exiting of the electron along some other almost straight orbit.

Experimentally only two of the three regions are observable. These regions are the asymptotic regions. The interaction region, being no more than a couple atoms in diameter, is not directly observable. As such we need to find a way to characterize scattering events by relating the in- and out-asymptotic regions.

We will say that the actual orbit, $x(t)$, as time proceeds to the infinite past, becomes indistinguishable from a completely interaction potential-free orbit labeled, $x_{in}(t)$. As time proceeds to the infinite future $x(t)$ approaches a different, but still indistinguishably free orbit labeled $x_{out}(t)$.

Not every orbit, $x(t)$, has a corresponding $x_{in}(t)$ and $x_{out}(t)$ asymptote. It is possible that the potential, along with the initial energetics of the system, supports a bound orbit or specifically a bound state. This electron would then never be able to leave the interaction region and therefore will never be able to take on an out-asymptotic

trajectory. For every $x_{in}(t)$ and $x_{out}(t)$ asymptote however we can reasonably expect there will be a corresponding scattering orbit $x(t)$[42].

Taking this example and applying it to quantum mechanics involves specifying quantum orbits or quantum trajectories. Where in the classical example we could specify initial position, velocity, and acceleration, for the quantum case we must use Schrodinger's equation to specify the time evolution of the state vector. For simple 1D systems the vector $|\psi(t)\rangle$ now represents our orbit. We will call its solution, $\widehat{\mathbf{U}}(t,t_0)\,|\psi(t_0)\rangle$, an orbit.

We note that asymptotic quantum orbits are those orbits where the interaction potential is equal to zero. These orbits are, $\widehat{\mathbf{U}}^0(t,t_0)\,|\psi(t_0)\rangle$, and the propagator is defined:

$$\widehat{\mathbf{U}}^0(t,t_0) = e^{-\frac{i}{\hbar}\widehat{\mathbf{H}}^0(t-t_0)} \tag{154}$$

where $\widehat{\mathbf{H}}^0$ is the Hamiltonian in the asymptotic region. So in analogue with $x_{in}(t)$ and $x_{out}(t)$ we now have the orbits $\widehat{\mathbf{U}}^0(t,t_0)\,|\psi_{in}\rangle$ and $\widehat{\mathbf{U}}^0(t,t_0)\,|\psi_{out}\rangle$.

As with the classical example the first and third regions of a scattering event must be indistinguishable from an interaction potential-free orbit as time proceeds to the infinite past and future. Mathematically, we write this condition as:

$$\lim_{t\to-\infty} ||\widehat{\mathbf{U}}(t,t_0)\,|\psi(t_0)\rangle - \widehat{\mathbf{U}}^0(t,t_0)\,|\psi_{in}\rangle\,|| \to 0 \tag{155}$$

and

$$\lim_{t\to+\infty} ||\widehat{\mathbf{U}}(t,t_0)\,|\psi(t_0)\rangle - \widehat{\mathbf{U}}^0(t,t_0)\,|\psi_{out}\rangle\,|| \to 0. \tag{156}$$

There are three conditions which the interaction potential must meet in order for these two limits to exist. For spherical potentials $V = V(r)$, which is the chief concern for this work, the conditions are[42]:

1. $|V(r)| \leq c|r|^{-3-\epsilon}$ as $r \to \infty$ (for some $\epsilon > 0$, c$\in\mathbb{R}$)

2. $|V(r)| \leq c|r|^{-2+\epsilon}$ as $r \to 0$ (for some $\epsilon > 0$, c$\in\mathbb{R}$)

3. $V(r)$ is continuous for $0 < r < \infty$, except perhaps at a finite number of discontinuities.

This excludes the electrostatic potential.

If the potential meets the above requirements then the initial kets $|\psi(t_0)\rangle$ in equations (155) and (156) can be isolated by multiplying by the adjoint of the propagator, $\widehat{\mathbf{U}}^{\dagger}(t, t_0)$,

$$|\psi(t_0)\rangle = \lim_{t\to-\infty} \widehat{\mathbf{U}}^{\dagger}(t, t_0)\widehat{\mathbf{U}}^{0}(t, t_0)\,|\psi_{in}\rangle \equiv \widehat{\mathbf{\Omega}}_{+}\,|\psi_{in}\rangle \tag{157}$$

$$|\psi(t_0)\rangle = \lim_{t\to+\infty} \widehat{\mathbf{U}}^{\dagger}(t, t_0)\widehat{\mathbf{U}}^{0}(t, t_0)\,|\psi_{out}\rangle \equiv \widehat{\mathbf{\Omega}}_{-}\,|\psi_{out}\rangle \tag{158}$$

where two new operators, $\widehat{\mathbf{\Omega}}_{+}$ and $\widehat{\mathbf{\Omega}}_{-}$, have been defined. These operators are called the *Moller In* and *Moller Out* wave operators[42]. It is clear that a Moller operator produces from an asymptotic state vector a scattering orbit or Moller state at a particular time t_0. For notational clarity the orbit produced from a Moller In operator is given a subscript '+' symbol and the orbit produced from a Moller Out operator is given a subscript '-' symbol:

$$|\psi_{+}(t)\rangle = \widehat{\mathbf{\Omega}}_{+}\,|\psi_{in}\rangle$$
$$|\psi_{-}(t)\rangle = \widehat{\mathbf{\Omega}}_{-}\,|\psi_{out}\rangle$$

One particular property of these Moller Operators is that they are isometric. An isometric operator on $\mathbb{H}$ is a linear operator, $\widehat{\mathbf{\Omega}}$, which is defined on all of $\mathbb{H}$ and preserves the norm. That is $\mathcal{D}(\widehat{\mathbf{\Omega}}) = \mathbb{H}$ and $\|\widehat{\mathbf{\Omega}}\Psi\| = \|\Psi\|$ for all $|\Psi\rangle$. It can be shown that since isometric operators preserve the norm that $\widehat{\mathbf{\Omega}}^{\dagger}\widehat{\mathbf{\Omega}} = 1$, however it is not generally true in the infinite dimensional case that $\widehat{\mathbf{\Omega}}\widehat{\mathbf{\Omega}}^{\dagger} = 1$[42].

The Hilbert space can be thought of as consisting of all asymptotic vectors $|\psi_{in}\rangle$

(or $|\psi_{out}\rangle$) such that when acted on by a Moller Operator represents a particular orbit for a scattering event. Conversely, the question can be asked does every orbit in $\mathbb{H}$ have corresponding in/out asymptotes? In general, just like in the classical case, the answer is no. Some orbits will be considered to be bounded such that the standard time-independent Schrödinger Equation applies. Being bounded orbits they could not have evolved from $|\psi_{out}\rangle$. Denoting these bound orbits by $|\phi\rangle$ the solution to their trajectories can be found by solving $\widehat{\mathbf{H}}\,|\phi\rangle = E\,|\phi\rangle$.

In this regard the Hilbert Space can be divided into two distinct spaces, bounded, $\mathbb{B}$, and unbounded, $\mathbb{S}$. The spaces are, in fact, orthogonal by observing the inner product of $|\phi\rangle$ and $|\psi\rangle$:

$$\begin{aligned}
\langle\phi(t)|\psi(t)\rangle &= \langle\phi|\,\mathbf{U}^{\dagger}(t)\mathbf{U}(t)\,|\psi\rangle \\
&= e^{iEt}\,\langle\phi|\,\mathbf{U}(t)\,|\psi\rangle \\
&= \lim_{t\to+\infty} e^{iEt}\,\langle\phi|\,\mathbf{U}^{0}(t)\,|\psi_{in}\rangle \\
&= 0
\end{aligned}$$

The last equality is the result of the fact that as time extends to infinity the bound state is confined to its orbit while the scattering state has now evolved to the asymptotic region. As such the overlap is zero. Seen from a more mathematical stand point the asymptotic wave packet spreads until each value of its wave function tends to zero and once again the inner product with the bound state is zero.

The picture is now almost complete. The Hilbert space for orbits is composed of two orthogonal subspaces. The first being those orbits which are bound and exist in $\mathbb{B}$. The second are those orbits which are scattered states, $\mathbb{S}$. Furthermore, $\mathbb{S}$ can be further divided in to $\mathbb{S}_+$, those $|\psi(t)\rangle$ that originate from asymptotic in states, and $\mathbb{S}_-$, those $|\psi(t)\rangle$ that originate from asymptotic out states. If $\mathbb{S}_+ = \mathbb{S}_-$ and $\mathbb{S}_+$ and $\mathbb{S}_-$

are orthogonal to $\mathbb{B}$ then the scattering theory is said to be asymptotically complete. So then every $|\psi(t)\rangle$ in $\mathbb{S}$ can be fashioned either from an asymptotic in or out state:

$$|\psi(t)\rangle = \widehat{\mathbf{\Omega}}_+ |\psi_{in}\rangle = \widehat{\mathbf{\Omega}}_- |\psi_{out}\rangle \tag{159}$$

Given that the Moller Operators are isometric, multiplying the previous equation from the left by $\Omega_-^\dagger$ yields the following:

$$\begin{aligned} |\psi_{out}\rangle &= \widehat{\mathbf{\Omega}}_-^\dagger \widehat{\mathbf{\Omega}}_+ |\psi_{in}\rangle \\ &= \widehat{\mathbf{S}} |\psi_{in}\rangle \end{aligned} \tag{160}$$

This is the famous $\widehat{\mathbf{S}}$-operator and in it contains all the information about the details of the scattering interaction and is the central point of calculation in this work. Given a particular asymptotic in state one can predict through the $\widehat{\mathbf{S}}$-operator what experimentally observable asymptotic out state the system should scatter to.

4.4 Properties of the $\widehat{\mathbf{S}}$-Operator

The most important property of the $\widehat{\mathbf{S}}$-Operator is that it is a unitary operator. The Moller operators are isometric operators on $\mathbb{H}$ that map a vector on to the subspace $\mathbb{S}$. $\widehat{\mathbf{\Omega}}_+$ is a linear norm preserving map of $\mathbb{H}$ onto $\mathbb{S}$ and $\widehat{\mathbf{\Omega}}_-^\dagger$ is a linear norm preserving map from $\mathbb{S}$ onto $\mathbb{H}$. It follows directly then that $\widehat{\mathbf{S}} = \widehat{\mathbf{\Omega}}_-^\dagger \widehat{\mathbf{\Omega}}_+$ is a linear norm preserving map from $\mathbb{H}$ onto $\mathbb{H}$ when the scattering subspace is asymptotically complete. Therefore $\widehat{\mathbf{S}}$ is unitary and $\widehat{\mathbf{S}}^\dagger\widehat{\mathbf{S}} = \widehat{\mathbf{S}}\widehat{\mathbf{S}}^\dagger = 1$. This property will be the ultimate verification for any simulation when a simple analytic solution for comparison does not exist. If any aspect of a calculation say doesn't converge, creates a poor Moller state, or breaks an approximation, etc, the problem will reveal itself by breaking the $\widehat{\mathbf{S}}$-Operator's unitarity.

The probability amplitude that a state $|\psi_+(t)\rangle$ scatters to a state $|\psi_-(t)\rangle$ at particular time t is simply the dot product of the two vectors. Therefore the transition probability from initial to final state is

$$\begin{aligned}\mathcal{P}_{f\leftarrow i} &= |\langle\psi_-(t)|\psi_+(t)\rangle|^2 \\ &= |\langle\psi_{out}|\widehat{\mathbf{\Omega}}_-^\dagger\widehat{\mathbf{\Omega}}_+|\psi_{in}\rangle|^2 \\ &= |\langle\psi_{out}|\widehat{\mathbf{S}}|\psi_{in}\rangle|^2 \qquad (161)\end{aligned}$$

$$(162)$$

The $\widehat{\mathbf{S}}$-Matrix is defined to be the $\widehat{\mathbf{S}}$-Operator represented in k-space. The incoming wave vector will have some initial momentum, k_i, and scatter to some final state momentum, k_f. The transmission probability, $\mathcal{P}_{k_f\leftarrow k_i}$, also called the transmission coefficient, $T_{k_f\leftarrow k_i}$, is therefore $|\langle k_i|\widehat{\mathbf{S}}|k_f\rangle|^2$. There are three possible outcomes:

1. Total Transmission, $k_i = k_f$
2. Total Reflection, $k_i = -k_f$
3. Energy Transfer, $k_i \neq k_f$

The first two outcomes are a case of elastic collisions. The third is a case of inelastic scattering and the case that we are concerned with. Ultimately we seek out how kinetic energy is transferred amongst internal states.

The $\widehat{\mathbf{S}}$-Matrix is greatly simplified by making some smart choices. Consider a

three-level system in which the $\widehat{\mathbf{S}}$-Matrix would be a 6x6 matrix:

$$\begin{pmatrix} S_{+k_1,+k_1} & S_{+k_1,-k_1} & S_{+k_1,+k_2} & S_{+k_1,-k_2} & S_{+k_1,+k_3} & S_{+k_1,-k_3} \\ S_{-k_1,+k_1} & S_{-k_1,-k_1} & S_{-k_1,+k_2} & S_{-k_1,-k_2} & S_{-k_1,+k_3} & S_{-k_1,-k_3} \\ S_{+k_2,+k_1} & S_{+k_2,-k_1} & S_{+k_2,+k_2} & S_{+k_2,-k_2} & S_{+k_2,+k_3} & S_{+k_2,-k_3} \\ S_{-k_2,+k_1} & S_{-k_2,-k_1} & S_{-k_2,+k_2} & S_{-k_2,-k_2} & S_{-k_2,+k_3} & S_{-k_2,-k_3} \\ S_{+k_3,+k_1} & S_{+k_3,-k_1} & S_{+k_3,+k_2} & S_{+k_3,-k_2} & S_{+k_3,+k_3} & S_{+k_3,-k_3} \\ S_{-k_3,+k_1} & S_{-k_3,-k_1} & S_{-k_3,+k_2} & S_{-k_3,-k_2} & S_{-k_3,+k_3} & S_{-k_3,-k_3} \end{pmatrix} \tag{163}$$

For an incoming wave packet it makes sense that its momentum content be completely directed at the interaction potential. For an outgoing wave packet it makes sense that its momentum content be directed away from the interaction potential. More so if we confine the incoming state to be only on one level, say the first $-k_1$, then all other incoming momentum states, $-k_2$, $-k_3$, $+k_1$, $+k_2$, $+k_3$ are zero. The outgoing state can be up to a combination of $+k_1$, $+k_2$, $+k_3$. All other outgoing states directed toward the interaction potential, $-k_1$, $-k_2$, $-k_3$, are zero as well. The only non-zero $\widehat{\mathbf{S}}$-Matrix elements are then $S_{+k_1,-k_1}$, $_{+k_2,-k_1}$, and $S_{+k_3,-k_1}$. Since the $\widehat{\mathbf{S}}$-Matrix is unitary the following equation is valid:

$$|S_{+k_1,-k_1}|^2 + |S_{+k_2,-k_1}|^2 + |S_{+k_3,-k_1}|^2 = R_{+k_1\leftarrow -k_1} + T_{+k_2\leftarrow -k_1} + T_{+k_3\leftarrow -k_1} = 1. \tag{164}$$

When the state scatters back on to itself we term that a reflection. If the initial conditions are set as explained then the verification of unitarity simply becomes the addition of the reflection and transmission coefficients.

In practice one does not actually observe the transmission probability. However the transmission probability is used to calculate the cross section of collision which is experimentally observable.

4.5 Collisional Cross Section

The classical definition for the collisional cross section is given in terms of a transition probability from initial to final state:

$$\sigma(k_f \leftarrow k_i) = 2\pi \int_0^\infty db \mathcal{P}_b(k_f \leftarrow k_i) b \tag{165}$$

where k_i/k_f are the initial and final state wave numbers, $\mathcal{P}_b$ the probability of transition, and b the impact parameter of the collision. The relation between the impact parameter b and the quantum number L is[17]

$$b^2 = \frac{L(L+1)}{k_f^2}. \tag{166}$$

Taking derivatives of both sides we have that

$$bdb = \frac{(2L+1)dL}{2k_f^2}. \tag{167}$$

In the quantal limit the smallest value a change in nuclear angular momentum can take is 1 so $dL = 1$. Inserting this expression for bdb in to the classical definition for the cross section the quantum definition for a collisional cross section becomes:

$$\sigma(k_f \leftarrow k_i) = \frac{\pi}{k_f^2} \sum_{L=0}^{\infty} (2L+1) \mathcal{P}_L(k_f \leftarrow k_i) \tag{168}$$

Of course as seen in the previous section the transition probability, $\mathcal{P}_L$, is the transmission coefficient or $|S_L(k_f \leftarrow k_i)|^2$.

$$\sigma(k_f \leftarrow k_i) = \frac{\pi}{k_f^2} \sum_{L=0}^{\infty} (2L+1) |S_L(k_f \leftarrow k_i)|^2 \tag{169}$$

4.6 Summary

By appealing to classical scattering theory we have formulated a quantum scattering theory. This theory is a time-dependent approach through the use of the isometric Moller operators. What results is the $\widehat{\mathbf{S}}$-operator that relates asymptotic-in states to asymptotic-out states. This unitary operator contains all the information about the scattering potentials. The matrix elements of $\widehat{\mathbf{S}}$ aren't directly observable, but are used to calculate the cross section of collision. This cross section is directly related to the transition rate between various system levels.

V. Computational Scattering

5.1 Introduction

The time dependent expressions for the Moller operators motivate the use of wave packet propagation to compute $\widehat{\mathbf{S}}$-operator matrix elements. It is not often however that the solution to Schrodinger's time dependent equation is purely analytical. Even in the cases where an analytical solution exists, sometimes it contains infinite sums which don't have closed forms. Therefore we proceed to solve the time evolution of a wave vector by numerically iterating the time dependent Schrödinger equation from t_0 to a particular time, t, in time steps of Δt.

Once this background has been established the immediate goal is to calculate the $\widehat{\mathbf{S}}$-Matrix elements because it relates the two observable asymptotic trajectories that one would measure in the laboratory. To aid in this calculation the Channel Packet Method (CPM) of Weeks and Tannor[46][41] will be employed.

These numerical techniques will first be applied to square well scattering. The simplicity of this model will help elucidate the topics covered thus far. Also, the problem of square well scattering can be solved analytically and in this way can be used to verify the numerical simulation. We will then apply these numerical techniques to a 2-level coupled system to gain insight to how a multilevel system would work.

When dealing with atomic phenomenon it is very important to understand and choose a set of units that are natural to atomic scales. It is convenient to work in atomic units for both ease of equation derivation and computational accuracy. These units are listed in Table 1 and unless otherwise noted are used throughout this work.

Table 1. Atomic Units

Unit	Atomic Unit	SI Conversion Unit
Length	1 Bohr	$5.291772108(18) \times 10^{-11}$ m
Mass	1 a.u. (of mass)	$9.1093826(16) \times 10^{-31}$ kg
Time	1 a.u. (of time)	$2.418884326505 \times 10^{-17}$ s
$\hbar$	1 a.u. (of angular momentum)	$1.05457168(18) \times 10^{-35}$ Js
Energy	1 Hartree	$4.35974417(75) \times 10^{-18}$ J

5.2 The Split Operator

In order to propagate a wave packet one must pick a particular representation for the propagator. This amounts to picking a representation for $\widehat{\mathbf{T}}+\widehat{\mathbf{V}}$, the Hamiltonian. The most natural choices are to use the momentum and coordinate representations for the Hamiltonian. Individually, the kinetic energy operator in the momentum representation and the potential energy operator in the coordinate representation are local operators. Said another way, the operators are diagonal in their respective representations. This greatly simplifies our computational effort for the exponential of a diagonal matrix simply becomes a set of N multiplications. However, a complication arises when exponentiating the Hamiltonian, $\widehat{\mathbf{T}}+\widehat{\mathbf{V}}$. This complication is due to the fact that kinetic and potential energy operators do not commute and so neither the momentum or coordinate representation of the Hamiltonian operator will be local. To alleviate this problem one can turn to the split operator method.

The first split one might try is to use is the Baker-Campell-Hausdorff formula[10, 20] to reduce the propagator up to second order in time. This formula states that:

$$\mathrm{e}^{X+Y} \approx \mathrm{e}^{X}\mathrm{e}^{Y}\mathrm{e}^{-\frac{1}{2}[X,Y]} \tag{170}$$

for arbitrary square matrices X and Y. This formula applies to operators as well.

Setting the operators $X = -\frac{i}{\hbar}\Delta t\widehat{\mathbf{T}}$ and $Y = -\frac{i}{\hbar}\Delta t\widehat{\mathbf{V}}$ yields the following:

$$\mathrm{e}^{-\frac{i}{\hbar}\Delta t(\widehat{\mathbf{T}}+\widehat{\mathbf{V}})} \approx \mathrm{e}^{-\frac{i}{\hbar}\Delta t\widehat{\mathbf{T}}}\mathrm{e}^{-\frac{i}{\hbar}\Delta t\widehat{\mathbf{V}}}\mathrm{e}^{-\frac{\Delta t^2}{2\hbar}[\widehat{\mathbf{T}},\widehat{\mathbf{V}}]} \tag{171}$$

This approximation looks promising so long as Δt is small enough such that the propagator simply becomes the multiplication of the first two exponentials. This way one could start in a particular representation where one of the operators was local, perform the multiplication, transform to a different representation, perform the second multiplication, and so on. However this particular approximation has one fatal flaw, it does not exhibit time reversal symmetry for small Δt.

Alternatively, one can perform a Taylor expansion of the propagator and once again collecting all terms of first, second, and third order can show the propagator to be written as (Appendix A):

$$\widehat{\mathbf{U}} = \mathrm{e}^{\frac{\lambda\widehat{\mathbf{T}}}{2}}\mathrm{e}^{\lambda\widehat{\mathbf{V}}}\mathrm{e}^{\frac{\lambda\widehat{\mathbf{T}}}{2}} + \frac{1}{24}[\widehat{\mathbf{T}} + 2\widehat{\mathbf{V}}, [\widehat{\mathbf{T}}, \widehat{\mathbf{V}}]]\lambda^3 + \mathcal{O}(\lambda^4) \tag{172}$$

where $\lambda = -\frac{i}{\hbar}\Delta t$. This split preserves time reversal symmetry. The second term represents the error in this split operator method and also serves as computationally valuable estimate on the time step necessary for propagation. So long as either the term $(\widehat{\mathbf{T}} + 2\widehat{\mathbf{V}})\lambda^3$ or $[\widehat{\mathbf{T}}, \widehat{\mathbf{V}}]\lambda^3$ approaches zero it will be safe to assume that all orders of higher magnitude will be zero as well. This serves as a guide for the maximum size the time step can be. This time step will change based on the scale of each individual problem.

5.3 Coordinates, Momentum, and the Fourier Transform

The coordinate and momentum representations are related via a Fourier transformation. As mentioned in the previous section both representations are needed to

ensure that the kinetic and potential energy operators will be diagonal and therefore easier to use in computations.

The coordinate representation of the wave function can be restated as the following,

$$\psi(x) = \int dk \phi(k) \psi_k(x) \tag{173}$$

where $\{\psi_k(x)\}$ is a complete set of linearly independent basis functions. If these functions are basis functions of the momentum operator then $\phi(k)$ will contain the necessary information to reconstruct $\psi(x)$. The momentum operator and its eigenfunctions are:

$$\widehat{p} \leftrightarrow -i\hbar \frac{\partial}{\partial x} \tag{174}$$

$$\psi_k(x) = \frac{1}{\sqrt{2\pi}} e^{ikx} \tag{175}$$

with eigenvalues, $\hbar k$. The expansion is now complete and is obviously a Fourier transform:

$$\psi(x) = \frac{1}{\sqrt{2\pi}} \int dk \phi(k) e^{ikx} = [\mathcal{F}^{-1}\phi](x) \tag{176}$$

The very same analysis can be done to show the inverse:

$$\phi(k) = \frac{1}{\sqrt{2\pi}} \int dx \psi(x) e^{-ikx} = [\mathcal{F}\psi](k) \tag{177}$$

5.4 Computational Grids and the Fast Fourier Transform

In practice, we will not be using a continuous coordinate or momentum space. A computer simply cannot handle an infinite array of numbers. So instead we will be discretizing the computational grids. The smaller each grid step, in both coordinate and momentum space, the closer to the continuum we will reach, however it will be

at the expense of greater computational effort so a balance must be established. The details of computing a Fourier Transform on a discrete grid will not be talked about in great detail, but suffice to say that it is on the order of N^2 algebraic operations where N is the number of grid points on the computational grid. For an array of 10^6 entries it would roughly take 2 weeks of CPU time on a microsecond cycle time computer to perform just one transform[34]. Luckily, an alternate method exists called the Fast Fourier Transform which reduces the number of operation to $Nlog_2N$ or only 30 seconds of computer time.

The work of J.W. Cooley and J.W. Tukey[13] in the mid-1960s on FFT algorithms popularized them throughout the computing science community. Today there are many commercial and freely licensed FFT algorithms in existence. The one used in this work is FFTPack5 and it is a Fortran subroutine library written by Paul Swarztrauber and Richard Valent in the mid 1990s[39].

When using FFT algorithms it is important to realize that the grid sizes of a conjugate pair of variables are intricately linked. Starting in the coordinate representation the grid will be divided into N intervals. The FFT algorithm works most efficiently when N is a power of 2. From the total grid length and the number of divisions a step length, dx, is determined. Using these two values puts a limit on the maximum momentum that the momentum grid can support as well as the momentum grid resolution. These two max values are $k_{\pm} = \pm\frac{1}{2dx}$ and the resolution is $dk = \frac{1}{Ndx}$.

For example if $N = 512$ and $dx = 0.1$ then the corresponding momentum grid would have $k_{\pm} = \pm 5$ and $dk = 0.02$. What drives the choice of dx is the interaction potential. The resolution has to be fine enough in coordinate space to capture all the major features of the potential. However this particular choice cannot handle particles that would have momentum greater than or less than $k_{\pm}$. With each simulation awareness of these important relations must be maintained.

5.5 Description of the Propagation Scheme

The necessary tools are now in place for wave packet propagation. Once the grids have been properly constructed and an initial coordinate wave function chosen the following operations must take place for each time step:

1) Multiply $\psi(x_n, 0)$ by $e^{-\frac{i}{2\hbar}\Delta t\widehat{\mathbf{V}}(x_n)}$

2) Transform the multiplication in step 1 by way of the forward FFT

3) Multiply the k-space function by the phase $e^{-\frac{i}{2\hbar}\Delta t\widehat{\mathbf{T}}(k_n)}$

4) Perform a second transform back to coordinate space using a backward FFT

5) Multiply the result by $e^{-\frac{i}{2\hbar}\Delta t\widehat{\mathbf{V}}(x_n)}$

The initial wave function at $t = 0$ has now been propagated a short time Δt:

$$\psi(x_n, \Delta t) = e^{-\frac{i}{2\hbar}\Delta t\widehat{\mathbf{V}}(x_n)}\{\mathcal{F}^{-1}[e^{-\frac{i}{2\hbar}\Delta t\widehat{\mathbf{T}}(k_n)}\mathcal{F}(e^{-\frac{i}{2\hbar}\Delta t\widehat{\mathbf{V}}(x_n)}\psi(x_n, 0))]\} \tag{178}$$

The intermediate wave function $\psi(x_n, \Delta t)$ replaces $\psi(x_n, 0)$ in step 1 and the whole sequence is repeated resulting in $\psi(x_n, 2\Delta t)$. Once the desired number of time steps have been iterated the result is the numerical solution of $\psi(x_n, t)$ and the orbit will have been determined.

This propagation algorithm was programmed as a FORTRAN 90 subroutine and used to propagate a Gaussian wave function under zero potential. A sample subroutine is given in Appendix B. To check that the propagator code is working correctly it is compared to the freely propagating Gaussian wave which has the following analytical solution[12]:

$$\psi(x, t) = \left(\frac{2a^2}{\pi}\right)^{1/4} \frac{e^{i\phi}}{\left(a^4 + \frac{4\hbar^2t^2}{m^2}\right)^{1/4}} e^{ik_0(x-x_0)} exp\left\{-\frac{\left[(x - x_0) - \frac{\hbar k_0}{m}t\right]^2}{a^2 + \frac{2iht}{m}}\right\} \tag{179}$$

where x_0 is the initial position, k_0 is the initial momentum, $a = FWHM/(2\sqrt{ln2})$ at

$t = 0$, and $\phi = -\theta - \frac{\hbar k_0^2}{2m} t$ with $tan(2\theta) = \frac{2\hbar t}{ma^2}$.

The numerical and analytical solutions are shown in Figure 8 with the following parameters listed in Table 2. By inspection the numerical results are in excellent agreement with the analytical solution for the real and imaginary parts.

Table 2. Free Space Propagation Simulation Parameters

N	2^9	a	5
dx	0.39	x_0	15
Total Time	2^{13}	k_0	6
dt	1	Mass	916

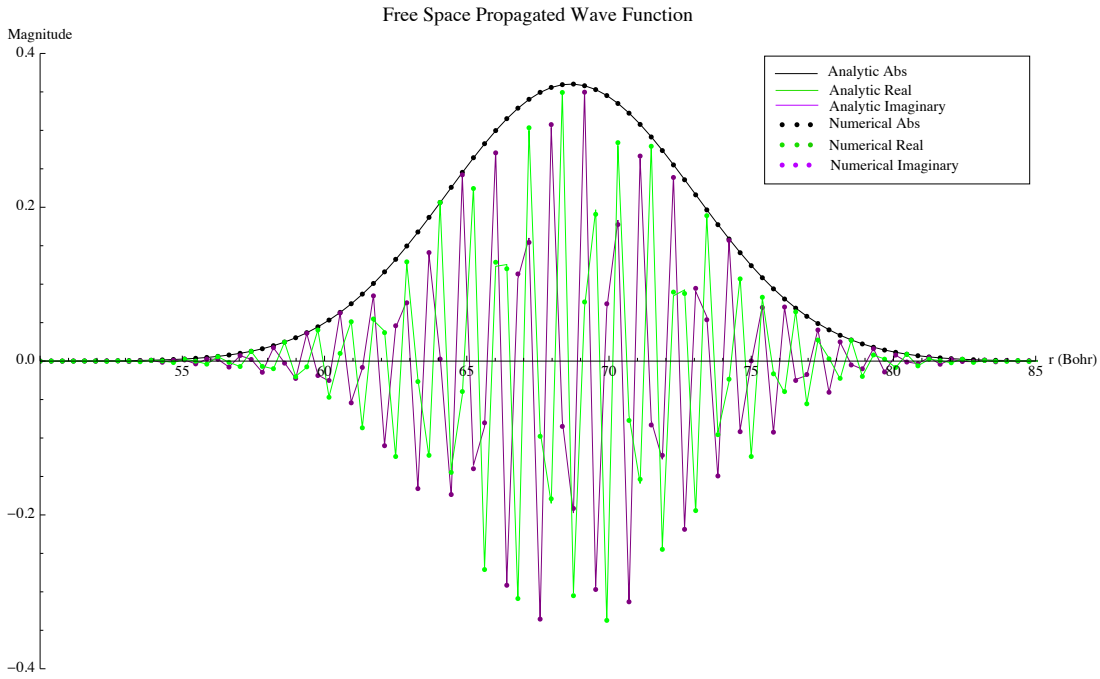

Figure 8. Numerical vs. Analytical wavefunction propagation at t = 8192 a.u.

5.6 S-Matrix Elements via the Channel Packet Method

With a properly working numerical propagator the Channel Packet Method (CPM) will now be implemented to compute numerical S-matrix elements. It is common ver-

nacular to refer to the in-asymptotic states as reactants and the out-asymptotic states as products. The rest of this paper will follow this convention.

This method begins by defining an asymptotic Hamiltonian that acts on a separable set of reactant and product states, $|k_\gamma, \gamma\rangle$, such that:

$$\begin{aligned}\widehat{\mathbf{H}}_0^\gamma |k_\gamma, \gamma\rangle &= (\widehat{\mathbf{H}}_{rel}^\gamma + \widehat{\mathbf{H}}_{int}^\gamma) |k_\gamma, \gamma\rangle \\ &= (\frac{1}{2\mu}\hbar^2 k_\gamma^2 + E_\gamma) |k_\gamma, \gamma\rangle \\ &= E |k_\gamma, \gamma\rangle \end{aligned} \tag{180}$$

The label γ is used to specify all internal quantum states of the reactants and products. These internal states can include, but are not limited to, spin, rotation, vibration, or electronic degrees of freedom. The label k_γ is used to specify relative momenta of the reactants or products with internal states γ. Together they help define the kets $|k_\gamma, \gamma\rangle$ which spans the γth channel Hilbert space and as such are a convenient basis to represent state vectors. $\widehat{\mathbf{H}}_{rel}^\gamma$ therefore governs the relative motion and $\widehat{\mathbf{H}}_{int}^\gamma$ governs the internal dynamics.

When acted upon by the Moller Operators these basis states are transformed in to another set of states labeled $|k_\gamma, \gamma_\pm\rangle$:

$$|k_\gamma, \gamma_\pm\rangle = \widehat{\mathbf{\Omega}}_\pm^\gamma |k_\gamma, \gamma\rangle \tag{181}$$

One can show however through the intertwining relation[42] that the $|k_\gamma, \gamma_\pm\rangle$ are

actually eigenstates of the full Hamiltonian.

$$\begin{aligned}\widehat{\mathbf{\Omega}}_{\pm}^{\gamma}\widehat{\mathbf{H}}_{0}^{\gamma}\left|k_{\gamma},\gamma\right\rangle &= \widehat{\mathbf{H}}\widehat{\mathbf{\Omega}}_{\pm}^{\gamma}\left|k_{\gamma},\gamma\right\rangle = H\left|k_{\gamma},\gamma\pm\right\rangle \\ &= (\frac{1}{2\mu}\hbar^{2}k_{\gamma}^{2}+E_{\gamma})\widehat{\mathbf{\Omega}}_{\pm}^{\gamma}\left|k_{\gamma},\gamma\right\rangle \\ &= (\frac{1}{2\mu}\hbar^{2}k_{\gamma}^{2}+E_{\gamma})\left|k_{\gamma},\gamma\pm\right\rangle \end{aligned} \tag{182}$$

So the eigenvalues of $\widehat{\mathbf{H}}$ acting on $|k_\gamma,\gamma\pm\rangle$ and the eigenvalues of $\widehat{\mathbf{H}}_0^\gamma$ acting on $|k_\gamma,\gamma\rangle$ are in fact the same.

The reason why the eigenstates of the full Hamiltonian are useful can be seen by expanding the initial asymptotic states in the γth channel Hilbert Space as:

$$\left|\psi_{in(out)}^{\gamma}\right\rangle = \int_{-\infty}^{\infty} dk_{\gamma}\eta_{\pm}(k_{\gamma})\left|k_{\gamma},\gamma\right\rangle \tag{183}$$

Upon operating on the asymptotic basis states with the Moller operator we notice that the expansion coefficients of the asymptotic states in terms of $|k_\gamma,\gamma\rangle$ are the same as the expansion coefficients for the Moller states in terms of $|k_\gamma,\gamma_\pm\rangle$.

$$\begin{aligned}\left|\psi_{\pm}^{\gamma}\right\rangle &= \widehat{\mathbf{\Omega}}_{\pm}^{\gamma}\left|\psi_{in(out)}^{\gamma}\right\rangle \\ &= \int_{-\infty}^{\infty} dk_{\gamma}\eta_{\pm}(k_{\gamma})\left|k_{\gamma},\gamma_{\pm}\right\rangle \end{aligned} \tag{184}$$

The orthogonality relationships of the Moller basis states are[46],

$$\begin{aligned}\langle k'_{\gamma'},\gamma'_{\pm}|k_{\gamma},\gamma_{\pm}\rangle &= \langle k'_{\gamma'},\gamma'|\,\widehat{\mathbf{\Omega}}_{\pm}^{\gamma'\dagger}\widehat{\mathbf{\Omega}}_{\pm}^{\gamma}\left|k_{\gamma},\gamma\right\rangle \\ &= \left\langle k'_{\gamma'},\gamma'\right|\mathbb{I}\left|k_{\gamma},\gamma\right\rangle \\ &= \delta_{\gamma',\gamma}\delta(k'_{\gamma'}-k_{\gamma}) \end{aligned} \tag{185}$$

and

$$\begin{aligned}\langle k'_{\gamma'}, \gamma'_- | k_\gamma, \gamma_+ \rangle &= \langle k'_{\gamma'}, \gamma' | \, \widehat{\mathbf{\Omega}}_-^{\gamma'\dagger} \widehat{\mathbf{\Omega}}_+^{\gamma} \, | k_\gamma, \gamma \rangle \\ &= \left\langle k'_{\gamma'}, \gamma' \right| \widehat{\mathbf{S}} \left| k_\gamma, \gamma \right\rangle \\ &= \{ |k'_{\gamma'}||k_\gamma| \}^{1/2} \delta(E' - E) S^{\gamma'\gamma}_{k'_{\gamma} k_\gamma} \end{aligned} \tag{186}$$

where $|k_\gamma| = \partial E / \partial |k_\gamma|$ is the density of states.

The probability to scatter from an initial Moller reactant state to an outgoing Moller product state is proportional to the overlap or dot product of those states[42]. Since the Moller states are expanded in terms of the Moller basis states we can make use of the orthogonality relationships to solve for $S^{\gamma'\gamma}_{k'_{\gamma} k_\gamma}$ contained in equation (186). This on-shell S-matrix element gives the probability amplitude to scatter from the γth channel with momentum k_γ to the γ'th channel with momentum k'_γ.

In order to do so we take advantage of the time/energy relationship via another Fourier Transform. The Fourier transform of the time evolution of the Moller state $|\psi_+^\gamma\rangle$ is

$$|A_+^\gamma(E)\rangle = \int_{-\infty}^{+\infty} e^{iEt} e^{-\frac{i}{\hbar}\widehat{\mathbf{H}}t} \, |\psi_+^\gamma\rangle \, dt \tag{187}$$

Substituting equation (184) in to equation (187) and recognizing that through equations (182) we can resolve $exp(-iHt) \, |\psi_+^\gamma\rangle$ then equation (187) is really an unormalized eigenvector of the full Hamiltonian:

$$|A_+^\gamma(E)\rangle = \frac{2\pi}{|k_\gamma|} [\eta_+(+k_\gamma) \, |+k_\gamma, \gamma+\rangle + \eta_+(-k_\gamma) \, |-k_\gamma, \gamma+\rangle \tag{188}$$

where the + and - notation symbolize the degenerate states of the full Hamiltonian; That is asymptotic states with positive as well as negative momentum.

The scattering matrix elements can now be solved for by taking the dot product

of equation (188) with a product state $\left|\psi_{-}^{\gamma'}\right\rangle$ and making use of the orthogonality relations of the channel states,

$$\begin{aligned}\langle\psi_{-}^{\gamma'}|A_{+}^{\gamma}(E)\rangle = 2\pi\{|k'_{\gamma'}||k_{\gamma}|\}^{1/2} \\ \times [\eta_{-}^{*}(+k'_{\gamma'})\eta_{+}(+k_{\gamma})S^{\gamma'\gamma}_{+k'_{\gamma'}+k_{\gamma}} \\ + \eta_{-}^{*}(+k'_{\gamma'})\eta_{+}(-k_{\gamma})S^{\gamma'\gamma}_{+k'_{\gamma'}-k_{\gamma}} \\ + \eta_{-}^{*}(-k'_{\gamma'})\eta_{+}(+k_{\gamma})S^{\gamma'\gamma}_{-k'_{\gamma'}+k_{\gamma}} \\ + \eta_{-}^{*}(-k'_{\gamma'})\eta_{+}(-k_{\gamma})S^{\gamma'\gamma}_{-k'_{\gamma'}-k_{\gamma}}]\end{aligned} \tag{189}$$

As long as the $\left|\psi_{in(out)}^{\gamma}\right\rangle$ are members of the γth channel Hilbert space we are free to choose what expansion coefficients they have without any loss of generality. For instance it is quite natural to specify reactant states to have momentum only in the direction of the interaction region and for product states to have momentum only in the direction away from the interaction region. If this were the case then $\eta_{+}(-k_{\gamma}) = 0$ and $\eta_{-}^{*}(+k'_{\gamma'}) = 0$. This would cause all but the third term in equation (189) to be zero and we could isolate and solve the $S^{\gamma'\gamma}_{-k'_{\gamma'}+k_{\gamma}}$. Similar considerations can be made for the remaining $\widehat{\mathbf{S}}$-matrix elements in (189).

This observation allows the $\widehat{\mathbf{S}}$-matrix elements to be succinctly written as,

$$S^{\gamma'\gamma}_{\pm k'_{\gamma'}\pm k_{\gamma}} = \frac{\hbar^2(|k'_{\gamma'}||k_{\gamma}|)^{1/2}}{(2\pi\mu)\eta_{-}^{*}(\pm k'_{\gamma'})\eta_{+}(\pm k_{\gamma})} \times \langle^{\pm}\psi_{-}^{\gamma'}|^{\pm}A_{+}^{\gamma}(E)\rangle \tag{190}$$

where the $\pm$ notation represents the four possible combinations for asymptotic momentum representations. The dot product in equation (190) can also be slightly re-written as the following to gain insight, computationally, to what is happening.

$$\langle\psi_{-}^{\gamma'}|A_{+}^{\gamma}(E)\rangle = \int_{-\infty}^{+\infty} e^{iEt}\left\langle\psi_{-}^{\gamma'}\right| exp(-\frac{i}{\hbar}\widehat{\mathbf{H}}t)\left|\psi_{+}^{\gamma}\right\rangle dt \tag{191}$$

We see that as the reactant state propagates we are computing the overlap of it with the product state. This function is known as the Correlation function and relies completely on a numerically accurate propagation scheme. Once this correlation function is computed and a Fourier transform performed then the various $\widehat{\mathbf{S}}$-matrix elements can be computed. It is also useful to note that the range of energies computed by this method is solely dependent upon the expansion coefficients of the reactant and product states. This is computationally valuable because we can choose the energy ranges of interest instead of calculating all energies, individually.

5.7 Example: Square Well Scattering

The channel packet method for computing $\widehat{\mathbf{S}}$-matrix elements will now be applied to the square well model, the first of two examples, and compared with analytic results. The computational parameters used for this simulation are listed in Table 3 and the initial parameters for the reactant and products are listed in Table 4.

Table 3. Square Well $\widehat{\mathbf{S}}$-Matrix Simulation Parameters (a.u.)

Grid Length	200	Propagation Time	1638.40
N	2048	Time Steps	16384
dr	4.88×10^{-2}	dt	0.1
dk	3.14×10^{-2}	dE	3.83×10^{-3}
$k_{max/min}$	$\pm$64.34	$E_{max/min}$	$\pm$31.42

Table 4. Square Well $\widehat{\mathbf{S}}$-Matrix Gaussian Reactant/Product Parameters (a.u.)

	Reactant	Product A	Product B
Mass	5.0	5.0	5.0
a	2.00	2.00	2.00
x_0	75.00	125.00	75.00
k_0	2.70	-2.70	2.70

For this particular simulation we do not need to concern ourselves with any internal quantum states. We will freeze all internal degrees of freedom such that $E_\gamma = 0$. The particular form of $\left|\psi_{in/out}\right\rangle$ used is a Gaussian wave packet. We initially place these wave packets in the asymptotic region where the potential is equal to zero. This will save us computation time because the effect of the Moller operator is to propagate the reactant (product) backwards (forwards) in time toward infinity under H_0 and then propagate that orbit forwards (backwards) to the present (past) time under H. Under this scenario H_0 and H are the same in the asymptotic regions of the square well potential, so $|\psi_{in}\rangle = |\psi_+\rangle$ and $|\psi_{out}\rangle = |\psi_-\rangle$. This does not always have to be the case. There is nothing in the theory preventing us from initially placing $\left|\psi_{in/out}\right\rangle$ in the square well and proceeding with the Moller operators. If this choice is made then $|\psi_{in}\rangle \neq |\psi_+\rangle$ and $|\psi_{out}\rangle \neq |\psi_-\rangle$.

The initial configurations are depicted in Figures 9, 10, 11, 12, and 13.

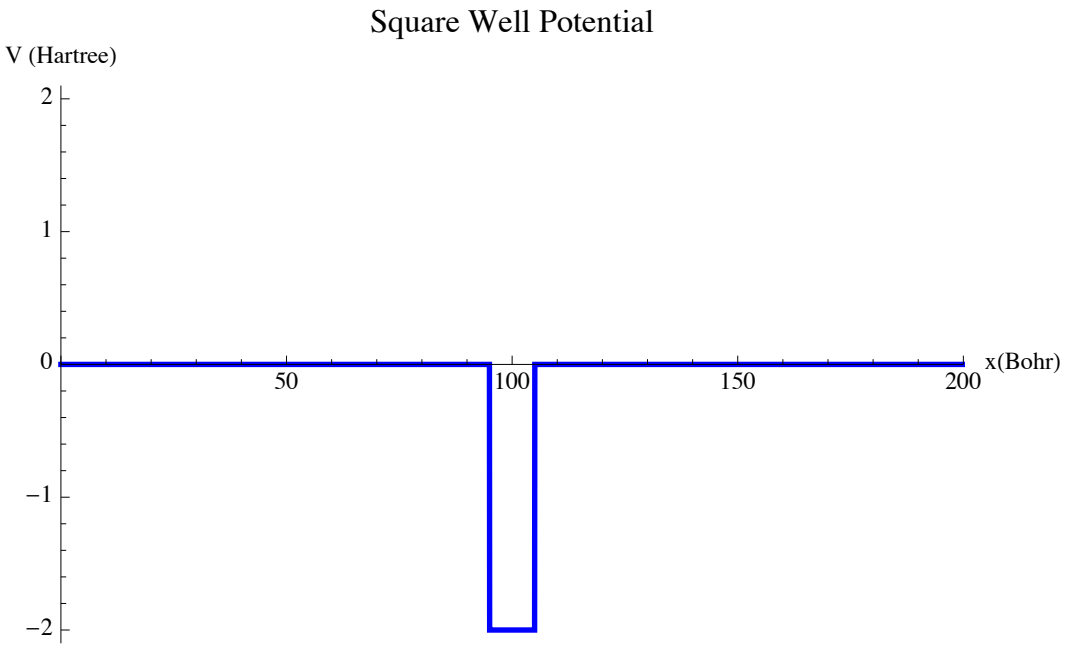

Figure 9. Square Well on 200 a.u. grid. Depth: -2 a.u. Width: 10 a.u.

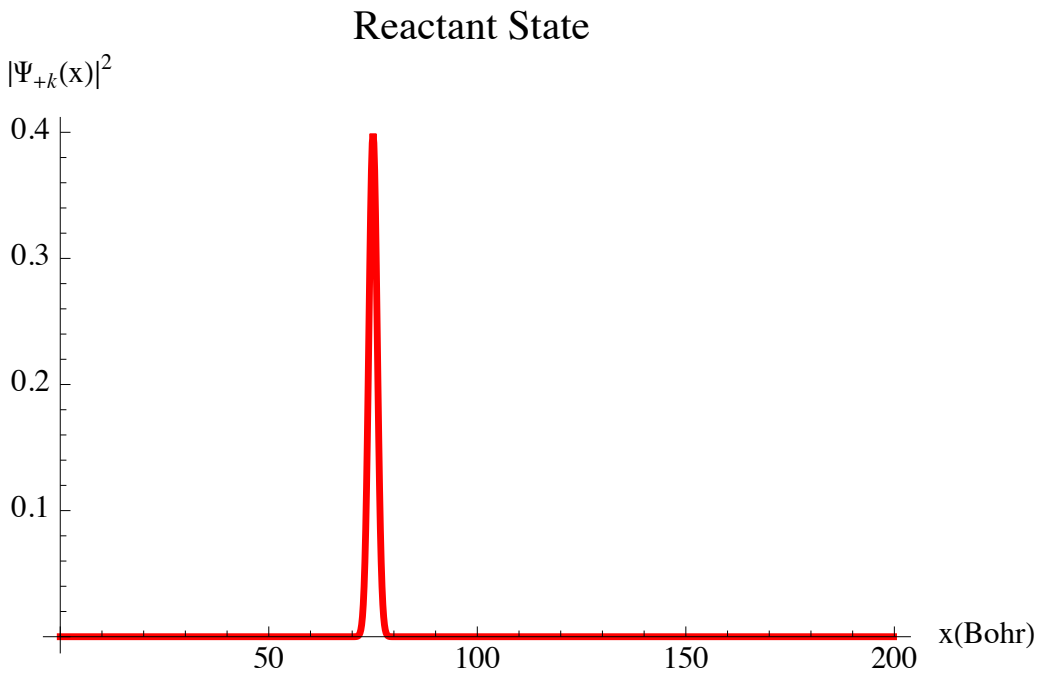

Figure 10. Reactant Moller Wave Function Centered at 75.00 a.u.

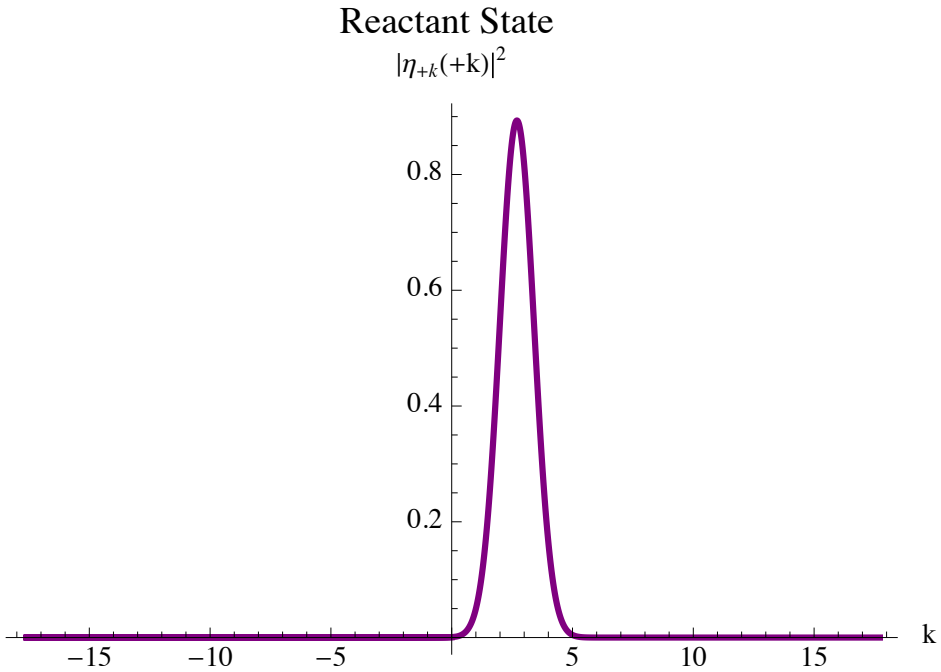

Figure 11. Reactant Moller Wave Function Centered at $k = 2.70$.

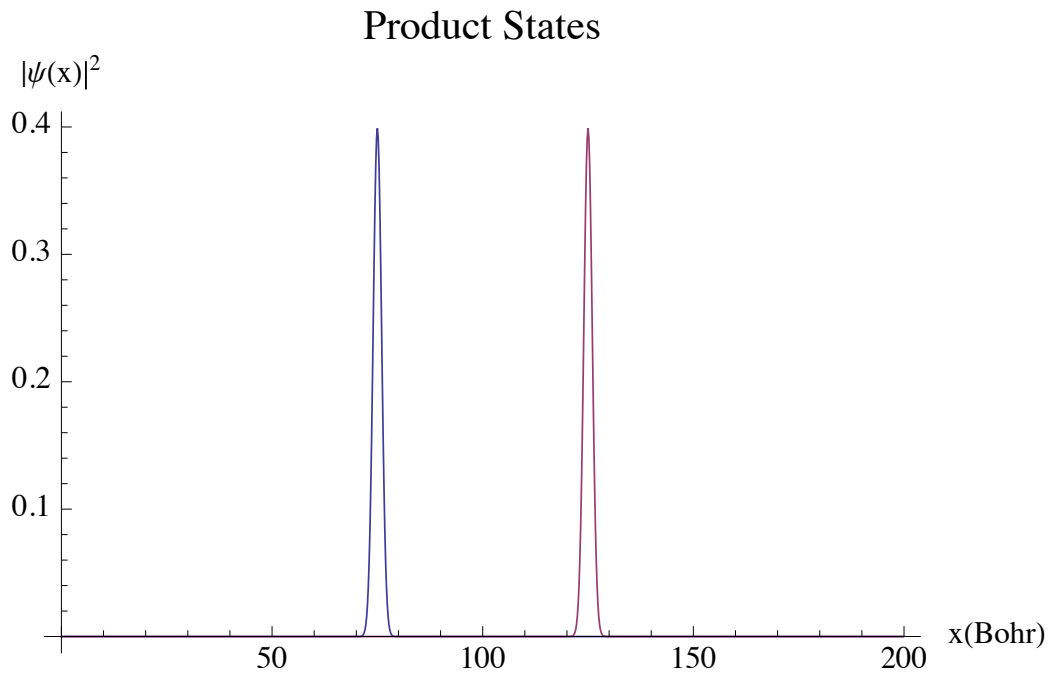

Figure 12. Product Moller Wave Functions Centered at 75.00 a.u. and 125.00 a.u.

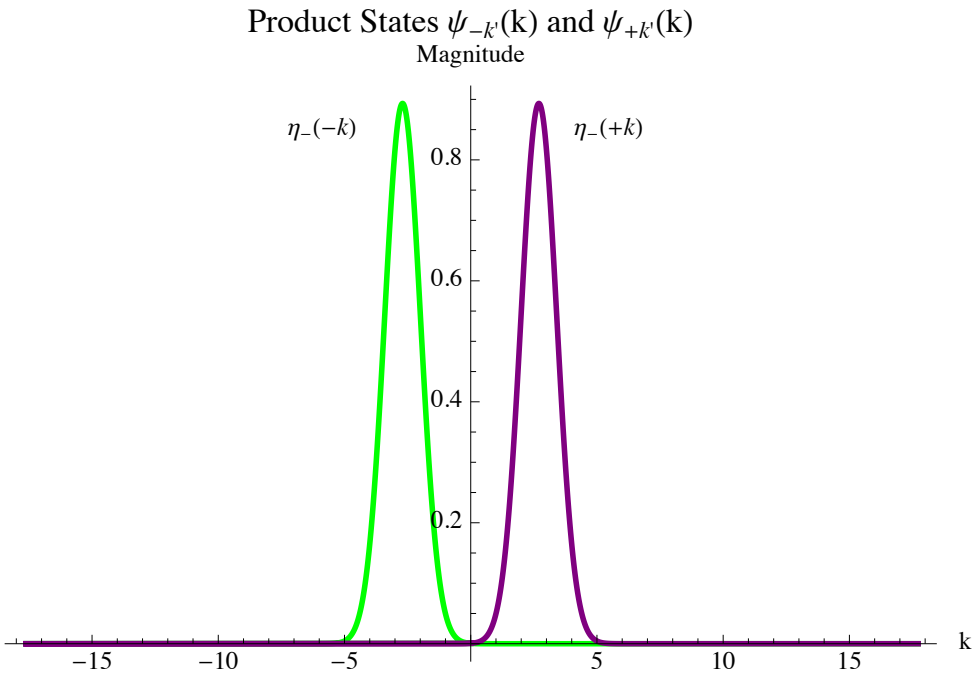

Figure 13. Product Moller Wave Functions Centered at $k = -2.70$ and $k = 2.70$.

One benefit of this channel packet method is that due to its dependence on evolving

a state explicitly in time, snapshots of how the wave function is physically evolving can be depicted. Figures 14 depict the evolving reactant state. The Moller product states are also plotted to emphasize the overlap occurring between the propagating reactant state.

At each time step, Δt, the overlap of the reactant and products are calculated to produce the correlation function. The correlation of the reactant with the -k product, $C_{-k,+k}$, and the that with the +k product, $C_{+k,+k}$ are depicted in Figure 15 as a function in time.

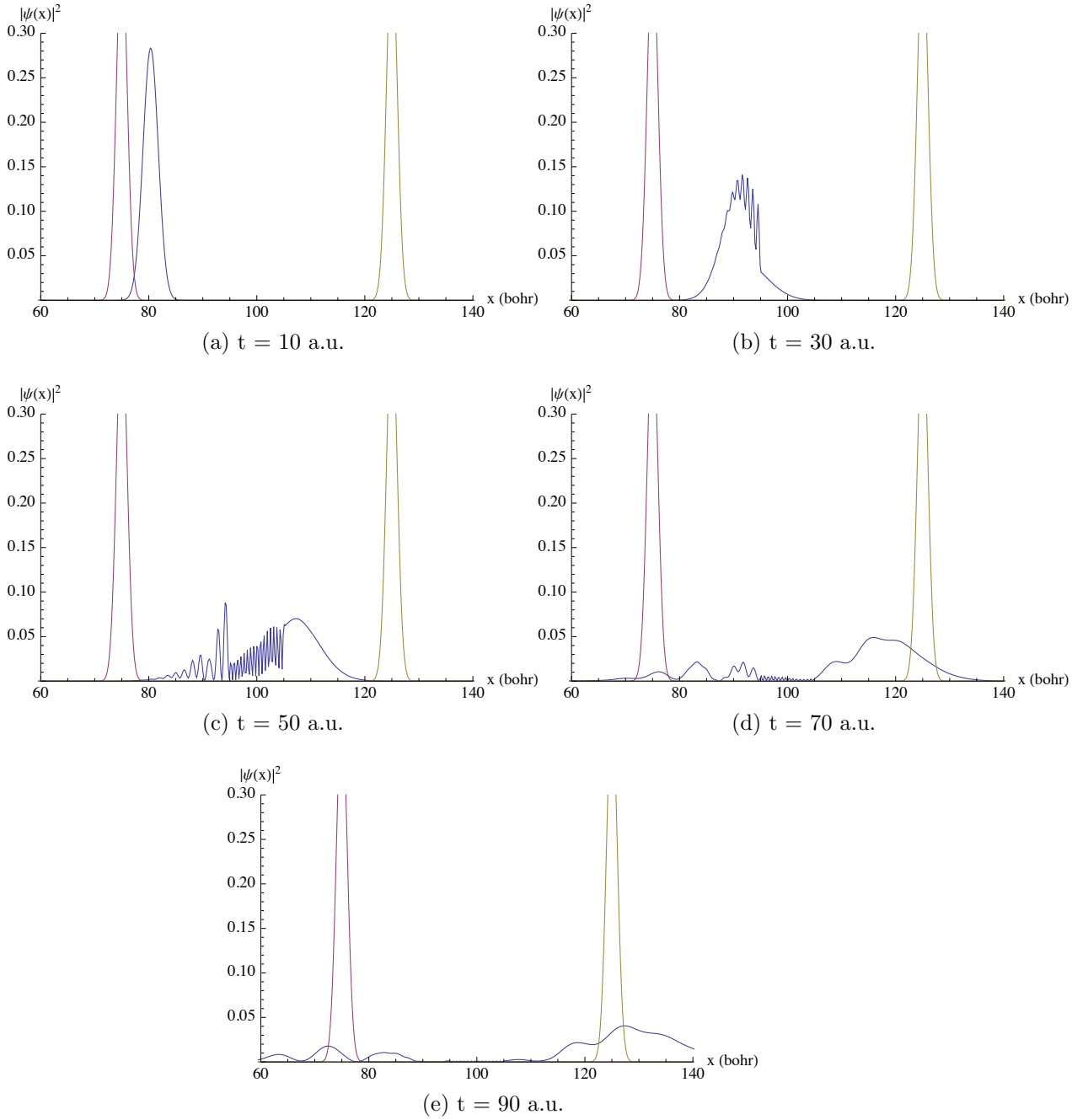

(a) t = 10 a.u.

(b) t = 30 a.u.

(c) t = 50 a.u.

(d) t = 70 a.u.

(e) t = 90 a.u.

Figure 14. Time evolution of the reactant state and the Moller product states.

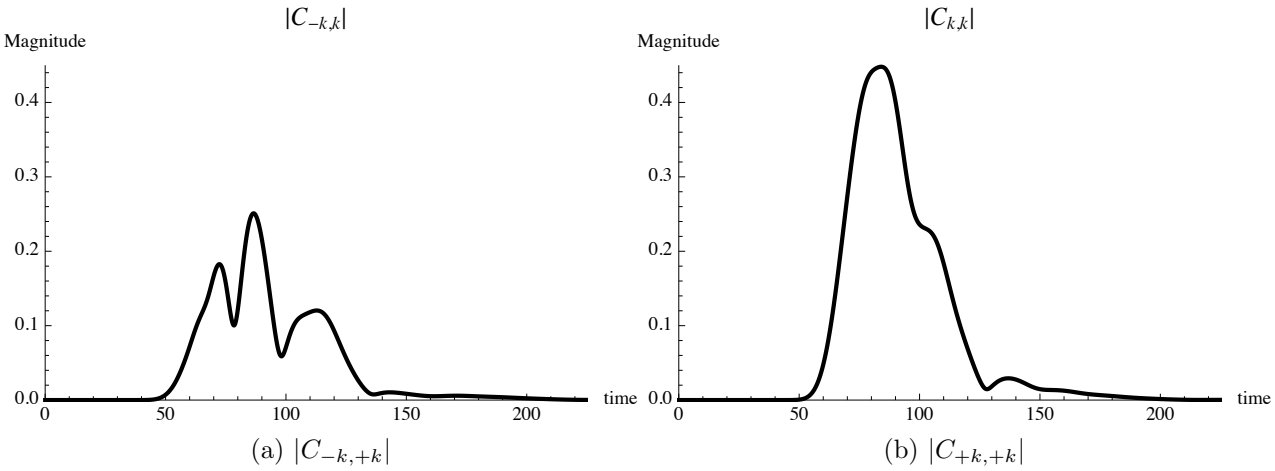

(a) $|C_{-k,+k}|$ (b) $|C_{+k,+k}|$

Figure 15. Correlation functions of the reactant with -k and +k product states.

Once the wave packet has propagated through the potential and beyond the Moller product states the wave function is no longer needed. We can absorb this unneeded wave function by employing absorbing boundary conditions in the form of a completely imaginary potential:

$$V(R) = V_0(R) + iV_{ABC}(R) \tag{192}$$

where $V_0(R)$ is the interaction potential or in this example the square well potential. This will be of great use computationally because we can truncate the length of the grid which reduces the number of operations the FFT has to perform. Also for some potentials the time scale for which the wave packet completely exits the interaction region might be large. The absorbing boundaries will make sure that particular constituents of the wave packet do not traverse the grid more than once. Any function can be used for $V_{ABC}(R)$, but a broad Gaussian in coordinate space centered at the edge of the grid will ensure that minimal reflections take place.

Finally, the correlation functions are transformed via a time/energy FFT and normalized according to equation (190) to produce the desired S-matrix elements. The

numerical square well S-matrix elements were computed and then squared separately to produce the transmission and reflection coefficients. These coefficients are plotted in Figures 16 and 17 as a function of energy. Note that the reactants momentum content ranges from approximately [0,5], reference Figure 11. Using the relation $k = \sqrt{\frac{2mE}{\hbar^2}}$ we should only expect $\widehat{\mathbf{S}}$-matrix elements in the energy range of [0,2.5]. After an energy of 2.5 the numerical calculation starts oscillating. Said another way the signal to noise ratio is low where momentum content is minimal. If these higher energies were desired then one would simply need to change the momentum content of the reactant and product states.

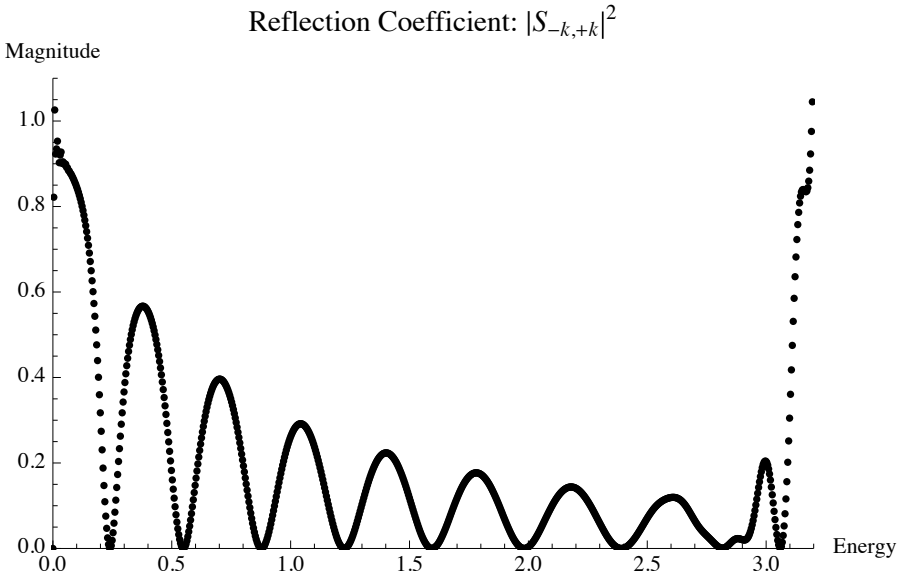

Figure 16. Numerical reflection coefficient for square well potential scattering.

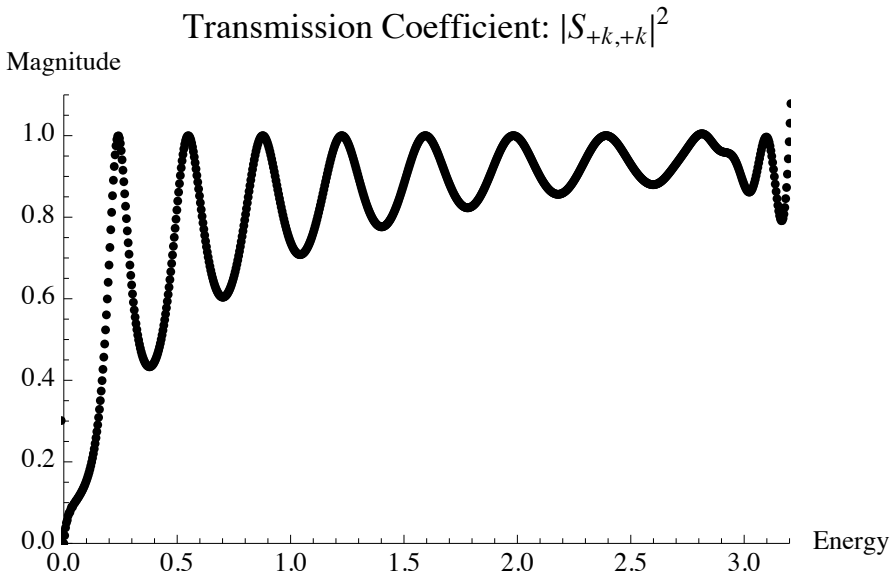

Figure 17. Numerical transmission coefficient for square well potential scattering.

One last independent check on the convergence of the numerical simulation is to make sure that both the reflection and transmission coefficients add to one for the particular energy range. This is shown in Figure 18 to be the case.

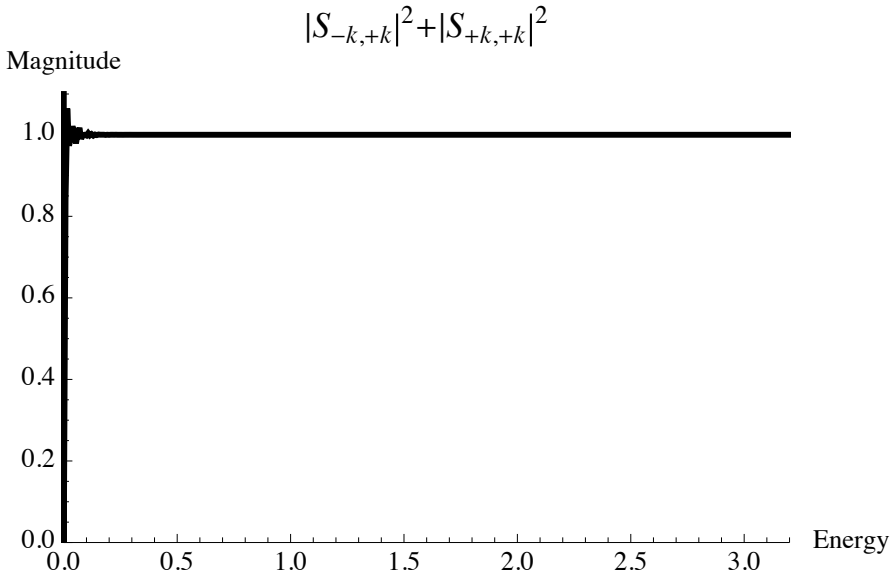

Figure 18. Sum of Numerical Reflection and Transmission Coefficient.

5.8 Analytical Square Well S-Matrix Elements

Square well scattering can be solved analytically as well. This will serve as a validation for the computational results derived in the previous section.

First start by describing the undetermined wave function in all three regions:

$$\langle x|\psi\rangle = \psi(x) = \begin{cases} Ae^{ik_1 x} + Be^{-ik_1 x} & \text{Asymptotic Region} \\ Ce^{ik_2 x} + De^{-ik_2 x} & \text{Interaction Region} \\ Fe^{ik_3 x} + Ge^{-ik_3 x} & \text{Asymptotic Region} \end{cases} \tag{193}$$

where the momentum, k, is given by the total energy and potential in each region:

$$k_1 = \sqrt{\frac{2m}{h^2}E} \tag{194}$$

$$k_2 = \sqrt{\frac{2m}{h^2}(E-V)} \tag{195}$$

$$k_3 = \sqrt{\frac{2m}{h^2}E} \tag{196}$$

and A, B, C, D, F, and G are expansion coefficients that contain momentum information. For the ease of calculation solitary plane waves are used to describe the right moving and left moving wave in each region. Although plane waves are not $\mathcal{L}^2$ functions, a finite combination of them, like a Gaussian wavefunction, are square integrable. For this reason plane waves are admitted in this analysis.

The boundary conditions specify that at the interface of each region the wavefunction and its derivative must be continuous. These two equations will yield relationships between the coefficients A, B, C, and D between regions 1 and 2. The same can be done for the interface of regions 2 and 3 yielding relationships between C, D,

F, and G. The coefficients relate in the following way:

$$\begin{pmatrix} A \\ B \end{pmatrix} = \begin{pmatrix} \frac{1}{2}(1+\frac{k_2}{k_1}) & \frac{1}{2}(1-\frac{k_2}{k_1}) \\ \frac{1}{2}(1-\frac{k_2}{k_1}) & \frac{1}{2}(1+\frac{k_2}{k_1}) \end{pmatrix} \begin{pmatrix} C \\ D \end{pmatrix} = \begin{pmatrix} a & b \\ b & a \end{pmatrix} \begin{pmatrix} C \\ D \end{pmatrix} \tag{197}$$

$$\begin{pmatrix} C \\ D \end{pmatrix} = \begin{pmatrix} \frac{1}{2}(1+\frac{k_3}{k_2})e^{ik_3w-ik_2w} & \frac{1}{2}(1-\frac{k_3}{k_2})e^{-ik_3w-ik_2w} \\ \frac{1}{2}(1-\frac{k_3}{k_2})e^{ik_3w+ik_2w} & \frac{1}{2}(1+\frac{k_3}{k_2})e^{-ik_3w+ik_2w} \end{pmatrix} \begin{pmatrix} F \\ G \end{pmatrix} = \begin{pmatrix} c & d \\ d^* & c^* \end{pmatrix} \begin{pmatrix} F \\ G \end{pmatrix} \tag{198}$$

where w is the width of the square well.

Substituting Equation (198) into Equation (197) will yield how the two asymptotic wavefunctions are connected to each other.

$$\begin{pmatrix} A \\ B \end{pmatrix} = \begin{pmatrix} a & b \\ b & a \end{pmatrix} \begin{pmatrix} c & d \\ d^* & c^* \end{pmatrix} \begin{pmatrix} F \\ G \end{pmatrix} = \begin{pmatrix} ac+bd^* & ad+bc^* \\ ad^*+bc & ac^*+bd \end{pmatrix} \begin{pmatrix} F \\ G \end{pmatrix} = \begin{pmatrix} g & f \\ f^* & g^* \end{pmatrix} \begin{pmatrix} F \\ G \end{pmatrix} \tag{199}$$

Notice that the coefficients B and G in Equation (193) represent outgoing waves or waves moving away from the interaction region and the coefficients A and F in (193) represent waves moving towards the interaction region. A little bit of algebra yields a matrix equation that relates the outgoing wave packets with the incoming wave

packets:

$$\begin{pmatrix} B(-k) \\ F(+k) \end{pmatrix} = \begin{pmatrix} \frac{f^*}{g} & \frac{1}{g} \\ \frac{1}{g} & \frac{-f}{g} \end{pmatrix} \begin{pmatrix} A(+k) \\ G(-k) \end{pmatrix} = \begin{pmatrix} S_{11} & S_{12} \\ S_{21} & S_{22} \end{pmatrix} \begin{pmatrix} A(+k) \\ G(-k) \end{pmatrix} \tag{200}$$

Another way to express equation (200) is,

$$\begin{pmatrix} \langle -k|\psi_{out}\rangle \\ \langle +k|\psi_{out}\rangle \end{pmatrix} = \begin{pmatrix} \langle -k|\, S\, |+k\rangle & \langle -k|\, S\, |-k\rangle \\ \langle +k|\, S\, |+k\rangle & \langle +k|\, S\, |-k\rangle \end{pmatrix} \begin{pmatrix} \langle +k|\psi_{in}\rangle \\ \langle -k|\psi_{in}\rangle \end{pmatrix}$$

Where $\langle -k|\psi_{out}\rangle = B(-k)$, $\langle +k|\psi_{out}\rangle = F(+k)$, $\langle +k|\psi_{in}\rangle = A(+k)$, $\langle -k|\psi_{in}\rangle = G(-k)$, and $\langle \pm k|\, S\, |\pm k\rangle = S_{\pm k,\pm k} = S_{ij}$. This is the desired final result, $\langle k'|\psi_{out}\rangle = \langle k'|\, S\, |k\rangle\, \langle k|\psi_{in}\rangle$.

To compare with the numerical results we set the $G = 0$. This signifies that the reactant is only traversing from the left of the square well to the interaction region. We proceed to plot $|S_{11}|^2$, the transmission coefficient, and $|S_{21}|^2$, the reflection coefficient as a function of energy and compare with the numerical results.

The error incurred by the numerical answer comes from the fact that when the square well is discretized it is approximated as a trapezoidal well. In order to resolve this, the number of grid points must be increased, but it is at the expense of greater computational time and effort so a balance needs to be met.

The structure of Figure 19 and 20 is best understood by appealing to resonance phenomena. A system exhibits resonances where the transmission coefficient has pronounced peaks (here at T=1). For square well scattering this correspondence amounts to when the well width is an integral multiple of half the particle wavelength[12]. Us-

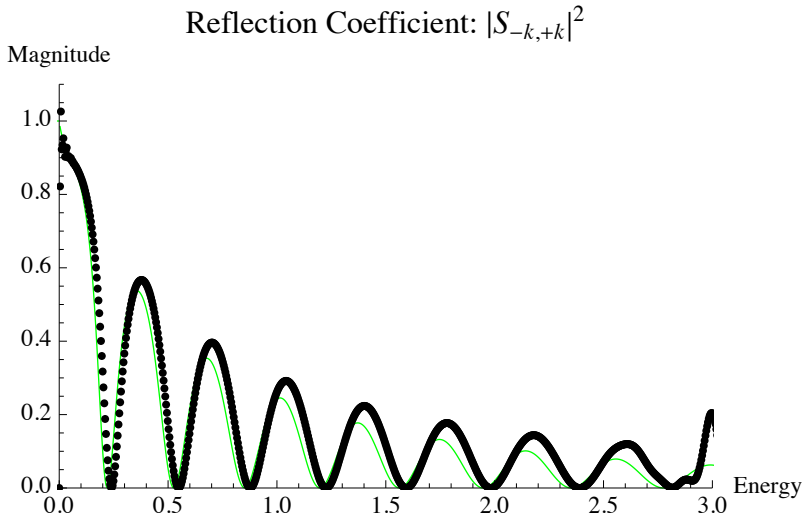

Figure 19. The analytic reflection coefficient is the solid line and the numeric reflection coefficient the dotted line.

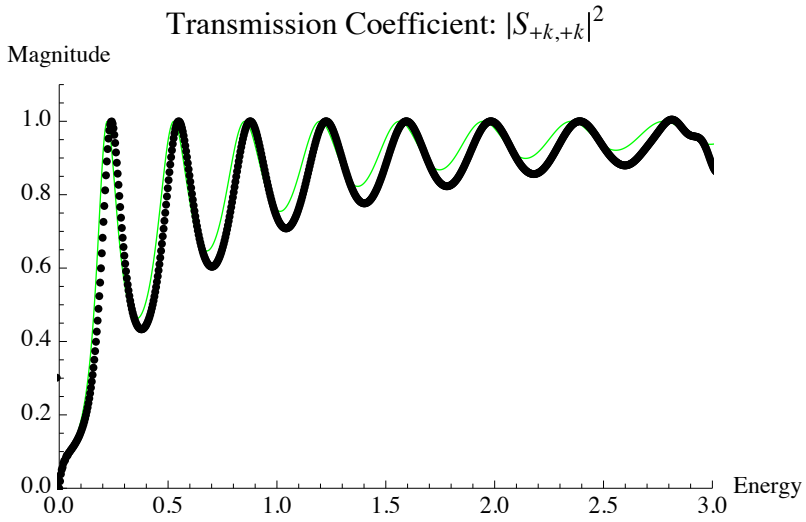

Figure 20. The analytic transmission coefficient is the solid line and the numeric transmission the dotted line.

ing this fact in conjunction with the de Broglie relation for matter waves, $\lambda = \frac{2\pi}{k}$, we seek energy values that correspond to a momentum of $k = \frac{n\pi}{w}$:

$$E = \left(\frac{n\pi}{w}\right)^2 \frac{1}{2m} + V_0 \tag{201}$$

Using the same parameters for mass, potential width, and potential depth, the first three positive values of E correspond to a value of n of 15, 16, and 17. The corresponding energies are 0.22, 0.53, and 0.85, the first three peaks shown in Figure 20. The energy spectrum predicted by equation (201) is the same as the energy spectrum of an infinitely deep square well. Resonances occur at the the eigen energies of the infinite square well of the same width.

5.9 Example: Two State Scattering

For the curve crossing example we start with a set of diabatic surfaces. It is important to note once again that diabatic surfaces are never calculated through *ab-initio* techniques. The purpose of this example is to explore the dynamics of a coupled two level system. Starting with a simple model in the strictly diabatic form has the advantage of having the derivative couplings mixed in to the potential and so the transformation is easy to compute.

We begin as Alvarellos and Metiu[2] by defining a two level strictly diabatic Hamiltonian:

$$\begin{aligned}
\widehat{\mathbf{H}} &= \widehat{\mathbf{T}} + \widehat{\mathbf{V}} \\
&= -\frac{1}{2\mu} \overset{2}{\overbrace{\begin{array}{cc} |1\rangle & |2\rangle \end{array}}} \begin{pmatrix} \frac{d}{dR} & 0 \\ 0 & \frac{d}{dR} \end{pmatrix} + \overbrace{\begin{array}{cc} |1\rangle & |2\rangle \end{array}}^{} \begin{pmatrix} D_{11}(R) & D_{12}(R) \\ D_{21}(R) & D_{22}(R) \end{pmatrix}
\end{aligned} \tag{202}$$

where,

$$D_{11}(R) = W_0\{exp[-2\alpha(R - R_0)] - 2 \cdot exp[-\alpha(R - R_0)]\} + \Delta\epsilon \quad (203)$$

$$D_{22}(R) = W_0\{exp[-2\alpha(R - R_0)] + 2 \cdot exp[-\alpha(R - R_0)]\} \quad (204)$$

$$D_{12}(R) = D_{21}(R) = (\beta\Delta\epsilon/2)exp[-\alpha^2(R - R_c)^2] \quad (205)$$

Once again we freeze all internal degrees of freedom and in doing so do not have to keep track of internal states. The strictly diabatic matrix elements are plotted in Figure 21 with the parameters listed in Table 5. Observe that D_{11} and D_{22} cross at 8.8 bohr.

Table 5. Curve Crossing Diabatic Potential Energy Surface Parameters

W_0	0.184 hartree	α^{-1}	2.5 bohr
R_0	5.0 bohr	β	0.3
$\Delta\epsilon$	0.147 hartree	R_c	8.8 bohr

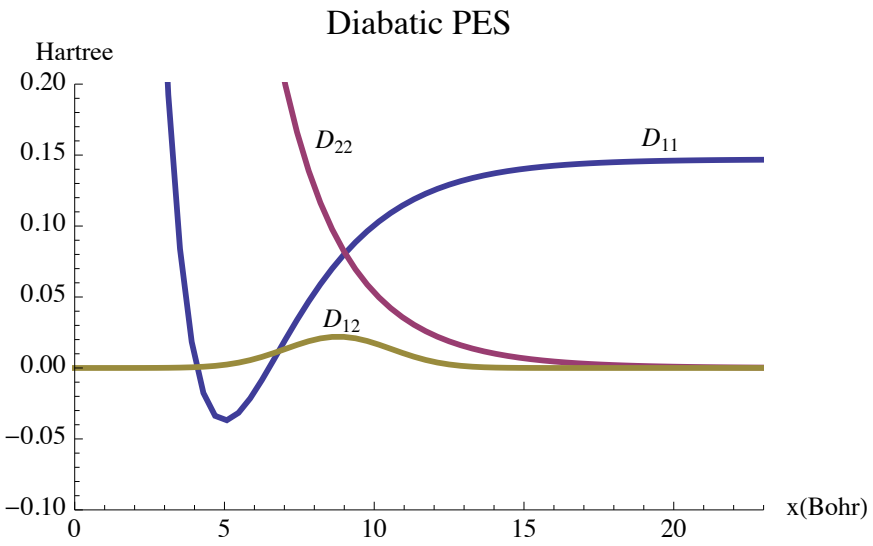

Figure 21. Diabatic PES.

In this diabatic form we see that the functions D_{12} and D_{21} serve to couple the ground diabatic state, D_{22}, to the excited diabatic state, D_{11}. We determine which state is ground and excited by their relative asymptotic energies.

Since we are given a set of strictly diabatic surfaces the kinetic energy operator is already diagonal and there is no need to produce a transformation matrix from derivative coupling terms. This information is already encoded in to the diabatic surfaces. Performing a simple numerical matrix diagonalization on the diabatic surfaces will produce the ground adiabatic state, A_{11} and the excited adiabatic state, A_{22}.

$$V^A = UV^D U_F^\dagger = \begin{pmatrix} A_{11}(R) & 0 \\ 0 & A_{22}(R) \end{pmatrix} \tag{206}$$

Upon numerical diagonalization the diabatic PES become adiabatic PES and are plotted in Figure 22.

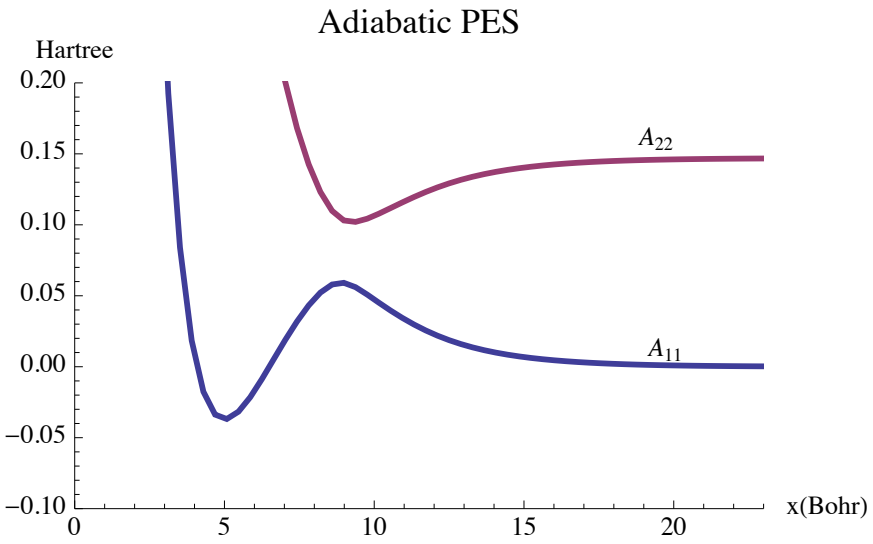

Figure 22. Adiabatic PES.

Observe that A_{11} and A_{22} approach each other at 8.8 bohr where the strictly diabatic potentials cross. By referring to equation (77), it would be ill advised to use

the adiabatic approximation. Since the adiabatic energies are approaching each other in this vicinity the derivative couplings are no longer small.

The matrix element D_{12} gives and indication of how strong and over what range the two states are coupled. To understand the picture physically imagine two atomic species approaching each other in their ground state along D_{22}. At a particular distance during this collision, if the system has enough kinetic energy, it will couple and exit on the excited state surface D_{11}. How much of the initial wave function is excited to the higher level depends on how strongly the states are coupled in the diabatic representation.

The nuclear wave function itself will then be a two component wave function since our group only contains two states. All internal degrees of freedom are frozen so $E_\gamma = 0$. Designate ϕ_G as the ground component and ϕ_E as the excited component so the total wave function is:

$$\Psi(R) = \begin{pmatrix} \phi_E(R) \\ \phi_G(R) \end{pmatrix} \tag{207}$$

The short time propagation scheme, equation (178), has to be modified using the transformation function that rotates the strictly diabatic states in to the adiabatic states. This is the same transformation function that was used to transform the diabatic PES in to the adiabatic PES. The transformation will be written down as $U_F^\dagger(R) = \langle a(R)|d(R)\rangle$ and $U_F(R) = \langle d(R)|a(R)\rangle$ and the propagation scheme is now the following:

1) Starting with a diabatic wave function rotate to an adiabatic function: $U_F^\dagger(R_n)\psi(R_n, 0)$

2) Multiply the result by $e^{-\frac{i}{2\hbar}\Delta t V^A(R_n)}$

3) Transform back to the diabatic representation using $U_F(R_n)$

4) By use of a forward FFT transform the result to momentum space

5) Multiply the k-space function by the phase $e^{-\frac{i}{2\hbar}\Delta t\widehat{\mathbf{T}}(k_n)}$

6) Perform a second transform back to coordinate space using a backward FFT

7) Once again transform to adiabatic representation by $U_F^\dagger(R_n)$

8) Multiply the result by $e^{-\frac{i}{2\hbar}\Delta t V^A(R_n)}$

9) Transform back the the diabatic representation with U_F

The short time propagation now looks like:

$$\psi(x_n,\Delta t) = U_F e^{-\frac{i}{2\hbar}\Delta t V^A(R_n)} U_F^\dagger(R_n)\{\mathcal{F}^{-1}[e^{-\frac{i}{2\hbar}\Delta t T(R_n)}\mathcal{F}(U_F e^{-\frac{i}{2\hbar}\Delta t V^A A(R_n)} U_F^\dagger(R_n)\psi(R_n,0))]\} \tag{208}$$

Starting in the diabatic representation we rotate the wave function in to its adiabatic form. Since we are in the adiabatic representation the exponential of the adiabatic PES, being a diagonal matrix, becomes a multiplication in step 2. Transforming back to the strictly diabatic representation before executing a FFT allows us to take advantage of the diagonal form of the kinetic energy operator. Once again the exponentiation of the kinetic energy operator becomes a multiplication in step 5. This iterative process repeats itself until enough time has passed for the wave function to leave the interaction region.

As required by the channel packet method we start with Moller wave functions. Similar to the square well example we can place a Gaussian wave function in the asymptotic region such that when it propagates backwards in time under no interaction potential and then forward in time under the full Hamiltonian it remains the same. This Moller wave function will be propagated in to the interaction region where it will be subjected to the potentials shown in Figures 21 and 22. We will only look at state to state collisions meaning we pick the initial state to be completely ground or completely excited. The first run will initially proceed with $\phi_E = 0$ and the Gaussian placed in ϕ_G. The second run will be the opposite, $\phi_G = 0$ and the Gaussian placed in ϕ_E.

With significant coupling we expect wave function to exit out on both the ground and excited state surfaces. This propagated state will then be correlated with two product states, one that is purely on the ground energy surface and the other which is purely on the excited energy surface, so that S-matrix elements can be calculated. The parameters used for this curve crossing simulation are listed in Tables 6 and 7.

Table 6. Curve Crossing Simulation Parameters (a.u.)

Grid Length	100	Propagation Time	10485760
N	2048	Time Steps	2097152
dr	4.88×10^{-2}	dt	5.0
dk	6.28×10^{-2}	dE	3.84×10^{-5}
$k_{max/min}$	± 64.34	$E_{max/min}$	± 1.257

Table 7. Curve Crossing Reactant/Product Parameters (a.u.)

	Reactant	Product A	Product B
Mass	918.00	918.00	918.00
a	0.35	0.35	0.35
x_0	40.00	40.00	40.00
k_0	-14.50	14.50	14.50

Just like in the square well example we also display graphically the initial conditions of the simulation.

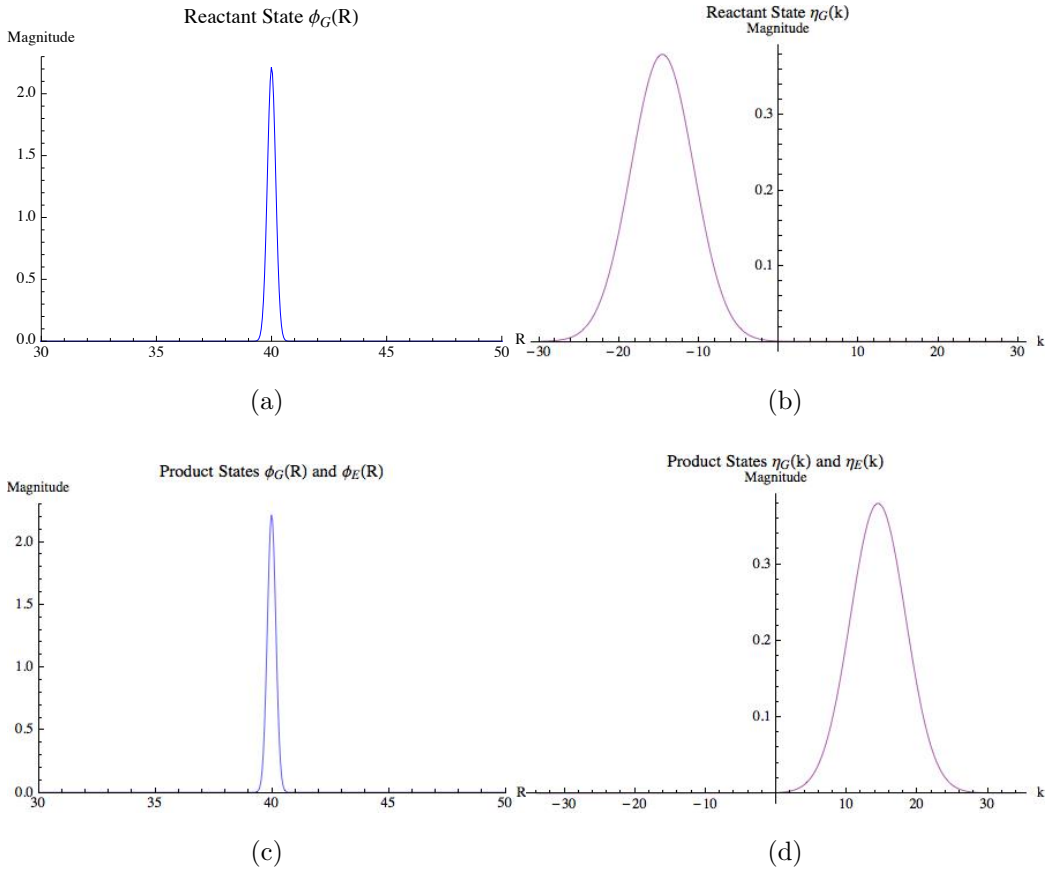

Figure 23. Initial conditions for the reactant state centered at $x = 40.0$ and $k_0 = -14.50$ and for the product states centered at $x = 40.0$ and $k_0 = 14.50$.

Time snap shots of both the ground and excited state wave functions are taken to show how the evolution proceeds in a coupled state problem.

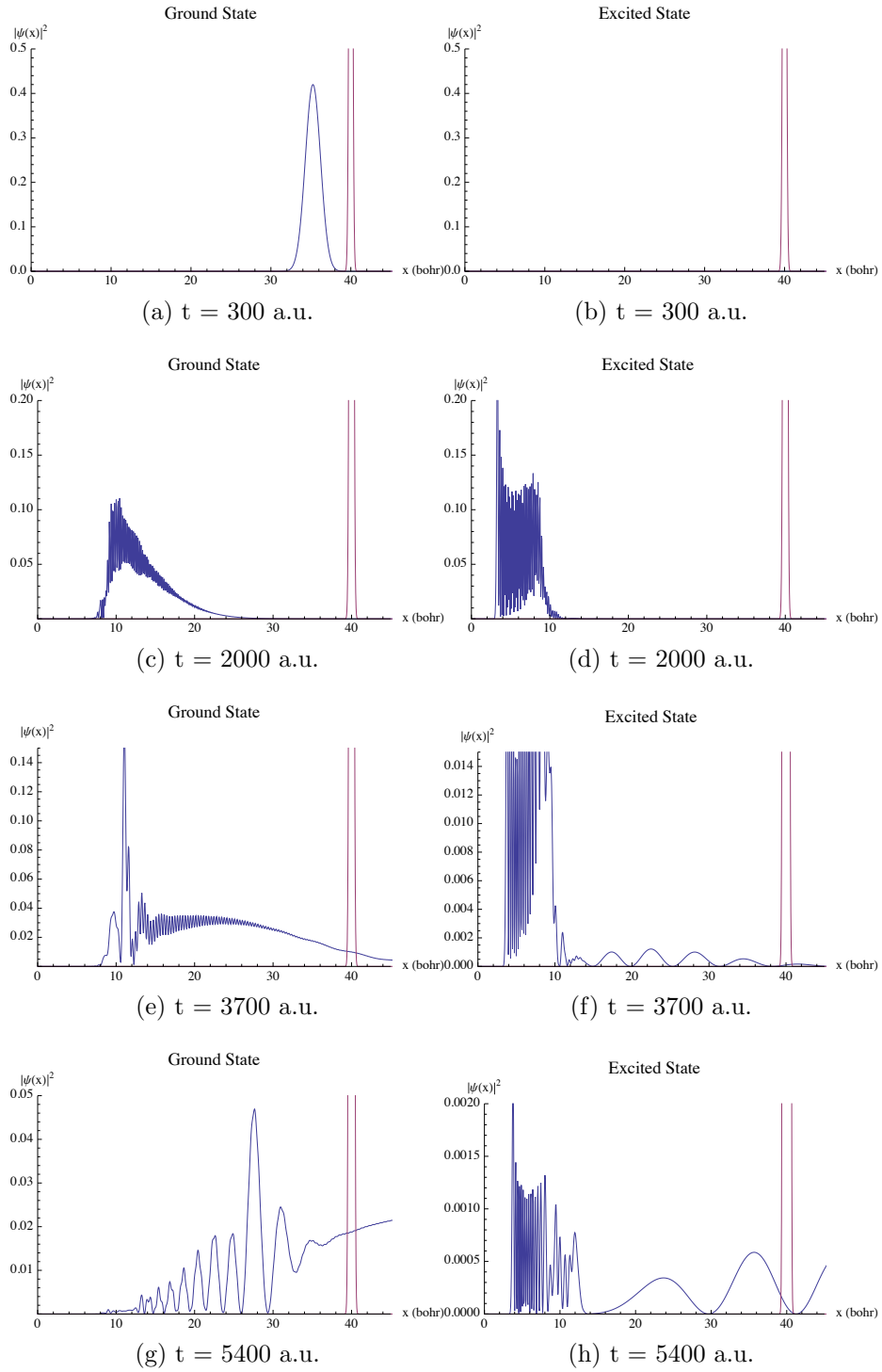

(a) t = 300 a.u. (b) t = 300 a.u.

(c) t = 2000 a.u. (d) t = 2000 a.u.

(e) t = 3700 a.u. (f) t = 3700 a.u.

(g) t = 5400 a.u. (h) t = 5400 a.u.

Figure 24. Time evolution of the Moller reactant state. (a), (c), (e), and (g) show the evolution of the ground state and (b), (d), (f), and (h) show the evolution of the excited state. Notice the magnitude scale changes for each plot in order to show details of the wave function.

Notice how in Figures 24c and 24d the ground state wave function has entered the region in space where the coupling is strongest, $R_c = 8.8$ bohr. Since the initial wave function had enough kinetic energy we see the system accessing the excited case. In order to exit the excited channel however only components of energy greater than 0.147 Hartree, the asymptotic excited region potential, will be able to do so. Any component with lower energy will exit back out on the ground energy surface.

As the total wave function leaves the interaction region toward the asymptotic region it no longer is just in its ground state. The total wave function now has both ground and excited character. In essence we have collided an asymptotically ground system of reduced mass 918 a.u. and produced a system that now asymptotically has a non-zero probability of being excited. Upon exiting the interaction region, Figures 24g and 24h, the correlation between the evolving state and the product Moller functions are computed.

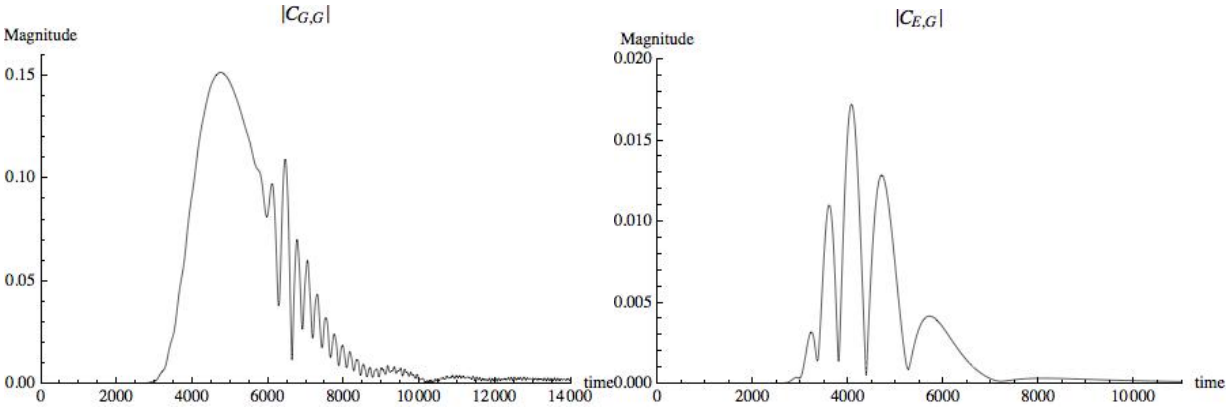

Figure 25. a.) Correlation function from ground state to ground state b.) Correlation function from ground state to excited state.

These correlation functions undergo a time/energy Fourier Transform and upon normalization using the correct momentum channels, S-matrix elements are produced. Although these matrix elements are not analytically derivable as in the square well

potential one can always take the sum of the transmission and reflection coefficient and check that they add up to unity. This signifies that the solution has converged. The results are plotted in Figure 26.

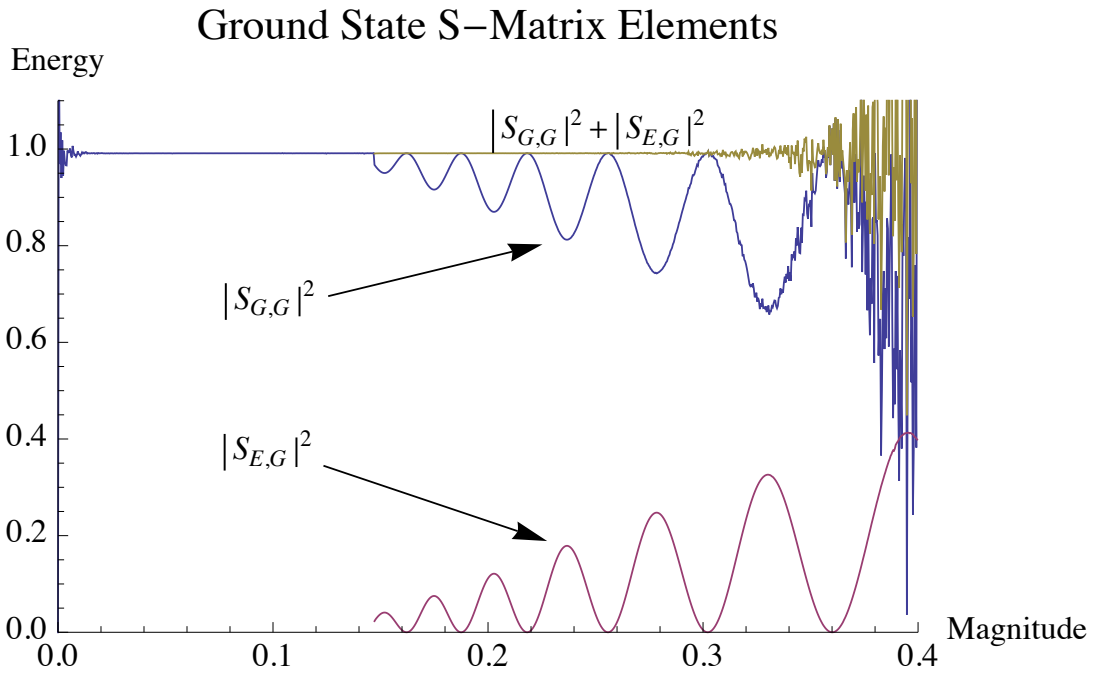

Figure 26. Displayed are the absolute value square S-matrix elements of the ground state to ground state and ground state to excited state transitions. Notice the excited channel is closed until the asymptotic energy 0.147.

The simulation was run again except starting with an initial Moller state that is completely excited: $\phi_G = 0$ and the Gaussian placed in ϕ_E. In this regime we expect de-excitation to occur through the interaction region. This is indeed the case and the correlation function and state to state S-matrix elements are given in Figures 27 and 28.

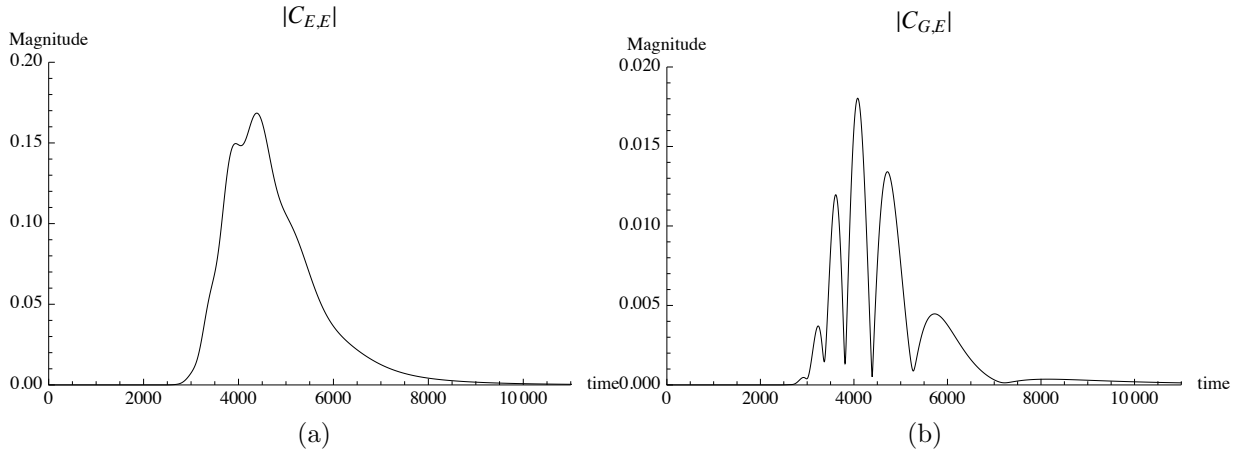

Figure 27. a.) Correlation function from excited state to excited state b.) Correlation function from excited state to ground state.

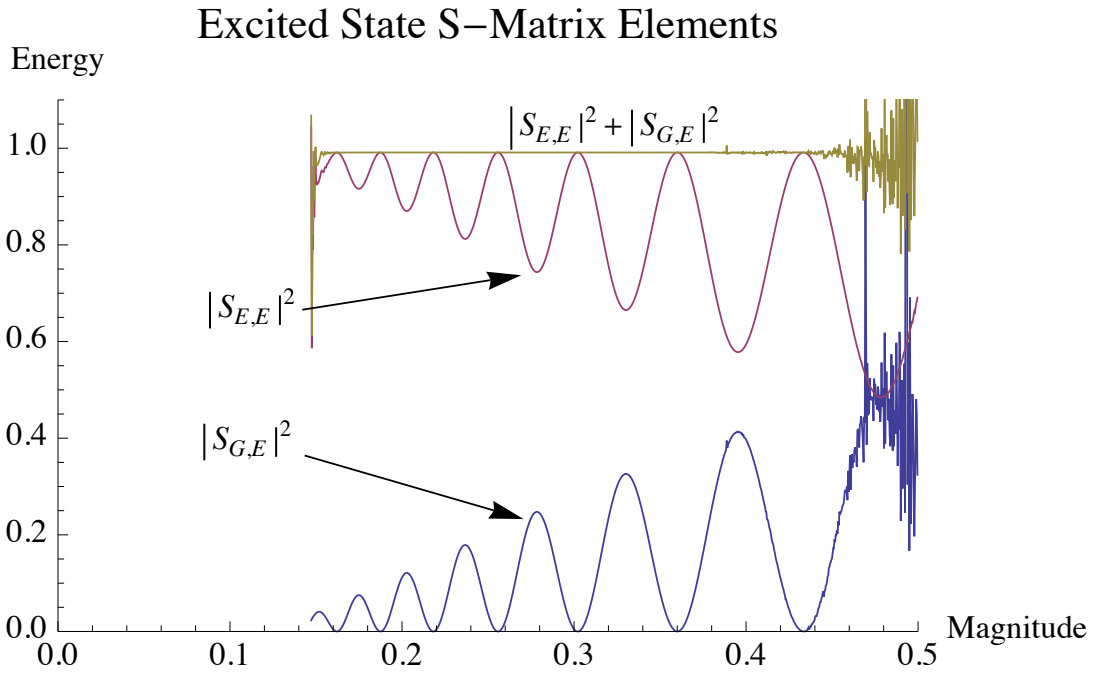

Figure 28. Displayed are the absolute value square S-matrix elements of the excited state to excited state and excited state to ground state transitions. The straight line is their sum. Notice no transitions occur below the 0.147 hartree asymptotic energy of the excited state.

5.10 Summary

By approximating the propagator using the split operator method we were able to develop a short time propagator algorithm to propagate wave packets through time. In doing so we took advantage of the fact that the kinetic exponential and potential exponential operators are local in their respective representations. The Fast Fourier Transform allowed us to switch representations with great expediency. The nature of most modern FFT algorithms involve many recursive loops and as such are easily parallelizeable to multi-core multi-CPU computing systems. For the computational alkali noble gas collisions we will be making use of 16 and 32 core clusters.

With the advantage of the FFTs speed however comes the disadvantage of a restrictive grid. Depending on the region of interest in the coordinate/momentum space or the time/energy space vast portions of the computation grid might not be needed and simply are wasted computations. Also depending on the resolution needed the FFT transforms could cause stack overflow or memory bound errors if the vectors are too large. The problem is compounded even more when using double precision complex vectors. The easiest way to resolve such issues is to simply move back to the standard Fourier Transform. Even though the FT is on the order of N^2 operations and can not be parallelized there are no restrictions on the grid. With an FT we can choose the region of interest and resolution to what ever degree desired. Both the FFT and FT will be used judiciously in the next chapter.

The Channel Packet Method was developed to calculate $\widehat{\mathbf{S}}$-Matrix elements. If the reactant and product channels are selected to be solely incoming or outgoing wave packets then we can isolate and calculate each $\widehat{\mathbf{S}}$-Matrix element separately. Since we chose the momentum content of the reactant and products we can compute $\widehat{\mathbf{S}}$-Matrix elements over a range of energies. At the heart of the calculation is the correlation function and this depends on an accurate propagation algorithm.

In the next chapter we will not be able to test the numerical accuracy of the calculation by comparing the answer to an analytical solution. However we can always test the convergence of the solution because the $\widehat{\mathbf{S}}$-Matrix is unitary. This amounts to ensuring that over the energy range of interest the transmission and reflection coefficients add up to unity. When the elements do add to unity we can be certain that the accuracy of the prediction then is a function of how accurate the potential energy surfaces and derivative couplings are. All errors induced by the time-dependent $\widehat{\mathbf{S}}$-Matrix algorithm, too large a time step, truncating the correlation function too early, insufficient coordinate or momentum resolution, improper Moller states, etc, will be revealed as a violation of unity.

VI. Computational Dynamics of Alkali-Noble Gas Collisions

6.1 Introduction

With the computational algorithms developed and verified we can now turn our attention to the calculation of S-Matrix elements for Alkali-Noble Gas pairs. There are two sets of inputs that are needed to solve equation (143), the Close-Couple Hamiltonian. First, we will need the $\Sigma(R)$ and $\Pi(R)$ potentially energy surfaces along with the spin-orbit coupling parameter $a(R)$. Second we will need the rotation angle, $\alpha(R)$, used to create U_F which rotates the basis vectors such that the derivative couplings are minimized. With the correct manipulations of the close-coupled equations both a strictly diabatic form and adiabatic form will be used in the same manner as in the two level example.

Creation of the Moller states will not be as simple as in the square well and two level system cases. In those two examples the asymptotic Hamiltonian and the interaction Hamiltonian were equivalent up to the initial placement of the original Gaussian. This is no longer the case because in this real world system we have to take in to account the centrifugal potential. As we increase the angular momentum this centrifugal barrier eventually overcomes the interaction potential and the system will no longer interact. However since the centrifugal potential falls off as R^{-2} it is present everywhere along the computational grid. Propagating under $\widehat{\mathbf{H}}_0$ out towards infinity can be done analytically, but propagating back under the full Hamiltonian, $\widehat{\mathbf{H}}$, must be done numerically.

In this work we will pre-compute the Moller States, which is not typically done. Usually one would start by placing an initial wave packet extremely far out in the asymptotic region where the centrifugal potential is negligible and proceed with the interaction calculation. The disadvantage to this is two fold. One, the computation

will require an enormous amount of time to converge because the slower energy components of the wave packet will take a long time to propagate in to the interaction region, interact, then an equally long time to leave the interaction region to correlate. Secondly, if any resonance phenomenon exist the wave packet will slowly "leak" out of the interaction region. Each one of these energy components must then make the return journey to be correlated. By pre-computing the Moller States we can shorten the interaction grid length. This forgoes any unnecessary propagation in the asymptotic region. It also decreases the number of points the FFT has to transform. With every iteration of the short time propagator twelve FFTs must be performed for our 6x6 block. This represents a major computational sink, so the shorter the grid the less time is spent transforming vectors. Lastly, the Moller states need only be computed once for a specific energy range. If these states are stored then they can be used more than once.

Table 8. Alkali Metal-Noble Gas Pairs

Alkali Metal	Noble Gas
Potassium (K)	Helium (He), Neon (Ne), Argon (Ar)
Rubidium (Rb)	Helium (He), Neon (Ne), Argon (Ar)
Cesium (Cs)	Helium (He), Neon (Ne), Argon (Ar)

Table 8 lists all the collision pairs that will be studied. With each pair we will be able to compare the effects of both spin-orbit coupling and Coriolis coupling. In addition to the spin-orbit and Coriolis coupling the radial derivative couplings have been computed by Belcher[7] for the Potassium-Helium system. All nine collisions will be simulated and cross sections calculated. For the remainder this chapter the analysis will concentrate specifically on the KHe system since we have all necessary inputs. Also, KHe systems have been known to lase on their own under relatively tame laboratory conditions due to the small spin-orbit parameter energy. The results

of the remaining nine collisions will be presented in the next chapter.

We first start by defining the alkali-noble gas Hamiltonian, (143) in its diabatic form:

$$
H = -\frac{1}{2\mu}\begin{pmatrix}
\left|\begin{smallmatrix} J & 3/2 \\ 3/2 & 3/2 \end{smallmatrix}\right\rangle & \left|\begin{smallmatrix} J & 3/2 \\ 1/2 & 1/2 \end{smallmatrix}\right\rangle & \left|\begin{smallmatrix} J & 1/2 \\ 1/2 & 1/2 \end{smallmatrix}\right\rangle & \left|\begin{smallmatrix} J & 3/2 \\ -3/2 & -3/2 \end{smallmatrix}\right\rangle & \left|\begin{smallmatrix} J & 3/2 \\ -1/2 & -1/2 \end{smallmatrix}\right\rangle & \left|\begin{smallmatrix} J & 1/2 \\ -1/2 & -1/2 \end{smallmatrix}\right\rangle \\
\frac{d}{dR} & 0 & 0 & 0 & 0 & 0 \\
0 & \frac{d}{dR} & F & 0 & 0 & 0 \\
0 & F & \frac{d}{dR} & 0 & 0 & 0 \\
0 & 0 & 0 & \frac{d}{dR} & 0 & 0 \\
0 & 0 & 0 & 0 & \frac{d}{dR} & F \\
0 & 0 & 0 & 0 & F & \frac{d}{dR}
\end{pmatrix}^2 + \tag{209}
$$

$$
\begin{array}{c}
\left|\begin{smallmatrix} J & 3/2 \\ 3/2 & 3/2 \end{smallmatrix}\right\rangle \\
\left(\begin{array}{c}
\Pi + \frac{a(R)}{2} \\
0 \\
0 \\
0 \\
0 \\
0
\end{array}\right.
\end{array}
\begin{array}{c}
\left|\begin{smallmatrix} J & 3/2 \\ 1/2 & 1/2 \end{smallmatrix}\right\rangle \\
\left(\begin{array}{c}
0 \\
\frac{(2\Sigma+\Pi)}{3} + \frac{a(R)}{2} \\
-\frac{\sqrt{2}}{3}(\Sigma - \Pi) \\
0 \\
0 \\
0
\end{array}\right.
\end{array}
\begin{array}{c}
\left|\begin{smallmatrix} J & 1/2 \\ 1/2 & 1/2 \end{smallmatrix}\right\rangle \\
\left(\begin{array}{c}
0 \\
-\frac{\sqrt{2}}{3}(\Sigma - \Pi) \\
\frac{(\Sigma+2\Pi)}{3} - a(R) \\
0 \\
0 \\
0
\end{array}\right.
\end{array}
\begin{array}{c}
\left|\begin{smallmatrix} J & 3/2 \\ -3/2 & -3/2 \end{smallmatrix}\right\rangle \\
\left(\begin{array}{c}
0 \\
0 \\
0 \\
\Pi + \frac{a(R)}{2} \\
0 \\
0
\end{array}\right.
\end{array}
\begin{array}{c}
\left|\begin{smallmatrix} J & 3/2 \\ -1/2 & -1/2 \end{smallmatrix}\right\rangle \\
\left(\begin{array}{c}
0 \\
0 \\
0 \\
0 \\
\frac{(2\Sigma+\Pi)}{3} + \frac{a(R)}{2} \\
\frac{\sqrt{2}}{3}(\Sigma - \Pi)
\end{array}\right.
\end{array}
\begin{array}{c}
\left|\begin{smallmatrix} J & 1/2 \\ -1/2 & -1/2 \end{smallmatrix}\right\rangle \\
\left(\begin{array}{c}
0 \\
0 \\
0 \\
0 \\
\frac{\sqrt{2}}{3}(\Sigma - \Pi) \\
\frac{(\Sigma+2\Pi)}{3} - a(R)
\end{array}\right)
\end{array}
\tag{210}
$$

$$
\begin{array}{c}
\left|\begin{smallmatrix} J & 3/2 \\ 3/2 & 3/2 \end{smallmatrix}\right\rangle \\
\left(\begin{array}{c}
\frac{J(J+1)-\frac{3}{4}}{2\mu R^2} \\
-\frac{[3(J-\frac{1}{2})(J+\frac{3}{2})]^{1/2}}{2\mu R^2} \\
0 \\
0 \\
0 \\
0
\end{array}\right.
\end{array}
\begin{array}{c}
\left|\begin{smallmatrix} J & 3/2 \\ 1/2 & 1/2 \end{smallmatrix}\right\rangle \\
\left(\begin{array}{c}
-\frac{[3(J-\frac{1}{2})(J+\frac{3}{2})]^{1/2}}{2\mu R^2} \\
\frac{J(J+1)+\frac{13}{4}}{2\mu R^2} \\
0 \\
0 \\
-\frac{2(J+1)}{2\mu R^2} \\
0
\end{array}\right.
\end{array}
\begin{array}{c}
\left|\begin{smallmatrix} J & 1/2 \\ 1/2 & 1/2 \end{smallmatrix}\right\rangle \\
\left(\begin{array}{c}
0 \\
0 \\
\frac{J(J+1)+\frac{3}{4}}{2\mu R^2} \\
0 \\
-\frac{[3(J-\frac{1}{2})(J+\frac{3}{2})]^{1/2}}{2\mu R^2} \\
-\frac{J+1}{2\mu R^2}
\end{array}\right.
\end{array}
\begin{array}{c}
\left|\begin{smallmatrix} J & 3/2 \\ -3/2 & -3/2 \end{smallmatrix}\right\rangle \\
\left(\begin{array}{c}
0 \\
0 \\
0 \\
\frac{J(J+1)-\frac{3}{4}}{2\mu R^2} \\
0 \\
0
\end{array}\right.
\end{array}
\begin{array}{c}
\left|\begin{smallmatrix} J & 3/2 \\ -1/2 & -1/2 \end{smallmatrix}\right\rangle \\
\left(\begin{array}{c}
0 \\
-\frac{2(J+1)}{2\mu R^2} \\
0 \\
-\frac{[3(J-\frac{1}{2})(J+\frac{3}{2})]^{1/2}}{2\mu R^2} \\
\frac{J(J+1)+\frac{13}{4}}{2\mu R^2} \\
0
\end{array}\right.
\end{array}
\begin{array}{c}
\left|\begin{smallmatrix} J & 1/2 \\ -1/2 & -1/2 \end{smallmatrix}\right\rangle \\
\left(\begin{array}{c}
0 \\
0 \\
-\frac{J+1}{2\mu R^2} \\
0 \\
0 \\
\frac{J(J+1)+\frac{3}{4}}{2\mu R^2}
\end{array}\right)
\end{array}
\tag{211}
$$

The propagation algorithm will be modified to handle up to six surfaces instead of two. First, we will present the potential energy surfaces and make various transformations to produce the adiabatic and strictly diabatic forms. Second, we will pre-compute the Moller states and discuss the various issues surrounding this calculation. Third, the properly constructed Moller states are used to propagate in to the interaction region. Once in the interaction region we can take snap shots in time of the wave functions behavior. Fourth, as the wave functions exits on one, two, or all three surfaces the correlation function will be calculated and then normalized. This is repeated for all values of J up to where the centrifugal barrier prevents the system from entering the interaction region. Finally, when this limit is reached every one of the transmission coefficients are summed up according to equation (169) and the collisional cross section as a function of energy is produced.

6.2 Computing non-SOCI Potential Energy Surfaces from SOCI Potential Energy Surfaces

We start with the KHe Spin-Orbit Configuration Interaction (SOCI) adiabatic potential energy surfaces with respect to the electrostatic and magnetic operators as calculated by Blank[8]. These SOCI surfaces were computed using a many body quantum code called COLUMBUS. The method employed was a spin-orbit multi-reference configuration interaction singles and doubles with state averaged multi-configuration self consistent field reference orbitals. The particular basis used for the outer eight electrons was a Def2-TZVPP all electron segmented contracted gaussian basis of triple zeta quality that used symmeterized spin orbitals for the molecular wave functions. For the remaining core electrons a Stuttgart two component psuedopotential was used that included relativistic effects.

The molecular wave functions were subjected to $\widehat{\mathbf{H}}^0_{KHe}+\widehat{\mathbf{V}}^K_{ls}$ according to the Born-Oppenheimer method and are displayed in Figure 31. After the surfaces were calcu-

lated a Davidson-Silver correction was applied to ameliorate size consistency error[15] and the asymptotic spin-orbit split energy was set to the potassium D1=0.05916 Hartree and D2=0.05942 Hartree National Institute of Standards and Technology (NIST) values[35]. Equilibrium positions, well depths, and vibrational energy levels computed using these surfaces compare favorably to experimental observations and other theoretical calculations[8].

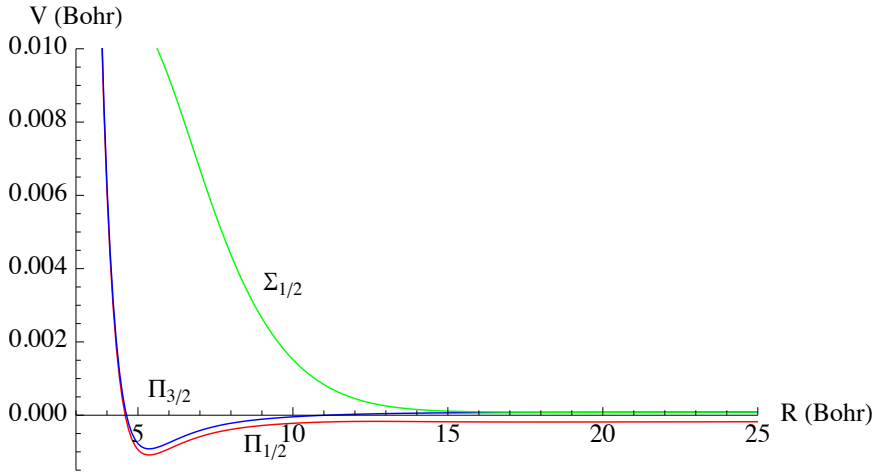

(a) KHe Spin-Orbit Split CI Adiabatic Surfaces

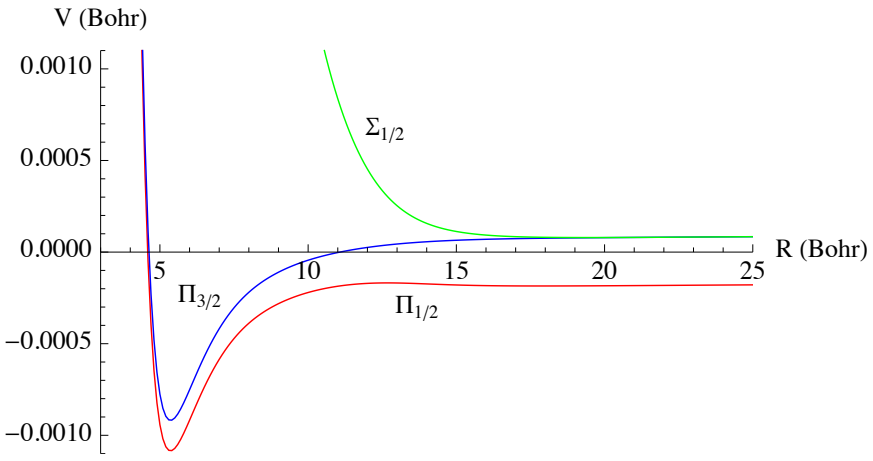

(b) KHe Spin-Orbit Split CI Adiabatic Surfaces zoomed in

Figure 29. KHe Spin-Orbit Split CI Computational Potential Energy Surfaces.

The surfaces were calculated between the values of $R = 3 - 200$ Bohr. Between

$3-15$ Bohr the surfaces were computed in increments of 0.1 Bohr which also was the discretization coordinate step used in these simulations, $dR = 0.1$. From $15-30$ Bohr the surfaces were calculated in increments of 0.2 Bohr, from $30-40$ increments of 0.5 Bohr, from $40-60$ Bohr increments of 1.0 Bohr, from $60-100$ Bohr increments of 5.0 Bohr, and finally from $100-200$ Bohr increments of 10.0 Bohr. Beyond 15 Bohr the surfaces do not change dramatically so a linear interpolation of grid step $dR = 0.1$ was used.

These surfaces are represented in what we will call the spin-orbit molecular basis. However our close-coupled Hamiltonian is represented in the Born-Oppenheimer molecular basis. Fortunately, the spin-orbit basis can be calculated from the Born-Oppenheimer basis. The spin-orbit molecular basis is a result of diagonalizing the electronic and magnetic terms represented in the Born-Oppenheimer basis. First start with the expression of $\widehat{\mathbf{H}}^0_{KHe} + \widehat{\mathbf{V}}^K_{ls}$ in the Born-Oppenheimer molecular basis,

$$\widehat{\mathbf{H}}^0_{KHe} + \widehat{\mathbf{V}}^K_{ls} = \begin{array}{c} \left|{}^{J\ \ 3/2}_{3/2\ 3/2}\right\rangle \quad \left|{}^{J\ \ 3/2}_{1/2\ 1/2}\right\rangle \quad \left|{}^{J\ \ 1/2}_{1/2\ 1/2}\right\rangle \\ \begin{pmatrix} \Pi + \frac{a(R)}{2} & 0 & 0 \\ 0 & \frac{(2\Sigma+\Pi)}{3} + \frac{a(R)}{2} & \mp\frac{\sqrt{2}}{3}(\Sigma-\Pi) \\ 0 & \mp\frac{\sqrt{2}}{3}(\Sigma-\Pi) & \frac{(\Sigma+2\Pi)}{3} - a(R) \end{pmatrix} \end{array}. \tag{212}$$

By diagonalizing this matrix we create the adiabatic representation with respect to the electrostatic and magnetic potential. The eigenvalues, λ_i, are

$$\begin{aligned} \lambda_1 &= \Pi + \frac{a}{2} \\ \lambda_2 &= \frac{1}{4}\left(-a + 2(\Sigma+\Pi) + \sqrt{9a^2 + 4a(\Sigma-\Pi) + 4(\Sigma-\Pi)^2}\right) \\ \lambda_3 &= \frac{1}{4}\left(-a + 2(\Sigma+\Pi) - \sqrt{9a^2 + 4a(\Sigma-\Pi) + 4(\Sigma-\Pi)^2}\right) \end{aligned} \tag{213}$$

where a, Σ, and Π are all understood to be functions of R.

From molecular orbital theory we can infer which spin-orbit molecular surface corresponds to the correct eigenvalue. To start, notice the first 1x1 block is in itself already diagonal. The eigenvalue that will be associated with this 1x1 block will have an total electronic angular momentum value of $j = 3/2$. Since in the P-manifold we have one electron with a spin of $1/2$ we know the electronic angular momentum is $l = 1/2$. So the first eigenvalue will correspond to a Π molecular surface. Further more this state has a projection of $\pm 3/2$ and as such we can by inspection associate the molecular state $\Pi_{3/2}$ with the eigenvalue λ_1.

We can also see in Figure 31b that the $\Pi_{3/2}$ molecular surface in the asymptotic region is spin orbit split by a value of $+\frac{a}{2}$ just like the 1,1 element of $\widehat{\mathbf{H}}^0_{KHe} + \widehat{\mathbf{V}}^K_{ls}$ in the Born-Oppenheimer molecular basis. This makes sense because in the Born-Oppenheimer basis the spin-orbit operator is diagonal, that is the parameter $a(R)$ only appears along the diagonal. The remaining 2x2 block will then diagonalize to produce $\Pi_{1/2}$ and $\Sigma_{1/2}$ surfaces.

Once again by observation of Figure 31b and the fact that the a terms are already diagonal we can associate the $\Sigma_{1/2}$ molecular surface with the eigenvalue λ_2. This molecular surface asymptotically corresponds to the atomic state that has a total electronic angular momentum value of $j = 1/2$ and therefore an electronic angular momentum value $l = 0$. The projection is $\pm 1/2$ and is spin orbit split by $+\frac{a}{2}$.

Finally, by process of elimination and by observing an asymptotic spin orbit split of $-a$ the final molecular state $\Pi_{1/2}$ is associated with the last eigenvalue λ_3. Now we have a set of equations that relate the SOCI surfaces, $\Pi_{3/2}$, $\Sigma_{1/2}$, and $\Pi_{1/2}$, to the

non-spin orbit split CI surfaces, Π and Σ, and the spin orbit parameter $a(R)$:

$$\begin{aligned}
\Pi_{3/2} &= \Pi + \frac{a}{2} \\
\Sigma_{1/2} &= \frac{1}{4}\left(-a + 2(\Sigma+\Pi) + \sqrt{9a^2 + 4a(\Sigma-\Pi) + 4(\Sigma-\Pi)^2}\right) \\
\Pi_{1/2} &= \frac{1}{4}\left(-a + 2(\Sigma+\Pi) - \sqrt{9a^2 + 4a(\Sigma-\Pi) + 4(\Sigma-\Pi)^2}\right)
\end{aligned} \tag{214}$$

The unitary transformation for this diagonalization process is $\mathbf{U}_{so}$. It tells us how the Born-Oppenheimer basis relates to the spin-orbit molecular basis labeled $\left|\Pi_{3/2}\right\rangle$, $\left|\Sigma_{1/2}\right\rangle$, and $\left|\Pi_{1/2}\right\rangle$:

$$\mathbf{U}_{so} = \begin{array}{c} \\ \left\langle {}^{J}_{3/2}\,{}^{3/2}_{3/2}\right| \\ \left\langle {}^{J}_{1/2}\,{}^{3/2}_{1/2}\right| \\ \left\langle {}^{J}_{1/2}\,{}^{1/2}_{1/2}\right| \end{array} \begin{array}{c} \begin{array}{ccc} \left|{}^{J}_{3/2}\,\Pi_{3/2}\right\rangle & \left|{}^{J}_{1/2}\,\Sigma_{1/2}\right\rangle & \left|{}^{J}_{1/2}\,\Pi_{1/2}\right\rangle \end{array} \\ \begin{pmatrix} 1 & 0 & 0 \\ 0 & \delta(R) & \epsilon(R) \\ 0 & -\epsilon(R) & \delta(R) \end{pmatrix} \end{array}. \tag{215}$$

The $\delta(R), \epsilon(R), \xi(R)$, and $\eta(R)$ functions are algebraically unwieldy to present however we can plot these functions relatively easily:

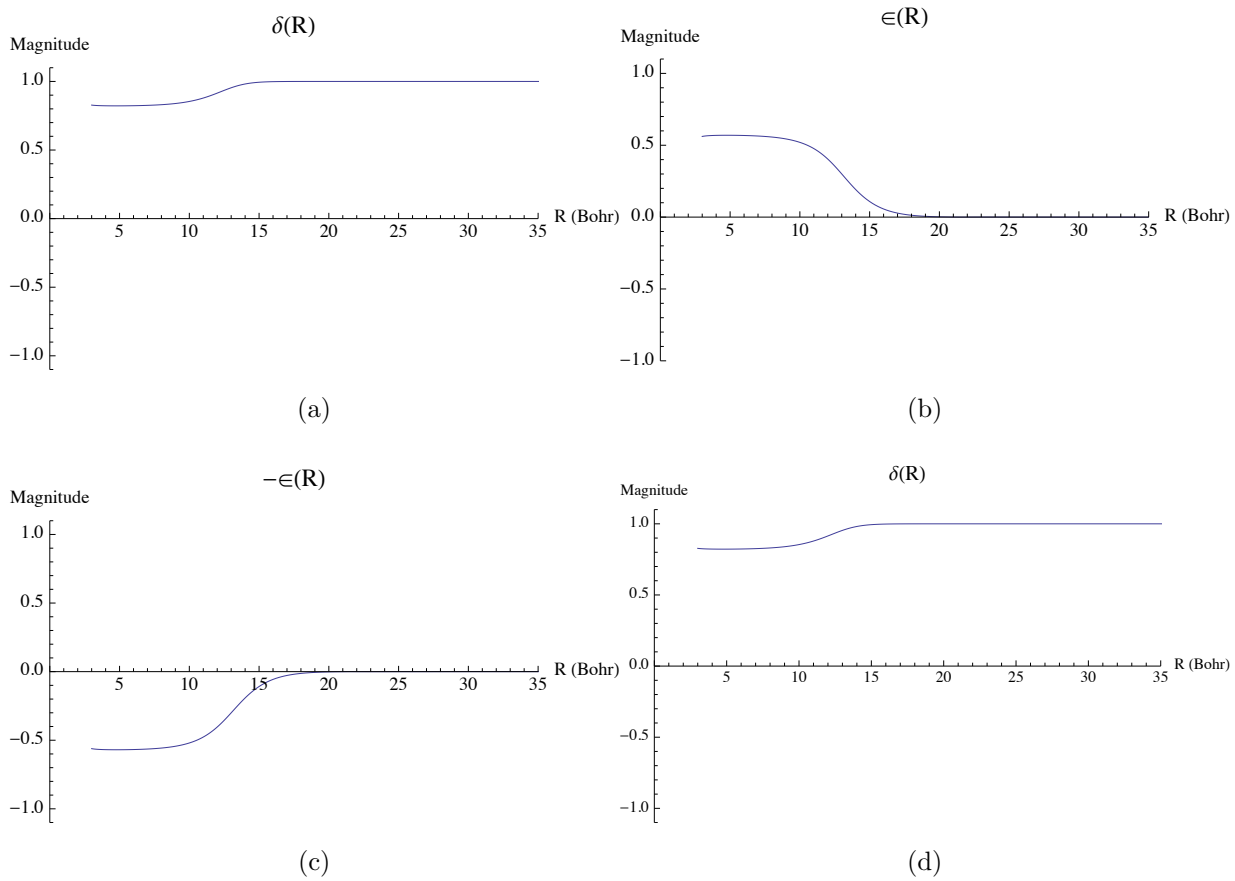

Figure 30. Spin-Orbit Transformation Functions.

Notice that outside the interaction region ($\sim R > 20$) $\mathbf{U}_{so}$ becomes the identity matrix and there no longer is a distinction between the Born-Oppenheimer basis and the spin-orbit molecular basis. From the standpoint of the Born-Oppenheimer basis the spin-orbit molecular basis rotates as we enter the interaction region through the functions $\delta(R)$ and $\epsilon(R)$:

$$\left|{}^{J}_{3/2}\,{}^{3/2}_{3/2}\right\rangle = \left|{}^{J}_{3/2}\,\Pi_{3/2}\right\rangle \tag{216}$$

$$\left|{}^{J}_{1/2}\,{}^{3/2}_{1/2}\right\rangle = \delta(R)\left|{}^{J}_{1/2}\,\Sigma_{1/2}\right\rangle + \epsilon(R)\left|{}^{J}_{1/2}\,\Pi_{1/2}\right\rangle$$

$$\left|{}^{J}_{1/2}\,{}^{1/2}_{1/2}\right\rangle = -\epsilon(R)\left|{}^{J}_{1/2}\,\Sigma_{1/2}\right\rangle + \delta(R)\left|{}^{J}_{1/2}\,\Pi_{1/2}\right\rangle \tag{217}$$

Equations (214) are inverted to yield,

$$\Sigma = \frac{2\Pi_{1/2} - \Pi_{3/2} + 2\Sigma_{1/2}}{3} + \frac{1}{3}\sqrt{\Pi_{1/2}^2 + 2\Pi_{1/2}\Pi_{3/2} - 2\Pi_{3/2}^2 - 4\Pi_{1/2}\Sigma_{1/2} + 2\Pi_{3/2}\Sigma_{1/2} + \Sigma_{1/2}^2}$$

$$\Pi = \frac{1}{6}\left(\Pi_{1/2} + 4\Pi_{3/2} + \Sigma_{1/2} - \sqrt{\Pi_{1/2}^2 + 2\Pi_{1/2}\Pi_{3/2} - 2\Pi_{3/2}^2 - 4\Pi_{1/2}\Sigma_{1/2} + 2\Pi_{3/2}\Sigma_{1/2} + \Sigma_{1/2}^2}\right)$$

$$a = \frac{1}{3}\left(-\Pi_{1/2} + 2\Pi_{3/2} - \Sigma_{1/2} + \sqrt{\Pi_{1/2}^2 + 2\Pi_{1/2}\Pi_{3/2} - 2\Pi_{3/2}^2 - 4\Pi_{1/2}\Sigma_{1/2} + 2\Pi_{3/2}\Sigma_{1/2} + \Sigma_{1/2}^2}\right)$$

Now we can plot the non spin-orbit split CI surfaces and spin-orbit parameter which were calculated from Blank's SOCI surfaces.

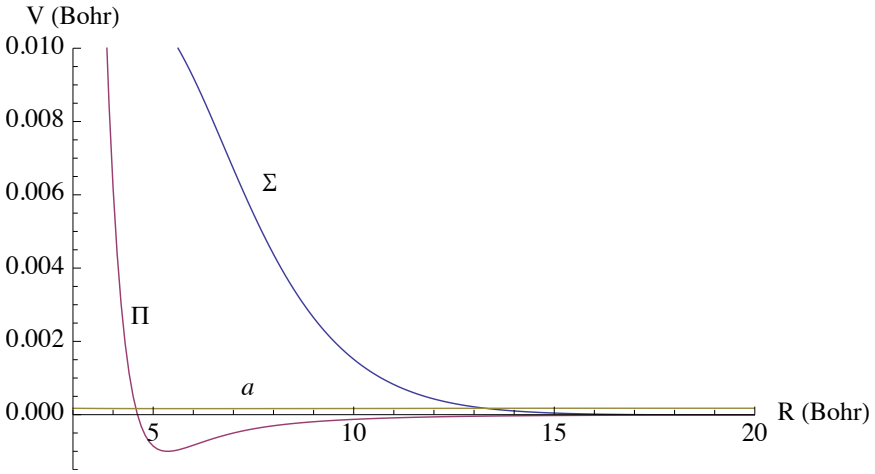

(a) KHe non Spin-Orbit Split CI Adiabatic Surfaces

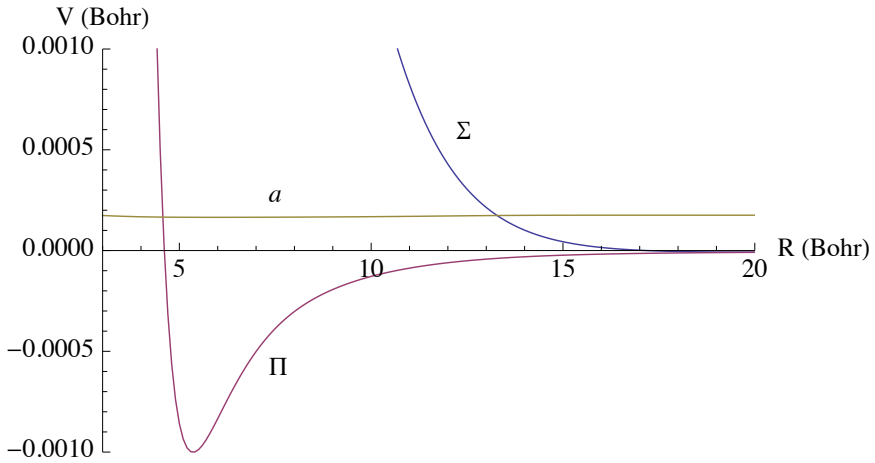

(b) KHe non Spin-Orbit Split CI Adiabatic Surfaces zoomed in

Figure 31. KHe non Spin-Orbit Split CI Computational Potential Energy Surfaces.

Notice within the interaction region the value of the spin-orbit parameter changes only slightly with R. Mies[30] concluded in his analysis that sometimes it might be possible to simply use the asymptotic value of a and just set it constant throughout all R. However since this might not always be reliable it is best to just evaluate the molecular spin-orbit operator. By undiagonalizing the spin-orbit molecular surfaces we can calculate the R dependence of $a(R)$. For KHe the spin-orbit parameter is nearly constant. For other systems included in this study the values of a vary with R to differing degrees. See Appendix C for these details.

Moving forward with the non spin-orbit split CI surfaces and the spin-orbit parameter we are now in a position to plot the diabatic potential energy surfaces, equation (212), along with the off diagonal spin-orbit coupling function:

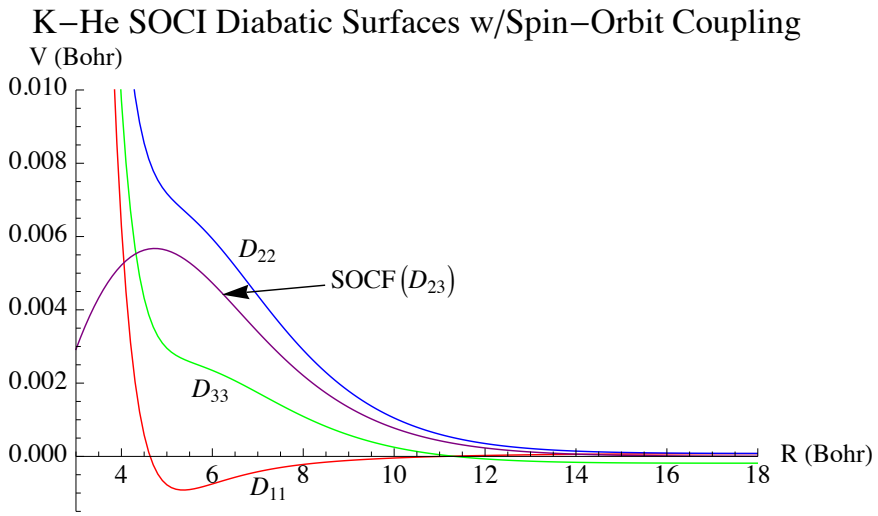

Figure 32. KHe Diabatic Potential Energy Surfaces w/Spin-Orbit Coupling, labeled by their matrix element.

Compare these surfaces with the model surfaces in the two level example, Figure 21. The Spin Orbit Coupling (SOC) function acts much like the exponential coupling function, D_{12}, in the two level model. The Born-Oppenheimer basis states that are coupled by this SOC function are the $\left|\frac{3}{2},\frac{1}{2}\right\rangle$ and $\left|\frac{1}{2},\frac{1}{2}\right\rangle$ states. The $\left|\frac{3}{2},\frac{3}{2}\right\rangle$ diabatic

state is uncoupled by the spin-orbit potential.

With the diabatic surfaces we can now compute $\widehat{\mathbf{S}}$-Matrix elements, but before this is done the Moller states must be calculated.

6.3 Moller State Creation and Calculation

Computing the Moller states starts out exactly the same way as in the square well and two level examples. First, we pick the expansion functions which are also chosen to be Gaussian wave functions. In particular we will probe an energy range between $0 - 0.01$ Bohr. This corresponds to a system temperature between 0 and 3157.75 Kelvin. The initial position of the expansion function in coordinate space can be placed anywhere on the computation grid. We could even place it in the middle of the interaction potential. A wise placement however would be outside the interaction region, but at the same time close to it. This will enable the interaction region calculation to be done on as small a grid as possible. The parameters for the Moller State calculation are listed below:

Table 9. KHe Moller State Calculation Parameters

N	2^{17}	a	0.5
dR	0.1	x_0	100
Time at "± Infinity"	±5000000	k_0	±7.0
dt	8000	KHe Reduced Mass	6614.7881

The initial Gaussian conditions are plotted below:

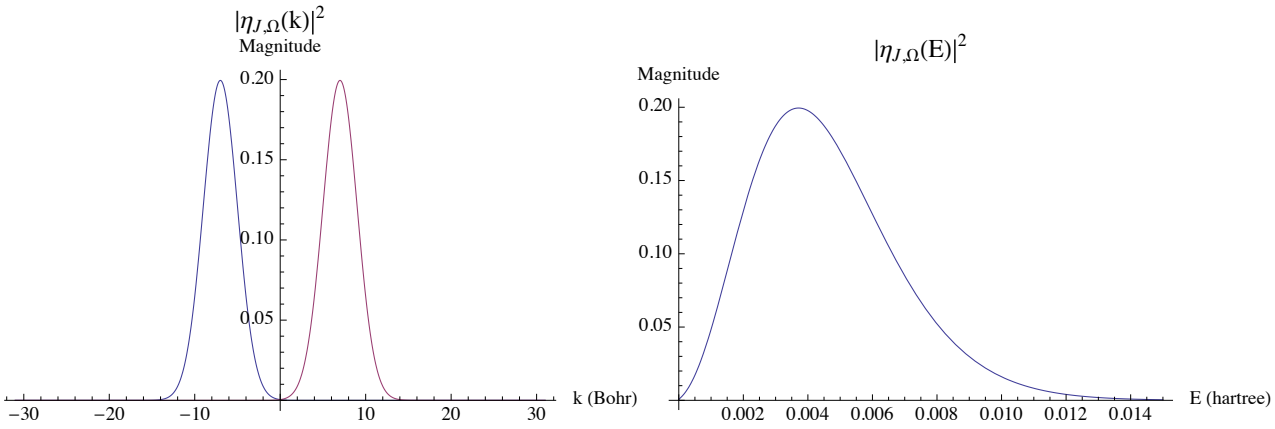

(a) Momentum Representation

(b) Energy Representation

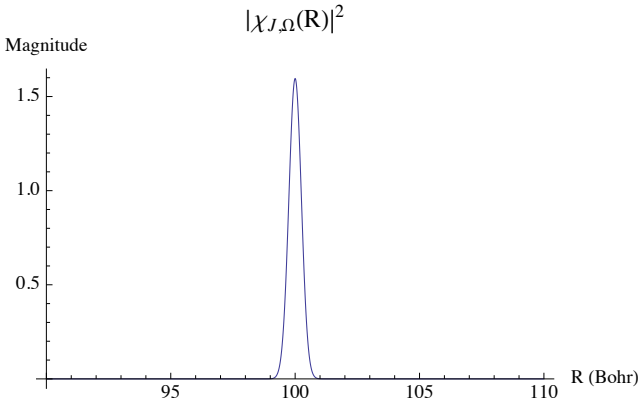

(c) Coordinate Representation

Figure 33. KHe Initial Conditions.

Second, we propagate backwards (forwards) in time towards infinity under $\widehat{\mathbf{H}}^0$. This can be done analytically since the interaction and centrifugal potentials are not included in the asymptotic Hamiltonian. Of course in practice we do not propagate forever under $\widehat{\mathbf{H}}^0$. We only need to propagate until the Gaussian is completely in the asymptotic region.

The asymptotic region however changes with the angular momentum value J. As we increase in J the centrifugal potential tends to prevent the interaction region from being energetically accessible up to the point where the system no longer interacts. As this happens the asymptotic region moves increasing further from the interaction

region. The spin-orbit CI adiabatic surfaces are plotted with the inclusion of the centrifugal potential for values of $J = 0.5$, 50.5, 100.5, 150.5, 200.5, and 250.5 in Figures 34. The spin-orbit coupling function is also presented in these plots to get a sense over what range the system would spin-orbit couple. By inspection for $J = 0.5$ we could reasonably assume that the asymptotic region begins at around 20 Bohr. Beyond this point the centrifugal potential and spin-orbit coupling have reached their asymptotic values. However as J increases the centrifugal potential begins to dominate to the point where at $J = 250.5$ any wave function propagating in to this region below an energy of 0.01 would not be able to penetrate far enough to access the spin-orbit coupling. Also for $J = 250.0$ the asymptotic region no longer begins at 20 Bohr, but rather by inspection looks to begin at about 400 Bohr.

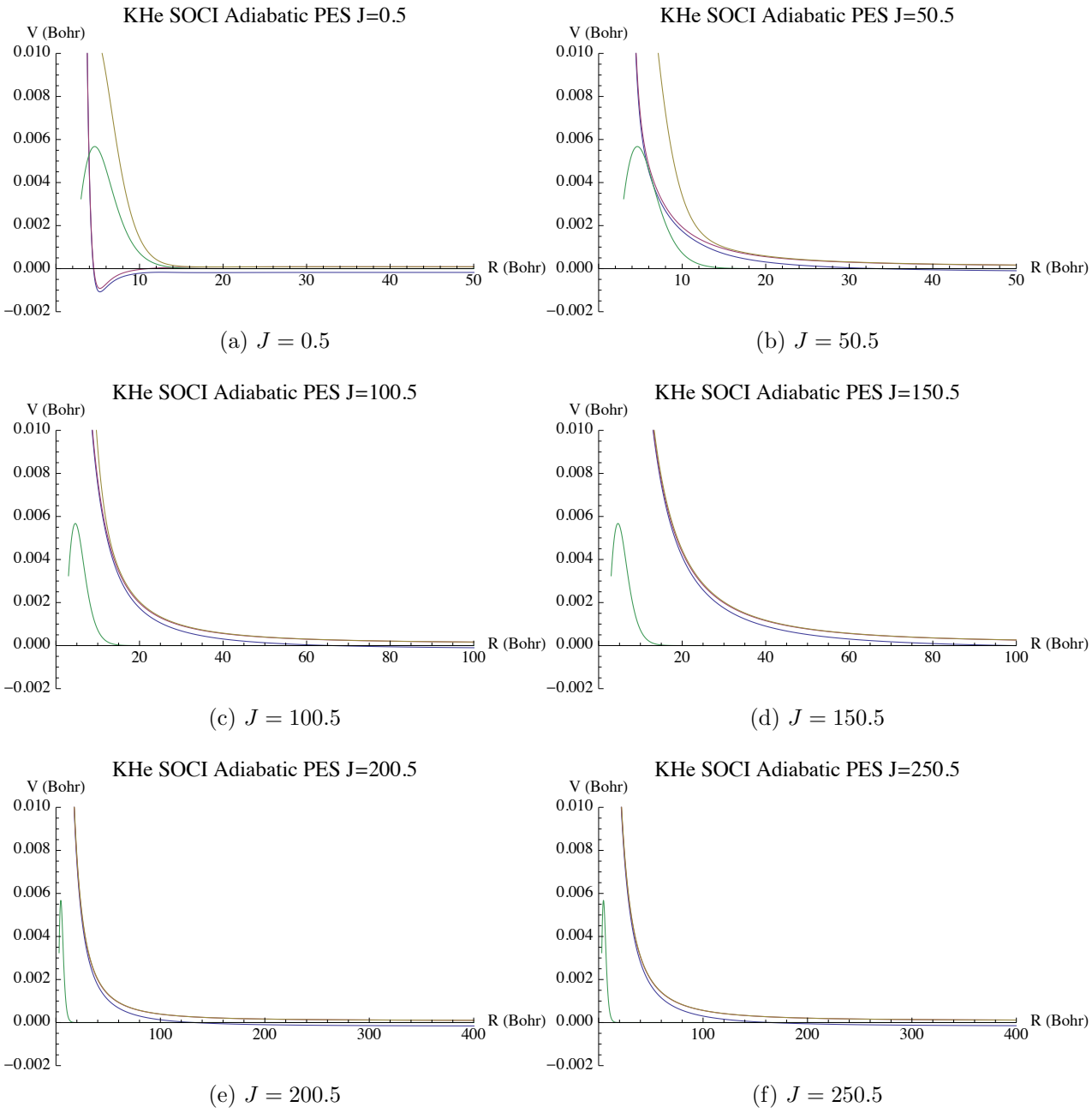

(a) $J = 0.5$ (b) $J = 50.5$

(c) $J = 100.5$ (d) $J = 150.5$

(e) $J = 200.5$ (f) $J = 250.5$

Figure 34. KHe SOCI Computational Potential Energy Surfaces w/Centrifugal Potential.

Since the asymptotic region is a function of J the decision was made to define the asymptotic region to be that region where the surface with the highest J value falls to its asymptotic value. The reason for doing this is so that all of the Moller states can be calculated with on simple FORTRAN subroutine. The max asymptotic region does differ between collision species. For the KHe collision $J = 250.5$ is the maximum angular momentum value needed such that no interaction takes place in the energy range of interest. Inspecting Figure 36f it appears that the asymptotic region begins at about 400 Bohr. So as we propagate out towards infinity the coordinate representation must not contain any components between $0 \sim 400$ Bohr. In order to achieve this for the KHe system the initial Gaussian must be propagated toward infinity by a value of $t = 5000000$.

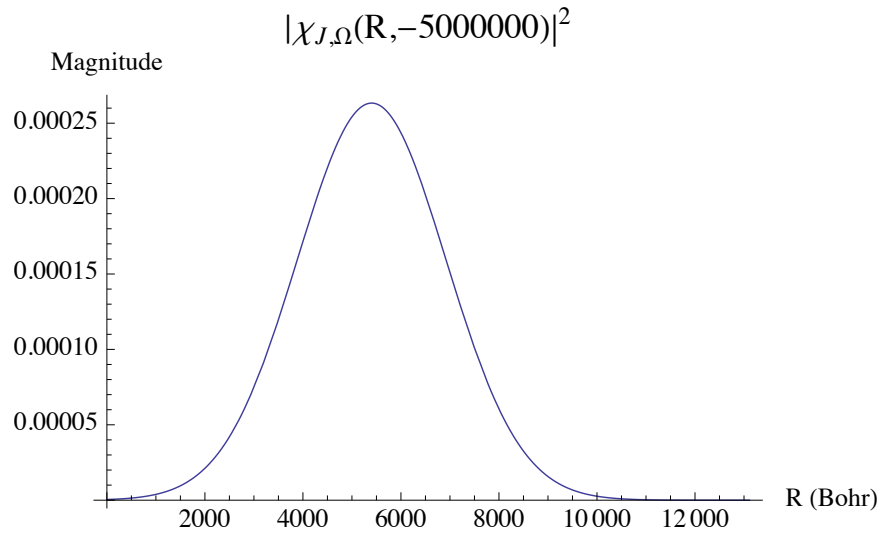

Figure 35. KHe Moller State at $t = \pm 5000000$.

It is clear that the higher energy components are obviously in the asymptotic region, however the slower energy components just barely reach the asymptotic limit. This in fact can represent a frustration with the time-dependent formulation of Moller state calculations. Grid sizes could become enormously unwieldy because the lower energy components tend to creep along the computational grids. Nonetheless the check of whether or not the wave function is completely in the interaction region is done by summing up the $\widehat{\mathbf{S}}$-matrix elements to ensure unity is achieved. The wave function in Figure 35 is now propagated back to $t = 0$ with a time step of $dt = 8000$ for each surface and one for each value of J. In total we have created 750 Moller Reactant states, 250 for each surface. The same process is then repeated to create Moller Product states.

Since in the asymptotic regions the potential is small, but not negligible we can use a large time step, $dt = 8000$, compared to the time step in the interaction region (typically on the order of $dt = 100$) without violating the split operator approximation. This represents a huge computational advantage. The Moller reactant states are plotted for multiple values of J in Figures 34 and compared with the initial Gaussians in coordinate space.

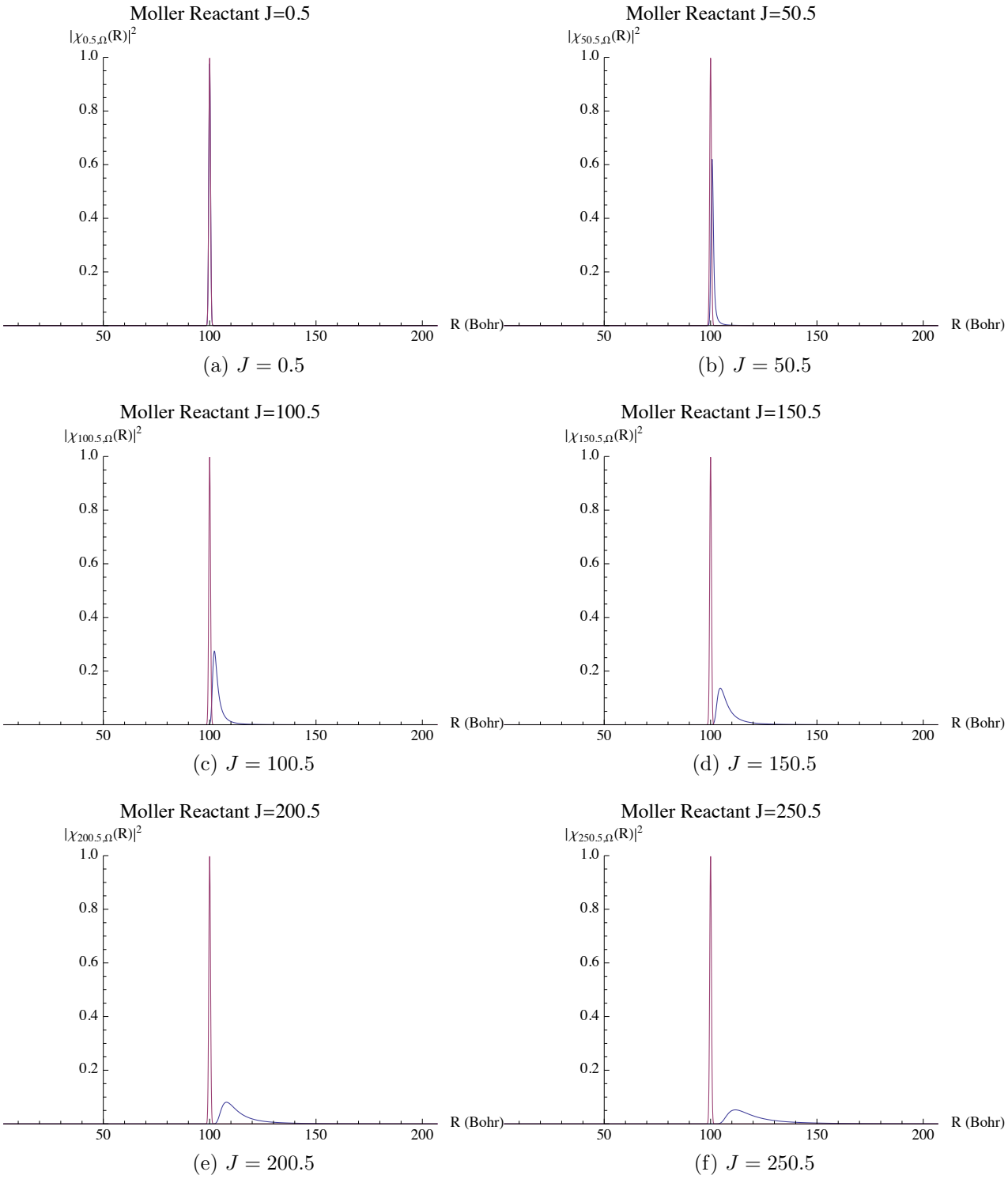

(a) $J = 0.5$ (b) $J = 50.5$

(c) $J = 100.5$ (d) $J = 150.5$

(e) $J = 200.5$ (f) $J = 250.5$

Figure 36. KHe Moller States for $J = 0.5$, 50.5, 100.5, 150.5, 200.5, and 250.5.

The Moller Reactant for $J = 0.5$ does not differ much from the original Gaussian, however as we step up in angular momentum it is clear that the slower energy components begin to "crawl up" the centrifugal potential and can not completely return to the original position. Because of this the Moller state develops a long tail. The interaction grid must be long enough to contain these Moller state features.

Much like the analytic solution for freely propagating particle there also exists an analytic solution for a particle under the influence of a $1/R^2$ potential. Utilizing a Green's function method and elementary canonical transformations of the Hamiltonian the analytic solution for a particle in a centrifugal potential is[44]:

$$\Psi(x;t) = \int_{-\infty}^{\infty} \Psi(x';0) i^{2\beta_{\pm}-1/2} \frac{\sqrt{xx'}}{t} exp\left(\frac{ix^2}{2t} + \frac{x'^2}{2t}\right) J_{2\beta_{\pm}-1/2}\left(\frac{xx'}{t}\right) dx' \qquad (218)$$

where,

$\beta_{\pm} = (-1 \pm \sqrt{1+8U})/4$

$U = \frac{J^2+j^2-2j_z^2}{2}$

$J_{\alpha}(x) = \sum_{m=0}^{\infty} \frac{(-1)^m}{m!\Gamma(m+\alpha+1)} \left(\frac{1}{2}x\right)^{2m+\alpha}$ is the Bessel Function.

Although somewhat complicated this analytic solution would be computationally tractable if it were not for the infinite sum contained in the Bessel Function in conjunction with the form of β. No closed form expression could be found for this sum so this idea was abandoned in in favor of the split operator method. Even if this analytic solution can be put in to a computationally tractable form the true test of its efficacy will be how quickly its solution is computed versus the split operator method.

These 750 Moller reactants and 750 Moller products will now be used to compute correlation functions and $\widehat{\mathbf{S}}$-matrix elements in the next section for the Spin-Orbit interaction.

6.4 Interaction Region Calculation: Spin-Orbit Coupling

The first interaction region calculation that will be performed is the spin-orbit interaction calculation. This calculation will proceed very much like the two state example. We take the close-coupled equations, (143), and artificially set the Born-Oppenheimer radial derivative couplings, F, and the Coriolis coupling elements to zero:

$$\widehat{\mathbf{H}} =$$

$$-\frac{1}{2\mu}\begin{pmatrix} \left|{}^{J\ \ 3/2}_{\pm 3/2\ \pm 3/2}\right\rangle & \left|{}^{J\ \ 3/2}_{\pm 1/2\ \pm 1/2}\right\rangle & \left|{}^{J\ \ 1/2}_{\pm 1/2\ \pm 1/2}\right\rangle \\ \frac{d}{dR} & 0 & 0 \\ 0 & \frac{d}{dR} & 0 \\ 0 & 0 & \frac{d}{dR} \end{pmatrix}^2 +$$

$$\begin{pmatrix} \left|{}^{J\ \ 3/2}_{\pm 3/2\ \pm 3/2}\right\rangle & \left|{}^{J\ \ 3/2}_{\pm 1/2\ \pm 1/2}\right\rangle & \left|{}^{J\ \ 1/2}_{\pm 1/2\ \pm 1/2}\right\rangle \\ \Pi + \frac{a(R)}{2} + \frac{J(J+1)-\frac{3}{4}}{2\mu R^2} & 0 & 0 \\ 0 & \frac{(2\Sigma+\Pi)}{3} + \frac{a(R)}{2} + \frac{J(J+1)+\frac{13}{4}}{2\mu R^2} & \mp\frac{\sqrt{2}}{3}(\Sigma-\Pi) \\ 0 & \mp\frac{\sqrt{2}}{3}(\Sigma-\Pi) & \frac{(\Sigma+2\Pi)}{3} - a(R) + \frac{J(J+1)+\frac{3}{4}}{2\mu R^2} \end{pmatrix}. \tag{219}$$

Notice that in the absence of radial derivative and Coriolis coupling the two 3x3 blocks are degenerate. Since this Hamiltonian exhibits no coupling of the $\left|{}^{J\ \ 3/2}_{\pm 3/2\ \pm 3/2}\right\rangle$ state it is essentially a two level system between the $\left|{}^{J\ \ 3/2}_{\pm 1/2\ \pm 1/2}\right\rangle$ and $\left|{}^{J\ \ 1/2}_{\pm 1/2\ \pm 1/2}\right\rangle$ states with the spin-orbit coupling function that has been discussed earlier.

We will completely confine the Moller reactant to the $\left|{}^{J\ \ 1/2}_{\pm 1/2\ \pm 1/2}\right\rangle$ asymptotic state

so that the six component wave vector describing nuclear dynamics at time $t = 0$ is

$$\chi = \begin{pmatrix} 0 \\ 0 \\ \widehat{\mathbf{\Omega}}_{+}^{J,1/2} \left|\psi_{in}\right\rangle \\ 0 \\ 0 \\ \widehat{\mathbf{\Omega}}_{+}^{J,-1/2} \left|\psi_{in}\right\rangle \end{pmatrix}. \tag{220}$$

Since we are propagating in on the $\left|{}^{J}_{\pm 1/2}\,{}^{1/2}_{\pm 1/2}\right\rangle$ asymptotic surface we expect to compute three correlation functions and three $\widehat{\mathbf{S}}$-matrix elements for each 3x3 block. There will be one reflection transition, $\left|{}^{J}_{\pm 1/2}\,{}^{1/2}_{\pm 1/2}\right\rangle \rightarrow \left|{}^{J}_{\pm 1/2}\,{}^{1/2}_{\pm 1/2}\right\rangle$, and two transmission transitions, $\left|{}^{J}_{\pm 1/2}\,{}^{1/2}_{\pm 1/2}\right\rangle \rightarrow \left|{}^{J}_{\pm 3/2}\,{}^{3/2}_{\pm 1/2}\right\rangle$ and $\left|{}^{J}_{\pm 1/2}\,{}^{1/2}_{\pm 1/2}\right\rangle \rightarrow \left|{}^{J}_{\pm 1/2}\,{}^{3/2}_{\pm 3/2}\right\rangle$. Of course since we artificially set the Coriolis coupling to zero we expect nothing to exit out on the $\left|{}^{J}_{\pm 3/2}\,{}^{3/2}_{\pm 3/2}\right\rangle$ surface. The following simulation parameters were used for this KHe spin-orbit interaction calculation:

Table 10. KHe Interaction Calculation Parameters

N	2^{14}	dR	0.1
t	$2,000,000$	dt	10.0

Now the results of this calculation are presented for the $+\omega$ 3x3 block. The results for the $-\omega$ 3x3 block will be exactly the same. First, for the $J = 0.5$ case we will show time snap shots of the nuclear wave vector, correlation functions, reflection and transmission coefficients, and finally the sum to unity to show convergence of the solution. Second, for the $J = 50.5$, 100.5, 150.5, 200.5, and 250.5 values of total angular momentum we will just present the reflection and transmission coefficients followed by the sum to unity. Finally, these coefficients will be summed according

to equation (169) and the cross section as a function of energy will be presented in section 6.7.

The time snap shots of the propagating nuclear wave function are presented at six different time intervals in Figures 37 and 38 along with the Moller Products for reference. No wave function was observed exiting on the $\left|{}^{J}_{\pm 3/2}\,{}^{3/2}_{\pm 3/2}\right\rangle$ surface. Only the $\left|{}^{J}_{\pm 1/2}\,{}^{1/2}_{\pm 1/2}\right\rangle$ reflection and $\left|{}^{J}_{\pm 3/2}\,{}^{3/2}_{\pm 1/2}\right\rangle$ transmission time snap shots are shown.

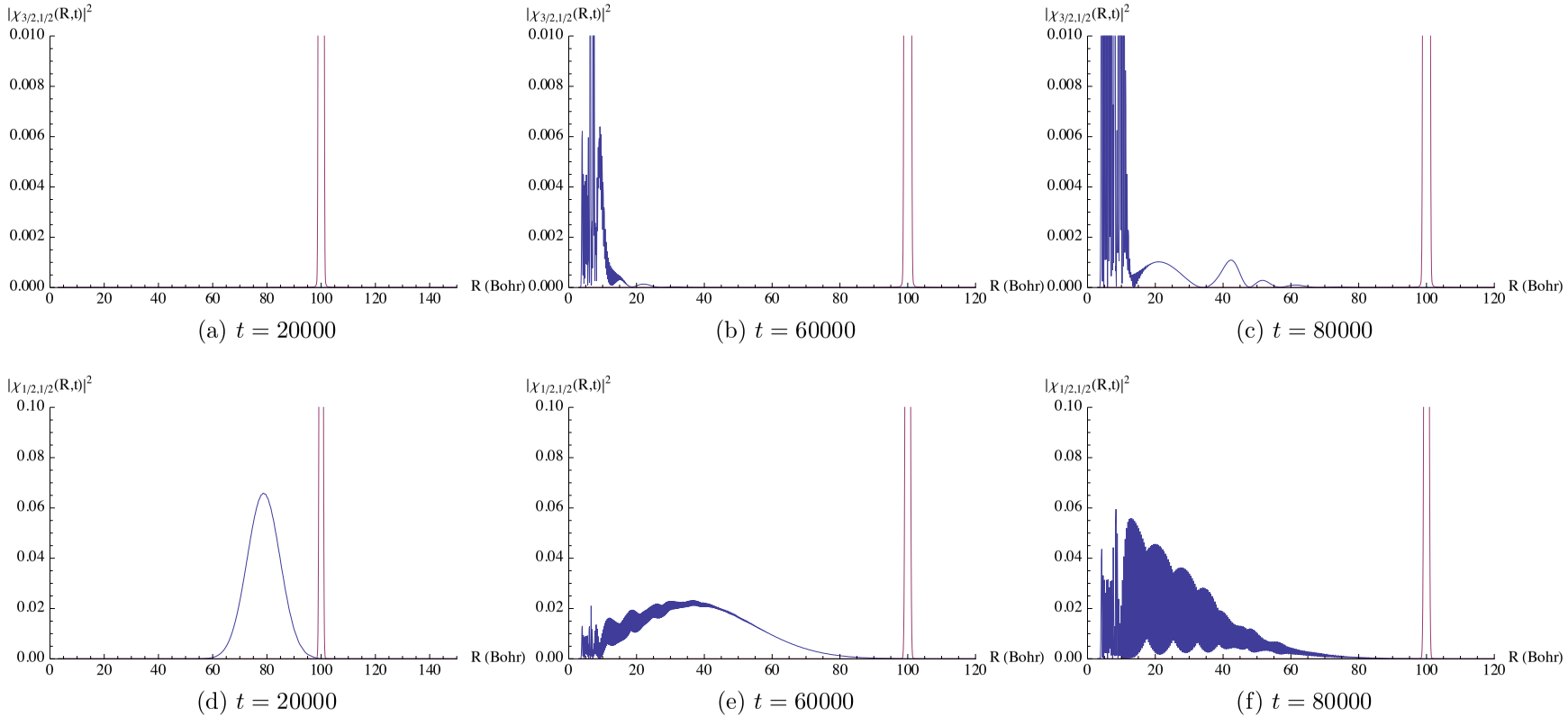

Figure 37. KHe Spin-Orbit Interaction wave functions at various t. The top row are the $\left|{}^{J}_{\pm 3/2}\,{}^{3/2}_{\pm 1/2}\right\rangle$ wave functions and bottom row the $\left|{}^{J}_{\pm 3/2}\,{}^{1/2}_{\pm 1/2}\right\rangle$ wave functions.

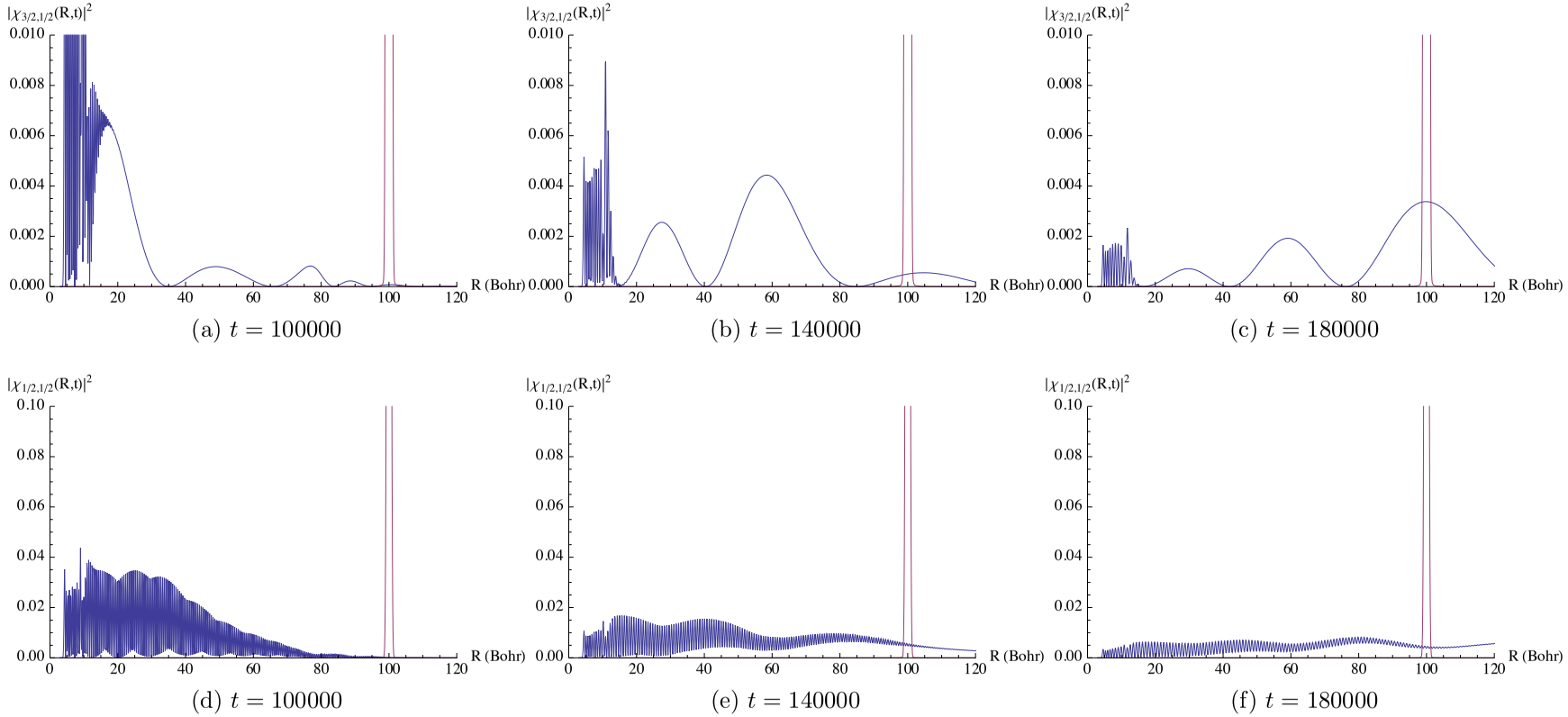

Figure 38. KHe Spin-Orbit Interaction wave functions at various t. The top row are the $\left|{}^{J}_{\pm 3/2}\,{}^{3/2}_{\pm 1/2}\right\rangle$ wave functions and bottom row the $\left|{}^{J}_{\pm 3/2}\,{}^{1/2}_{\pm 1/2}\right\rangle$ wave functions.

At each time step the the overlap of the interacting wave function and the Moller Product states are computed forming the correlation function. The reflection and transmission correlation functions are plotted in Figure 39.

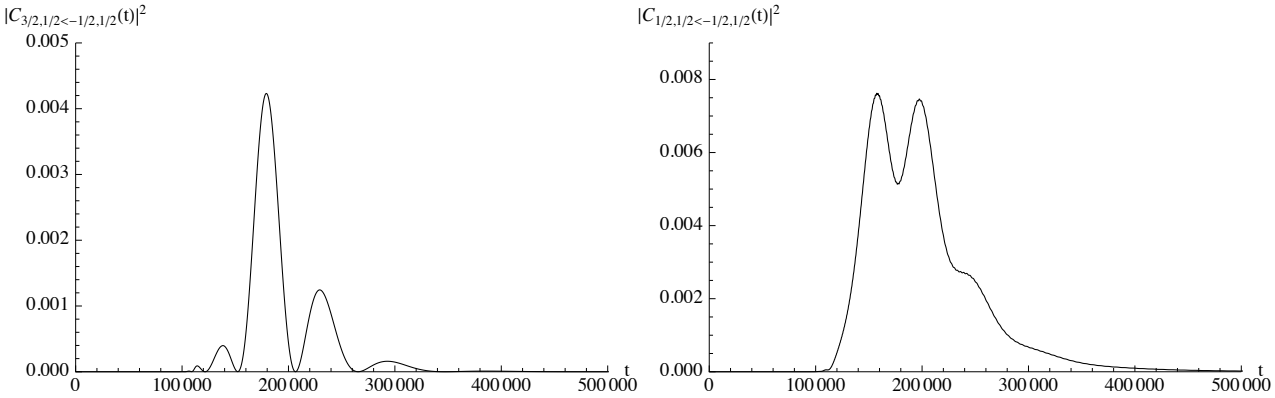

(a) Transmission Correlation Function (b) Reflection Correlation Function

Figure 39. KHe Spin-Orbit Interaction Correlation Functions, $J = 0.5$**.**

Next these correlation functions were transformed from time space to energy space via a Fourier Transform. A standard FT was used in this portion of the calculation with a selected energy resolution of $dE = 1.22 \times 10^{-6}$. The transformed correlation function was properly normalized according to the Chanel Packet Method and now we present the results for $J = 0.5$, $J = 50.5$, 100.5, 150.5, 200.5, and 250.5 in Figures 40, 41, 42. Notice how as J increases the transmission coefficient decreases in magnitude till at $J = 200.5$ it has nearly disappeared. By $J = 250.5$ the transmission coefficient is on the order of 10^{-7} across our energy range of interest. This tells us that the centrifugal potential has prevented the system from entering the interaction region.

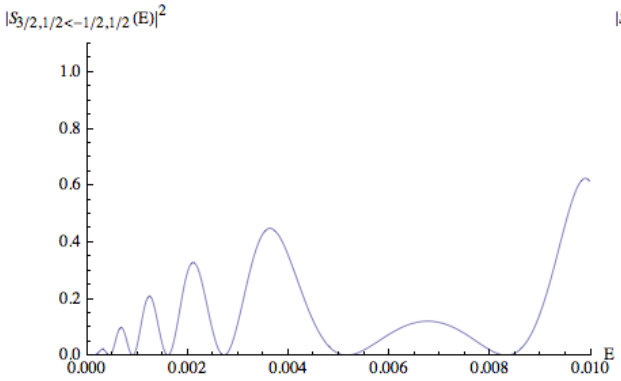

(a) $\left|\begin{smallmatrix}0.5 & 3/2\\ 1/2 & 1/2\end{smallmatrix}\right\rangle$ Transmission Coefficient

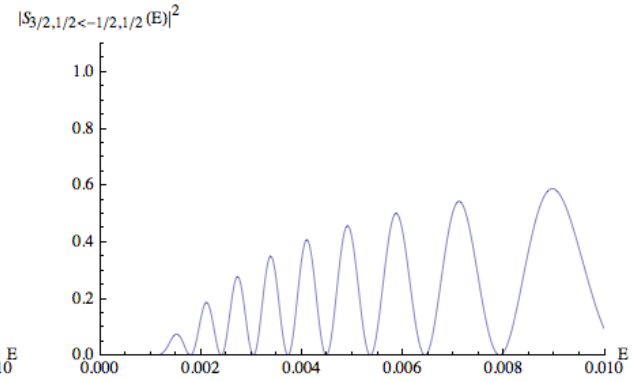

(b) $\left|\begin{smallmatrix}50.5 & 3/2\\ 1/2 & 1/2\end{smallmatrix}\right\rangle$ Transmission Coefficient

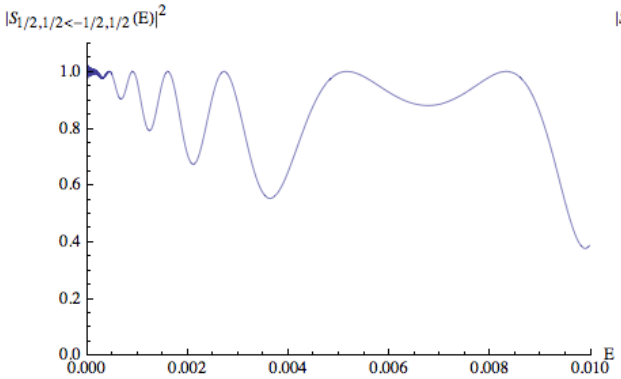

(c) $\left|\begin{smallmatrix}0.5 & 1/2\\ 1/2 & 1/2\end{smallmatrix}\right\rangle$ Reflection Coefficient

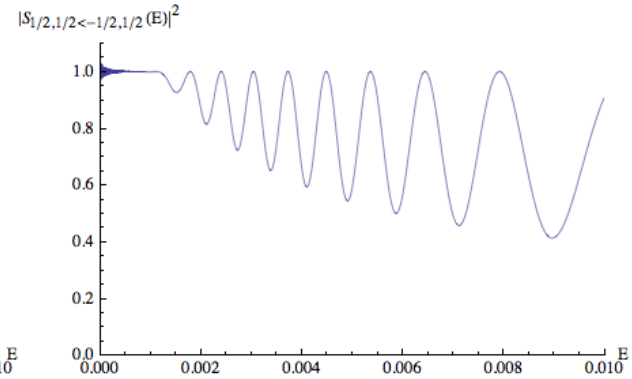

(d) $\left|\begin{smallmatrix}50.5 & 1/2\\ 1/2 & 1/2\end{smallmatrix}\right\rangle$ Reflection Coefficient

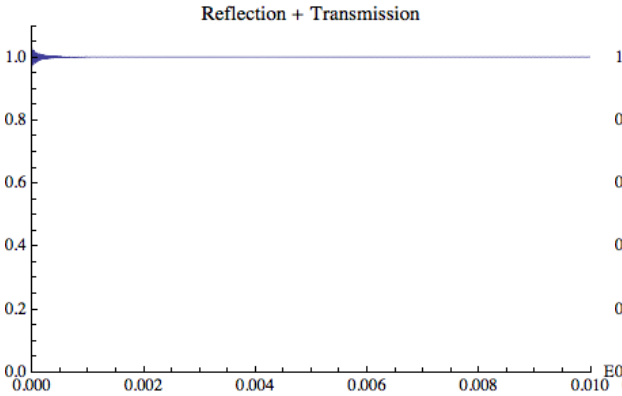

(e) Sum of Coefficients

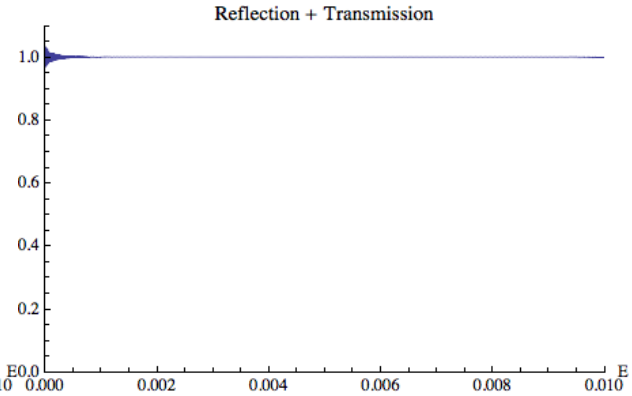

(f) Sum of Coefficients

Figure 40. KHe Spin-Orbit $\widehat{\mathbf{S}}$-Matrix Elements for $J = 0.5$ and 50.5.

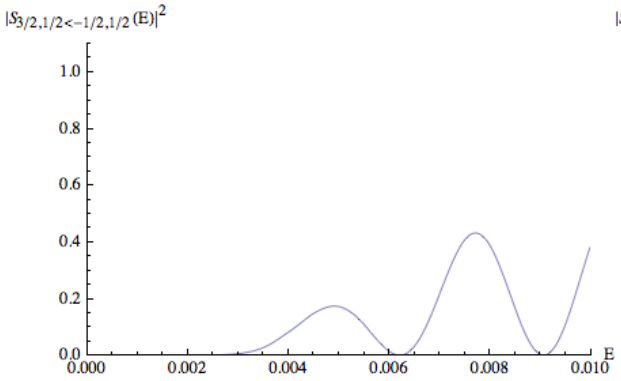

(a) $\left|\begin{smallmatrix}100.5 & 3/2\\ 1/2 & 1/2\end{smallmatrix}\right\rangle$ Transmission Coefficient

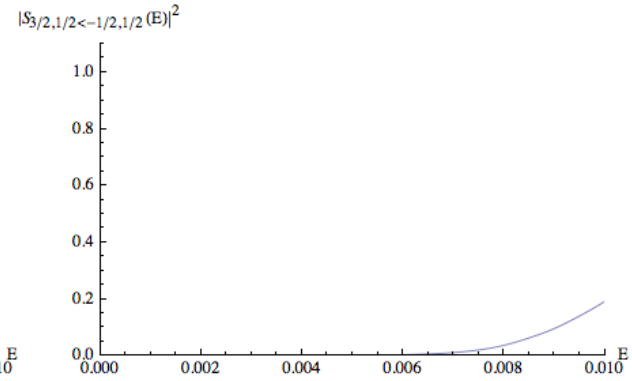

(b) $\left|\begin{smallmatrix}150.5 & 3/2\\ 1/2 & 1/2\end{smallmatrix}\right\rangle$ Transmission Coefficient

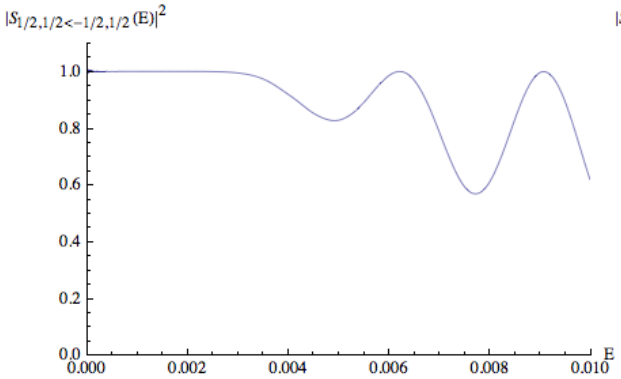

(c) $\left|\begin{smallmatrix}100.5 & 1/2\\ 1/2 & 1/2\end{smallmatrix}\right\rangle$ Reflection Coefficient

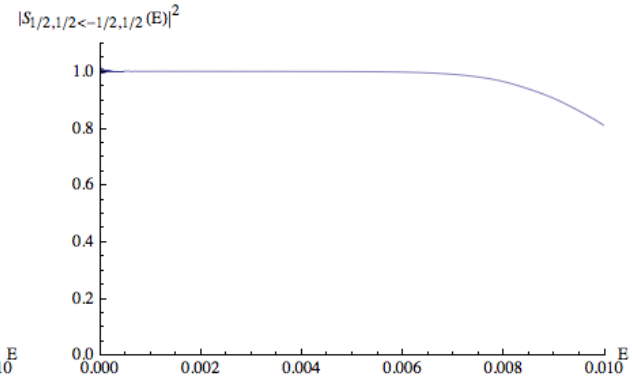

(d) $\left|\begin{smallmatrix}150.5 & 1/2\\ 1/2 & 1/2\end{smallmatrix}\right\rangle$ Reflection Coefficient

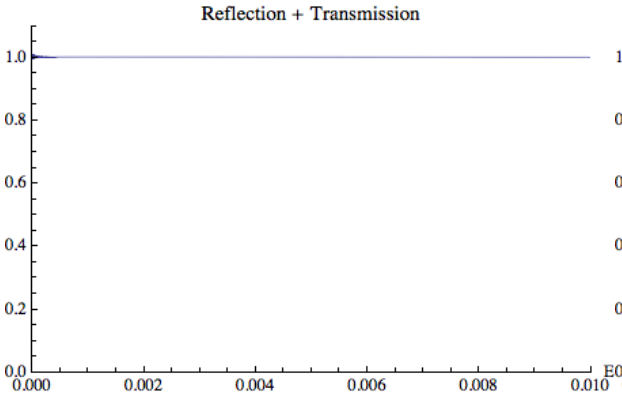

(e) Sum of Coefficients

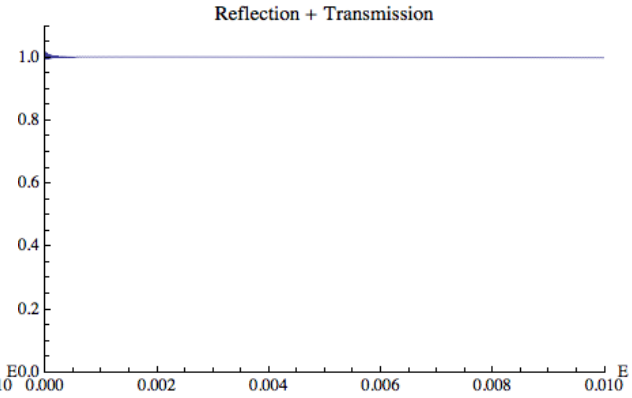

(f) Sum of Coefficients

Figure 41. KHe Spin-Orbit $\widehat{\mathbf{S}}$-Matrix Elements for $J = 100.5$ and 150.5.

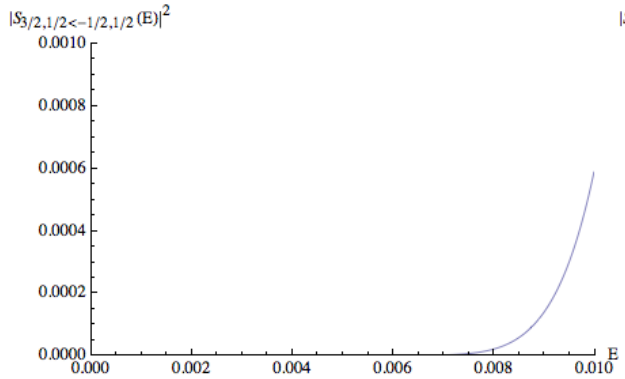

(a) $\left|\begin{smallmatrix}200.5 & 3/2\\ 1/2 & 1/2\end{smallmatrix}\right\rangle$ Transmission Coefficient

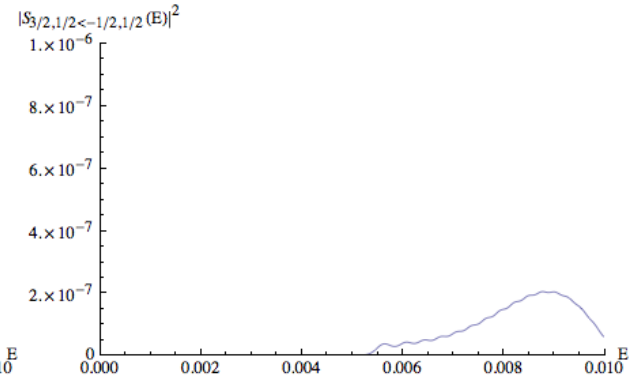

(b) $\left|\begin{smallmatrix}250.5 & 3/2\\ 1/2 & 1/2\end{smallmatrix}\right\rangle$ Transmission Coefficient

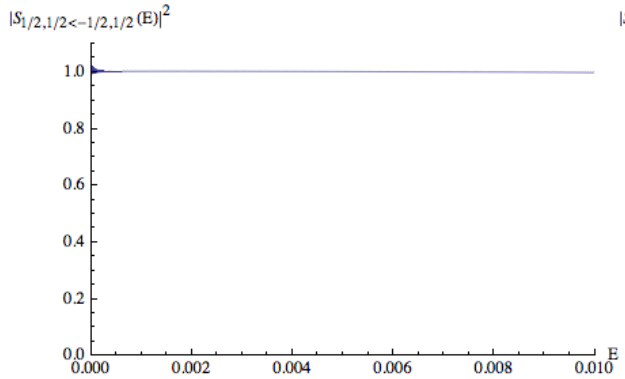

(c) $\left|\begin{smallmatrix}200.5 & 1/2\\ 1/2 & 1/2\end{smallmatrix}\right\rangle$ Reflection Coefficient

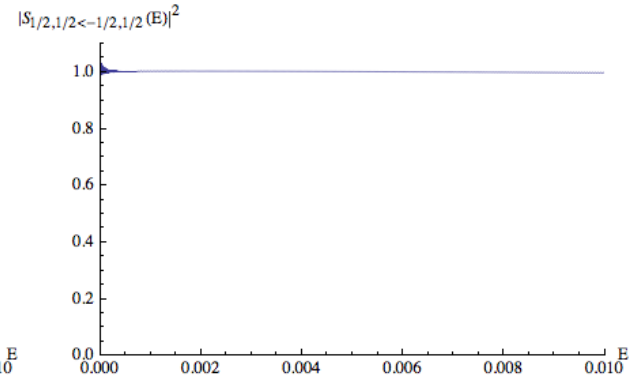

(d) $\left|\begin{smallmatrix}250.5 & 1/2\\ 1/2 & 1/2\end{smallmatrix}\right\rangle$ Reflection Coefficient

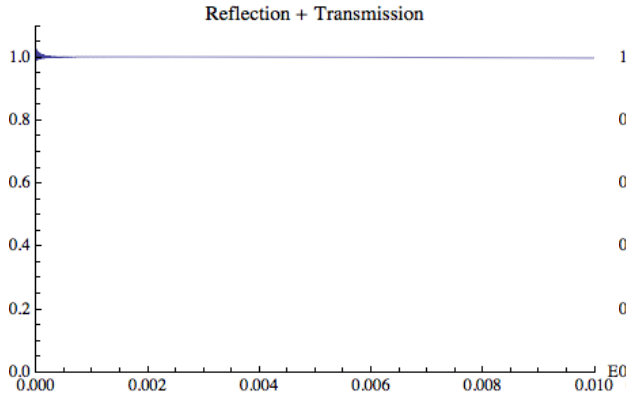

(e) Sum of Coefficients

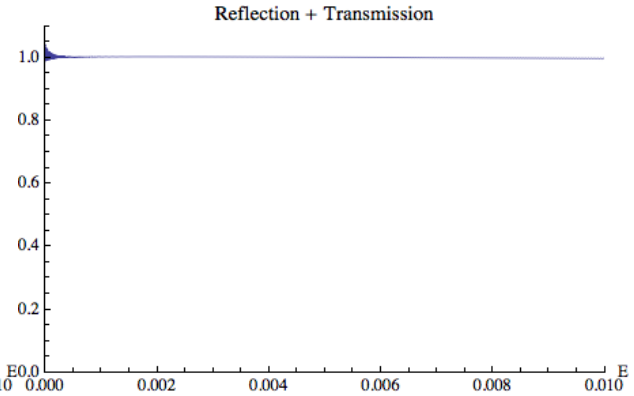

(f) Sum of Coefficients

Figure 42. KHe Spin-Orbit $\widehat{\mathbf{S}}$-Matrix Elements for $J = 200.5$ and 250.5.

The noise present in the reflection coefficients at energies less than 0.001 Bohr represents the low energy issue explained in section 6.3.

6.5 Interaction Region Calculation: Spin-Orbit and Radial Derivative Coupling

Now we analyze the effect of the Born-Oppenheimer radial derivative coupling. This time only the Coriolis couplings are artificially set to zero.

$$\widehat{\mathbf{H}} =$$

$$-\frac{1}{2\mu}\begin{pmatrix} \left|{}^{J\ \ 3/2}_{\pm 3/2\ \pm 3/2}\right\rangle & \left|{}^{J\ \ 3/2}_{\pm 1/2\ \pm 1/2}\right\rangle & \left|{}^{J\ \ 1/2}_{\pm 1/2\ \pm 1/2}\right\rangle \\ \frac{d}{dR} & 0 & 0 \\ 0 & \frac{d}{dR} & F \\ 0 & F & \frac{d}{dR} \end{pmatrix}^2 +$$

$$\begin{pmatrix} \left|{}^{J\ \ 3/2}_{\pm 3/2\ \pm 3/2}\right\rangle & \left|{}^{J\ \ 3/2}_{\pm 1/2\ \pm 1/2}\right\rangle & \left|{}^{J\ \ 1/2}_{\pm 1/2\ \pm 1/2}\right\rangle \\ \Pi + \frac{a(R)}{2} + \frac{J(J+1)-\frac{3}{4}}{2\mu R^2} & 0 & 0 \\ 0 & \frac{(2\Sigma+\Pi)}{3} + \frac{a(R)}{2} + \frac{J(J+1)+\frac{13}{4}}{2\mu R^2} & \mp\frac{\sqrt{2}}{3}(\Sigma-\Pi) \\ 0 & \mp\frac{\sqrt{2}}{3}(\Sigma-\Pi) & \frac{(\Sigma+2\Pi)}{3} - a(R) + \frac{J(J+1)+\frac{3}{4}}{2\mu R^2} \end{pmatrix}. \tag{221}$$

Once again the two 3x3 blocks are uncoupled and degenerate in this approximation.

The radial derivative couplings computed by Belcher were not computed in the Born-Oppenheimer basis, but rather in the spin-orbit molecular basis. This transfor-

mation was already discussed in section 6.2. The above total Hamiltonian becomes,

$$\widehat{\mathbf{H}} =$$

$$-\frac{1}{2\mu}\mathbf{U}^{\dagger}_{so}(R)\begin{pmatrix} \left|{}^{J}_{\pm 3/2}\,\Pi_{3/2}\right\rangle & \left|{}^{J}_{\pm 1/2}\,\Sigma_{1/2}\right\rangle & \left|{}^{J}_{\pm 1/2}\,\Pi_{1/2}\right\rangle \\ \frac{d}{dR} & 0 & 0 \\ 0 & \frac{d}{dR} & F \\ 0 & F & \frac{d}{dR} \end{pmatrix}^{2}\mathbf{U}_{so}(R)+$$

$$\begin{pmatrix} \left|{}^{J}_{\pm 3/2}\,\Pi_{3/2}\right\rangle & \left|{}^{J}_{\pm 1/2}\,\Sigma_{1/2}\right\rangle & \left|{}^{J}_{\pm 1/2}\,\Pi_{1/2}\right\rangle \\ \Pi_{3/2}+\frac{J(J+1)-\frac{3}{4}}{2\mu R^2} & 0 & 0 \\ 0 & \Sigma_{1/2}+\frac{J(J+1)+\frac{13}{4}}{2\mu R^2} & 0 \\ 0 & 0 & \Pi_{1/2}+\frac{J(J+1)+\frac{3}{4}}{2\mu R^2} \end{pmatrix}. \qquad (222)$$

Belcher showed that the dressed kinetic energy operator, $(\mathbb{I}\nabla+\mathbf{F})^2$, is both locally and globally gauge invariant. This means that when $(\mathbb{I}\nabla+\mathbf{F})^2$ is transformed by a unitary transformation the mathematical form of $(\mathbb{I}\nabla+\mathbf{F})^2$ remains the same. In the case of $\mathbf{U}_{so}(R)$, it is unitary, but also a function of R. So the derivative couplings will operate on $\mathbf{U}_{so}(R)$, however the dressed kinetic energy operator form will remain the same. We denote this difference by labeling the derivative couplings with a tilde and

write the Hamiltonian as,

$$\widehat{\mathbf{H}} =$$

$$-\frac{1}{2\mu}\begin{pmatrix} \left|{}^{J}_{\pm 3/2}\,\Pi_{3/2}\right\rangle & \left|{}^{J}_{\pm 1/2}\,\Sigma_{1/2}\right\rangle & \left|{}^{J}_{\pm 1/2}\,\Pi_{1/2}\right\rangle \\ \frac{d}{dR} & 0 & 0 \\ 0 & \frac{d}{dR} & \widetilde{F} \\ 0 & \widetilde{F} & \frac{d}{dR} \end{pmatrix}^{2} +$$

$$\begin{pmatrix} \left|{}^{J}_{\pm 3/2}\,\Pi_{3/2}\right\rangle & \left|{}^{J}_{\pm 1/2}\,\Sigma_{1/2}\right\rangle & \left|{}^{J}_{\pm 1/2}\,\Pi_{1/2}\right\rangle \\ \Pi_{3/2} + \frac{J(J+1)-\frac{3}{4}}{2\mu R^2} & 0 & 0 \\ 0 & \Sigma_{1/2} + \frac{J(J+1)+\frac{13}{4}}{2\mu R^2} & 0 \\ 0 & 0 & \Pi_{1/2} + \frac{J(J+1)+\frac{3}{4}}{2\mu R^2} \end{pmatrix}. \tag{223}$$

These spin-orbit derivative couplings, $\widetilde{F}$, are given by Belcher.

These radial derivative couplings were calculated at the SOCI level. Unlike Blank however Belcher was not able to use symmeterized spin-orbitals. Nor did he apply any Davidson corrections. None the less using a Graphical Unitary Group Approach (GUGA) the $\widetilde{F} = \left\langle \Sigma_{1/2} \right| \frac{\partial}{\partial R} \left| \Pi_{1/2} \right\rangle$ was determined and plotted in Figure 43. In order to calculate the transformation that diagonalizes the dressed kinetic energy operator the mixing angle α has to be first calcuated. By taking the line integral along R of the derivative coupling from infinity to R, Equation (74), we determine $\alpha(R)$ and plot it in Figure 44.

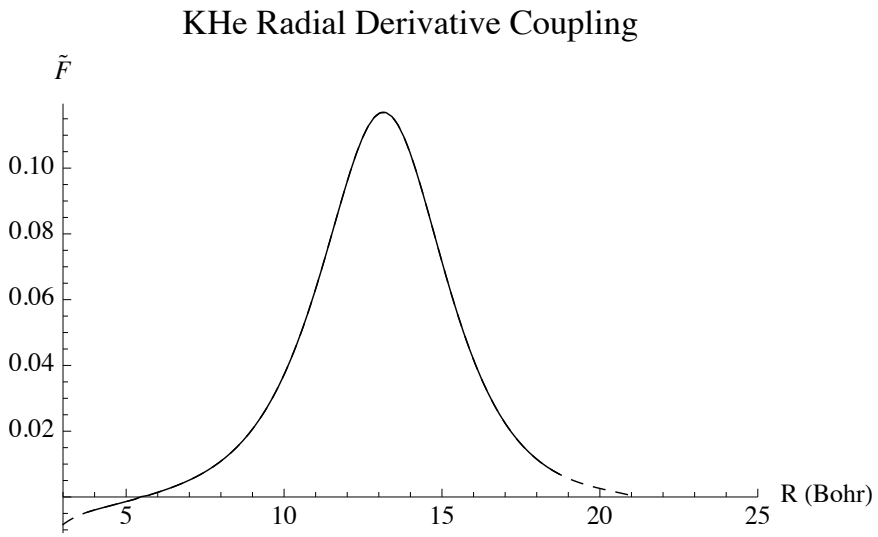

Figure 43. KHe Spin-Orbit derivative coupling. The solid line is the calculation done by Belcher. The dashed line is the spline interpolation and extrapolation used for interaction calculations.

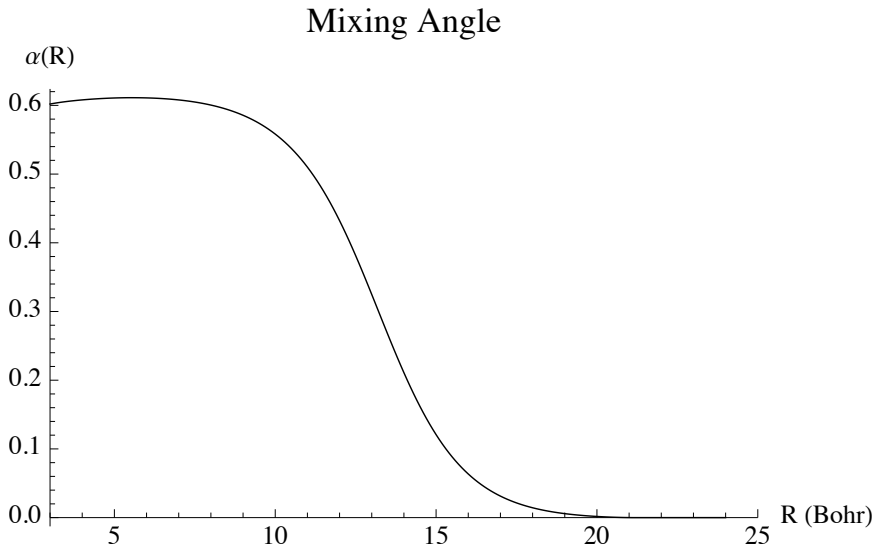

Figure 44. The mixing angle (radians) as a function of R that transforms away the spin-orbit radial derivative coupling term.

The transformation, $\mathbf{U}_F(R)$, is now determined.

$$\mathbf{U}_F(R) = \begin{pmatrix} cos(\alpha(\vec{R})) & -sin(\alpha(\vec{R})) \\ sin(\alpha(\vec{R})) & cos(\alpha(\vec{R})) \end{pmatrix} \tag{224}$$

This transformation is applied to Equation (223) and we present the strictly diabatic form of the Hamiltonian with respect to spin orbit and Born-Oppenheimer radial derivative coupling.

$$\widehat{\mathbf{H}} = -\frac{1}{2\mu}\begin{pmatrix} \left|{}^{J}_{\pm 3/2}\,\Pi^{F}_{3/2}\right\rangle & \left|{}^{J}_{\pm 1/2}\,\Sigma^{F}_{1/2}\right\rangle & \left|{}^{J}_{\pm 1/2}\,\Pi^{F}_{1/2}\right\rangle \\ \frac{d}{dR} & 0 & 0 \\ 0 & \frac{d}{dR} & 0 \\ 0 & 0 & \frac{d}{dR} \end{pmatrix}^2 +$$

$$\begin{pmatrix} \left|{}^{J}_{\pm 3/2}\,\Pi^{F}_{3/2}\right\rangle & \left|{}^{J}_{\pm 1/2}\,\Sigma^{F}_{1/2}\right\rangle & \left|{}^{J}_{\pm 1/2}\,\Pi^{F}_{1/2}\right\rangle \\ \Pi_{3/2} + \frac{J(J+1)-\frac{3}{4}}{2\mu R^2} & 0 & 0 \\ 0 & \Sigma_{1/2}cos^2\alpha + \Pi_{1/2}sin^2\alpha + \frac{J(J+1)+\frac{13}{4}}{2\mu R^2} & (\Sigma_{1/2} - \Pi_{1/2})sin\alpha cos\alpha \\ 0 & (\Sigma_{1/2} - \Pi_{1/2})sin\alpha cos\alpha & \Sigma_{1/2}sin^2\alpha + \Pi_{1/2}cos^2\alpha + \frac{J(J+1)+\frac{3}{4}}{2\mu R^2} \end{pmatrix}. \tag{225}$$

The strictly diabatic basis vectors are annotated with a superscript F recognizing that they are different from the spin-orbit molecular basis.

First, we wrote down the Born-Oppenheimer representation of $\mathbf{H}$. By diagonalizing this we transformed all spin-orbit coupling in to the kinetic energy operator, $(\mathbb{I}\nabla + \widetilde{\mathbf{F}})^2$. The $\widetilde{\mathbf{F}}$ represents both Born-Oppenheimer radial derivative coupling and

transformed spin-orbit coupling. Second, by utilizing Belcher's calculation the proper mixing angle was used to transform both couplings back in to the potential matrix creating a strictly diabatic representation. By comparing the Born-Oppenheimer diabatic surfaces to the strictly diabatic surfaces any difference can be attributed to the Born-Oppenheimer radial derivative coupling.

Astonishingly, when this comparison was made no difference between the Born-Oppenheimer diabatic surfaces, Equation (221), and the strictly diabatic surfaces. Equation (225), was observed. In particular we compare the spin-orbit coupling function in the Born-Oppenheimer representation, $\frac{\sqrt{2}}{3}(\Sigma - \Pi)$, to the radial derivative coupling in the strictly diabatic representation, $(\Sigma_{1/2} - \Pi_{1/2})sin(\alpha)cos(\alpha)$, and plot below.

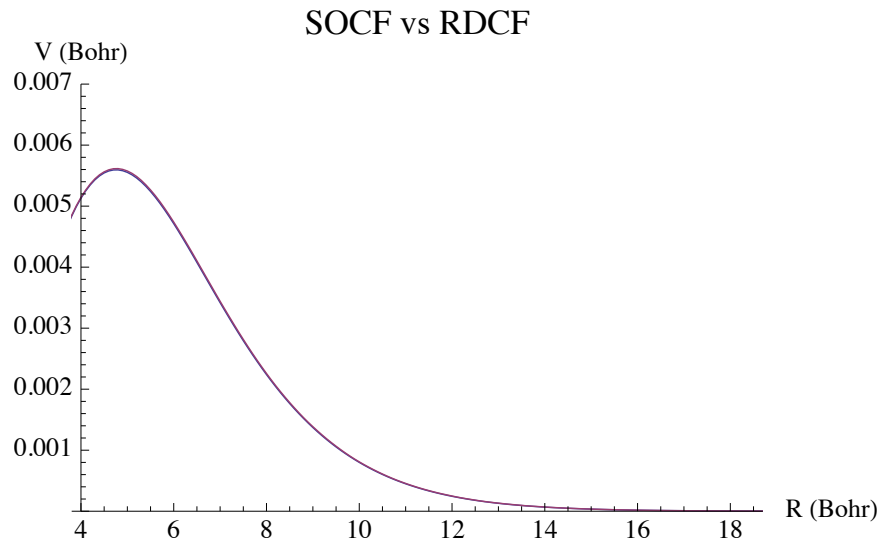

Figure 45. The Born-Oppenheimer Spin-Orbit Coupling Function vs the Strictly Diabatic Radial Derivative Coupling Function.

We expected these coupling functions to exhibit a significant difference. This difference being attributed to the Born-Oppenheimer radial derivative coupling terms. However this observation implies that $\mathbf{F} \approx 0$. This is echoed in the literature. Mies[30] in studying $F+H^+$ collisions determined using perturbation theory that the first order

correction to **F** is zero. Delos[16] states that in general due to the Hellmann-Feynman theorem the **F** vanish for systems in which **l** and **s** are not coupled. When other authors simply neglect or approximate away these Born-Oppenheimer non-adiabatic terms then this issue never comes to the foreground. It was unknown at the time whether or not this would apply to the KHe collision.

This does lead to a nice consequence. For diatomic systems where a strictly diabatic transformation is possible the mixing angle can be estimated from simply the SOCI surfaces by solving the equation,

$$sin(\alpha(R))cos(\alpha(R)) = \frac{\frac{\sqrt{2}}{3}(\Sigma - \Pi)}{\Sigma_{1/2} - \Pi_{1/2}}. \tag{226}$$

From the mixing angle we can calculate the spin-orbit radial derivative couplings. The predictions for $\widetilde{F}$ of all nine collision partners are shown in Appendix D.

Viewed in the Born-Oppenheimer basis spin-orbit coupling appears in the off diagonal diabatic potential. Viewed in the adiabatic spin-orbit molecular basis, the spin-orbit coupling appears as radial derivative coupling. Both descriptions are correct and spin-orbit coupling should not be deemed different than radial derivative couplings in the case of diatomics. Having now seen that the Born-Oppenheimer radial derivative couplings contribute little to no impact we analyze the last coupling phenomenon, Coriolis coupling.

6.6 Interaction Region Calculation: Spin-Orbit and Coriolis Coupling

We will proceed in the same fashion as in Section 6.4 to include the Coriolis coupling terms. From the previous section we know the Born-Oppenheimer radial derivative couplings are zero so the close-coupled potential, (143), reads:

$$
H = -\frac{1}{2\mu}\frac{d^2}{dR^2}\begin{pmatrix}
\left|J\ 3/2\ 3/2\right\rangle & \left|J\ 3/2\ 1/2\right\rangle & \left|J\ 1/2\ 1/2\right\rangle & \left|J\ 3/2\ -3/2\right\rangle & \left|J\ 3/2\ -1/2\right\rangle & \left|J\ 1/2\ -1/2\right\rangle \\
\frac{d}{dR} & 0 & 0 & 0 & 0 & 0 \\
0 & \frac{d}{dR} & 0 & 0 & 0 & 0 \\
0 & 0 & \frac{d}{dR} & 0 & 0 & 0 \\
0 & 0 & 0 & \frac{d}{dR} & 0 & 0 \\
0 & 0 & 0 & 0 & \frac{d}{dR} & 0 \\
0 & 0 & 0 & 0 & 0 & \frac{d}{dR}
\end{pmatrix}^2 + \tag{227}
$$

$$
\begin{array}{c}
\left|\begin{smallmatrix} J & 3/2 \\ 3/2 & 3/2 \end{smallmatrix}\right\rangle \\
\left(\begin{array}{c}
\Pi + \frac{a(R)}{2} \\
0 \\
0 \\
0 \\
0 \\
0
\end{array}\right.
\end{array}
\begin{array}{c}
\left|\begin{smallmatrix} J & 3/2 \\ 1/2 & 1/2 \end{smallmatrix}\right\rangle \\
\left(\begin{array}{c}
0 \\
\frac{(2\Sigma+\Pi)}{3} + \frac{a(R)}{2} \\
-\frac{\sqrt{2}}{3}(\Sigma - \Pi) \\
0 \\
0 \\
0
\end{array}\right.
\end{array}
\begin{array}{c}
\left|\begin{smallmatrix} J & 1/2 \\ 1/2 & 1/2 \end{smallmatrix}\right\rangle \\
\left(\begin{array}{c}
0 \\
-\frac{\sqrt{2}}{3}(\Sigma - \Pi) \\
\frac{(\Sigma+2\Pi)}{3} - a(R) \\
0 \\
0 \\
0
\end{array}\right.
\end{array}
\begin{array}{c}
\left|\begin{smallmatrix} J & 3/2 \\ -3/2 & -3/2 \end{smallmatrix}\right\rangle \\
\left(\begin{array}{c}
0 \\
0 \\
0 \\
\Pi + \frac{a(R)}{2} \\
0 \\
0
\end{array}\right.
\end{array}
\begin{array}{c}
\left|\begin{smallmatrix} J & 3/2 \\ -1/2 & -1/2 \end{smallmatrix}\right\rangle \\
\left(\begin{array}{c}
0 \\
0 \\
0 \\
0 \\
\frac{(2\Sigma+\Pi)}{3} + \frac{a(R)}{2} \\
\frac{\sqrt{2}}{3}(\Sigma - \Pi)
\end{array}\right.
\end{array}
\begin{array}{c}
\left|\begin{smallmatrix} J & 1/2 \\ -1/2 & -1/2 \end{smallmatrix}\right\rangle \\
\left(\begin{array}{c}
0 \\
0 \\
0 \\
0 \\
\frac{\sqrt{2}}{3}(\Sigma - \Pi) \\
\frac{(\Sigma+2\Pi)}{3} - a(R)
\end{array}\right)
\end{array}
\tag{228}
$$

$$
\begin{array}{c}
\left|\begin{smallmatrix} J & 3/2 \\ 3/2 & 3/2 \end{smallmatrix}\right\rangle \\
\left(\begin{array}{c}
\frac{J(J+1)-\frac{3}{4}}{2\mu R^2} \\
-\frac{[3(J-\frac{1}{2})(J+\frac{3}{2})]^{1/2}}{2\mu R^2} \\
0 \\
0 \\
0
\end{array}\right.
\end{array}
\begin{array}{c}
\left|\begin{smallmatrix} J & 3/2 \\ 1/2 & 3/2 \end{smallmatrix}\right\rangle \\
\left(\begin{array}{c}
-\frac{[3(J-\frac{1}{2})(J+\frac{3}{2})]^{1/2}}{2\mu R^2} \\
\frac{J(J+1)+\frac{13}{4}}{2\mu R^2} \\
0 \\
0 \\
-\frac{2(J+1)}{2\mu R^2}
\end{array}\right.
\end{array}
\begin{array}{c}
\left|\begin{smallmatrix} J & 1/2 \\ 1/2 & 1/2 \end{smallmatrix}\right\rangle \\
\left(\begin{array}{c}
0 \\
0 \\
\frac{J(J+1)+\frac{3}{4}}{2\mu R^2} \\
0 \\
-\frac{J+1}{2\mu R^2}
\end{array}\right.
\end{array}
\begin{array}{c}
\left|\begin{smallmatrix} J & 3/2 \\ -3/2 & -3/2 \end{smallmatrix}\right\rangle \\
\left(\begin{array}{c}
0 \\
0 \\
0 \\
\frac{J(J+1)-\frac{3}{4}}{2\mu R^2} \\
-\frac{[3(J-\frac{1}{2})(J+\frac{3}{2})]^{1/2}}{2\mu R^2}
\end{array}\right.
\end{array}
\begin{array}{c}
\left|\begin{smallmatrix} J & 3/2 \\ -1/2 & -1/2 \end{smallmatrix}\right\rangle \\
\left(\begin{array}{c}
0 \\
0 \\
-\frac{2(J+1)}{2\mu R^2} \\
0 \\
-\frac{[3(J-\frac{1}{2})(J+\frac{3}{2})]^{1/2}}{2\mu R^2} \\
\frac{J(J+1)+\frac{13}{4}}{2\mu R^2}
\end{array}\right.
\end{array}
\begin{array}{c}
\left|\begin{smallmatrix} J & 1/2 \\ -1/2 & -1/2 \end{smallmatrix}\right\rangle \\
\left(\begin{array}{c}
0 \\
0 \\
-\frac{J+1}{2\mu R^2} \\
0 \\
0 \\
\frac{J(J+1)+\frac{3}{4}}{2\mu R^2}
\end{array}\right)
\end{array}
\tag{229}
$$

The Coriolis coupling functions are a function of total angular momentum, J, and projection, ω (which has already been factored in). These couplings fall off as R^{-2} similar to the centrifugal potential. However, whereas the numerator of the centrifugal potential is on the order of J^2, the Coriolis coupling function's numerators are on the order of J. Much like the centrifugal potential the Coriolis coupling function is a long range function, but because of this difference in magnitude it does not seem necessary to include the Coriolis coupling in the Moller state calculation. No error in S-Matrix calculation would come about, but a small error could be induced in the cross section when compared with experiment. In our scenario the Moller Reactants are unaffected by this observation because we constrain the reactants to start off only on the $\left|{}^{J\ \ 1/2}_{\pm 1/2\ \pm 1/2}\right\rangle$ surface.

Looking at the block structure of the potential lots of primary and secondary pathways are accessible between the various states. First, looking inside the diagonal 3x3 blocks we see that the Coriolis coupling couples the positive projection 1x1 block to the positive projection 2x2 block. The same goes for the negative projection 3x3 block. External to the diagonal 3x3 blocks the Coriolis coupling couples the positive projection 2x2 block to the negative projection 2x2 block. In fact since the Coriolis coupling is dependent on the magnetic projection the degeneracy of the 3x3 blocks is slightly lifted. It is possible to enter in on $\left|{}^{J\ \ 1/2}_{-1/2\ -1/2}\right\rangle$ state and exit out in all six states. For example we could begin in the $\left|{}^{J\ \ 1/2}_{-1/2\ -1/2}\right\rangle$ state, spin-orbit couple to the $\left|{}^{J\ \ 3/2}_{-1/2\ -1/2}\right\rangle$ state, Coriolis couple to the $\left|{}^{J\ \ 3/2}_{1/2\ 1/2}\right\rangle$, followed by another Coriolis transition to $\left|{}^{J\ \ 3/2}_{3/2\ 3/2}\right\rangle$ state and exit. This would be a $\left|{}^{J\ \ 1/2}_{-1/2\ -1/2}\right\rangle \rightarrow \left|{}^{J\ \ 3/2}_{3/2\ 3/2}\right\rangle$ transition.

This 6x6 Hamiltonian will be diagonalized for computation. The resultant adiabatic basis is not the spin-orbit molecular basis since the Coriolis coupling and spin-orbit couplings are being mutually diagonalized. Because the Coriolis coupling is a dynamic effect and diagonalizing the spin-orbit portion brings about spin-orbit

molecular character, we will call this new basis the dynamic adiabatic spin-orbit molecular basis. The surfaces transformed this way are the adiabatic potential energy surfaces with respect to Coriolis, electronic, and magnetic potentials. These surfaces are plotted below for $J = 50.5$, 100.5, 150.5, and 200.5 with the spin-orbit and Coriolis coupling functions plotted in the Born Oppenheimer electronic basis.

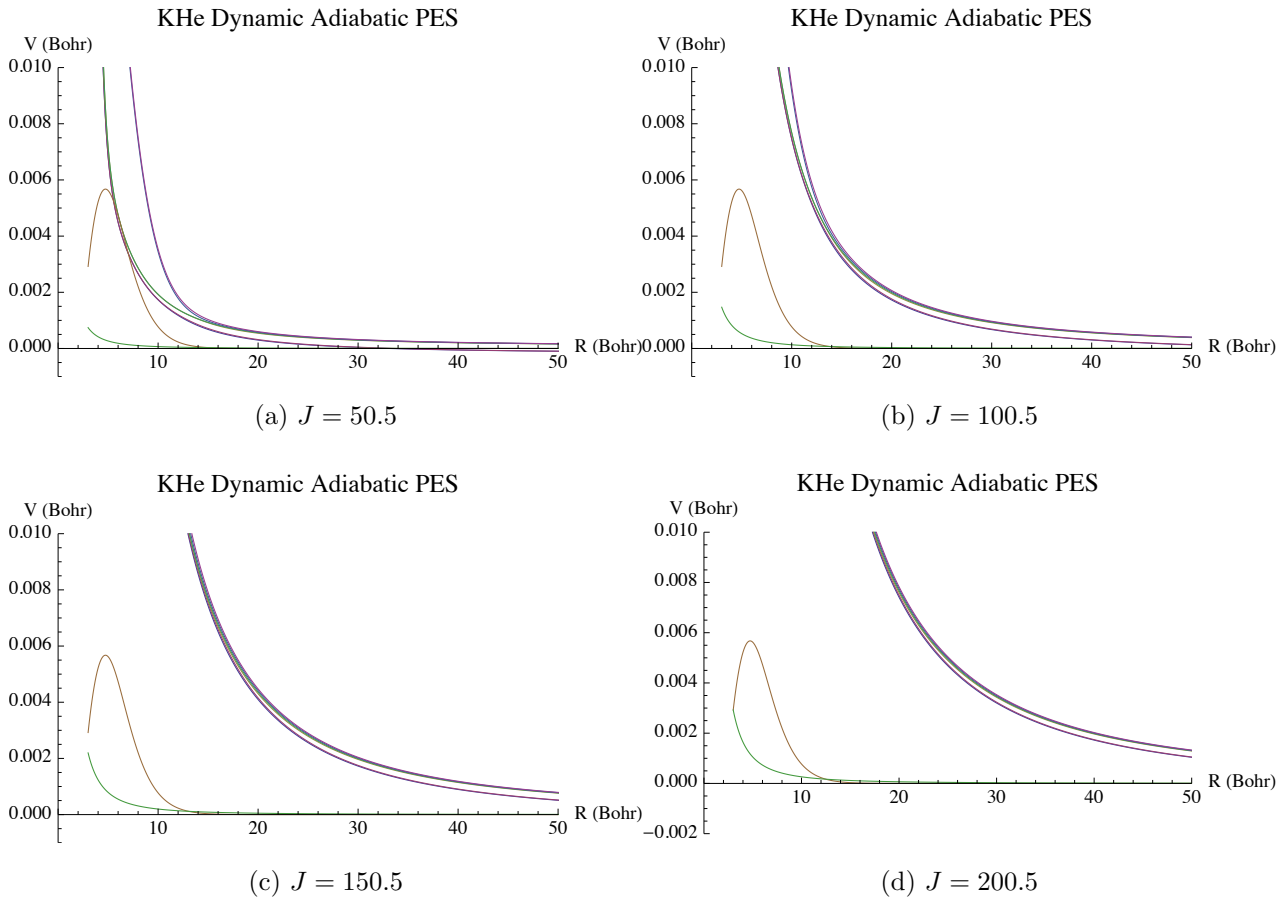

(a) $J = 50.5$ (b) $J = 100.5$

(c) $J = 150.5$ (d) $J = 200.5$

Figure 46. KHe Dynamic Adiabatic States with spin-orbit and Coriolis coupling for $J = 0.5$, 50.5, 100.5, 150.5, and 200.5.

The Coriolis coupling when compared to the spin-orbit coupling is smaller in magnitude at low nuclear angular momentum, but becomes comparable as J is increased for the same R. This signifies that as angular momentum increases an electronic transition via Coriolis coupling is more likely to occur. At extremely high J, spin-orbit

transitions would be insignificant compared to Coriolis transitions.

The same Moller reactants and products of the spin-orbit calculation are used for the spin-orbit plus Coriolis interaction calculation. Starting the system in the $\left|{}^{J\ \ 1/2}_{-1/2\ -1/2}\right\rangle$ state we expect wave function to exit on all six surfaces . Time snap shots of how these dynamics proceed are plotted for the $J = 50.5$ case as well as the correlation functions. Following those are the $\widehat{\mathbf{S}}$-Matrix elements for $J = 50.5$, 100.5, 150.5, and 200.5.

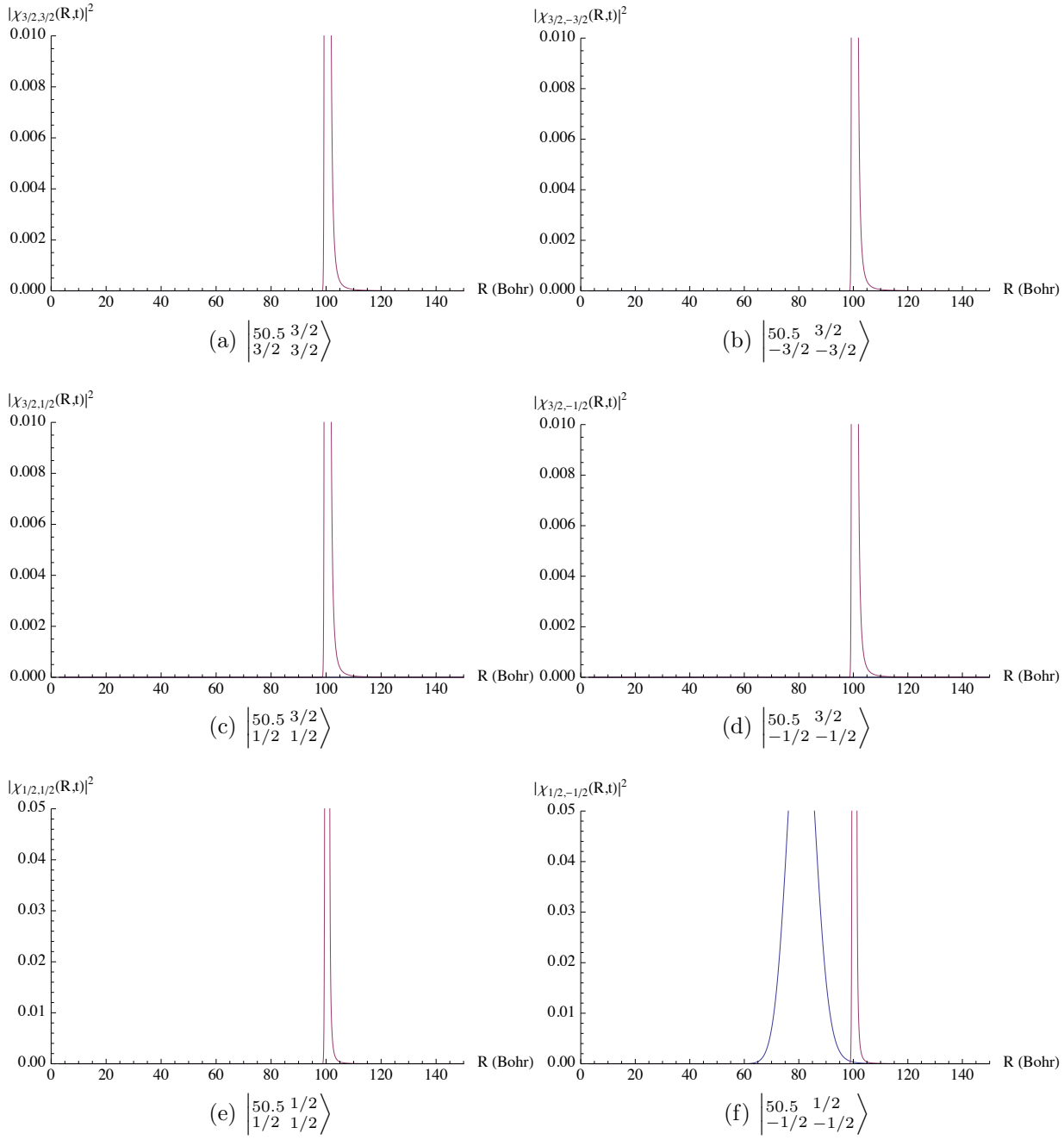

Figure 47. KHe Spin-Orbit plus Coriolis Interaction wave functions at t=20000.

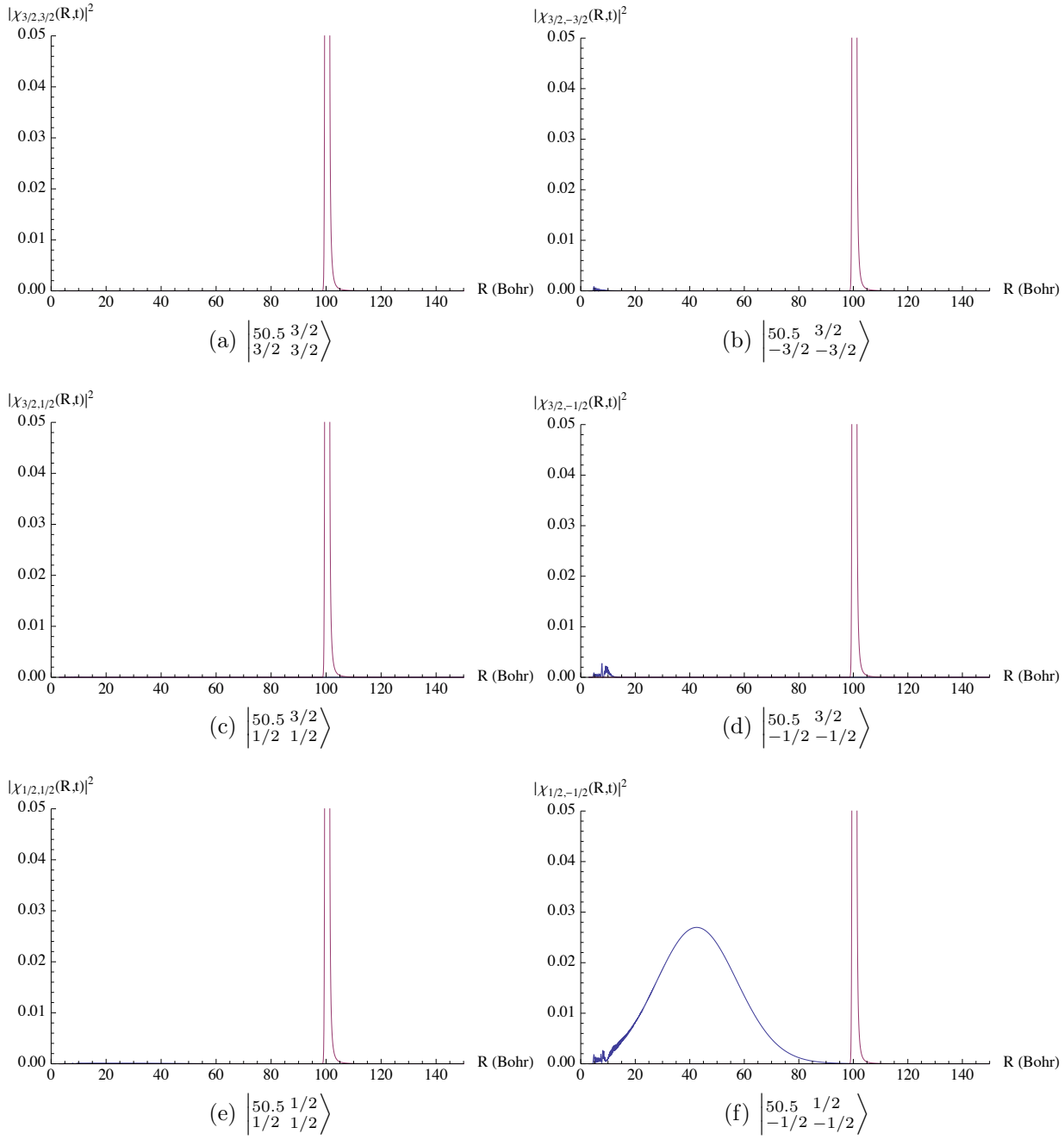

Figure 48. KHe Spin-Orbit plus Coriolis Interaction wave functions at t=60000.

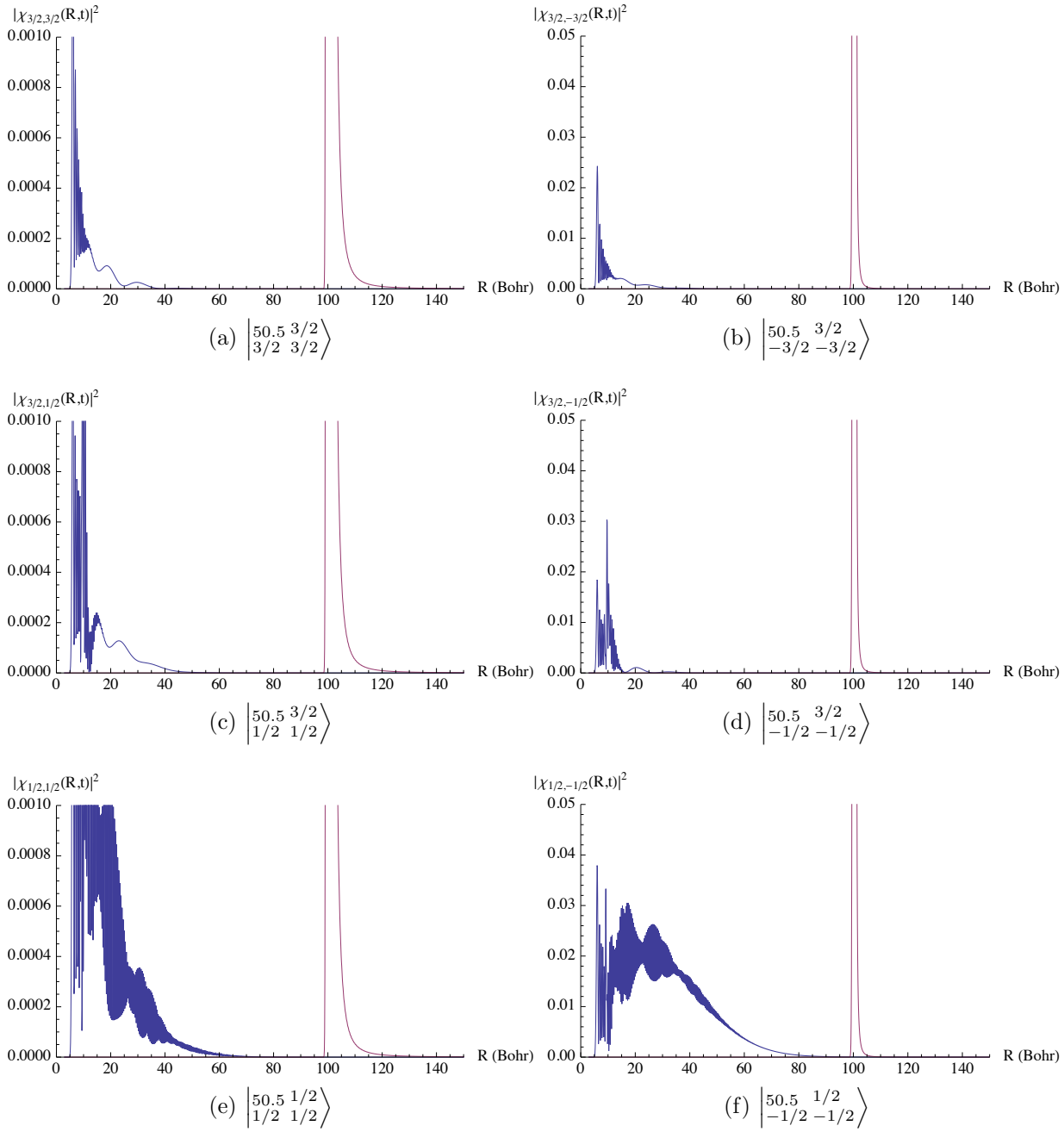

Figure 49. KHe Spin-Orbit plus Coriolis Interaction wave functions at t=80000. Note that the scale for wave functions exiting on the positive projection surfaces has been decreased to show wave function details.

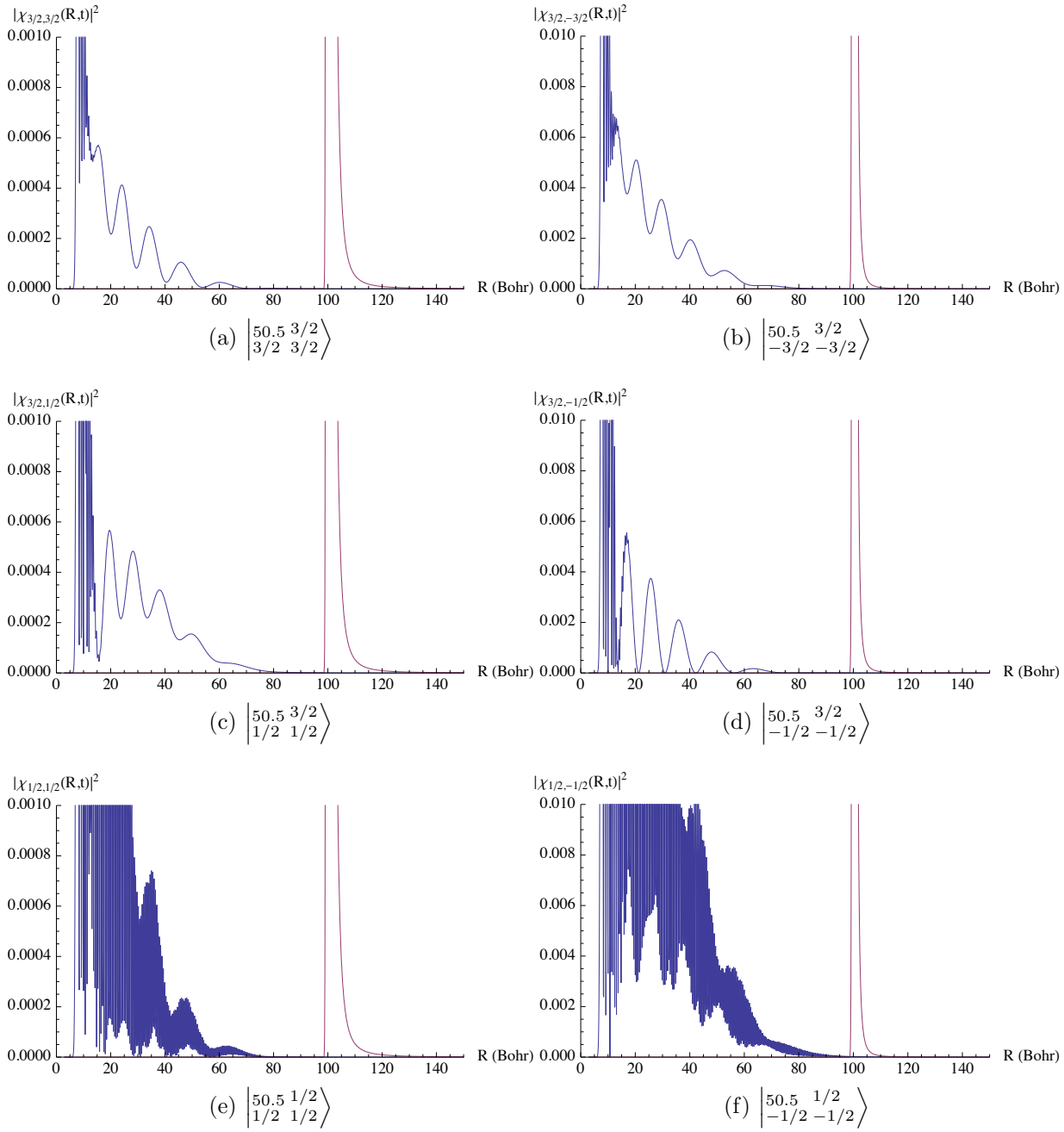

Figure 50. KHe Spin-Orbit plus Coriolis Interaction wave functions at t=100000. Note that the scale for wave functions exiting on the positive projection surfaces has been decreased to show wave function details.

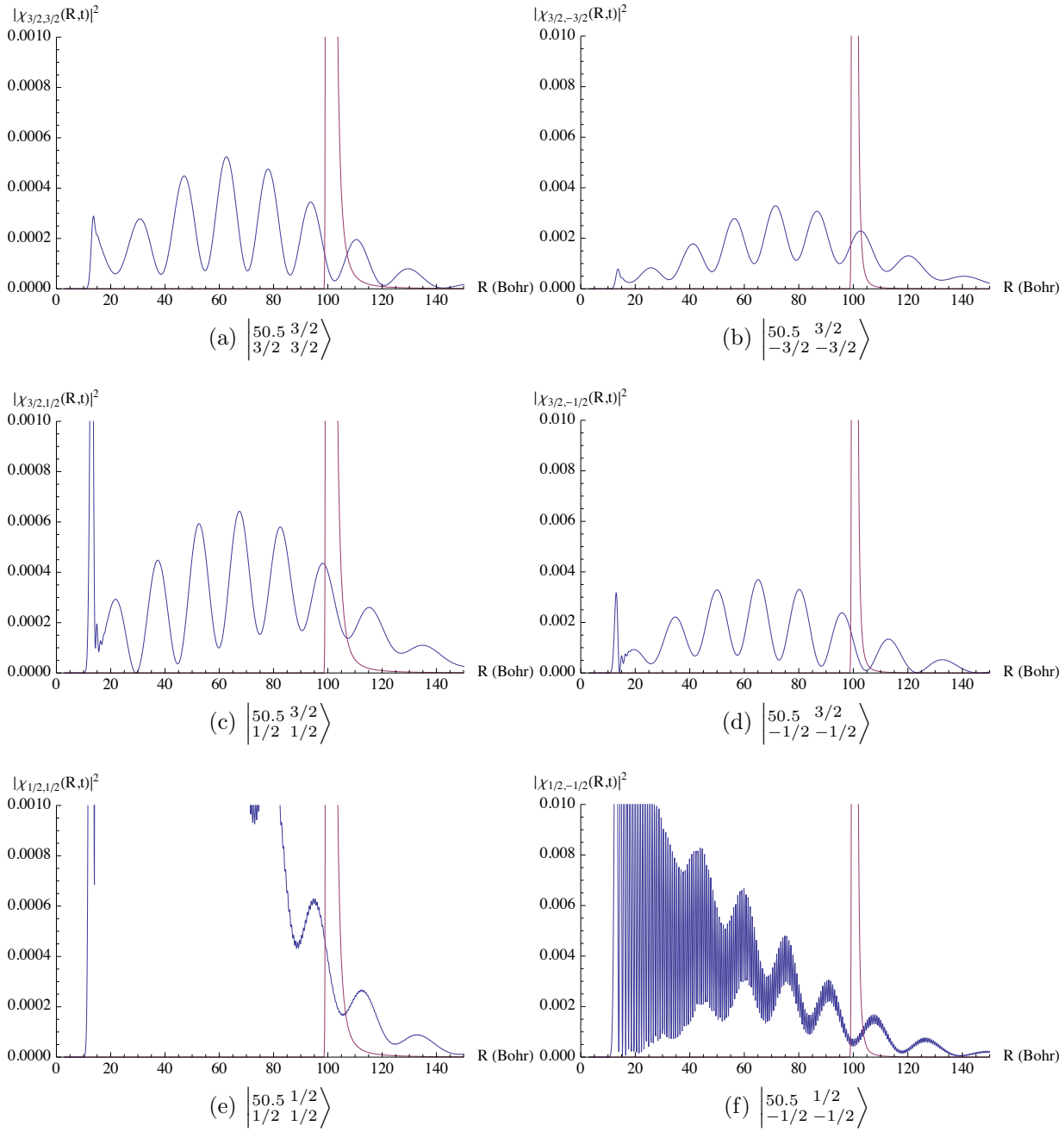

Figure 51. KHe Spin-Orbit plus Coriolis Interaction wave functions at t=160000. Note that the scale for wave functions exiting on the positive projection surfaces has been decreased to show wave function details.

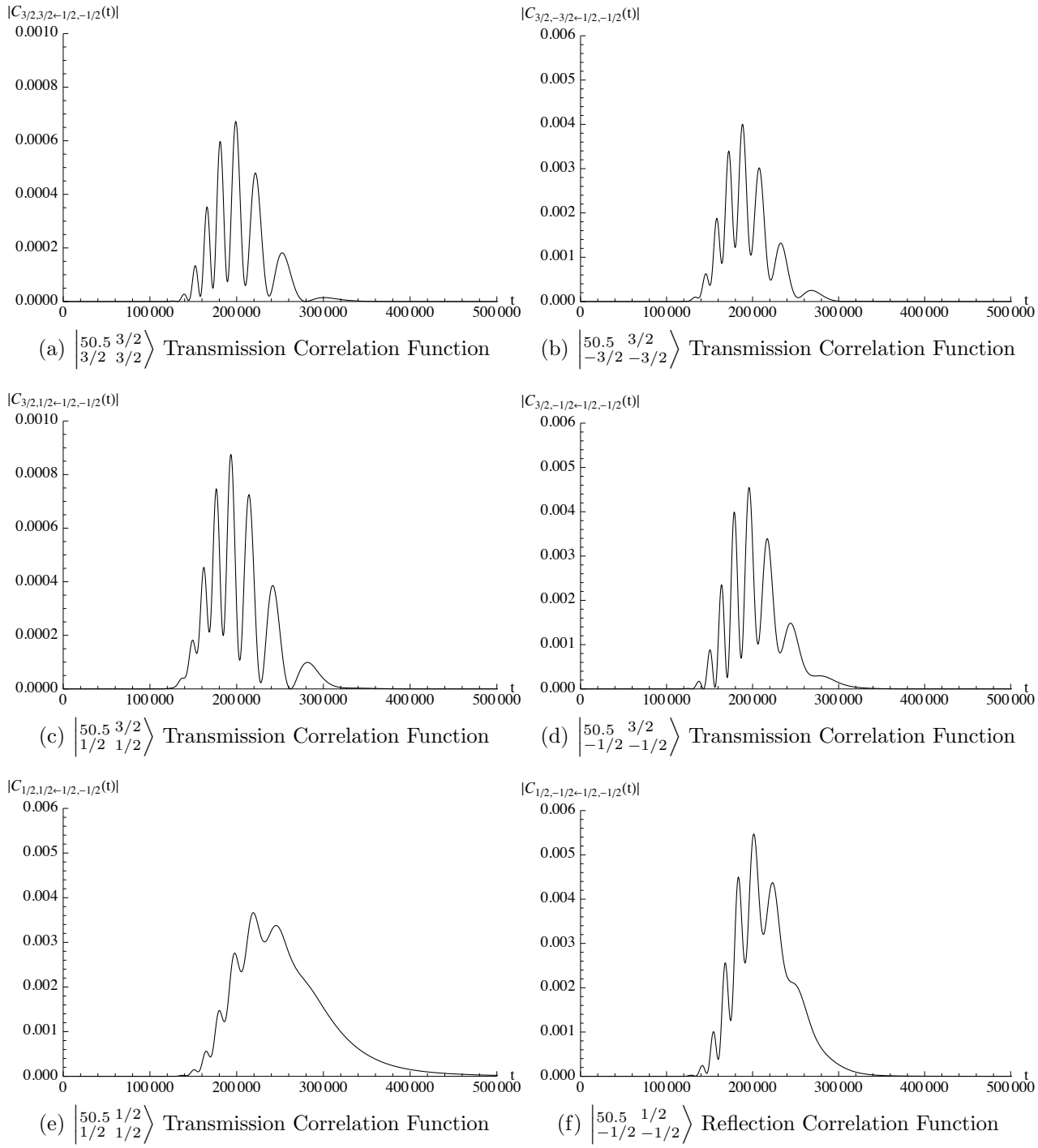

(a) $\left|\begin{smallmatrix}50.5 & 3/2\\ 3/2 & 3/2\end{smallmatrix}\right\rangle$ Transmission Correlation Function

(b) $\left|\begin{smallmatrix}50.5 & 3/2\\ -3/2 & -3/2\end{smallmatrix}\right\rangle$ Transmission Correlation Function

(c) $\left|\begin{smallmatrix}50.5 & 3/2\\ 1/2 & 1/2\end{smallmatrix}\right\rangle$ Transmission Correlation Function

(d) $\left|\begin{smallmatrix}50.5 & 3/2\\ -1/2 & -1/2\end{smallmatrix}\right\rangle$ Transmission Correlation Function

(e) $\left|\begin{smallmatrix}50.5 & 1/2\\ 1/2 & 1/2\end{smallmatrix}\right\rangle$ Transmission Correlation Function

(f) $\left|\begin{smallmatrix}50.5 & 1/2\\ -1/2 & -1/2\end{smallmatrix}\right\rangle$ Reflection Correlation Function

Figure 52. KHe Spin-Orbit plus Coriolis Interaction Correlation Functions, $J = 50.5$.

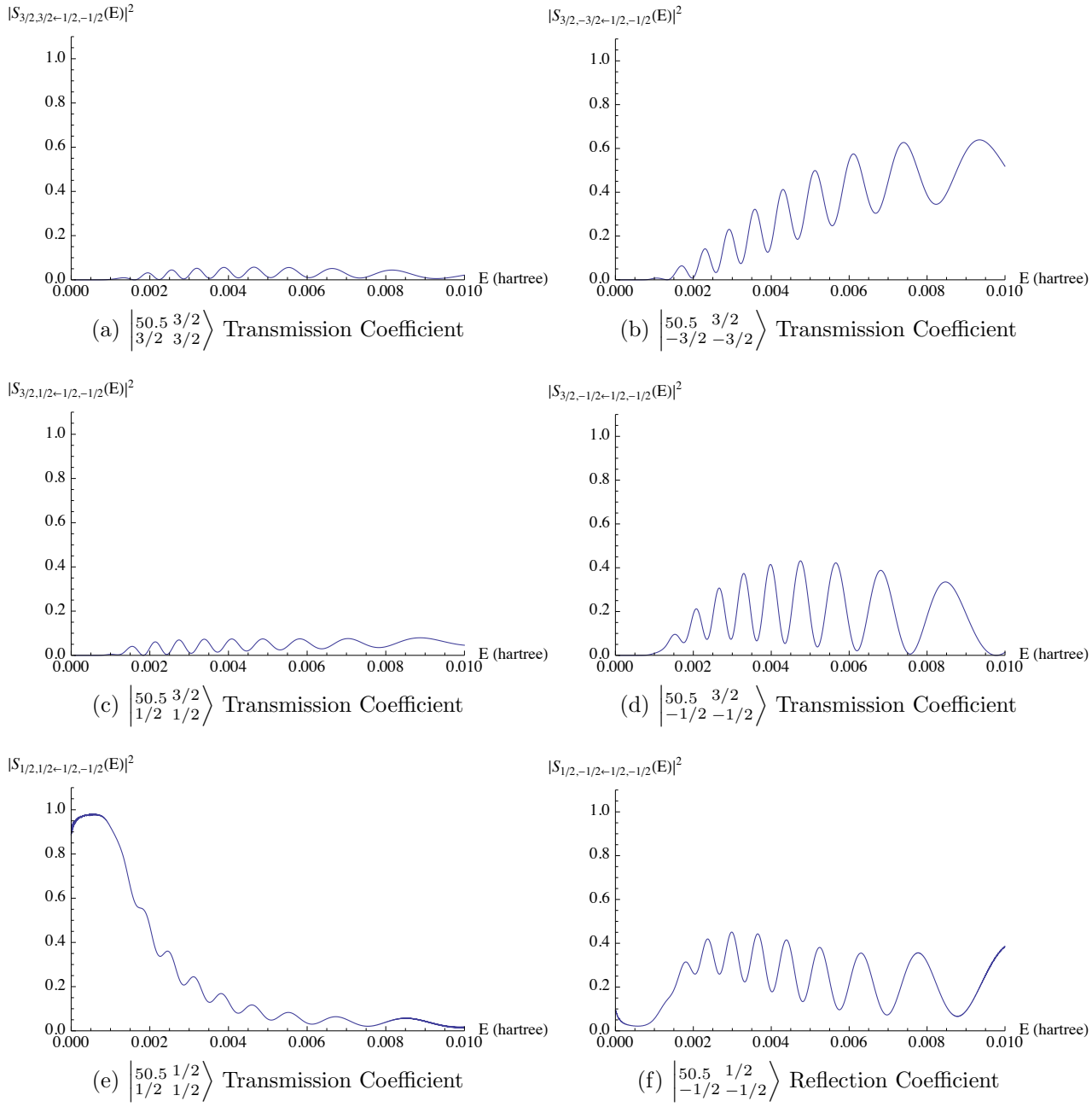

(a) $\left|\begin{smallmatrix}50.5 & 3/2\\ 3/2 & 3/2\end{smallmatrix}\right\rangle$ Transmission Coefficient

(b) $\left|\begin{smallmatrix}50.5 & 3/2\\ -3/2 & -3/2\end{smallmatrix}\right\rangle$ Transmission Coefficient

(c) $\left|\begin{smallmatrix}50.5 & 3/2\\ 1/2 & 1/2\end{smallmatrix}\right\rangle$ Transmission Coefficient

(d) $\left|\begin{smallmatrix}50.5 & 3/2\\ -1/2 & -1/2\end{smallmatrix}\right\rangle$ Transmission Coefficient

(e) $\left|\begin{smallmatrix}50.5 & 1/2\\ 1/2 & 1/2\end{smallmatrix}\right\rangle$ Transmission Coefficient

(f) $\left|\begin{smallmatrix}50.5 & 1/2\\ -1/2 & -1/2\end{smallmatrix}\right\rangle$ Reflection Coefficient

Figure 53. KHe Spin-Orbit plus Coriolis Interaction SMatrix Elements, $J = 50.5$.

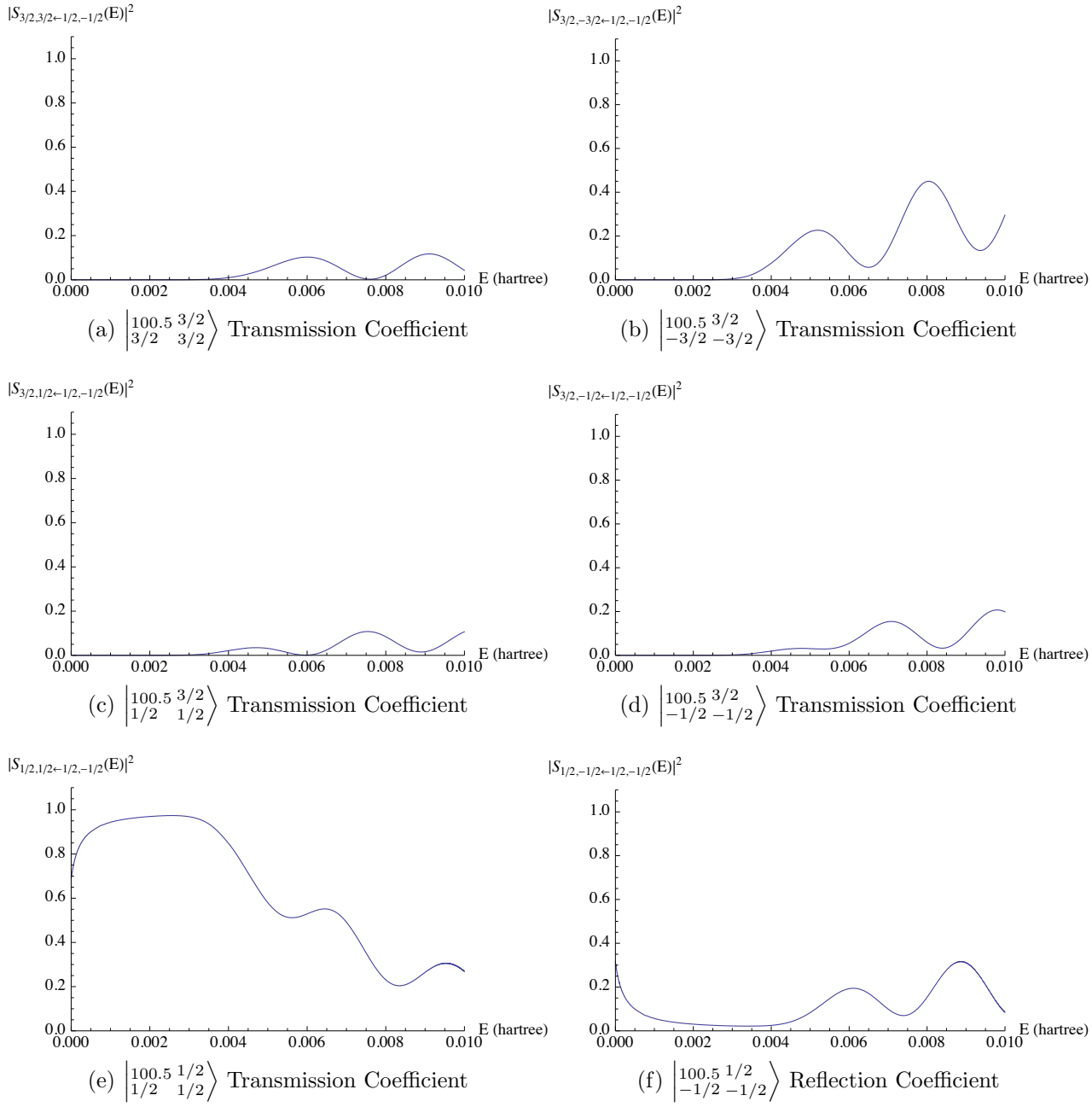

(a) $\left|\begin{matrix}100.5 & 3/2\\ 3/2 & 3/2\end{matrix}\right\rangle$ Transmission Coefficient

(b) $\left|\begin{matrix}100.5 & 3/2\\ -3/2 & -3/2\end{matrix}\right\rangle$ Transmission Coefficient

(c) $\left|\begin{matrix}100.5 & 3/2\\ 1/2 & 1/2\end{matrix}\right\rangle$ Transmission Coefficient

(d) $\left|\begin{matrix}100.5 & 3/2\\ -1/2 & -1/2\end{matrix}\right\rangle$ Transmission Coefficient

(e) $\left|\begin{matrix}100.5 & 1/2\\ 1/2 & 1/2\end{matrix}\right\rangle$ Transmission Coefficient

(f) $\left|\begin{matrix}100.5 & 1/2\\ -1/2 & -1/2\end{matrix}\right\rangle$ Reflection Coefficient

Figure 54. KHe Spin-Orbit plus Coriolis Interaction SMatrix Elements, $J = 100.5$.

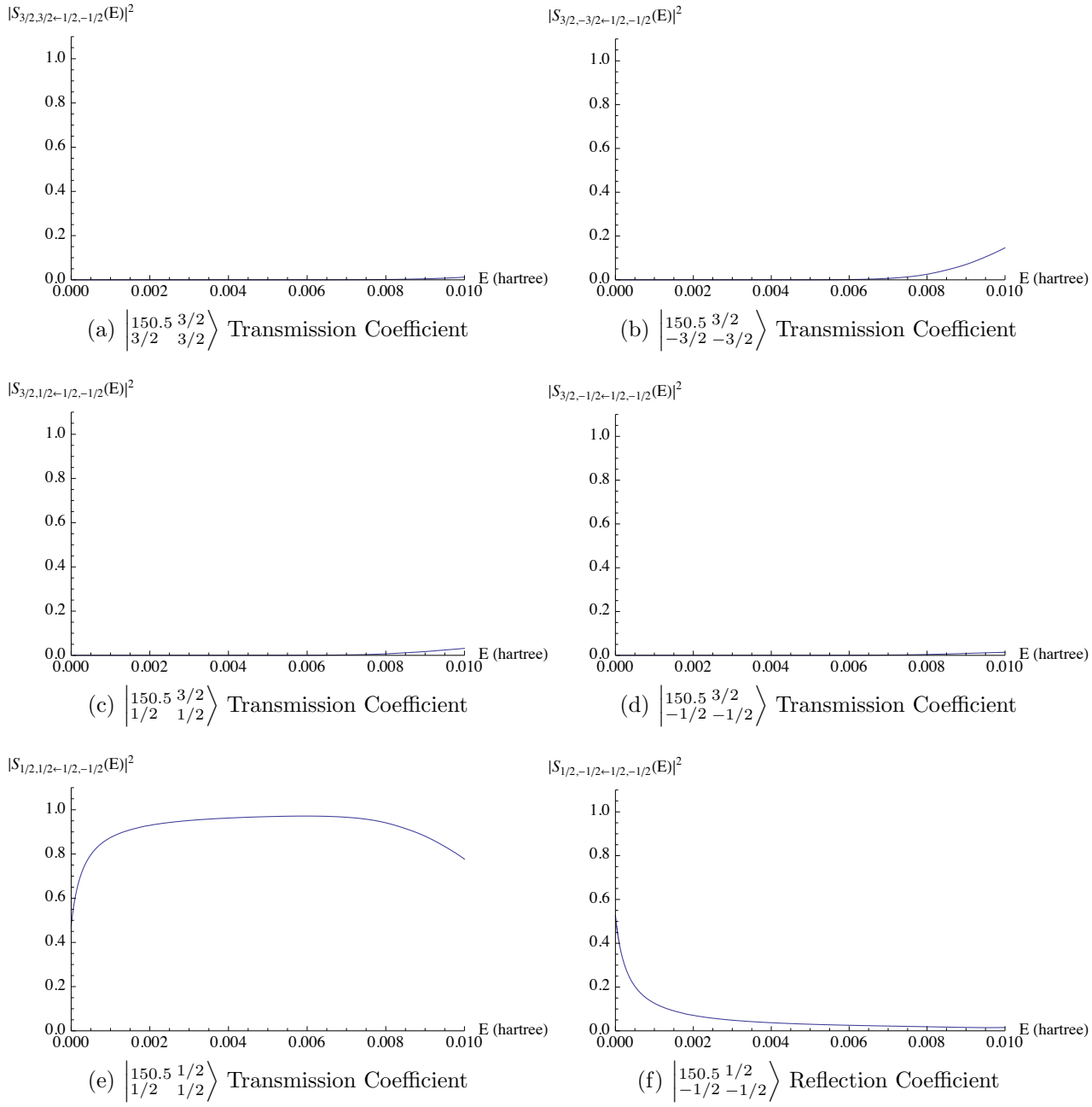

(a) $\left|\begin{matrix}150.5 & 3/2\\ 3/2 & 3/2\end{matrix}\right\rangle$ Transmission Coefficient

(b) $\left|\begin{matrix}150.5 & 3/2\\ -3/2 & -3/2\end{matrix}\right\rangle$ Transmission Coefficient

(c) $\left|\begin{matrix}150.5 & 3/2\\ 1/2 & 1/2\end{matrix}\right\rangle$ Transmission Coefficient

(d) $\left|\begin{matrix}150.5 & 3/2\\ -1/2 & -1/2\end{matrix}\right\rangle$ Transmission Coefficient

(e) $\left|\begin{matrix}150.5 & 1/2\\ 1/2 & 1/2\end{matrix}\right\rangle$ Transmission Coefficient

(f) $\left|\begin{matrix}150.5 & 1/2\\ -1/2 & -1/2\end{matrix}\right\rangle$ Reflection Coefficient

Figure 55. KHe Spin-Orbit plus Coriolis Interaction SMatrix Elements, $J = 150.5$.

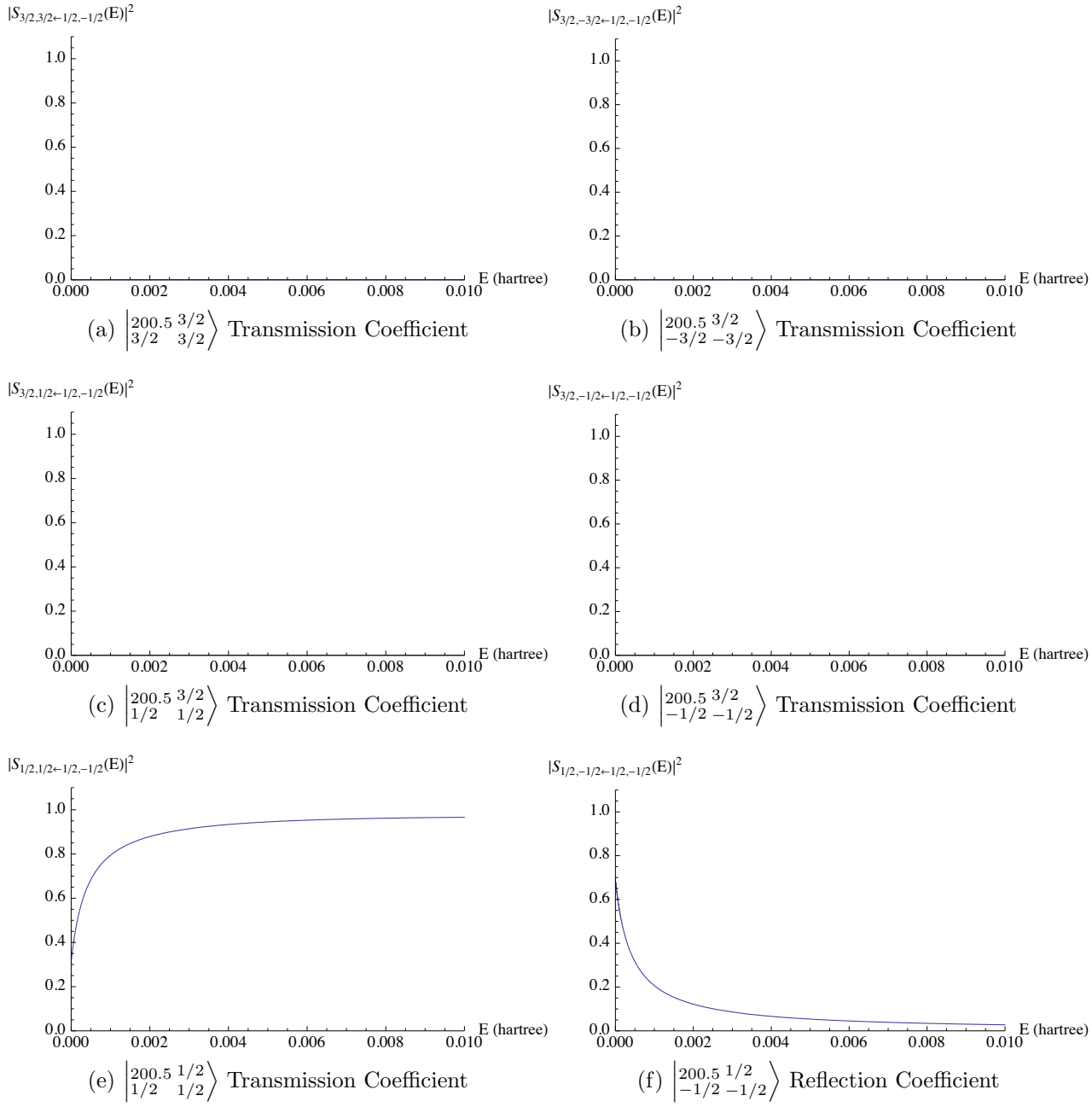

(a) $\left|\begin{smallmatrix}200.5 & 3/2\\ 3/2 & 3/2\end{smallmatrix}\right\rangle$ Transmission Coefficient

(b) $\left|\begin{smallmatrix}200.5 & 3/2\\ -3/2 & -3/2\end{smallmatrix}\right\rangle$ Transmission Coefficient

(c) $\left|\begin{smallmatrix}200.5 & 3/2\\ 1/2 & 1/2\end{smallmatrix}\right\rangle$ Transmission Coefficient

(d) $\left|\begin{smallmatrix}200.5 & 3/2\\ -1/2 & -1/2\end{smallmatrix}\right\rangle$ Transmission Coefficient

(e) $\left|\begin{smallmatrix}200.5 & 1/2\\ 1/2 & 1/2\end{smallmatrix}\right\rangle$ Transmission Coefficient

(f) $\left|\begin{smallmatrix}200.5 & 1/2\\ -1/2 & -1/2\end{smallmatrix}\right\rangle$ Reflection Coefficient

Figure 56. KHe Spin-Orbit plus Coriolis Interaction SMatrix Elements, $J = 200.5$.

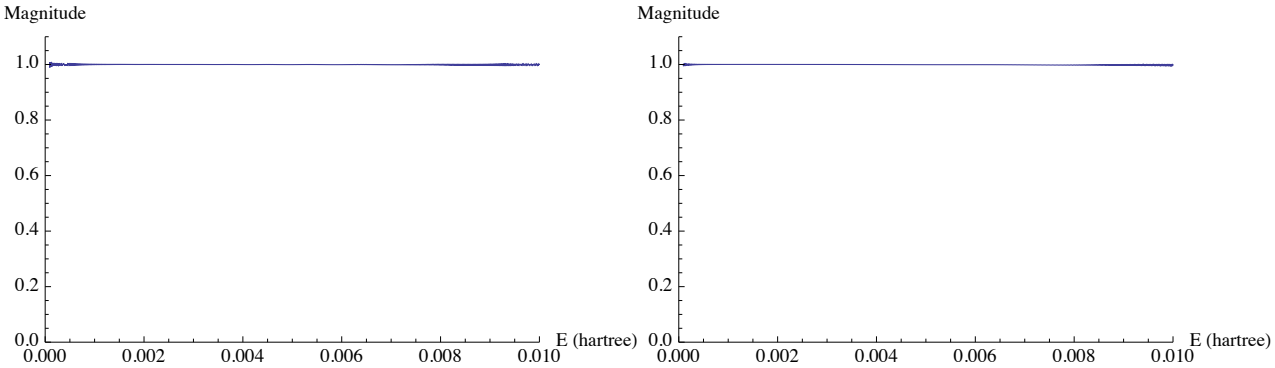

(a) $J = 50.5$

(b) $J = 100.5$

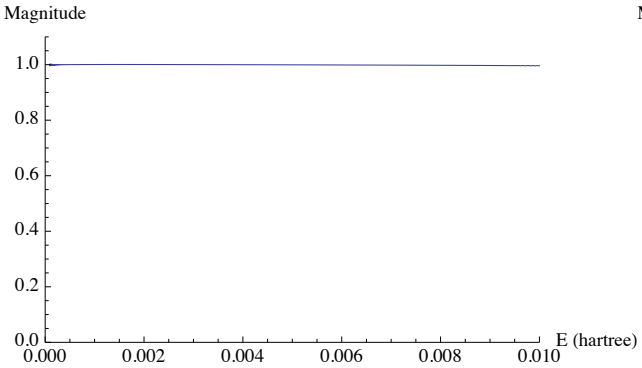

(c) $J = 150.5$

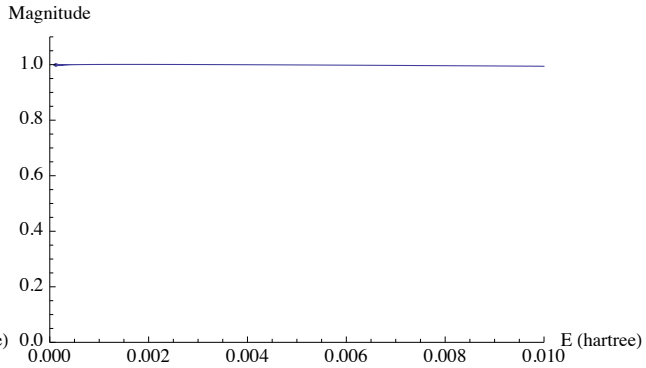

(d) $J = 200.5$

Figure 57. KHe Spin-Orbit plus Coriolis Interaction SMatrix Elements, Unitarity Check.

6.7 Cross Section Comparisons

Utilizing the Channel Packet Method we have calculated and verified $\widehat{\mathbf{S}}$-Matrix elements for both spin-orbit coupling and spin-orbit + Coriolis coupling. These $\widehat{\mathbf{S}}$-Matrix elements were summed up according to Equation (169) where we replace the quantum number L with J and sum starting at the lowest value which is $J = 0.5$:

$$\sigma(k_{j',\omega'} \leftarrow k_{j,\omega}) = \frac{\pi}{k^2_{j',\omega'}} \sum_{J=0.5}^{\infty} (2J+1)|S_J(k_{j',\omega'} \leftarrow k_{j,\omega})|^2 \tag{230}$$

In reality we do not sum to infinity, but merely up to the J value where the system stops interacting over the energy range of 0.0-0.01 Hartree. For example we plot the $\sigma(k_{3/2,3/2} \leftarrow k_{1/2,1/2})$ cross section as a function energy for six different values of J.

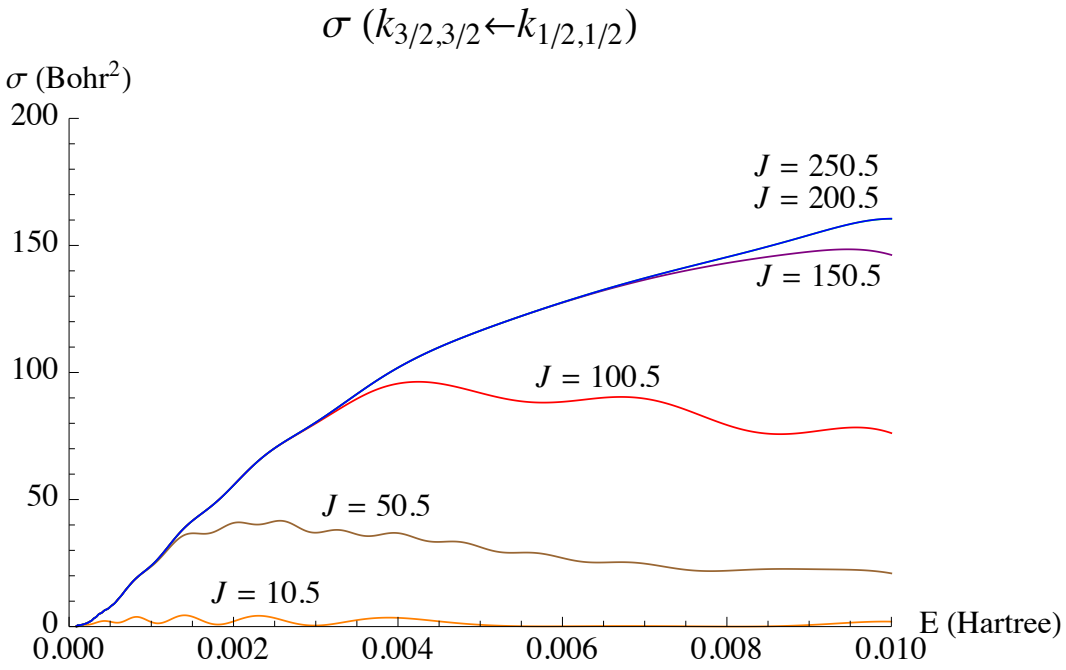

Figure 58. KHe $\sigma(k_{3/2,1/2} \leftarrow k_{1/2,1/2})$ for $J = 10.5$, $J = 50.5$, $J = 100.5$, $J = 150.5$, $J = 200.5$, and $J = 250.5$.

Looking at Figure 58, for a particular energy as J increases the cross section converges

to a maximum value. As explained before the centrifugal potential shields the interaction region. If the collision energy isn't high enough to over come the centrifugal barrier the system will not interact via the electronic and magnetic interaction potentials. For example if one were only interested in the cross section between system energies of 0.0-0.001 Hartree then the max value of J needed would be approximately 50.5. All other $\widehat{\mathbf{S}}$-Matrix elements of higher J would contribute zero to the sum.

We want to calculate the collision cross section from the ${}^2P_{1/2}$ asymptotic state to the ${}^2P_{3/2}$ asymptotic state. The two-fold degenerate Born-Oppenheimer states that correspond to the ${}^2P_{1/2}$ asymptotic state are the $\left|{}^{J\ \ 1/2}_{\pm 1/2\ \pm 1/2}\right\rangle$ states. The four-fold degenerate Born-Oppenheimer states that correspond to the ${}^2P_{3/2}$ asymptotic state are the $\left|{}^{J\ \ 3/2}_{\pm 3/2\ \pm 3/2}\right\rangle$ and the $\left|{}^{J\ \ 3/2}_{\pm 1/2\ \pm 1/2}\right\rangle$ states.

To calculate the $\sigma_{{}^2P_{3/2}\leftarrow{}^2P_{1/2}}$ cross section we have to combine these Born-Oppenheimer state to state cross sections in some fashion. In general if the fine structure population distribution of the ${}^2P_{1/2}$ is assumed to be some probability $\mathcal{P}(1/2,\omega)$ we can calculate the asymptotic cross section as:

$$\sigma_{{}^2P_{3/2}\leftarrow{}^2P_{1/2}}(E) = \sum_{\omega=-1/2}^{1/2} \mathcal{P}(1/2,\omega)[\sigma(k_{3/2,-3/2} \leftarrow k_{1/2,\omega}) + \sigma(k_{3/2,-1/2} \leftarrow k_{1/2,\omega}) + \sigma(k_{3/2,3/2} \leftarrow k_{1/2,\omega}) + \sigma(k_{3/2,1/2} \leftarrow k_{1/2,\omega})] \tag{231}$$

In the absence of any magnetic field we can reasonably assume that the ground state population contains an equal number of members in the $\left|{}^{J\ \ 1/2}_{1/2\ 1/2}\right\rangle$ and $\left|{}^{J\ \ 1/2}_{-1/2\ -1/2}\right\rangle$ states. With this is mind we set $\mathcal{P}(1/2,1/2) = \mathcal{P}(1/2,-1/2) = 1/2$.

For the spin-orbit coupling calculation we calculated the following state to state

cross sections:

$$\sigma(k_{3/2,-1/2} \leftarrow k_{1/2,-1/2}) = \frac{\pi}{k^2_{3/2,-1/2}} \sum_{J=0.5}^{250.5} (2J+1)|S_J(k_{3/2,-1/2} \leftarrow k_{1/2,-1/2})|^2 \quad (232)$$

$$\sigma(k_{3/2,1/2} \leftarrow k_{1/2,1/2}) = \frac{\pi}{k^2_{3/2,1/2}} \sum_{J=0.5}^{250.5} (2J+1)|S_J(k_{3/2,1/2} \leftarrow k_{1/2,1/2})|^2 \quad (233)$$

There was no coupling to the $\left|{}^{J}_{\pm 3/2}\,{}^{3/2}_{\pm 3/2}\right\rangle$ states. When these Born-Oppenheimer state to state cross sections are inserted in to Equation (231) we arrive at the collisional cross section to scatter from ${}^2P_{1/2}$ to ${}^2P_{3/2}$ for spin-orbit coupling only. This cross section is plotted in Figures 59 and 60.

Using the same equations we calculate the KHe collisional cross section from ${}^2P_{1/2}$ to ${}^2P_{3/2}$ for spin-orbit and Coriolis coupling. In this case, since the $\left|{}^{J}_{\pm 3/2}\,{}^{3/2}_{\pm 3/2}\right\rangle$ states are now coupled, we sum up eight Born-Oppenheimer state to state cross sections as opposed to just four in the spin-orbit coupling only case. The results are plotted in Figures 61 and 62 along with the spin-orbit only coupling for comparison.

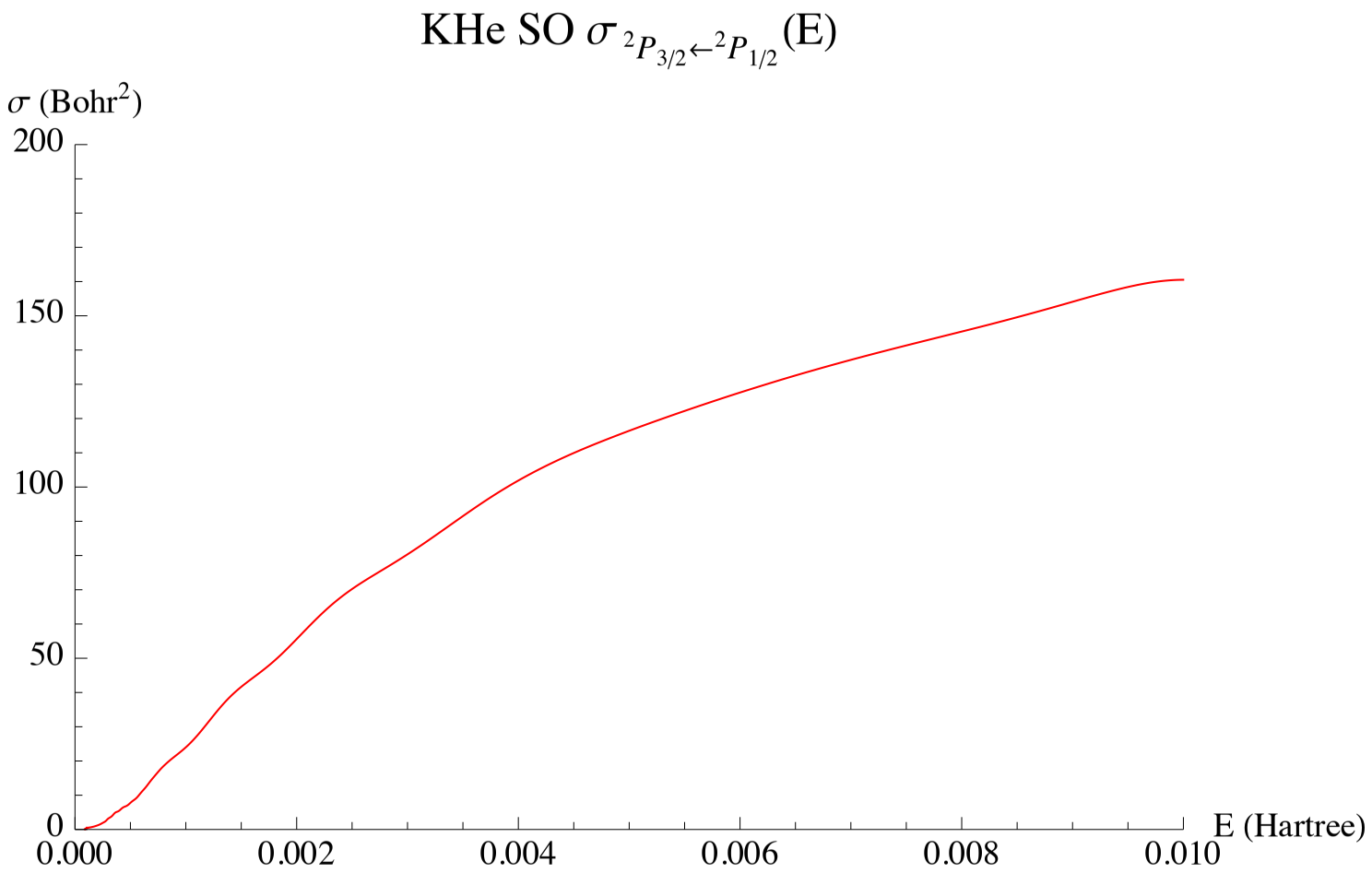

Figure 59. KHe Spin-Orbit $^2P_{1/2}$ to $^2P_{3/2}$ Cross Section.

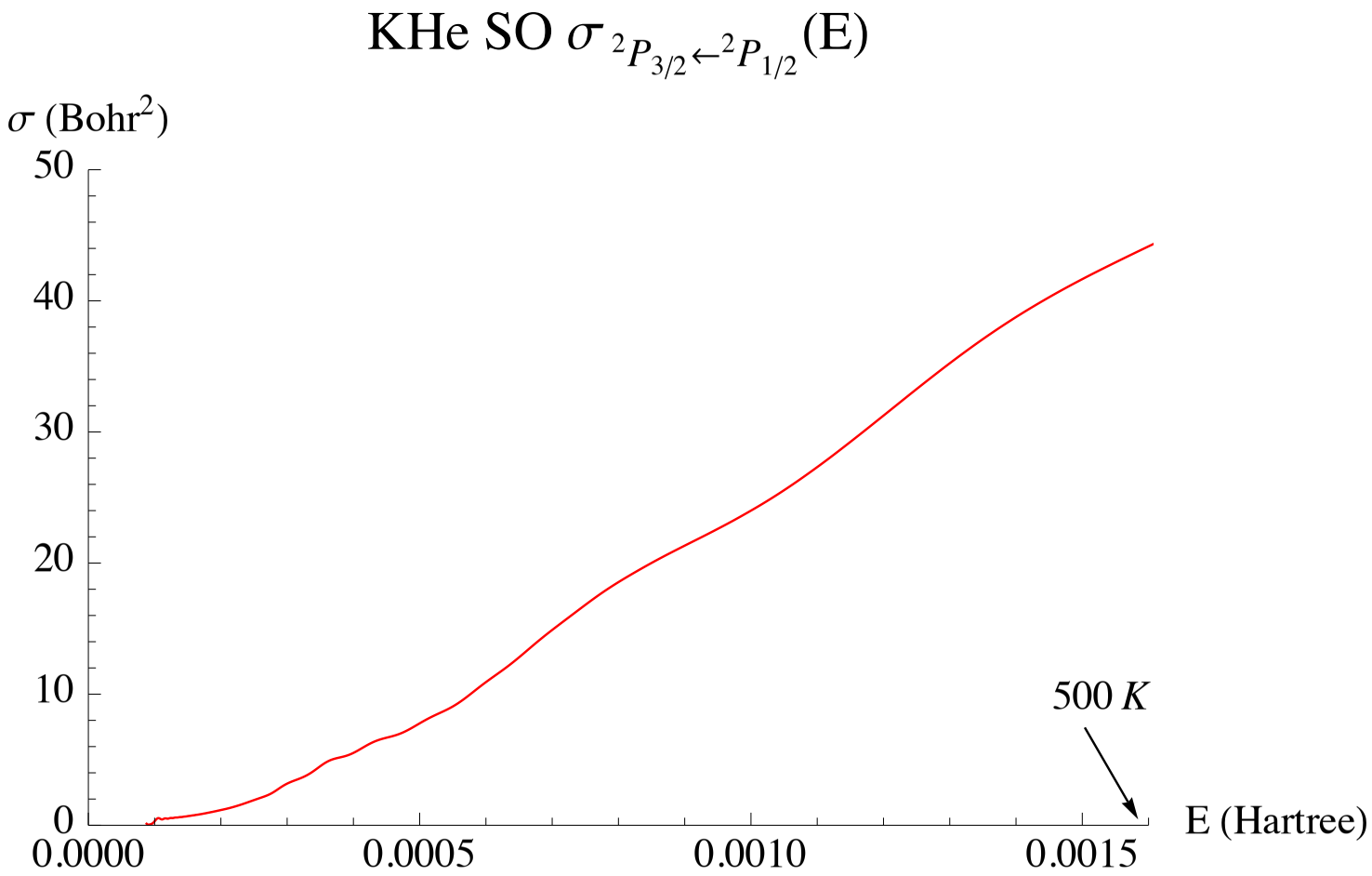

Figure 60. KHe Spin-Orbit $^2P_{1/2}$ to $^2P_{3/2}$ Cross Section 0-500K.

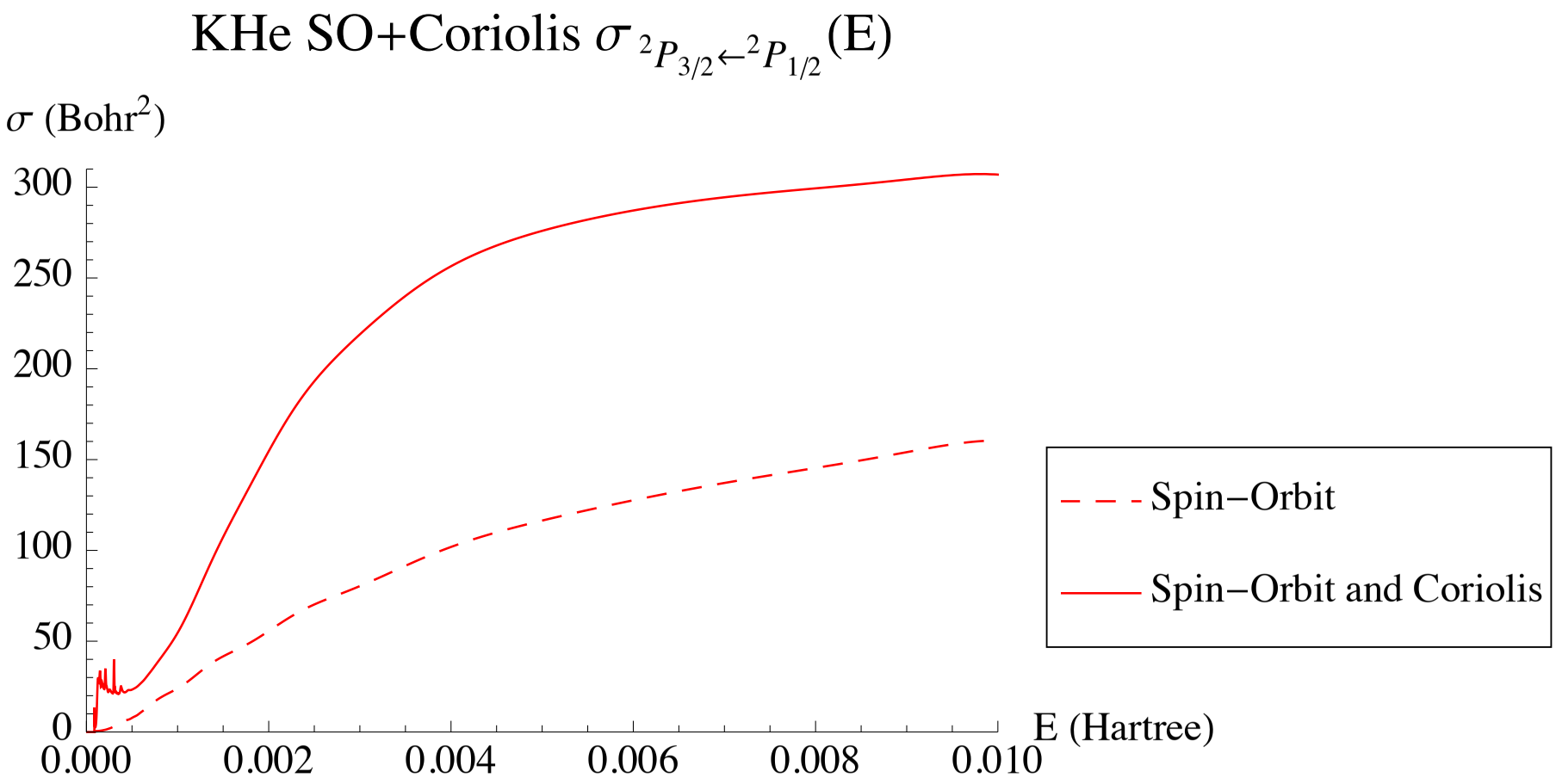

Figure 61. KHe Spin-Orbit + Coriolis $^2P_{1/2}$ to $^2P_{3/2}$ Cross Section.

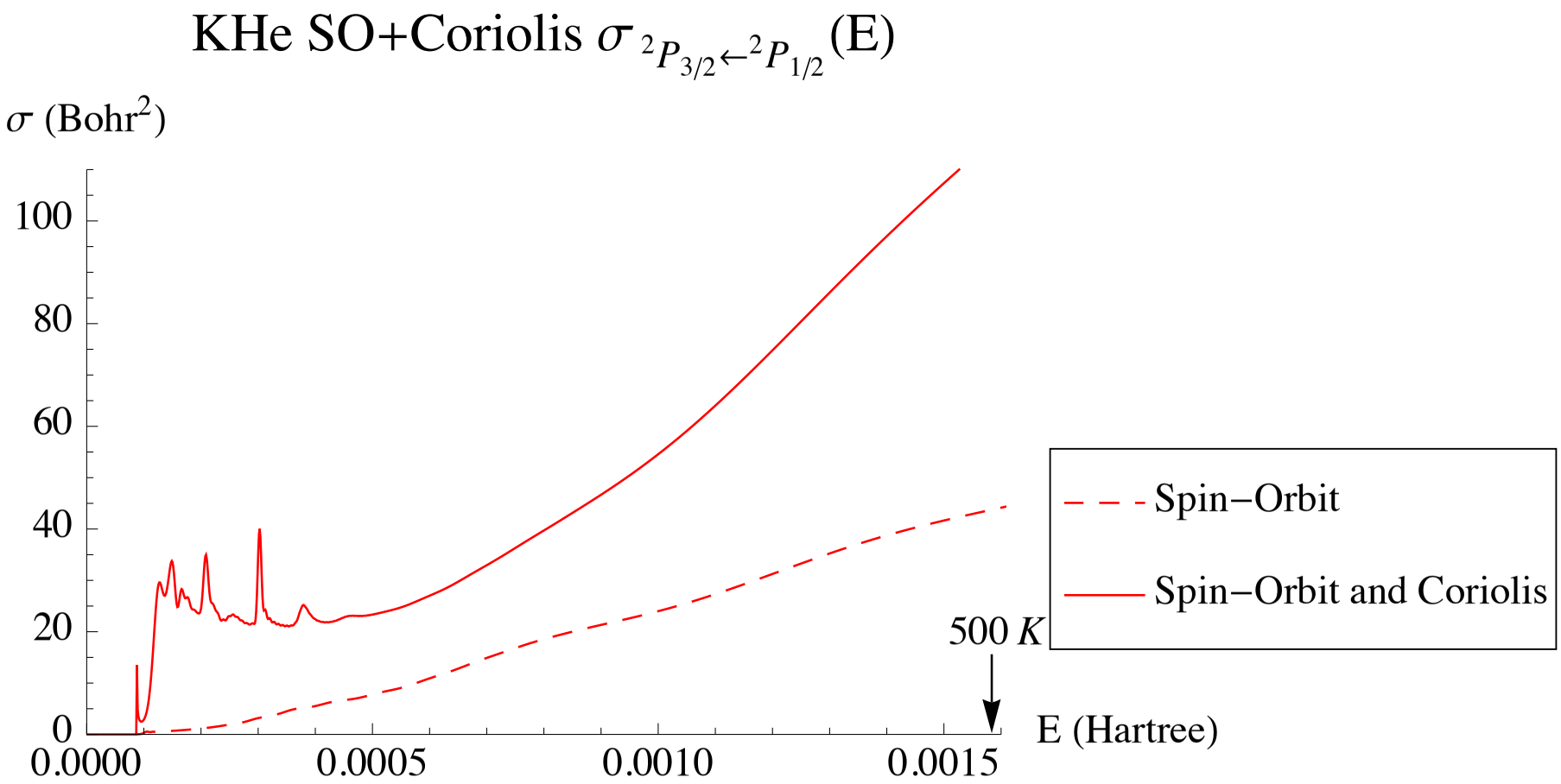

Figure 62. KHe Spin-Orbit + Coriolis $^2P_{1/2}$ to $^2P_{3/2}$ Cross Section 0-500K.

6.8 Comparison to Experiment

Experimentally one does not measure the theoretical cross sections calculated in the previous section. Rather what is observed is the rate of population among the spin-orbit split states. This rate, $Z(T)$, is proportional to the thermally averaged cross section, $Q(T)$, given by the equation:

$$Q(T) = \frac{Z(T)}{\overline{u}} \tag{234}$$

where $\overline{u}$ is the average relative speed of the colliding atoms. The rate at which population is transferred is given by[27]:

$$Z(T) = 4\pi \left(\frac{\mu}{2\pi k_b T}\right)^{3/2} \int_0^\infty u^3 e^{-\frac{\mu u^2}{2k_b T}} \sigma(u) du \tag{235}$$

where k_b is the familiar Boltzmann constant and $\sigma(u)$ is the theoretical cross section as a function of speed. This transition rate can be recast in terms of translational energy, E_T, by changing variables as $E_T = mu^2/2$ and $du = dE_T/(2\mu E_T)^{1/2}$:

$$Z(T) = \left(\frac{2}{k_b T}\right)^{3/2} \left(\frac{1}{\mu\pi}\right)^{1/2} \int_0^\infty e^{-\frac{E_T}{k_b T}} \sigma(E) E_T dE_T \tag{236}$$

where now $\sigma(E)$ is the theoretical cross section calculated in the previous section. The average relative speed is simply evaluated using the Maxwell-Boltzmann distribution, $f_{mb}(u)$, and is

$$\overline{u} = \int_0^\infty u f_{mb}(u) du = \left(\frac{8k_b T}{\pi\mu}\right)^{1/2}. \tag{237}$$

Combining these equations the following integral must be evaluated to compare the theoretical cross section to the experimentally determined thermal averaged cross

section:

$$Q(T) = (k_b T)^{-2} \int_0^\infty (E - E_{int}) e^{-\frac{(E-E_{int})}{k_b T}} \sigma(E) dE. \tag{238}$$

where we have replaced E_T, the translational energy, with $E - E_{int}$, the total energy minus the internal energy. This takes in to account that at a given temperature the colliding species will not all have a singular energy, but rather a distribution of energies given by the Maxwell-Boltzmann distribution.

The standard procedure for measuring the transition rates, $Z(T)$, is to excite a cell of alkali metal to its ^2P_j state with one "D Line" of the resonance doublet and to detect fluorescence of the other "D Line" caused by collisions with a foreign species[19]. This is sometimes called sensitized fluorescence. We compare the predicted results of the previous section to the experimental results of Ciurylo and Krause[11], Boggy and Franz[9], Krause[25], and Jordan and Franken[22] at various cell temperatures. Franken and Jordan measured $Q(^2P_{1/2} \leftarrow {}^2P_{3/2})$ so we used detailed balance to compute the $Q(^2P_{3/2} \leftarrow {}^2P_{1/2})$ result for comparison.

The thermally averaged predicted cross sections are compared in Table 13. Figure 66 compares the predicted thermally averaged cross sections to the experimental predictions for both spin-orbit and spin-orbit plus Coriolis coupling as a function of temperature from $T = 0 - 400K$ for KHe.

Table 11. KHe $Q(^2P_{3/2} \leftarrow^2 P_{1/2})$ Cross Section: Experiment vs Prediction. Units are in $Bohr^2$. Values with * were converted using detailed balance.

$Q(^2P_{3/2} \leftarrow^2 P_{1/2})$	KHe	Temp. (K)
Ciurylo and Krause[11]	93.92 ± 13.93	342.00
Predicted (SO)	54.36	
Predicted (SO+Coriolis)	140.39	
Boggy and Franz[9]	103.34 ± 33.92	380.15
Predicted (SO)	59.03	
Predicted (SO+Coriolis)	151.85	
Jordan and Franken[22]	$293.91 \pm 32.28^*$	333.15
Predicted (SO)	53.15	
Predicted (SO+Coriolis)	137.50	

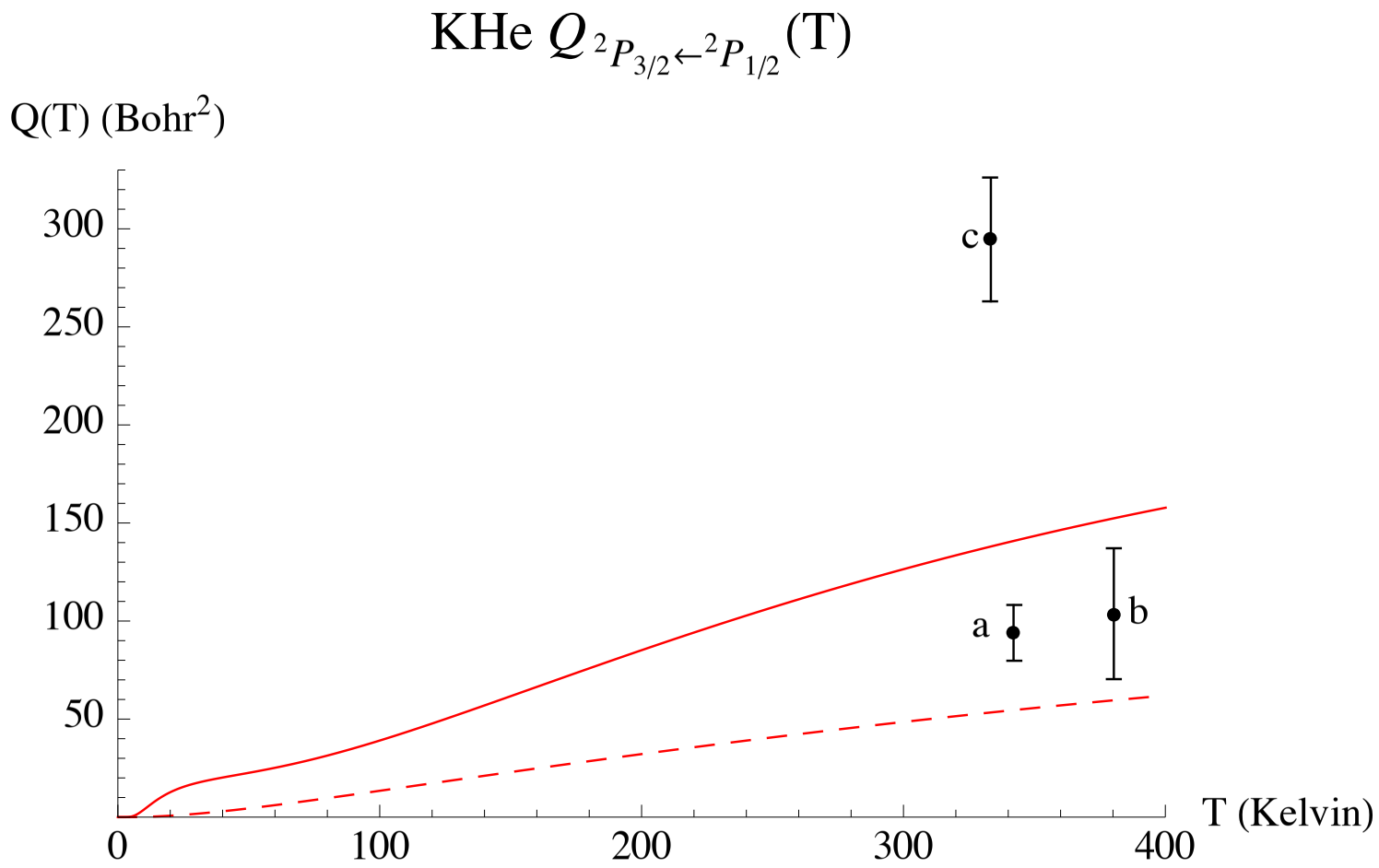

Figure 63. KHe Thermally Averaged Cross Sections from $0-400K$. The dashed line is spin-orbit coupling only and the solid line is spin-orbit plus Coriolis coupling. a) Ciurylo and Krause. b) Boggy and Franz. c) Jordan and Franken.

6.9 Summary

The theoretical and computational tools developed in this dissertation have been applied to the Alkali Metal - Noble Gas system. Starting with the SOCI surfaces computed by Blank we were able to calculate the non-SOCI split surfaces and spin-orbit parameter. These are the necessary inputs when representing the close coupled equations in the Born-Oppenheimer basis. Also using this method we discovered the transformation that related the Born-Oppenheimer basis to the spin-orbit molecular basis. What resulted was a picture in which the spin-orbit molecular basis in the interaction region rotates as a function of R relative to the Born-Oppenheimer basis. As R increases these states become asymptotically the same. This actually has implications that determine what SOCI surfaces are Coriolis coupled. This will be discussed in the final chapter.

The Moller states had to be computed separately by numerical iteration rather than analytically like in the square well and two state examples. This was because the centrifugal potential is a long range potential that falls off as R^{-2}. However since the potential was small outside the interaction region a big time step was utilized and the split operator approximation remained valid. On average it took about $2-3$ minutes to calculate one Moller state. Once the Moller states were calculated they were simply stored and used for both the spin-orbit and spin-orbit plus Coriolis interaction calculations.

The first interaction calculation was executed by enabling the spin-orbit couplings and disabling the Born-Oppenheimer radial derivative and Coriolis coupling. What resulted was not unlike the two level system example. We presented detailed figures of how the wave function evolved for $J = 0.5$ as well as a sample of $\widehat{\mathbf{S}}$-Matrix elements up through $J = 250.5$. Clearly, all the calculations converged as evident by the unitarity check on $\widehat{\mathbf{S}}$.

Second, we enabled the Born-Oppenheimer radial derivative coupling to the spin-orbit calculation.What resulted was very surprising, We discovered that the spin-orbit radial derivative coupling, as computed by Belcher, in the spin-orbit molecular basis was in fact the spin-orbit coupling in the Born-Oppenheimer basis. This implies that for the diatomic case that Born-Oppenheimer radial derivative coupling is negligible. This was not expected at the beginning of this study. It is not known at this time if this applies to systems with greater than three colliding bodies.

Finally, Coriolis coupling was enabled and the Hamiltonian became a 6x6 coupled matrix. The computational tools were modified for six surfaces and the results presented for wave packet evolution and another representative sampling of $\widehat{\mathbf{S}}$-Matrix elements at various J. Once again the calculations were shown to converge via the unitary property of $\widehat{\mathbf{S}}$.

To compare the theoretical cross sections, $\sigma(E)$, to the experimentally measured cross sections, $Q(T)$, we had to employ Maxwell-Boltzmann theory to relate the $\sigma(E)$ to the $Q(T)$. The state to state cross section were summed up accordingly and we compared the theoretical $Q(T)$ to various experimentally observed $Q(T)$. A final figure was presented of the KHe $P_{3/2} \leftarrow P_{1/2}$ $Q(T)$ as a function of temperature between 0 and $400K$.

The results and comparisons for the 8 other collision pairs are presented in the next chapter.

VII. Cross Section Results

7.1 Introduction

This chapter presents the theoretical cross sections for all collision partners studied from $0.00 - 0.01$ Hartree and from $0.00 - 0.0015$ Hartree. Also presented are the thermally averaged cross sections from 0 up to $500K$. The comparisons to experimental data are annotated tabularly and graphically. Notable features of each result will be described in each subsection of this chapter and discussion of the results will follow in the next chapter.

Experimental data [6, 9, 11, 19, 22, 25] were taken using a technique known as sensitized fluorescence. A cell containing alkali metal was continuously pumped optically, by a laser or lamp, to either the $P_{3/2}$ or $P_{1/2}$ state until a dynamic equilibrium is established. The dynamic processes of this equilibrium are the optical excitation/relaxation, the spontaneous decay, and the collisional fine structure mixing. These processes are expressed in a set of rate equations and are solved for in terms of the intensity ratios of the fluoresced light from the $P_{3/2}$ and $P_{1/2}$ states. Once the rate, Z, is experimentally determined through the fluorescence ratios, the thermally averaged cross section, Q, is calculated as

$$Z(T_0) = Q(T_0)\overline{u}(T_0) \tag{239}$$

where $\overline{u}$ is the average relative speed of the colliding partners and T_0 is the temperature of the cell.

All of the published experiments took special care to ensure that the alkali samples were pure and that radiation trapping was not a factor. Radiation trapping occurs when there is an abundance of alkali metal present in the cell or said another way

when the vapor pressure of the alkali metal is too high. The light fluoresced from one reaction is prematurely reabsorbed or trapped by another alkali before it can escape the cell to be measured. This phenomenon can lead to experimentally determined cross sections that are too high. By lowering the alkali vapor pressure radiation trapping ceases to be a factor.

Published data for the heavier alkalis are sparse. This most likely has to do with the increase in difficulty of measuring decreasing smaller cross sections. As we will see the the cross section decreases by orders of magnitude as the alkali partner changes from potassium, rubidium, and then cesium.

Lastly, the cross sections observed by Gallagher[19] were fashioned into a parameterized curve. The functional form of the fit and the parameters were then published for the rubidium and cesium collisions. The range off applicability was stated to be between $300 - 900K$. Where applicable these fits are plotted against the theoretical predictions.

7.2 KHe

The theoretical results for KHe show that the addition of Coriolis coupling at minimum doubles the cross section as compared to spin-orbit only. Also notice at low energies how the cross section exhibits sharp peaks at certain energies.

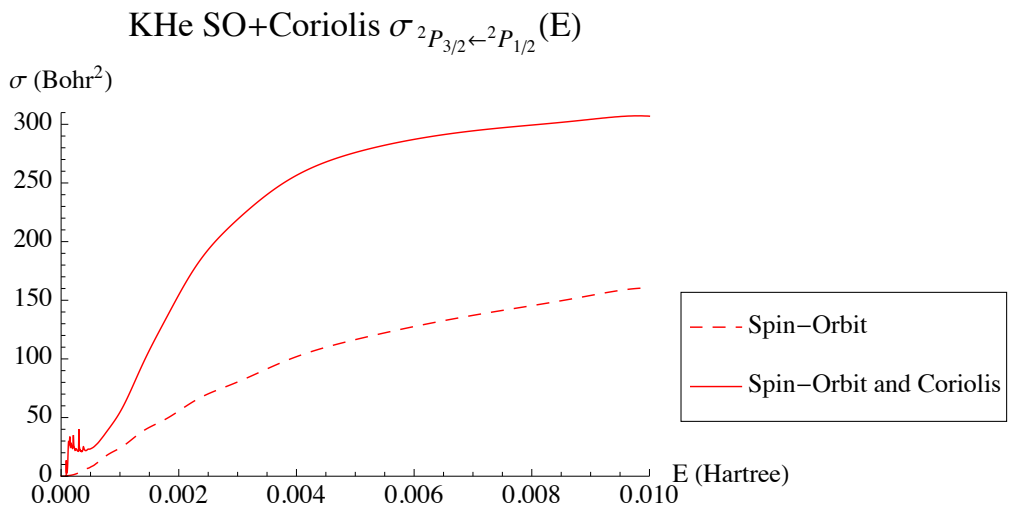

Figure 64. KHe Spin-Orbit + Coriolis $^2P_{1/2}$ to $^2P_{3/2}$ Cross Section.

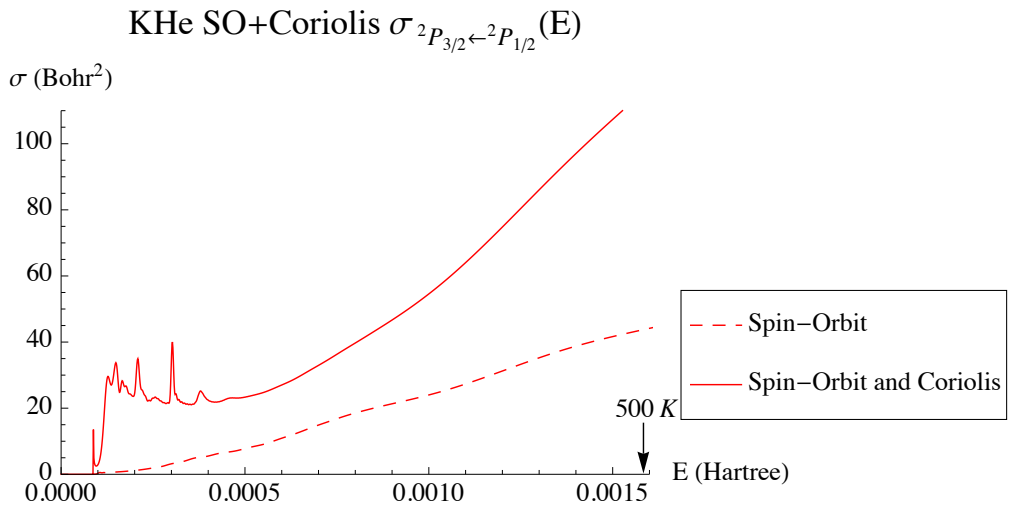

Figure 65. KHe Spin-Orbit + Coriolis $^2P_{1/2}$ to $^2P_{3/2}$ Cross Section 0-500K.

Table 12. KHe $Q(^2P_{3/2} \leftarrow^2 P_{1/2})$ Cross Section: Experiment vs Prediction. Units are in $Bohr^2$. Values with * were converted using detailed balance.

$Q(^2P_{3/2} \leftarrow^2 P_{1/2})$	KHe	Temp. (K)
Ciurylo and Krause[11]	93.92 ± 13.93	342.00
Predicted (SO)	54.36	
Predicted (SO+Coriolis)	140.39	
Boggy and Franz[9]	103.34 ± 33.92	380.15
Predicted (SO)	59.03	
Predicted (SO+Coriolis)	151.85	
Jordan and Franken[22]	$293.91 \pm 32.28^*$	333.15
Predicted (SO)	53.15	
Predicted (SO+Coriolis)	137.50	

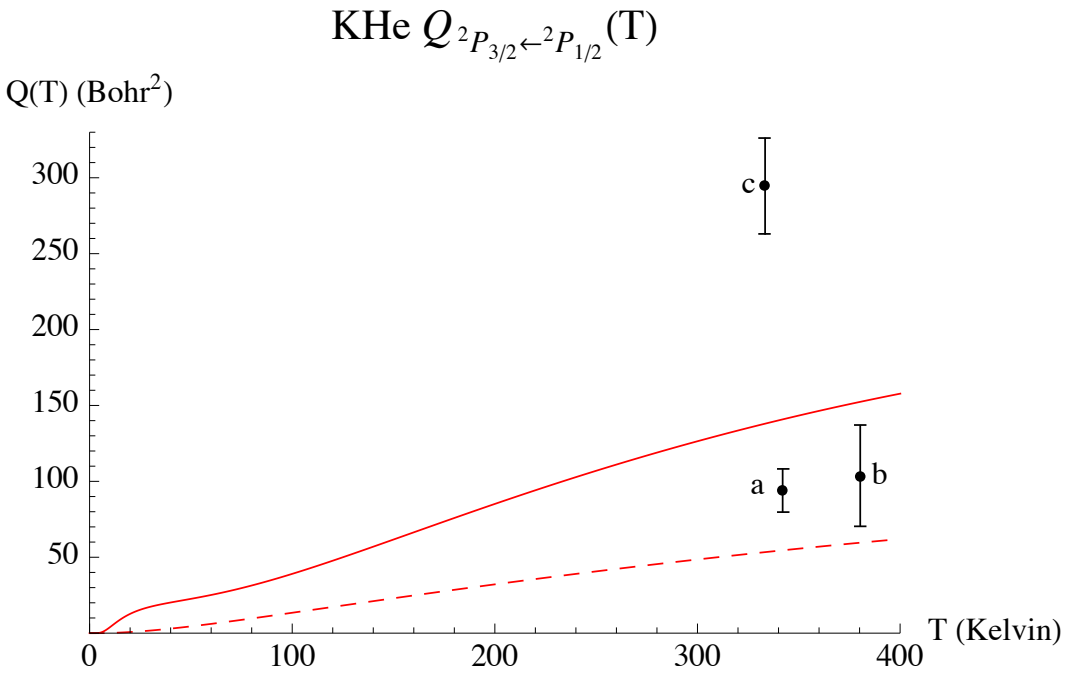

Figure 66. KHe Thermally Averaged Cross Sections from $0 - 400K$. The dashed line is spin-orbit coupling only and the solid line is spin-orbit plus Coriolis coupling. a) Ciurylo and Krause. b) Boggy and Franz. c) Franken and Jordan.

Compared to the thermally averaged data the theoretical prediction is slightly higher than that of Ciurylo and Krause and Boggy and Franz, but does trend similarly

with respect to temperature. In both of these experiments it was reported that detailed balance was achieved and that radiation trapping minimized. This led the experimenters to be very confident in their results. The third observation, done by Franken and Jordan, is suspect because the technique used, multi-line pumping via a lamp, is not as sensitive as single line pumping via a laser. The same technique was used to measure KNe and KAr cross sections and show a similarly large cross section compared to Ciurylo and Krause and Boggy and Franz.

7.3 KNe

The theoretical results for KNe show a similar increase of cross section due to the addition of Coriolis coupling, but the doubling of spin-orbit plus Coriolis over spin-orbit only begins at a higher energy. Also notice at the higher end of the energy range, starting at about 0.006 Bohr slight oscillatory-like behavior is observed. The same sharp peaks exist at the low end of the energy range, but are more pronounced than the KHe case.

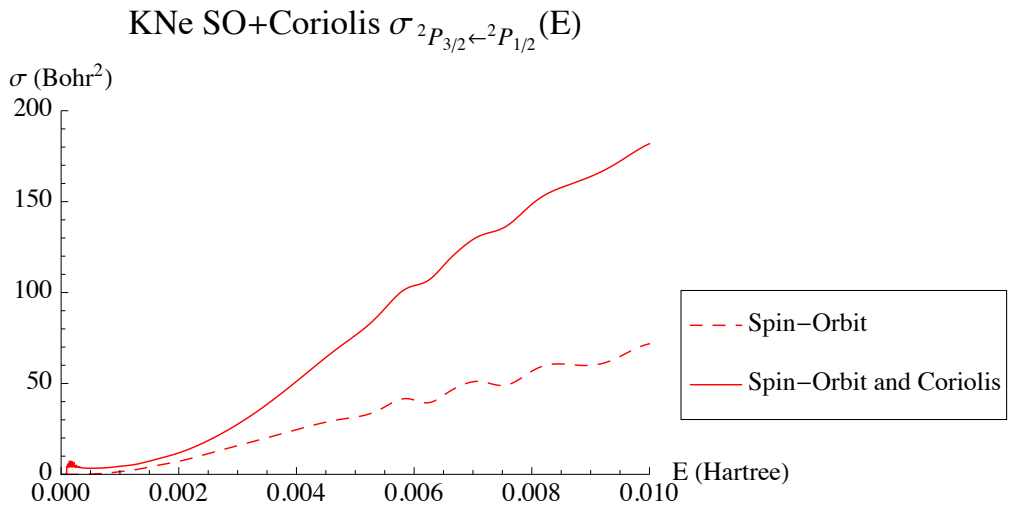

Figure 67. KNe Spin-Orbit + Coriolis $^2P_{1/2}$ to $^2P_{3/2}$ Cross Section.

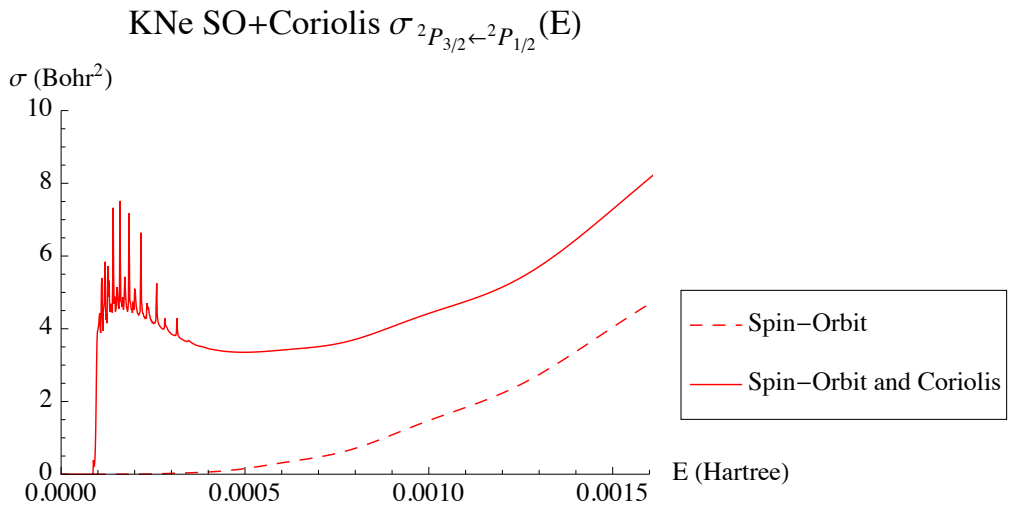

Figure 68. KNe Spin-Orbit + Coriolis $^2P_{1/2}$ to $^2P_{3/2}$ Cross Section 0-500K.

Table 13. KNe $Q(^2P_{3/2} \leftarrow^2 P_{1/2})$ Cross Section: Experiment vs Prediction. Units are in $Bohr^2$. Values with * were converted using detailed balance.

$Q(^2P_{3/2} \leftarrow^2 P_{1/2})$	KNe	Temp. (K)
Ciurylo and Krause[11]	22.85 ± 3.57	342.00
Predicted (SO)	10.05	
Predicted (SO+Coriolis)	21.19	
Boggy and Franz[9]	33.57 ± 14.28	380.15
Predicted (SO)	11.69	
Predicted (SO+Coriolis)	25.17	
Jordan and Franken[22]	$77.92 \pm 6.64^*$	333.15
Predicted (SO)	9.55	
Predicted (SO+Coriolis)	20.27	

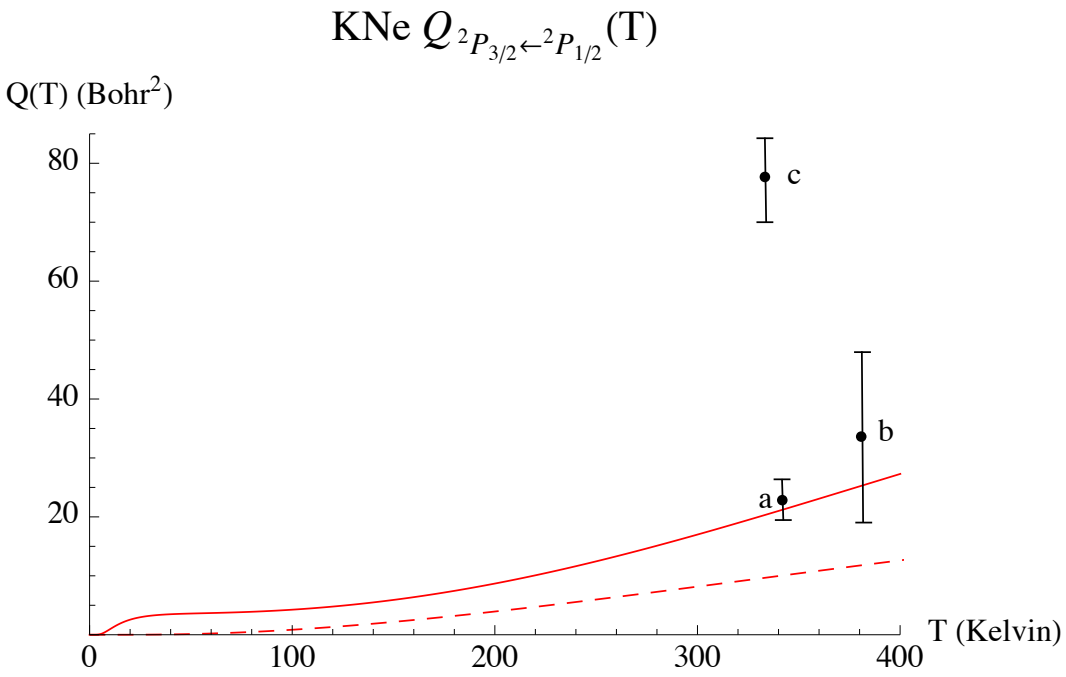

Figure 69. KNe Thermally Averaged Cross Sections from $0-400K$. The dashed line is spin-orbit coupling only and the solid line is spin-orbit plus Coriolis coupling. a) Ciurylo and Krause. b) Boggy and Franz. c) Jordan and Franken.

The KNe prediction shows within experimental error good agreement with the observed cross sections of Ciurylo and Krause and Boggy and Franz. Both experiments were confident in their result based on their detailed balance analysis and radiation trapping mitigation.

7.4 KAr

KAr shows many of the same features as the KHe and KNe theoretical cross sections. Note however that the dramatic increase of spin-orbit plus Coriolis over spin-orbit only begins at higher energies as the noble gas partner increases in mass. For He the effect is almost immediate. For Ne and Ar this increase does not begin until roughly 0.003 Hartree and 0.005 Hartree respectively.

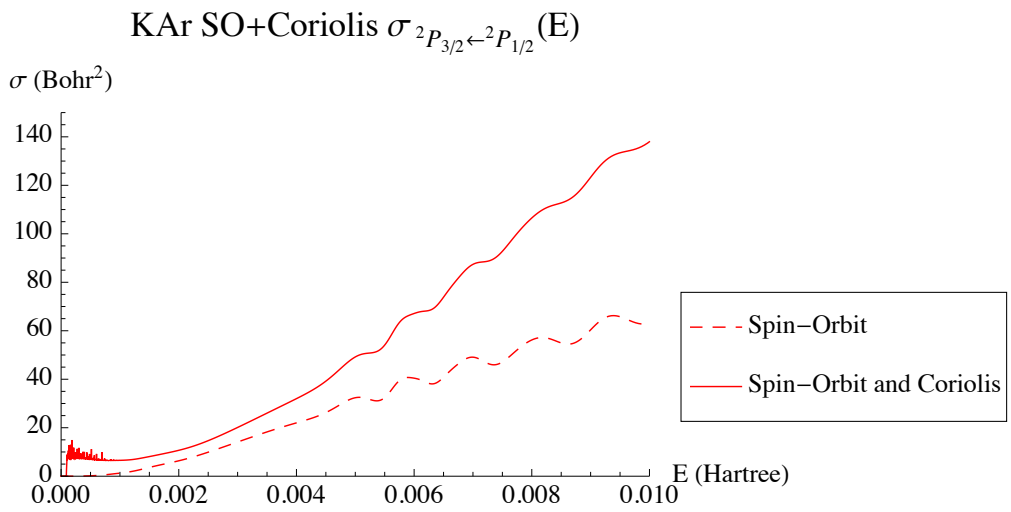

Figure 70. KAr Spin-Orbit + Coriolis $^2P_{1/2}$ to $^2P_{3/2}$ Cross Section.

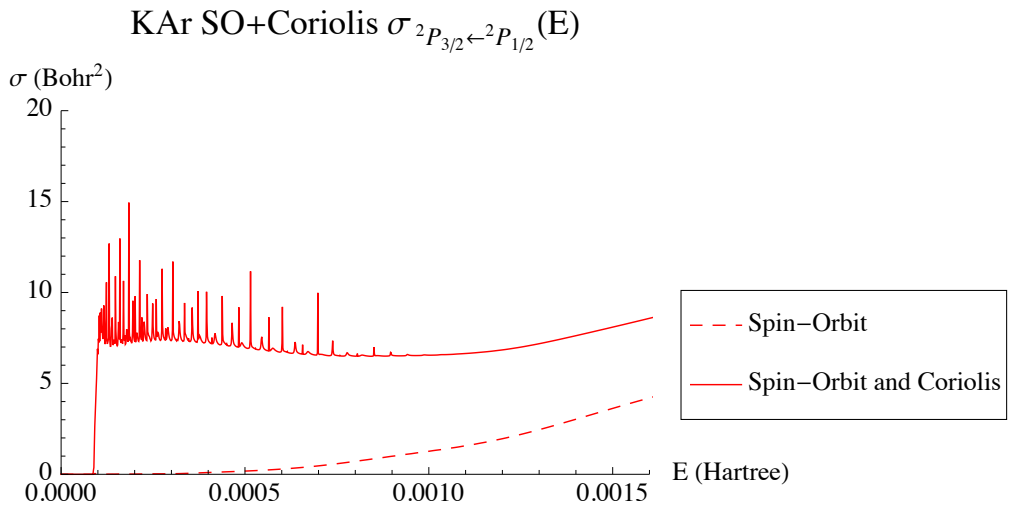

Figure 71. KAr Spin-Orbit + Coriolis $^2P_{1/2}$ to $^2P_{3/2}$ Cross Section 0-500K.

Table 14. KAr $Q(^2P_{3/2} \leftarrow^2 P_{1/2})$ Cross Section: Experiment vs Prediction. Units are in $Bohr^2$. Values with * were converted using detailed balance.

$Q(^2P_{3/2} \leftarrow^2 P_{1/2})$	KAr	Temp. (K)
Ciurylo and Krause[11]	57.14 ± 8.57	342.00
Predicted (SO)	9.21	
Predicted (SO+Coriolis)	16.54	
Jordan and Franken[22]	$189.27 \pm 17.26^*$	333.15
Predicted (SO)	8.84	
Predicted (SO+Coriolis)	16.05	

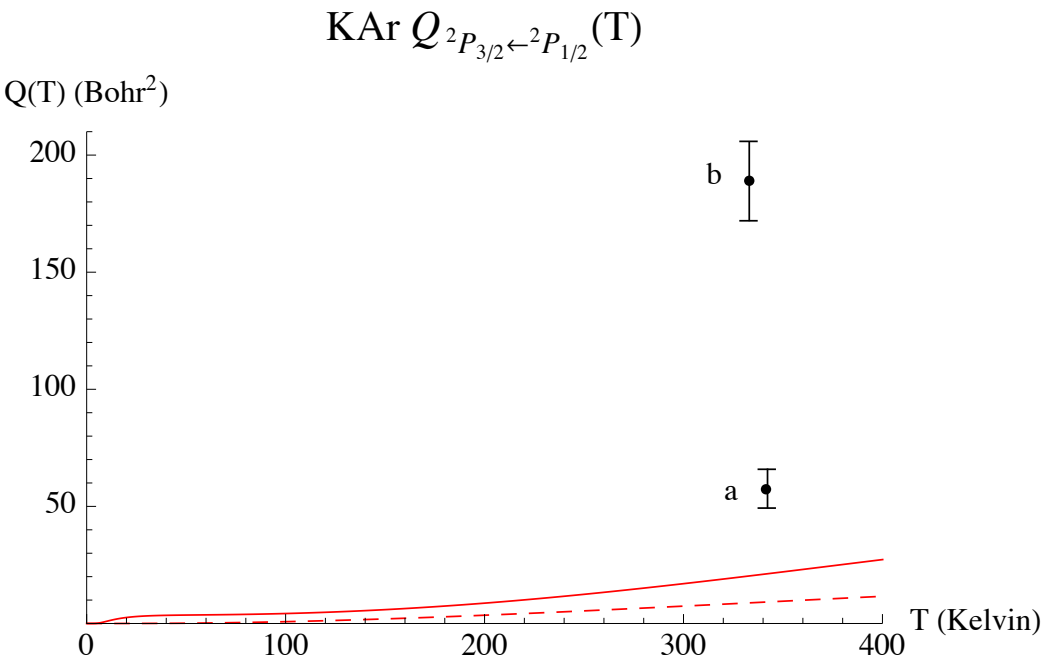

Figure 72. KAr Thermally Averaged Cross Sections from $0 - 400K$. The dashed line is spin-orbit coupling only and the solid line is spin-orbit plus Coriolis coupling. a) Ciurylo and Krause. b) Jordan and Franken.

The KAr prediction falls below the experimental observation of Ciurylo and Krause. They once again reported agreement with detailed balance and that radiation trapping was mitigated. Off all comparisons to experiment this prediction is the worse.

The KAr surface appears to be at fault in this calculation. The well depth of the ground state seems to be to low compared to the trends exhibited by the other

surfaces. Although we do not use the ground state, the same basis functions and algorithms were used to calculate the excited state. It is not known at the moment how this error may effect the excited state surfaces, and in turn, the cross section.

7.5 RbHe

First observe that for RbHe the magnitude of the cross section has decreased dramatically compared to the Potassium series of collisions. The addition of Coriolis coupling increases the cross section at about the same rate as spin-orbit only. This is different from what was seen in the Potassium series of collisions. The low energy sharp peaks also exist for RbHe.

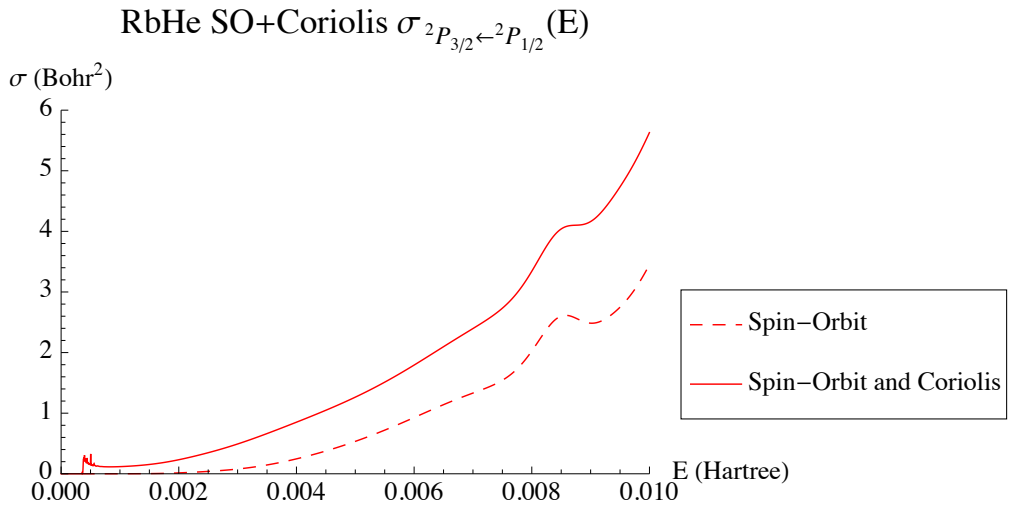

Figure 73. RbHe Spin-Orbit + Coriolis $^2P_{1/2}$ to $^2P_{3/2}$ Cross Section.

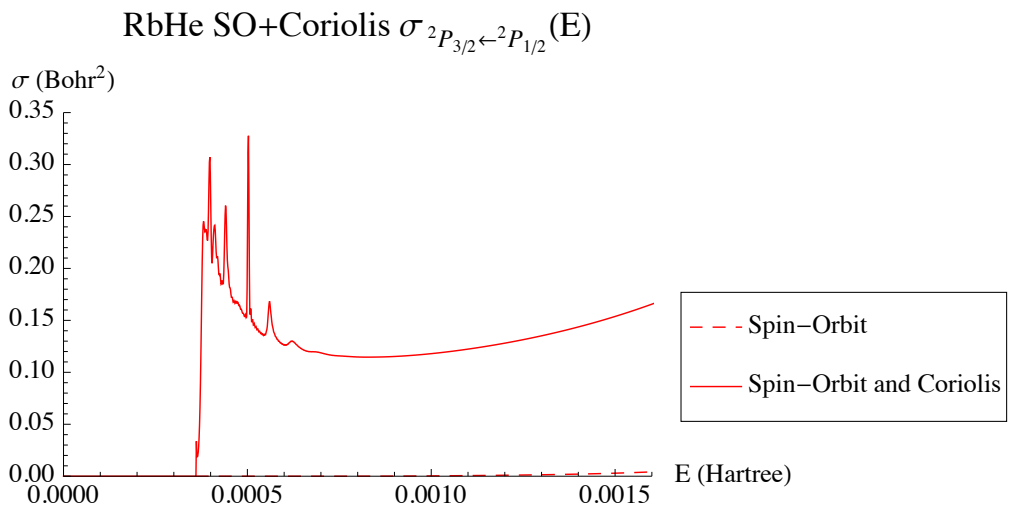

Figure 74. RbHe Spin-Orbit + Coriolis $^2P_{1/2}$ to $^2P_{3/2}$ Cross Section 0-500K.

Table 15. RbHe $Q(^2P_{3/2} \leftarrow^2 P_{1/2})$ Cross Section: Experiment vs Prediction. Units are in $Bohr^2$.

$Q(^2P_{3/2} \leftarrow^2 P_{1/2})$	RbHe	Temp. (K)
Krause[25]	0.27 ± 0.027	340.15
Predicted (SO)	0.10	
Predicted (SO+Coriolis)	0.39	
Beahn *et al.*[6]	0.36 ± 0.036	373.15
Predicted (SO)	0.13	
Predicted (SO+Coriolis)	0.45	

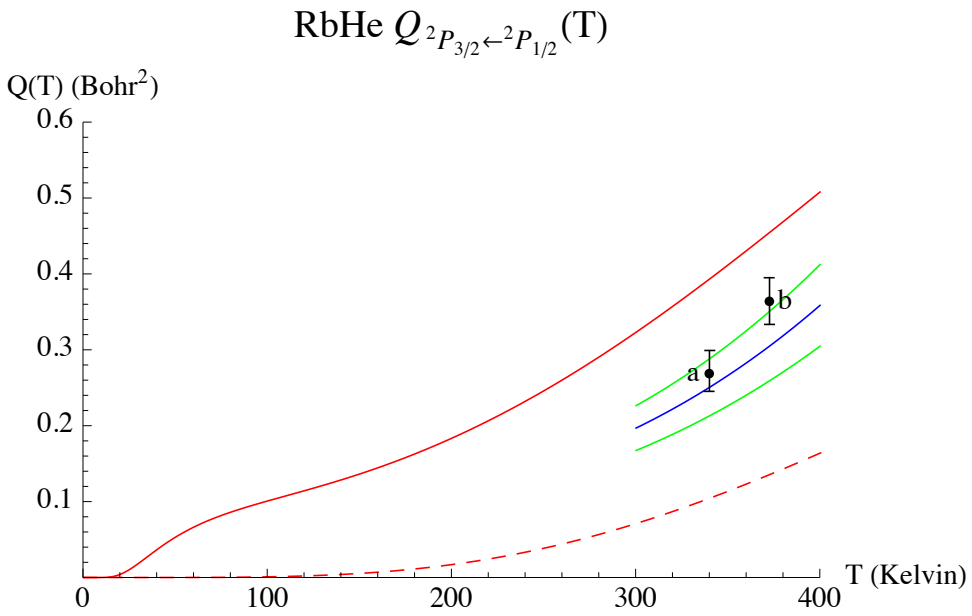

Figure 75. RbHe Thermally Averaged Cross Sections from $0-400K$. The dashed line is spin-orbit coupling only and the solid line is spin-orbit plus Coriolis coupling. a) Krause. b) Beahn. The solid blue line represents Alan Gallagher's[19] fit of experimental data with the green lines the estimated error.

The theoretical predictions are slightly higher than all three experimental data points, but the theoretical trend in temperature matches that of the experimental data.

Gallagher in his rubidium and cesium observations goes to great lengths to ensure that none of the sample cells contained contaminates and that radiation trapping was mitigated. A detailed balance analysis was likewise accomplished. For the RbHe, RbNe, and CsHe cross sections detailed balance was achieved. For the remaining rubidium and cesium cross sections detailed balance was not achieved and the suspicion is that polyatomic impurities still existed in the cell.

7.6 RbNe

The addition of Coriolis coupling dramatically increases the cross section of spin-orbit only. This is markedly different than the RbHe collision. Only one sharp peak however exists at the low energy range. The oscillatory-like behavior is also very

subtle between 0.006-0.01 Hartree for the spin-orbit plus Coriolis case.

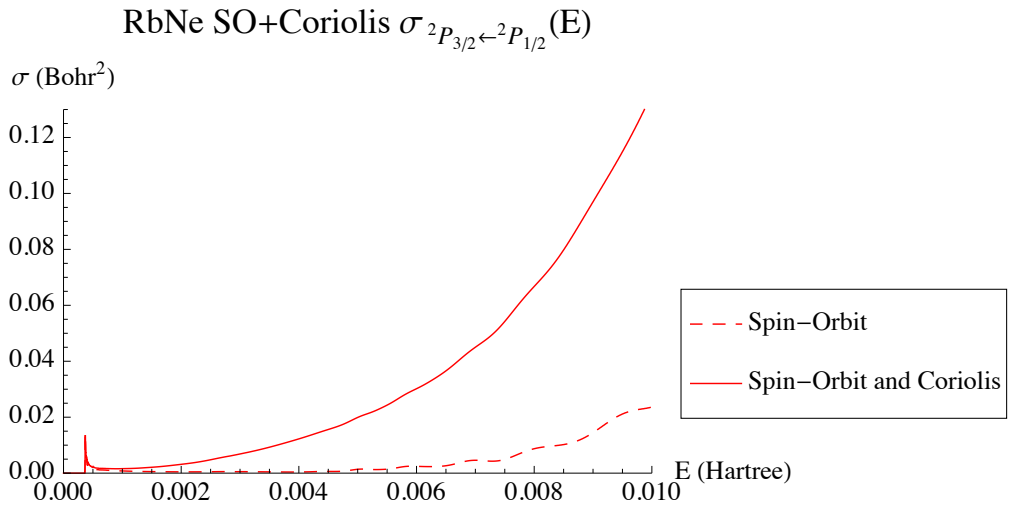

Figure 76. RbNe Spin-Orbit + Coriolis $^2P_{1/2}$ to $^2P_{3/2}$ Cross Section.

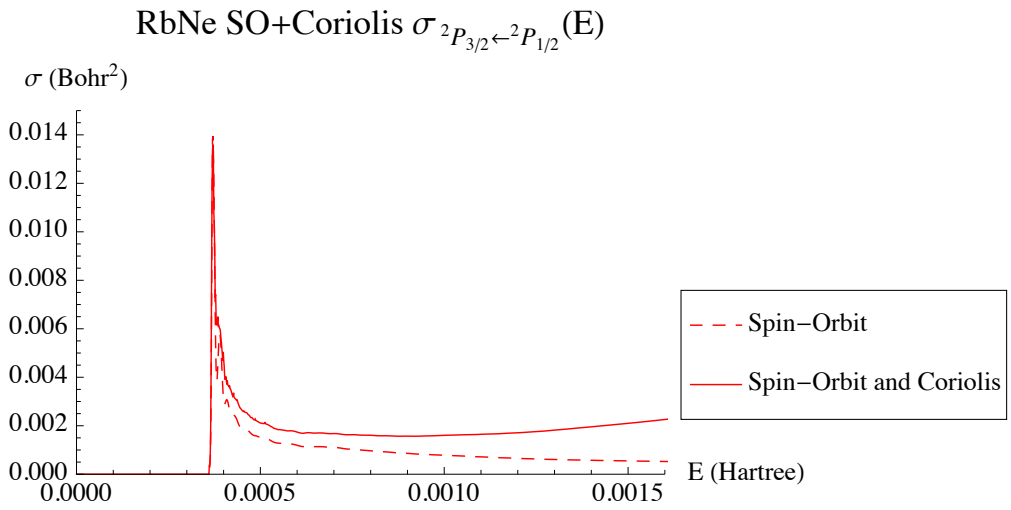

Figure 77. RbNe Spin-Orbit + Coriolis $^2P_{1/2}$ to $^2P_{3/2}$ Cross Section 0-500K.

Table 16. RbNe $Q(^2P_{3/2} \leftarrow^2 P_{1/2})$ Cross Section: Experiment vs Prediction. Units are in $Bohr^2$. Values with * were converted using detailed balance.

$Q(^2P_{3/2} \leftarrow^2 P_{1/2})$	RbNe	Temp. (K)
Krause[25]	0.0061 ± 0.00061	340.15
Predicted (SO)	0.00084	
Predicted (SO+Coriolis)	0.0060	
Beahn *et al.*[6]	$0.017 \pm 0.0086^*$	373.15
Predicted (SO)	0.00085	
Predicted (SO+Coriolis)	0.0071	

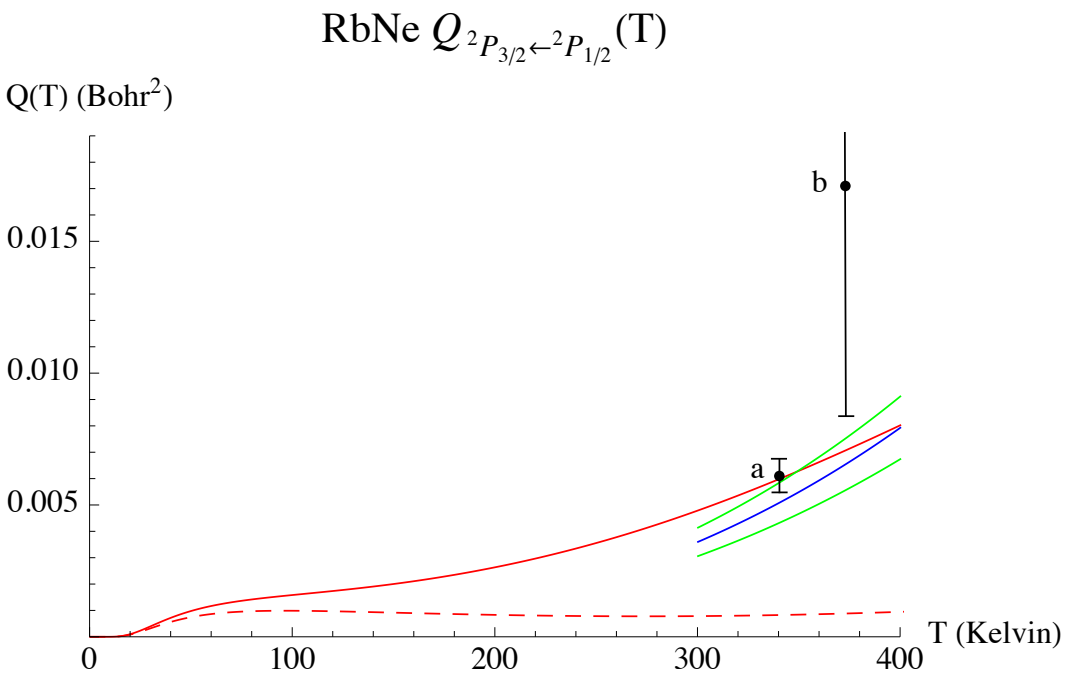

Figure 78. RbNe Thermally Averaged Cross Sections from $0-400K$. The dashed line is spin-orbit coupling only and the solid line is spin-orbit plus Coriolis coupling. a) Krause. b) Beahn. The solid blue line represents Alan Gallagher's[19] fit of experimental data with the green lines the estimated error.

The theoretical prediction intersects the Krause result and trends well with the Gallagher fit. The lower bound of Beahn's observation agrees as well.

7.7 RbAr

RbAr is prediction to have the lowest cross section of the Rubidium series. As the noble gas increases in mass the cross section for the Rubidium series of collisions has been decreasing. RbAr however shows the greatest relative increase of cross section due to the inclusion of Coriolis coupling. At the high end of the energy range this increase is nearly an order of magnitude.

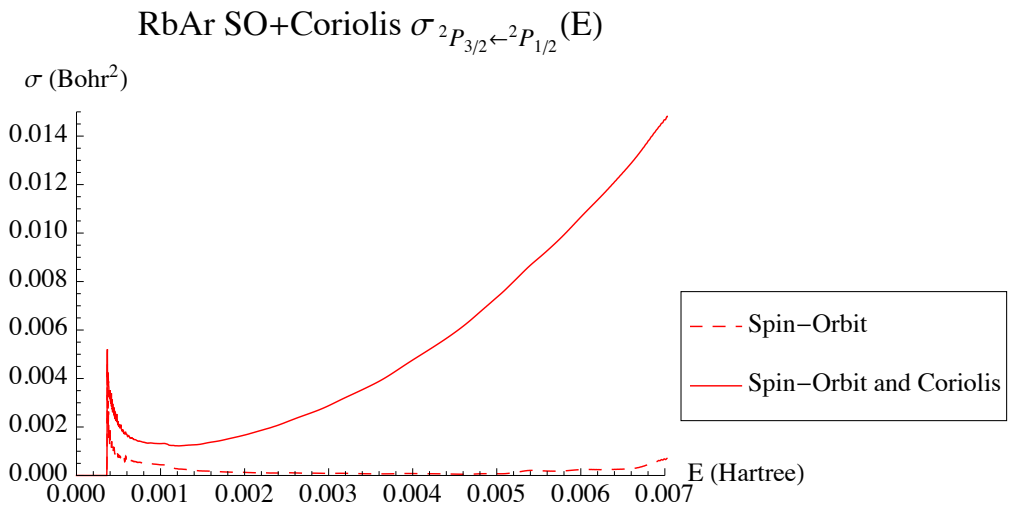

Figure 79. RbAr Spin-Orbit + Coriolis $^2P_{1/2}$ to $^2P_{3/2}$ Cross Section.

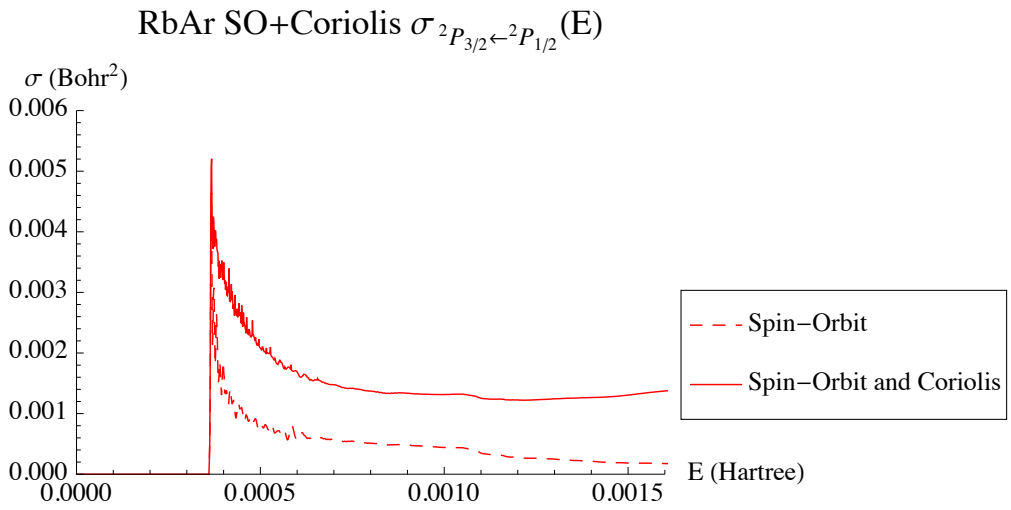

Figure 80. RbAr Spin-Orbit + Coriolis $^2P_{1/2}$ to $^2P_{3/2}$ Cross Section 0-500K.

Table 17. RbAr $Q(^2P_{3/2} \leftarrow^2 P_{1/2})$ Cross Section: Experiment vs Prediction. Units are in $Bohr^2$.

$Q(^2P_{3/2} \leftarrow^2 P_{1/2})$	RbAr	Temp. (K)
Krause[25]	0.0036 ± 0.00036	340.15
Predicted (SO)	0.00027	
Predicted (SO+Coriolis)	0.0026	

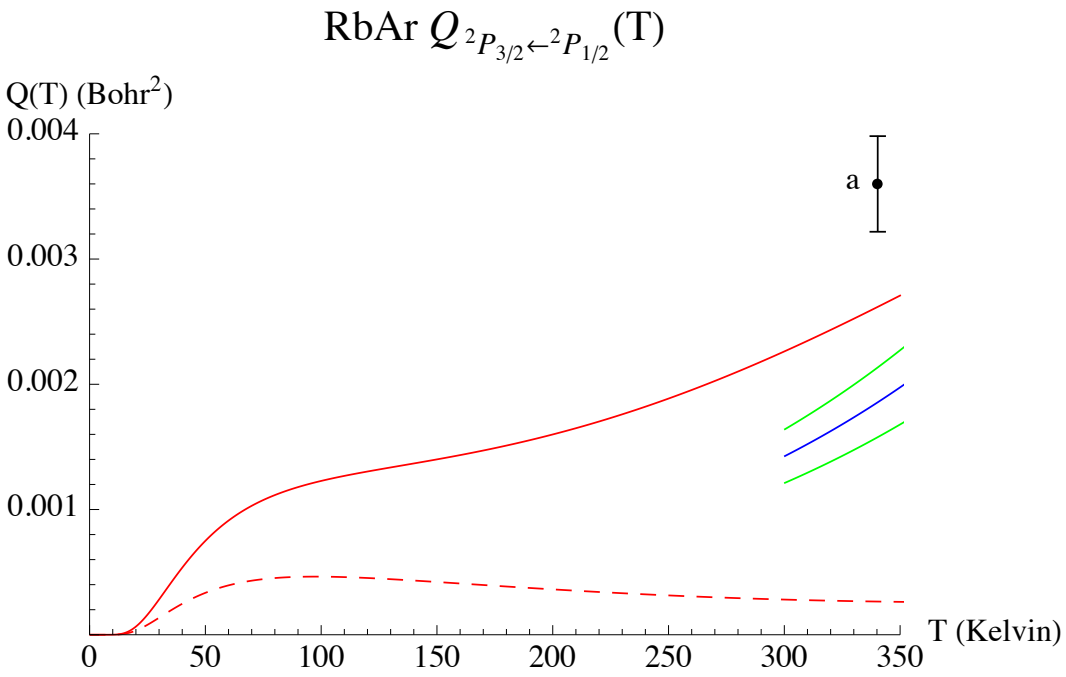

Figure 81. RbAr Thermally Averaged Cross Sections from $0-350K$. The dashed line is spin-orbit coupling only and the solid line is spin-orbit plus Coriolis coupling. a) Krause. The solid blue line represents Alan Gallagher's[19] fit of experimental data with the green lines the estimated error.

The theoretical prediction falls right in between the observations of Krause and Gallagher. The prediction also appears to follow the trend with temperature of Gallagher's fit.

7.8 CsHe

The CsHe theoretical cross section trends similarly to the KHe theoretical cross section. We see at least a doubling of cross section with the inclusion of Coriolis coupling and this observation is more pronounced as energy increases. Also we see the return of low energy peaks.

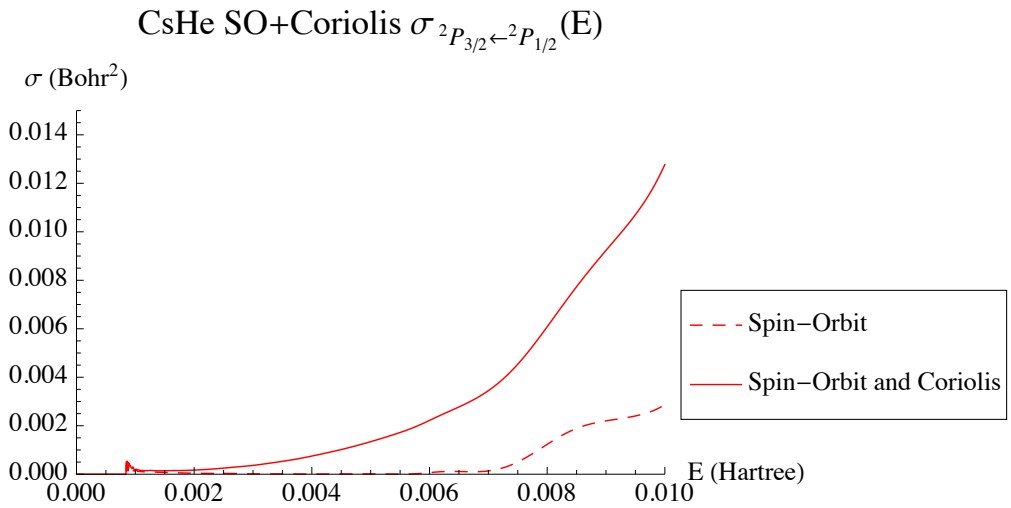

Figure 82. CsHe Spin-Orbit + Coriolis $^2P_{1/2}$ to $^2P_{3/2}$ Cross Section.

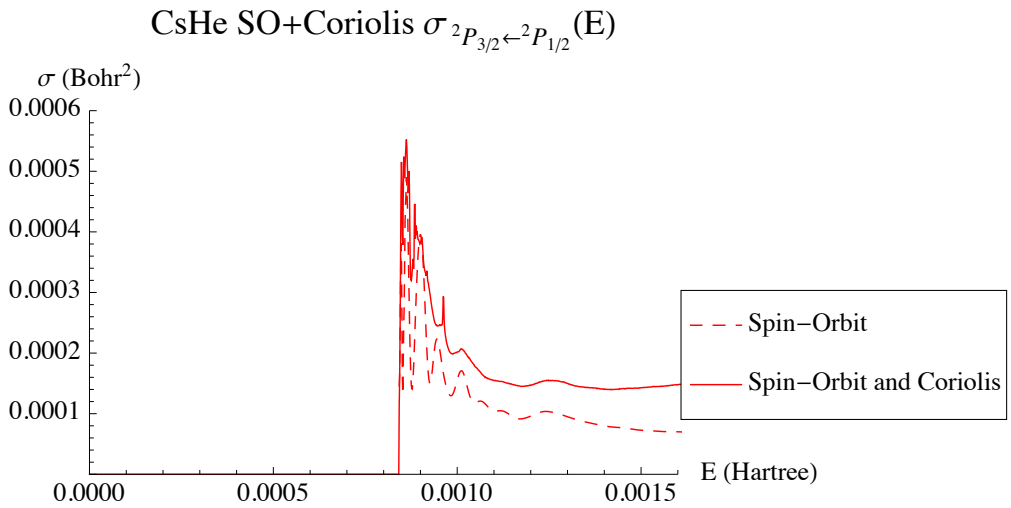

Figure 83. CsHe Spin-Orbit + Coriolis $^2P_{1/2}$ to $^2P_{3/2}$ Cross Section 0-500K.

Table 18. CsHe $Q(^2P_{3/2} \leftarrow^2 P_{1/2})$ Cross Section: Experiment vs Prediction. Units are in $Bohr^2$.

$Q(^2P_{3/2} \leftarrow^2 P_{1/2})$	CsHe	Temp. (K)
Krause[25]	$2.0 \times 10^{-4} \pm 2.0 \times 10^{-5}$	311.15
Predicted (SO)	5.7×10^{-5}	
Predicted (SO+Coriolis)	3.2×10^{-4}	

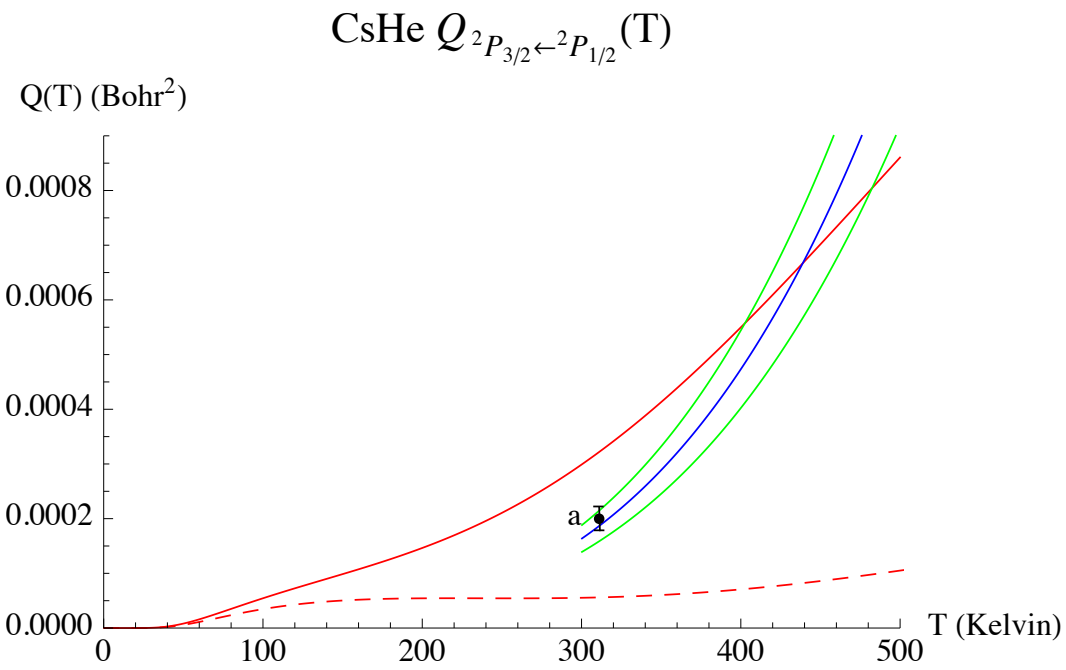

Figure 84. CsHe Thermally Averaged Cross Sections from $0-500K$. The dashed line is spin-orbit coupling only and the solid line is spin-orbit plus Coriolis coupling. a) Krause. The solid blue line represents Alan Gallagher's[19] fit of experimental data with the green lines the estimated error.

The theoretical prediction is slight higher than both the observed values at 311.15K. Also the increase of cross section with temperature appears to have a smaller slope than Gallagher's fit.

7.9 CsNe

CsNe shows the same type of increase in cross section with the inclusion of Coriolis coupling, but this increase does not take shape until a higher energy, approximately 0.006 Hartree. The low energy peaks are much less pronounced with the exception of the initial peak right around the minimum transition energy. A peculiar increase in cross section shows up at around 0.0036 Hartree. Also notice up until about 0.0045 Hartree the inclusion of Coriolis coupling shows no increase in cross section over spin-orbit only.

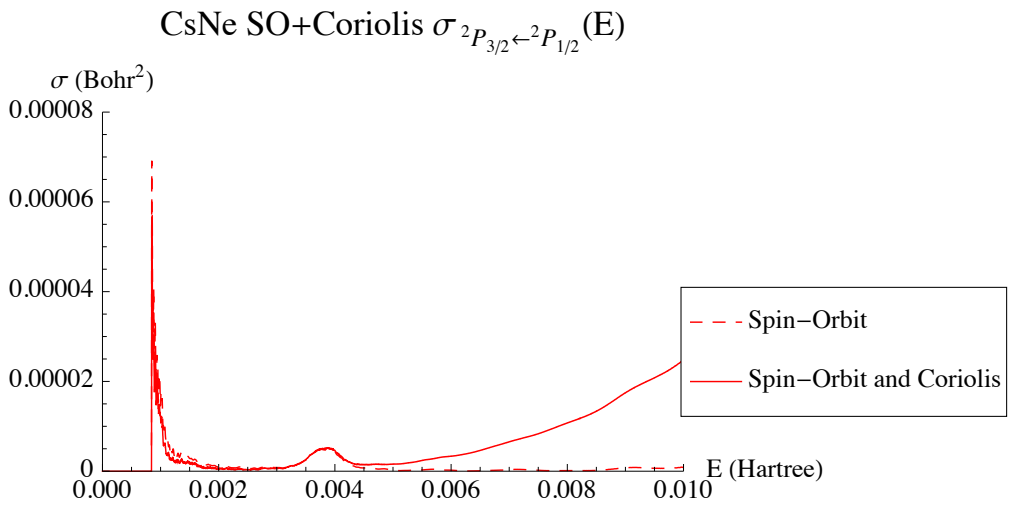

Figure 85. CsNe Spin-Orbit + Coriolis $^2P_{1/2}$ to $^2P_{3/2}$ Cross Section.

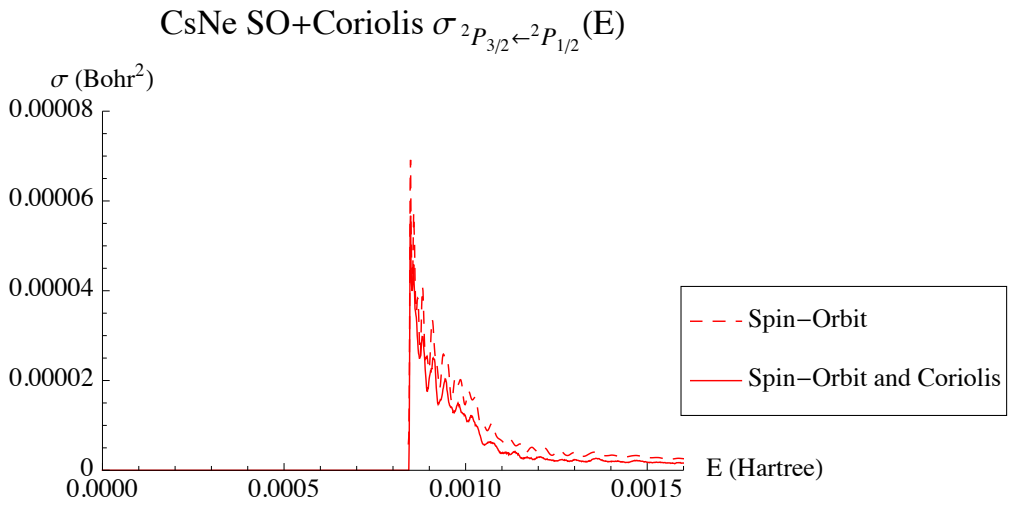

Figure 86. CsNe Spin-Orbit + Coriolis $^2P_{1/2}$ to $^2P_{3/2}$ Cross Section 0-500K.

Table 19. CsNe $Q(^2P_{3/2} \leftarrow^2 P_{1/2})$ Cross Section: Experiment vs Prediction. Units are in $Bohr^2$.

$Q(^2P_{3/2} \leftarrow^2 P_{1/2})$	CsNe	Temp. (K)
Krause[25]	$6.8 \times 10^{-5} \pm 6.8 \times 10^{-6}$	311.15
Predicted (SO)	3.38×10^{-6}	
Predicted (SO+Coriolis)	2.70×10^{-6}	

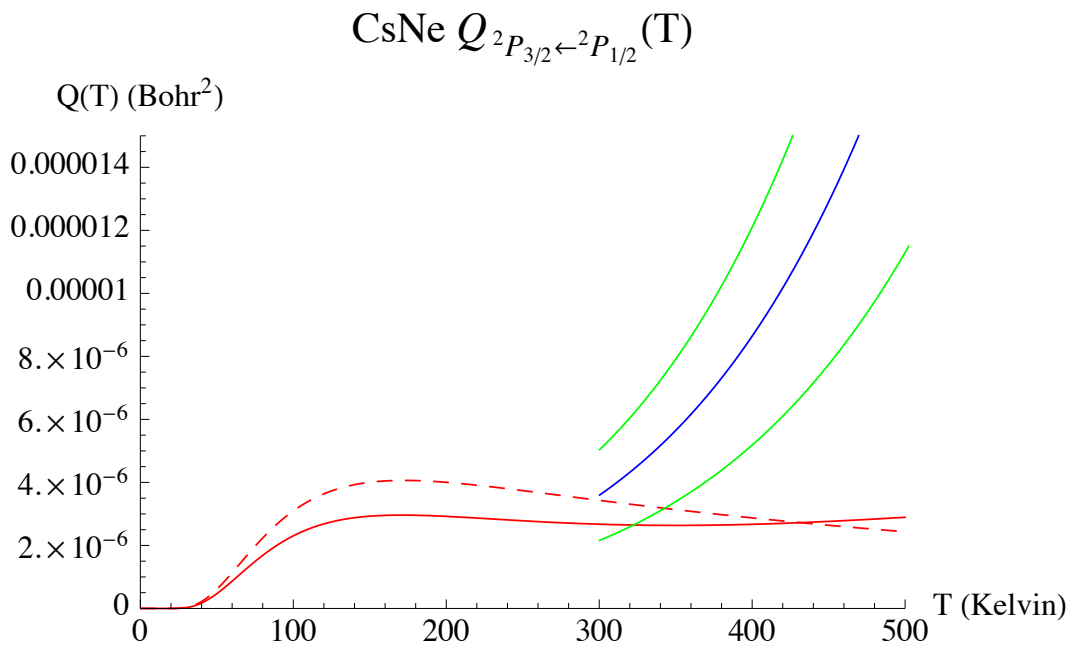

Figure 87. CsNe Thermally Averaged Cross Sections from $0-500K$. The dashed line is spin-orbit coupling only and the solid line is spin-orbit plus Coriolis coupling. The solid blue line represents Alan Gallagher's[19] fit of experimental data with the green lines the estimated error.

The comparison to experiment faired poorly against Krause who observed a value an order of magnitude above the prediction. However for this collision Krause reported that detailed balance was not achieved. Compared to Gallagher there appears to be some agreement between $300-350K$, but the trend with temperature does not compare well.

7.10 CsAr

CsAr the heaviest collision studied showed no increase in cross section when Coriolis coupling was included. Except for the low energy peak the cross section remains fairly constant and small.

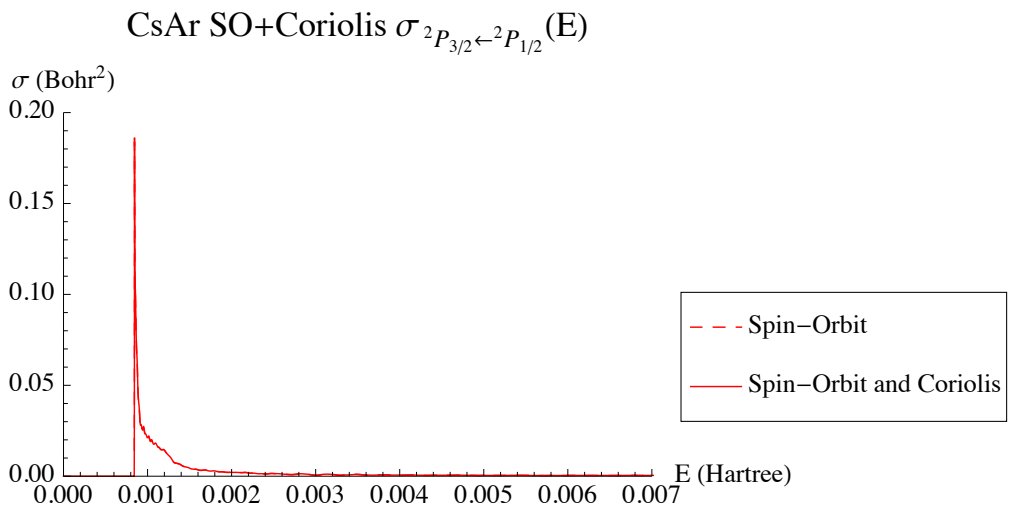

Figure 88. CsAr Spin-Orbit + Coriolis $^2P_{1/2}$ to $^2P_{3/2}$ Cross Section.

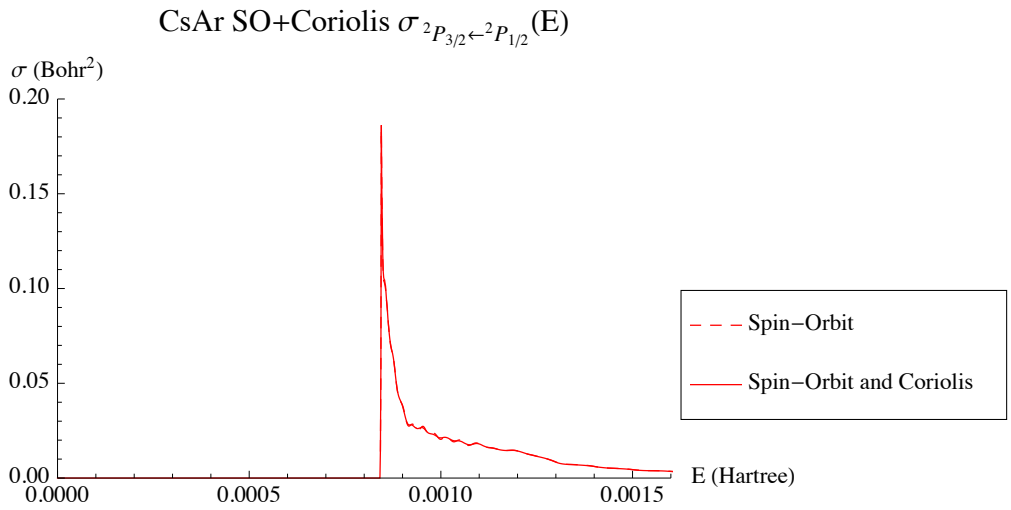

Figure 89. CsAr Spin-Orbit + Coriolis $^2P_{1/2}$ to $^2P_{3/2}$ Cross Section 0-500K.

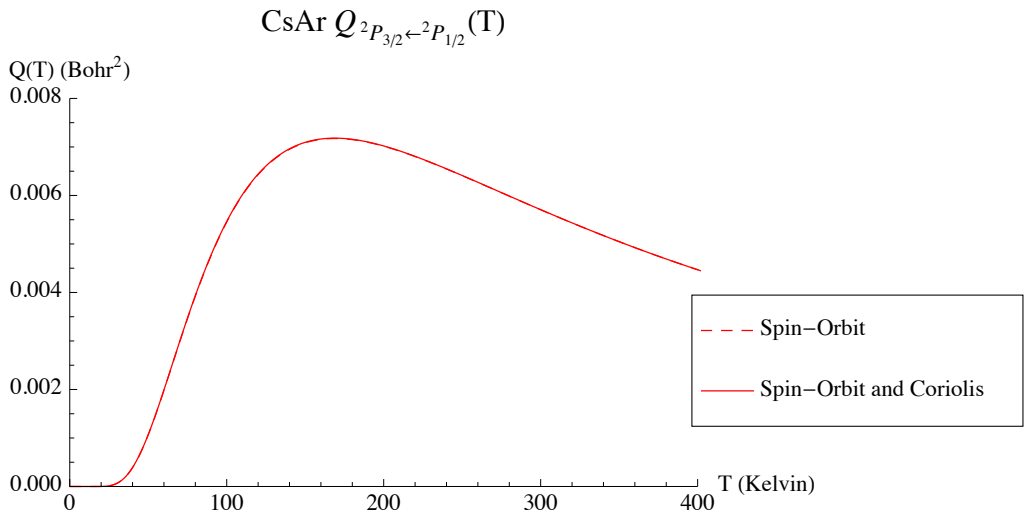

Figure 90. CsAr Thermally Averaged Cross Sections from $0 - 400K$. The dashed line is spin-orbit coupling only and the solid line is spin-orbit plus Coriolis coupling.

Krause reported a value of 5.7×10^{-5}, but once again detailed balance was not achieved. Even so the theoretical prediction seems to break the trend of decreasing cross section as noble gas partner is changed.

7.11 Conclusion

The theoretical thermally averaged results for KHe, RbHe, and CsHe compare slightly higher in magnitude against the experimental observations. However in all cases with helium the predicted trend with temperature matches well with what is observed.

The predicted results of KNe and RbNe compare the most favorably of all nine simulated collisions. The predictions fall within the observed experimental error. The CsNe cross section shows some agreement with Gallagher between $300 - 350$K, but does not trend well with temperature.

Finally, when comparing the argon series of collisions it is obvious that there is disagreement between the theoretical and observed results for KAr, however the RbAr

result compared favorably in magnitude and trend. The discrepancy in the KAr result likely falls to surfaces used in the theoretical calculation. The Ciurylo and Krause KAr result should be believed due to their detailed balance analysis and mitigation of radiation trapping. The issues associated with the accuracy of the potential energy surfaces with be discussed in Section 8.4.

VIII. Discussion

8.1 Time-Dependent Approach

The time-dependent approach proved to be very robust once validated against the unitary property of the $\widehat{\mathbf{S}}$-Operator. Throughout this study a number of major advantages and disadvantages appeared. Some of the major advantages to this method were:

1. Any range of energies, broad or narrow, can be explored all at once within one run of the simulation as long as the computational momentum grids can support the energetic dynamics of the system.
2. The accuracy of the split-operator can be taken out to higher orders thereby allowing for larger interaction time steps if desired.
3. The computation can be segmented and then optimized based on the interplay between system parameters and the surfaces much like we did with separating the Moller state calculation from the $\widehat{\mathbf{S}}$-Matrix calculation.
4. Once the algorithms are developed and verified it becomes a good tool to study the accuracy of calculated PES. One simply needs to input the surfaces and an answer for the cross section at any energy can be computed. If better or different one dimensional surfaces are computed the turn around time to compute cross sections is relatively short.

These advantages did come with a number of disadvantages. Some of the major ones were:

1. Calculating $\widehat{\mathbf{S}}$-Matrix elements and Moller states for energies near zero is difficult. This is because various components of the calculation converge slowly. This can be compounded by large computation grids and system resonances.
2. The time-dependent method scales with the number of states included in the group Born-Oppenheimer approximation. For each time step two FFTs must be computed for each Born-Oppenheimer state. For example with 6 states and 1000 time steps a total of 12000 FFTs must be performed. If one were to include for example the hyperfine structure or perhaps consider atom-diatom collisions the number of states could scale upwards of 100 and the fully quantum mechanical time-dependent approach could become computationally unwieldy.

In the end the time-dependent approach for diatomic collisions overall proved to be useful and manageable. One complete 6x6 coupled run took on the order of 7-10 days to complete including a one time Moller state calculation. This length of time was mostly a function of the initial energy range chosen, $0 - 0.01$ Bohr. This initial pick required upwards of $J = 100.5$ $\widehat{\mathbf{S}}$-Matrix calculations for the Cesium systems and nearly $J = 450.5$ for some of the Potassium systems. If one were to restrict their attention to a range of $0 - 0.003$ Bohr (roughly $0 - 1000$K) the highest J value needed for cross section convergence was on the order of 50.5. The total computational time then comes down to about 2-3 days.

8.2 Molecular Coriolis Coupling

Sometimes in the literature[14, 16, 32] it is stated that for diatomic collisions of similar nature that the $\left|\Pi^{\pm}_{3/2}\right\rangle$ and $\left|\Pi^{\pm}_{1/2}\right\rangle$ states are Coriolis coupled. We can check this by taking the Coriolis coupling "potential" written in the Born-Oppenheimer basis and transforming it into the spin-orbit molecular basis via $\mathbf{U}_{so}$, Equation (215). While it is true that the $\left|\Pi^{\pm}_{3/2}\right\rangle$ state is coupled to the $\left|\Pi^{\pm}_{1/2}\right\rangle$ state, mathematically it is also coupled to the $\left|\Sigma^{\pm}_{1/2}\right\rangle$ state as well. More so we also see Coriolis coupling between the positive projection and negative projection blocks.

$$
\mathbf{U}_{so}^{\dagger}\left\langle \begin{smallmatrix} J' & j' \\ \Omega' & \omega' \end{smallmatrix}\right| \frac{-(\mathbf{j}_{-}\mathbf{J}^{+}+\mathbf{j}_{+}\mathbf{J}^{-})}{2\mu R^{2}} \left|\begin{smallmatrix} J & j \\ \Omega & \omega \end{smallmatrix}\right\rangle \mathbf{U}_{so} =
$$

$$
\begin{array}{c}
\begin{array}{cccccc}
\left|\begin{smallmatrix} J \\ 3/2 \end{smallmatrix}\ \Pi_{3/2}^{+}\right\rangle & \left|\begin{smallmatrix} J \\ 1/2 \end{smallmatrix}\ \Sigma_{1/2}^{+}\right\rangle & \left|\begin{smallmatrix} J \\ 1/2 \end{smallmatrix}\ \Pi_{1/2}^{+}\right\rangle & \left|\begin{smallmatrix} J \\ 3/2 \end{smallmatrix}\ \Pi_{3/2}^{-}\right\rangle & \left|\begin{smallmatrix} J \\ 1/2 \end{smallmatrix}\ \Sigma_{1/2}^{-}\right\rangle & \left|\begin{smallmatrix} J \\ 1/2 \end{smallmatrix}\ \Pi_{1/2}^{-}\right\rangle
\end{array} \\
\left(\begin{array}{cccccc}
0 & -\frac{9\left(J-\frac{1}{2}\right)^{2}\left(J+\frac{3}{2}\right)^{2}\delta}{2R^{2}\mu} & -\frac{9\left(J-\frac{1}{2}\right)^{2}\left(J+\frac{3}{2}\right)^{2}\epsilon}{2R^{2}\mu} & 0 & 0 & 0 \\
-\frac{9\left(J-\frac{1}{2}\right)^{2}\left(J+\frac{3}{2}\right)^{2}\delta}{2R^{2}\mu} & 0 & 0 & 0 & -\frac{(J+1)\delta^{2}}{R^{2}\mu}-\frac{(J+1)\epsilon^{2}}{2R^{2}\mu} & -\frac{(J+1)\delta\epsilon}{2R^{2}\mu} \\
-\frac{9\left(J-\frac{1}{2}\right)^{2}\left(J+\frac{3}{2}\right)^{2}\epsilon}{2R^{2}\mu} & 0 & 0 & 0 & -\frac{(J+1)\delta\epsilon}{2R^{2}\mu} & -\frac{(J+1)\delta^{2}}{2R^{2}\mu}-\frac{(J+1)\epsilon^{2}}{R^{2}\mu} \\
0 & 0 & 0 & 0 & -\frac{9\left(J-\frac{1}{2}\right)^{2}\left(J+\frac{3}{2}\right)^{2}\delta}{2R^{2}\mu} & -\frac{9\left(J-\frac{1}{2}\right)^{2}\left(J+\frac{3}{2}\right)^{2}\epsilon}{2R^{2}\mu} \\
0 & -\frac{(J+1)\delta^{2}}{R^{2}\mu}-\frac{(J+1)\epsilon^{2}}{2R^{2}\mu} & -\frac{(J+1)\delta\epsilon}{2R^{2}\mu} & -\frac{9\left(J-\frac{1}{2}\right)^{2}\left(J+\frac{3}{2}\right)^{2}\delta}{2R^{2}\mu} & 0 & 0 \\
0 & -\frac{(J+1)\delta\epsilon}{2R^{2}\mu} & -\frac{(J+1)\delta^{2}}{2R^{2}\mu}-\frac{(J+1)\epsilon^{2}}{R^{2}\mu} & -\frac{9\left(J-\frac{1}{2}\right)^{2}\left(J+\frac{3}{2}\right)^{2}\epsilon}{2R^{2}\mu} & 0 & 0
\end{array}\right)
\end{array}
\tag{240}
$$

Energetically however one could argue that the Coriolis coupling between the $\Pi^{\pm}_{3/2}$ and $\Pi^{\pm}_{1/2}$ surfaces is more favored than the Coriolis coupling between the $\Pi^{\pm}_{3/2}$ surface and the $\Sigma^{\pm}_{1/2}$ surface. We take for example a plot of the spin-orbit adiabatic surfaces with a Coriolis coupling function plotted for $J = 50.5$. We see that where the Coriolis coupling is strongest ($R \lesssim 7$ Bohr) the $\Pi^{\pm}_{3/2}$ and $\Pi^{\pm}_{1/2}$ surfaces are nearly degenerate (the region between dashed lines). In this region it is energetically feasible to strongly transition then exit on a different surface. However to do the same for a $\left|\Pi^{\pm}_{3/2}\right\rangle$ to $\left|\Sigma^{\pm}_{1/2}\right\rangle$ transition we would have to be in a region $\gtrsim 15$ Bohr to be energetically favored to exit out on a transitioned surface. The Coriolis coupling however is very small in this region. Nonetheless the coupling still exist and influences the dynamics of the evolving system.

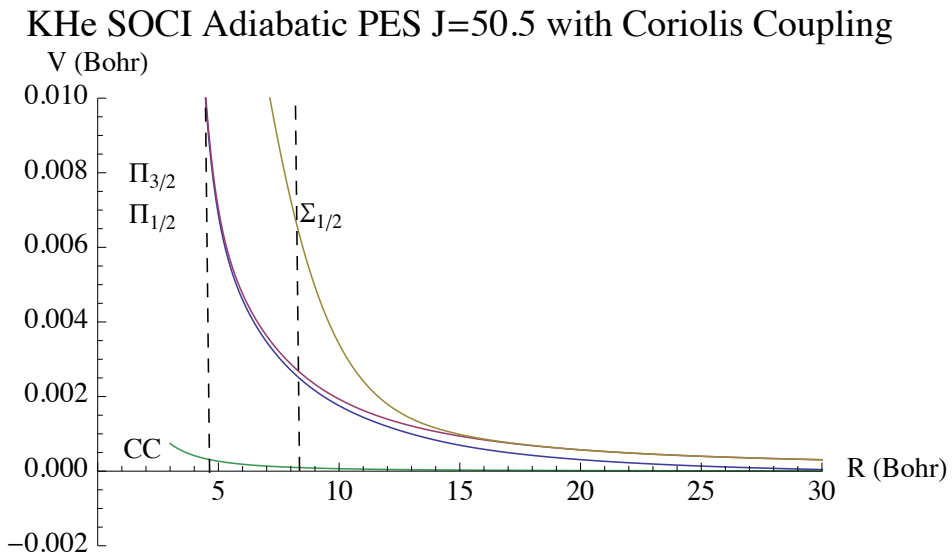

Figure 91. KHe Spin-Orbit Molecular Coriolis Coupling.

8.3 Features of the Theoretical Cross Section, $\sigma(E)$

One particularly noticeable feature of the theoretical cross sections are the low energy peaks. Because the cross section is a sum of many $\widehat{\mathbf{S}}$-Matrix elements we have to look at the low J $\widehat{\mathbf{S}}$-Matrix elements to understand the nature of these peaks. We plot in Figure 92 a sample of $\widehat{\mathbf{S}}$-Matrix elements for the KHe system in a range between $0 - 0.0005$ Hartree.

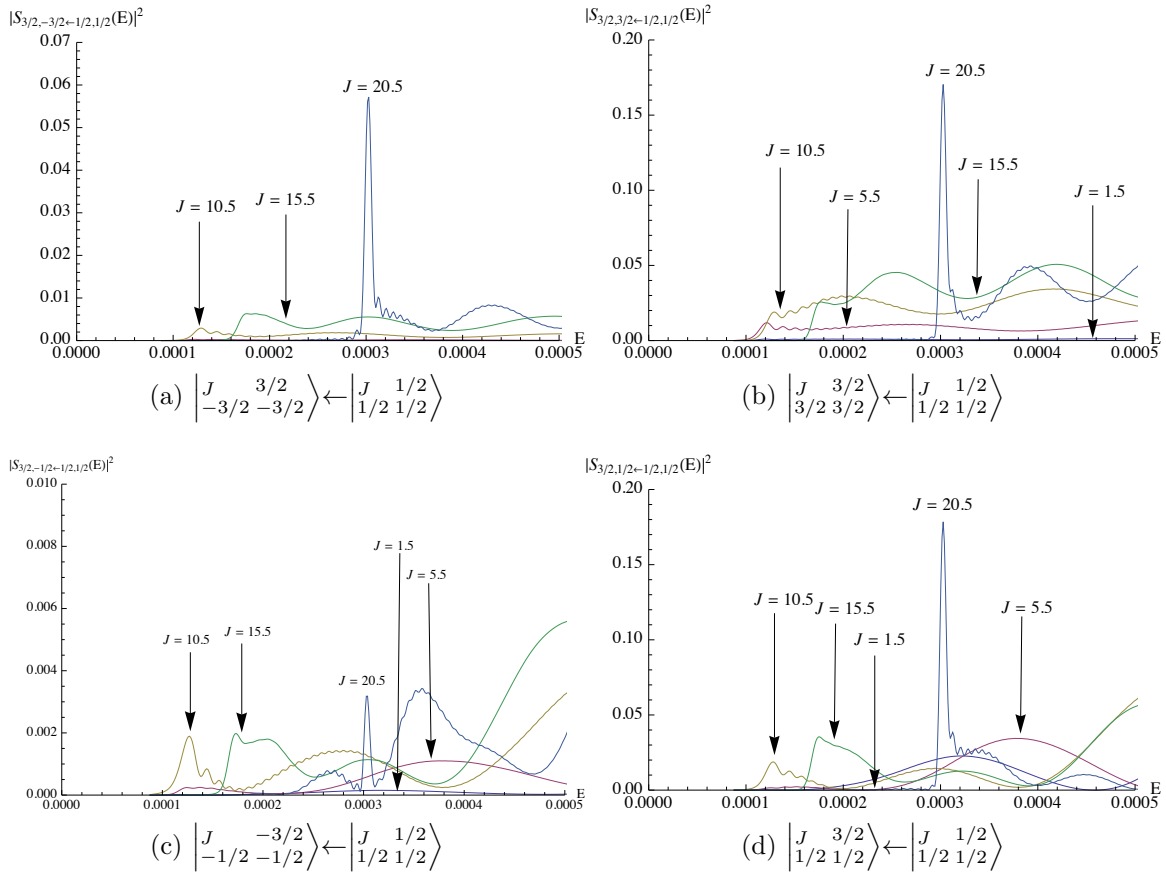

Figure 92. KHe Spin-Orbit plus Coriolis Interaction SMatrix Elements J = 1.5, 5.5, 10.5, 15.5, and 20.5.

The definitive peak seen at around 0.0003 Bohr is for the $J = 20.5$ $\widehat{\mathbf{S}}$-Matrix element. What we are seeing is a resonance peak at a particular energy. The dynamics and the energetics of the system for this value of $J = 20.5$ are such that they enable a

higher transition probability. The other $\widehat{\mathbf{S}}_j$-Matrix elements are relatively smooth in this energy region compared to this resonance peak. These effects tend to add up as we sum over the range of J to compute the cross section.

Looking back at Figure 62 we see these $J = 20.5$ resonance peaks showing up in the theoretical cross section at $E = 0.0003$ Hartree. All of the low energy cross section peaks can be understood in this way.

8.4 Accuracy of $Q(T)$ Results

One of the determining factors of whether or not the predictions of this time-dependent approach are accurate depends on how accurate the potential energy surfaces are. Since we verified that our method produces answers that converge through the properties of the $\widehat{\mathbf{S}}$-Operator we can rule out errors due to non-converging solutions. In principle any set of potential energy surfaces could be used. If the energy surfaces mimicked a real world system then the answer for the cross section should reflect that.

The calculation of the potential energy surfaces requires a tremendous amount of effort. Ideally one would like to treat every electron and proton separately, but that starts to become computationally intractable in systems with many electrons like CsAr. For this reason core potentials are used to model the inner electrons to include relativistic effects. However this does represent an approximation. One that has the potential to adversely effect the results of this calculation.

The modeling of the outer electrons is another facet of the many-body calculation that often comes under scrutiny. The basis functions used by Blank of triple zeta quality are one of many sets that can be used to individually model electrons. Each set comes with their own issues in terms of accuracy and implementation. In fact much like the surfaces were input to this body of this work, the basis sets to model

outer shell electrons are input to the many-body calculation. So the accuracy of the basis sets will ultimately effect our predicted outcomes. The error induced from the many-body calculation is likely the same error exhibited within our predicted cross sections.

Another particularly interesting question we can ask is do we need more than the P-Manifold set of states? While it is true that we do not expect to exit out on the D-Manifold (the NIST asymptotic values for Potassium are 0.09815 Hartree for the $D_{3/2}$ state and 0.09816 Hartree for the $D_{5/2}$ state) one can conceive of wave function from the P-Manifold Coriolis coupling to a potential well in the D-Manifold so long as that potential well is energetically accessible. Of course the wave function will not exit out on the D-Manifold, but the fact remains that coupling to a D-Manifold potential well would influence what P-Manifold surface the components of the wave function exit out on. A many-body calculation involving the D-Manifold would have to be accomplished to truly see if the D-Manifold is energetically inaccessible.

8.5 Spin-Orbit vs. Coriolis Coupling

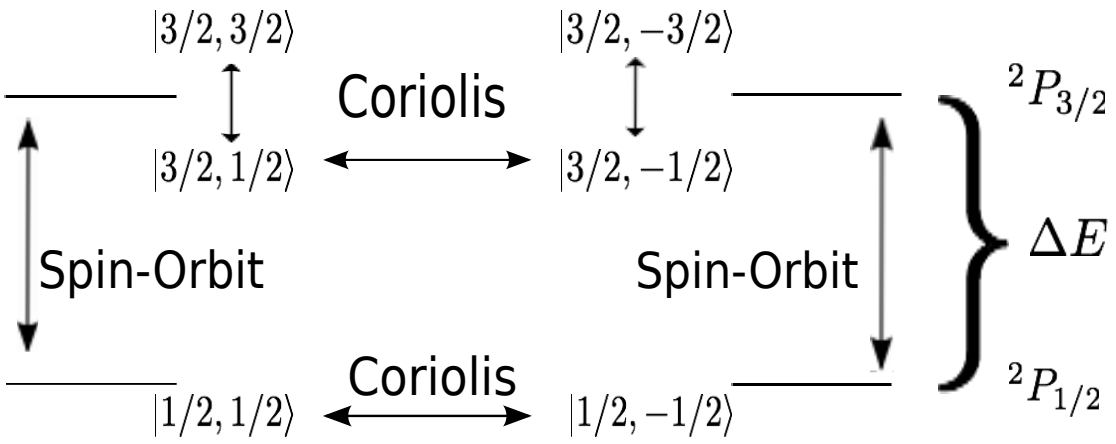

Figure 93. Diagram of Spin-Orbit and Coriolis Coupling Pathways.

Figure 93 depicts graphically the coupling pathways that are available to the Alkali Noble gas system as shown from the Born-Oppenheimer basis asymptotic region. Starting in the $^2P_{1/2}$ manifold there are only two pathways immediately available: 1) The Coriolis pathway within the $^2P_{1/2}$ manifold that mixes or realigns the $^2P_{1/2}$ manifold and 2) the Spin-Orbit pathway that couples to the $|3/2, \pm 1/2\rangle$ states of the $^2P_{3/2}$ manifold.

In the case of spin-orbit only coupling what determines whether or not a transition occurs depends on two parameters. The first is the strength of the spin-orbit coupling function and the second is the P-manifold energy splitting ΔE. Appendix B has as a function of R the spin-orbit coupling functions plotted along with the diabatic and adiabatic surfaces. As we step through heavier Alkali colliding partners one trend is clear, the magnitude of the spin-orbit coupling function decreases over most values of R. This reduction in magnitude is one contributing factor to decreased spin-orbit cross section starting with potassium, rubidium, and finally cesium.

The asymptotic spin-orbit split energy values, ΔE, are tabulated below.

Table 20. Spin-Orbit split energies of Potassium, Rubidium, and Cesium.

Alkali	ΔE (Hartree)	ΔT (Kelvin)
Potassium	0.0002629	83
Rubidium	0.001082	342
Cessium	0.002524	797

In section 6.5 we saw that spin-orbit coupling and radial derivative coupling were one in the same phenomenon. Looking at the matrix elements of the 6x6 Hamiltonian or Figure 93 notice that radial nuclear motion is the only source of wave function probability transfer between the $^2P_{3/2}$ and $^2P_{1/2}$ levels in the Born-Oppenheimer representation. There can be a probability transfer of electronic energy in to relative

nuclear kinetic energy or relative nuclear kinetic energy in to electronic energy. In order for a significant amount of transfer to occur the system energy needs to be greater than ΔE. Otherwise a strong transition is not expected. The theoretical cross section for the potassium series of collisions shows the radial coupling effect immediately starting at low energies. This would be expected since the spin-orbit splitting of potassium is 0.00026 Hartree. At $350K$ the spin-orbit splitting is approximately 1/4th the system energy. This would be energetically favorable.

For rubidium the radial coupling is expected to become a factor at higher system energies since the spin-orbit splitting is roughly 4 times that of potassium. This is observed in the rubidium series cross sections. Between $0.004 - 0.005$ Hartree the spin-orbit cross sections begin to become significant and increasing with E. At $350K$ the spin-orbit splitting of rubidium is approximately the same as the system energy.

For cesium the radial transition is nearly non-existent in the energy ranged studied. It is expected however that radial transitions would occur beyond $E > 0.01$ Hartree. At $350K$ the spin-orbit splitting of cesium is approximately 2.5 times that of the system. This is not energetically favorable with ΔE.

It appears there are some favored system energies for a number of the collisions studied. KNe, KAr, RbHe, RbNe, RbAr, and CsHe exhibit oscillatory like behavior in their theoretical spin-orbit cross sections as energy increases. The local increase in cross section signify energies that overlap well with ΔE.

Once Coriolis coupling is enabled three more coupling pathways open up. The first two pathways are Coriolis coupling between the two-fold degenerate $|3/2, \pm 3/2\rangle$ and $|3/2, \pm 1/2\rangle$ states of the same projection and the third is Coriolis coupling between the $|3/2, 1/2\rangle$ and $|3/2, -1/2\rangle$ states. Note that there is no Coriolis coupling between the $|3/2, 3/2\rangle$ and $|3/2, -3/2\rangle$ states.

Coriolis coupling has the effect of dramatically increasing the cross sections over

spin-orbit only coupling for all collisions except RbHe and CsAr. In some cases it more than doubles or even triples the prediction of spin-orbit only coupling at a given energy. There is a tendency by Coriolis coupling to prevent back scatter down to the $|1/2, \pm 1/2\rangle$ states. It is as if the wave function gets trapped in the $^2P_{3/2}$ manifold by oscillating between the $|3/2, \pm 3/2\rangle$ and $|3/2, \pm 1/2\rangle$ states. However this can only occur once wave function probability transfer has taken place through radial coupling. Once this happens the Coriolis trapping pathways are open. Coriolis coupling though does not transfer probability between intramultiplet split states in the way that radial coupling does.

The actual efficiency of Coriolis trapping in the $^2P_{3/2}$ manifold is difficult to gauge. First the strength of the Coriolis coupling varies as μ^{-1}, see equation (229). As the reduced mass decreases the Coriolis coupling function increases in magnitude over all R. When one colliding partner is much more massive than the other, the reduced mass is dominated by the lighter partner. The expectation then is for Coriolis coupling to become less significant as the collision partner is changed from Helium to Neon and from Neon to Argon while keeping a constant Alkali for a given energy. This trend applies to the potassium and cesium series of collisions and for RbNe to RbAr. RbHe however breaks this trend.

What is also important for Coriolis coupling is the velocity at which the colliding partners interact. For non head-on collisions the rate at which the molecular axis rotates increases with relative nuclear velocity. Eventually at high enough energies this rotation ceases being adiabatic and the molecular wave function will not be able to rotate fast enough. Therefore a transition will take place that changes the electronic projection. This idea appears to be most pronounced in the KNe, RbNe, RbAr, and CsNe cases. Coriolis coupling increases at a significantly faster rate than spin-orbit coupling as a function of energy.

It is clear that in order to adequately compare to experimental observations Coriolis coupling should not be neglected except in the case of RbHe and CsAr. In all cases the prediction for spin-orbit only coupling falls below observed values.

8.6 Isotopic Effects He^3 vs. He^4

Collision partner isotopic effects can be studied relatively easy with the methods devised in this dissertation. In particular we take a look at the KHe system. Changing the isotope of the Helium atom from He^4 to He^3 does not change the electronic or magnetic dynamics (so the surfaces remain the same), but it does change the nuclear dynamics. The reduced mass of the system changes from 6614 a.u. to 5101 a.u.

There are three areas in which the reduction of reduced mass will affect the calculation. First, this reduction in reduced mass causes the Coriolis coupling function to increase. As discussed before this coupling function is proportional to μ^{-1}. So over all R the Coriolis coupling function will be stronger. Second, all of the radial kinetic energy terms, including the radial derivative coupling terms, will increase because they too are being divided by μ^{-1}, see equation (137). Lastly, each $\widehat{\mathbf{S}}$-Matrix element will increase, including both reflection and transmission, due to the same reliance on μ^{-1}, see equation (190).

With a lower reduced mass and stronger coupling function the expectation is that KHe^3 will exhibit a greater thermally averaged cross section than KHe^4. The thermally averaged results for He^3 vs. He^4 are shown in Figure 94 and the difference between the He^3 and He^4 cross sections are plotted as a function of temperature in Figure 95. The results show that the thermally averaged cross section of KHe^3 is greater than KHe^4.

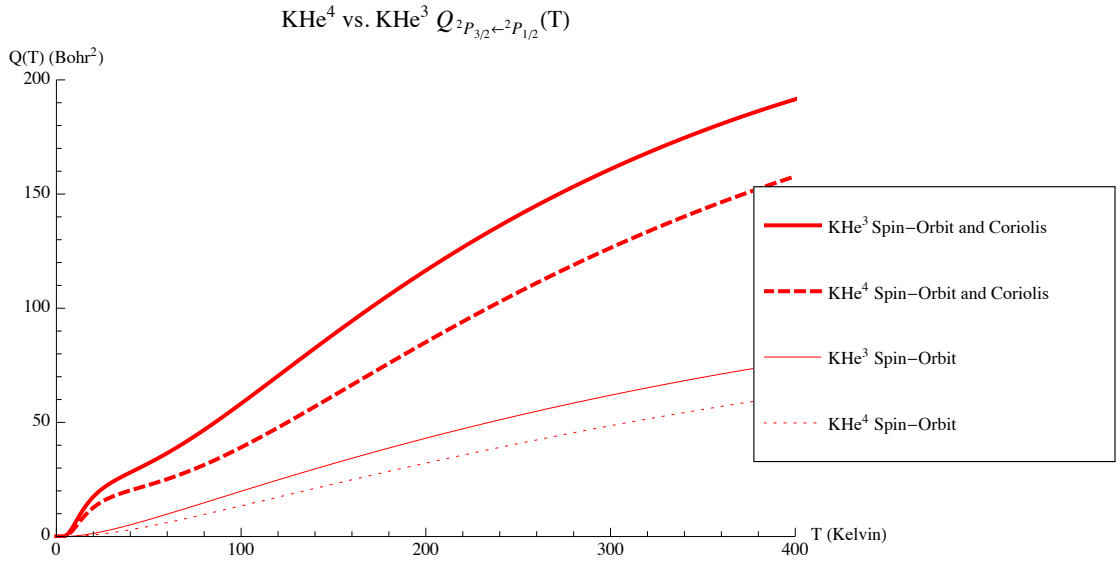

Figure 94. KHe^3 vs. KHe^4 Q(T) from $0 - 1000$ K.

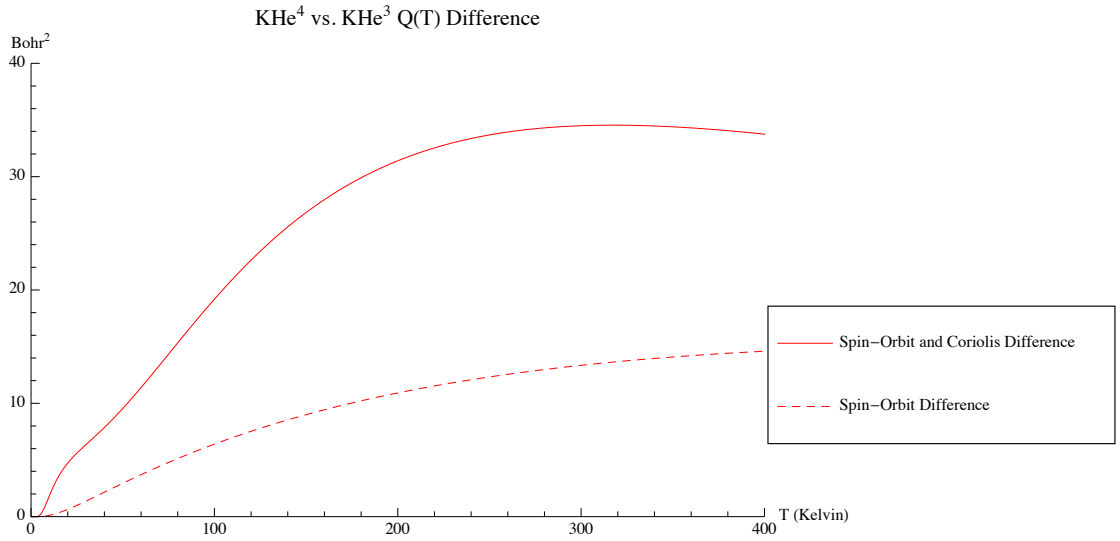

Figure 95. KHe^3 vs. KHe^4 Q(T) Difference.

Figure 95 shows that reducing the reduced mass causes the cross section to increase more for the spin-orbit plus Coriolis coupling over the spin-orbit coupling only case. We can calculate the relative percentage increase in cross section as follows: take the cross section difference of the He^3 and He^4 isotopes and divide it by the cross section

for the He^4 collision partner. This is shown in Figure 96.

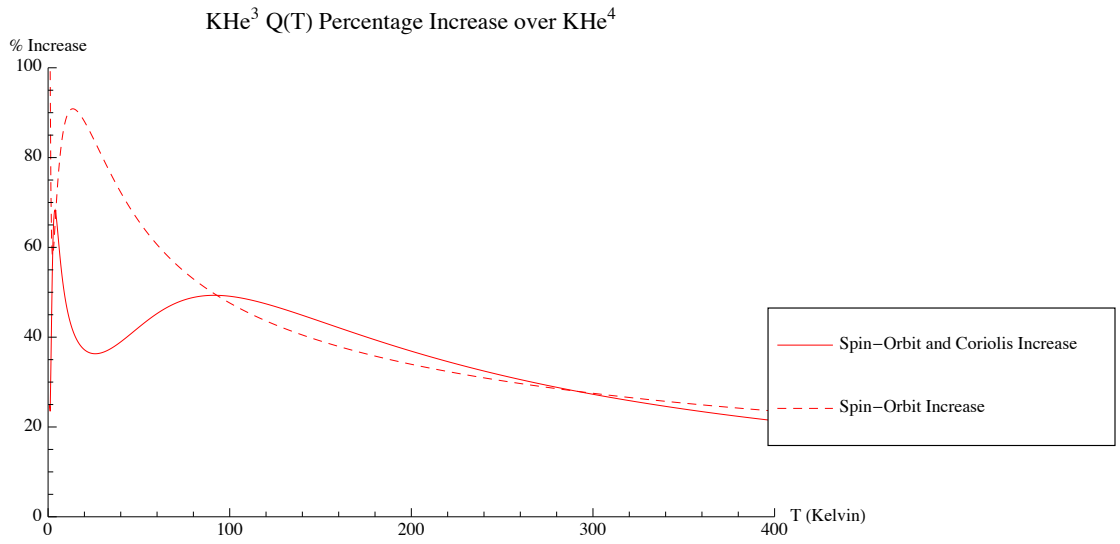

Figure 96. KHe^3 vs. KHe^4 Q(T) Percentage Increase.

For example at 350K the KHe^3 Spin-Orbit plus Coriolis thermally averaged cross section shows a 24.15% increase over the KHe^4 Spin-Orbit plus Coriolis thermally averaged cross section. While the relative percentage increase in cross section is roughly the same between spin-orbit plus Coriolis coupling and spin-orbit only coupling, the absolute difference, Figure 95, shows a greater increase in cross section due to Coriolis coupling over spin-orbit only coupling.

This phenomenon is echoed experimentally in the literature. Zweiback and Krumpke[48] when presenting results for a hydrocarbon-free Rubidium laser saw an increase in output power from $24W$ to $28W$, a 16% increase, by switching the buffer gas from naturally occurring He to isotopic He3. This is induced by a higher collisional de-excitation rate which follows from an increase in collisional cross section. We have seen that this increase in cross section is due to the reduction of reduced mass which increases both radial and Coriolis coupling.

IX. Conclusion

Utilizing the mathematics of Quantum Mechanics and the methods of Born-Oppenheimer we have given a description of the Alkali Metal - Noble Gas collision diatom in body-fixed coordinates. We saw that while restricting the system to the P-manifold two major form of Born-Oppeheimer state to state coupling became important: spin-orbit and Coriolis. These two coupling phenomena allowed all six states of the close-coupled Hamiltonian to be coupled by single step or multistep coupling mechanisms.

This close-coupled Hamiltonian was then subjected to a time-dependent approach, the Channel Packet Method, to compute $\widehat{\mathbf{S}}$-Matrix elements over a range of desired energies. The computational tools developed made extensive use of the Fast Fourier Transform such that the split operator approximation became a viable method. Convergence of the technique was shown through verifying that the unitary property of the $\widehat{\mathbf{S}}$-Operator was not violated.

Using the potential energy surfaces calculated by Blank we computed $\widehat{\mathbf{S}}$-Matrix elements for nine MNg (M = K, Rb, Cs and Ng = He, Ne, and Ar) collisions. These $\widehat{\mathbf{S}}$-Matrix elements were summed accordingly and theoretical ${}^2P_{3/2} \leftarrow {}^2P_{1/2}$ cross sections were computed between the energies of $0.00 - 0.01$ Hartree. In order to compare the experimental observation the theoretical cross sections were convolved with Maxwell-Boltzmann distributions. These calculated temperature averaged cross sections were finally compared to available experimental data. Our calculated results confirm the experimental observations of Krause and Gallagher for which radiation trapping was kept to a minimum and detailed balance achieved except for the case of KAr in which the discrepancy is likely due to the potential energy surfaces.

For application to DPAL systems we have also seen an increase in cross section when switching from helium-4 to helium-3. By reducing the reduced mass a higher

cross section was predicted. This is due in part to the higher impact of helium-3 over helium-4 and in part to the increase of Coriolis coupling. This application brings theoretical understanding of how changing the isotope of the buffer gas can lead to a higher average output power as demonstrated by Zweiback and Krumplke[48].

9.1 Recommendations for Further Work

The time-dependent method proved to be successful and is recommended based on the ability to choose a narrow or broad range of energies to interrogate. It is also recommended based on the strong condition that the $\widehat{\mathbf{S}}$-Operator must be unitary to insure complete convergence. However a significant amount of work could be done to further optimize grid lengths and time steps. What would be very advantageous is if the algorithm could actively change computational parameters based on what region of the potential is being interrogated. This would be more efficient than just setting upper and lower limits.

If these time-dependent algorithms could be optimized from days to hours one then might try to start from the experimental observations and work backwards to modify the potential energy surfaces. The idea would be for example to experimentally determine $Q(T)$ for a small range of T, say 300-400K. Then take existing surfaces and slightly modify aspects of them such as well depth or barrier heights. Calculate a new set of $Q(T)$ over the same temperature range and compare the results. By monitoring how changing aspects of the surfaces change the fit to experimental data once could constrain the surfaces to produce experimental results. In a sense this becomes a surface optimization problem. The resulting surfaces could be termed semi-empirical non-spin orbit split surfaces.

It is quite difficult to get a handle on how Coriolis trapping works in terms of the surfaces and coupling functions. This is compounded by the fact that for each J

value the surfaces change. The question arises, once population has been transferred from the $P_{1/2}$ manifold to the $P_{3/2}$ manifold via radial coupling, does the probability oscillate between the Coriolis coupled states or is there a one time transfer of probability between Coriolis coupled states. One possible way to answer this question would be to literally create and watch a movie of the evolving wave function and note how the wave function exits on each surface. Another possible way to answer this question would be to calculate the Wigner distribution which can be fashioned from the correlation functions. This distribution would show as a function of time what energy components of the wave function are present in the interaction region. This would show if any particular energy components resonate between Coriolis coupled surfaces or not.

Other work that would be interesting would be to add a magnetic field to the close-coupled Hamiltonian. Then a direct comparison to the experimental Zeeman mixing cross sections could be made. of course this could introduce another interesting aspect and this is coupling to the hyperfine structure. Not only could we compare with other experimental evidence, but one could explore whether or not introducing a magnetic field around the cell would dramatically increase or decrease the thermally averaged cross section for a particular energy and strength of magnetic field. Extending the state structure to the hyperfine level and adding a magnetic term to the close-coupled Hamiltonian is very manageable with these newly developed tools.

Appendix A. Split Operator Derivation

The equivalence of the split operator to the the propagator can be shown by use of a Taylor Series expansion. Setting $\lambda = -it/\hbar$ the expansion of the propagator up to third order is:

$$\begin{aligned} e^{\lambda(\widehat{\mathbf{T}}+\widehat{\mathbf{V}})} &= 1 + \lambda(\widehat{\mathbf{T}}+\widehat{\mathbf{V}}) + \frac{\lambda^2}{2!}(\widehat{\mathbf{T}}+\widehat{\mathbf{V}})^2 + \frac{\lambda^3}{3!}(\widehat{\mathbf{T}}+\widehat{\mathbf{V}})^3 + ... \\ &= 1 + \lambda\widehat{\mathbf{T}} + \lambda\widehat{\mathbf{V}} + \frac{\lambda^2}{2!}(\widehat{\mathbf{T}}^2 + \widehat{\mathbf{T}}\widehat{\mathbf{V}} + \widehat{\mathbf{V}}\widehat{\mathbf{T}} + \widehat{\mathbf{V}}^2) \\ &+ \frac{\lambda^3}{3!}(\widehat{\mathbf{T}}^3 + \widehat{\mathbf{T}}\widehat{\mathbf{V}}\widehat{\mathbf{T}} + \widehat{\mathbf{V}}\widehat{\mathbf{T}}^2 + \widehat{\mathbf{V}}^2\widehat{\mathbf{T}} + \widehat{\mathbf{T}}^2\widehat{\mathbf{V}} + \widehat{\mathbf{T}}\widehat{\mathbf{V}}^2 + \widehat{\mathbf{V}}\widehat{\mathbf{T}}\widehat{\mathbf{V}} + \widehat{\mathbf{V}}^3) + ... \end{aligned} \quad (241)$$

Now expanding the kinetic referenced split operator up to $\mathcal{O}(\lambda^3)$ using the same expansions:

$$\begin{aligned} & e^{\lambda(\widehat{\mathbf{T}}/2)}e^{\lambda\widehat{\mathbf{V}}}e^{\lambda(\widehat{\mathbf{T}}/2)} \approx \left[1 + \frac{\lambda\widehat{\mathbf{T}}}{2} + \left(\frac{\lambda}{2}\right)^2\frac{\widehat{\mathbf{T}}^2}{2!} + \left(\frac{\lambda}{2}\right)^3\frac{\widehat{\mathbf{T}}^3}{3!}\right]\left[1 + \frac{\lambda\widehat{\mathbf{V}}}{2} + \frac{\lambda^2\widehat{\mathbf{V}}^2}{2!} + \frac{\lambda^3 V^3}{3!}\right] \times \\ & \left[1 + \frac{\lambda\widehat{\mathbf{T}}}{2} + \left(\frac{\lambda}{2}\right)^2\frac{\widehat{\mathbf{T}}^2}{2!} + \left(\frac{\lambda}{2}\right)^3\frac{\widehat{\mathbf{T}}^3}{3!}\right] \\ & \approx \left[1 + \lambda\widehat{\mathbf{V}} + \frac{\lambda^2\widehat{\mathbf{V}}^2}{2!} + \frac{\lambda^3 V^3}{3!} + \frac{\lambda\widehat{\mathbf{T}}}{2} + \frac{\lambda^2}{2}(\widehat{\mathbf{T}}\widehat{\mathbf{V}}) + \frac{\lambda^3\widehat{\mathbf{T}}\widehat{\mathbf{V}}^2}{2\cdot 2} + \left(\frac{\lambda}{2}\right)\frac{\widehat{\mathbf{T}}^2}{2!} + \frac{\lambda^3}{2^2}\frac{\widehat{\mathbf{T}}^2\widehat{\mathbf{V}}}{2!} + \left(\frac{\lambda}{2}\right)^3\frac{\widehat{\mathbf{T}}^3}{3!}\right] \times \\ & \left[1 + \frac{\lambda\widehat{\mathbf{V}}}{2} + \frac{\lambda^2\widehat{\mathbf{V}}^2}{2!} + \frac{\lambda^3\widehat{\mathbf{V}}^3}{3!}\right] \\ & \approx 1 + \lambda\left(\frac{\widehat{\mathbf{T}}}{2} + \widehat{\mathbf{V}} + \frac{\widehat{\mathbf{T}}}{2}\right) + \lambda^2\left(\frac{1}{4}\frac{\widehat{\mathbf{T}}^2}{2!} + \frac{1}{2}\widehat{\mathbf{V}}\widehat{\mathbf{T}} + \frac{\widehat{\mathbf{V}}^2}{2!} + \frac{1}{4}\widehat{\mathbf{T}}^2 + \frac{1}{2}\widehat{\mathbf{T}}\widehat{\mathbf{V}} + \frac{1}{4}\frac{\widehat{\mathbf{T}}^2}{2!}\right) + \mathcal{O}(\lambda^3) \\ & \approx 1 + \lambda\widehat{\mathbf{T}} + \lambda\widehat{\mathbf{V}} + \frac{\lambda^2}{2!}(\widehat{\mathbf{T}}^2 + \widehat{\mathbf{T}}\widehat{\mathbf{V}} + \widehat{\mathbf{V}}\widehat{\mathbf{T}} + \widehat{\mathbf{V}}^2) + \mathcal{O}(\lambda^3) \end{aligned} \quad (242)$$

Through these expansions we see the split operator is indeed equivalent up to third order in time with the propagator. One can also make a potential referenced second order split operator by swapping $\widehat{\mathbf{T}}$ and $\widehat{\mathbf{V}}$ before the initial expansion. The derivation that follows presents the same conclusion so either second order split may be used.

One can further split the operator such that it is accurate up to third order. Bandrauk and Shen[4] showed that the following split of the propagator is more efficient than the above second order split operator:

$$e^{\lambda(\widehat{\mathbf{T}}+\widehat{\mathbf{V}})} \approx e^{\gamma\lambda\widehat{\mathbf{T}}/2} e^{\gamma\lambda\widehat{\mathbf{V}}} e^{(1-\gamma)\lambda\widehat{\mathbf{T}}/2} e^{(1-2\gamma)\lambda\widehat{\mathbf{V}}} e^{(1-\gamma)\lambda\widehat{\mathbf{T}}/2} e^{\gamma\lambda\widehat{\mathbf{V}}} e^{\gamma\lambda\widehat{\mathbf{T}}/2} \tag{243}$$

where $\gamma = 1/(2 - 2^{1/3})$. The advantage of this split is that the error correction would be on the order of $(\Delta t)^4$ so if necessary a bigger time step may be used and convergence still achieved.

Appendix B. Spin-Orbit Configuration Interaction PES

This appendix displays the M+Ng spin-orbit configuration interaction potential energy surfaces in both the adiabatic and diabatic forms.

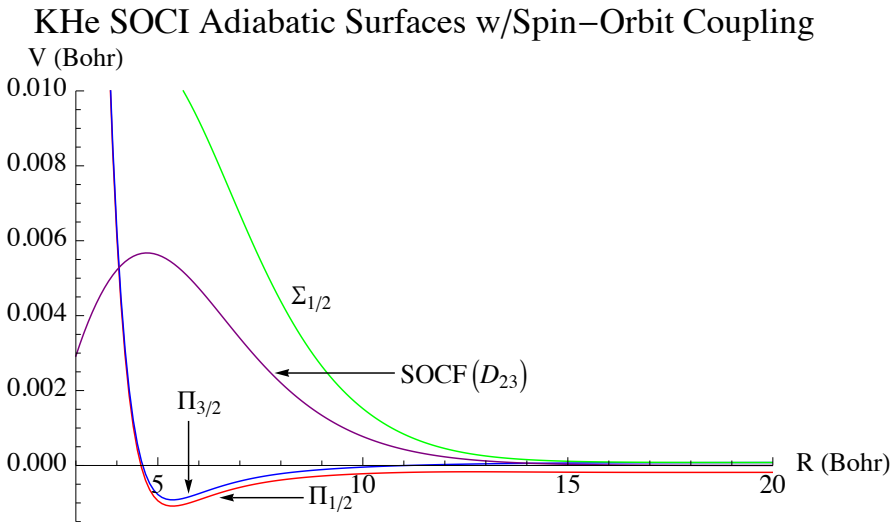

Figure 97. KHe Spin-Orbit CI Adiabatic PES w/Spin-Orbit Coupling.

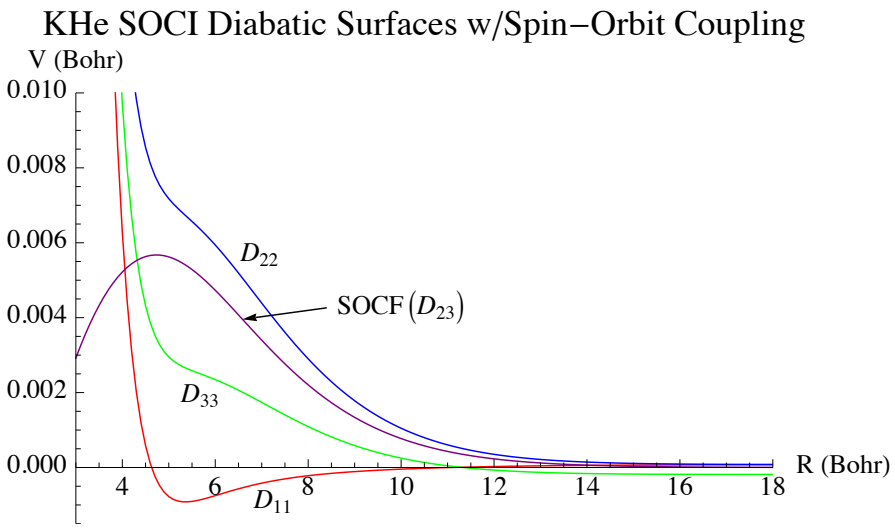

Figure 98. KHe Spin-Orbit CI Diabatic PES w/Spin-Orbit Coupling.

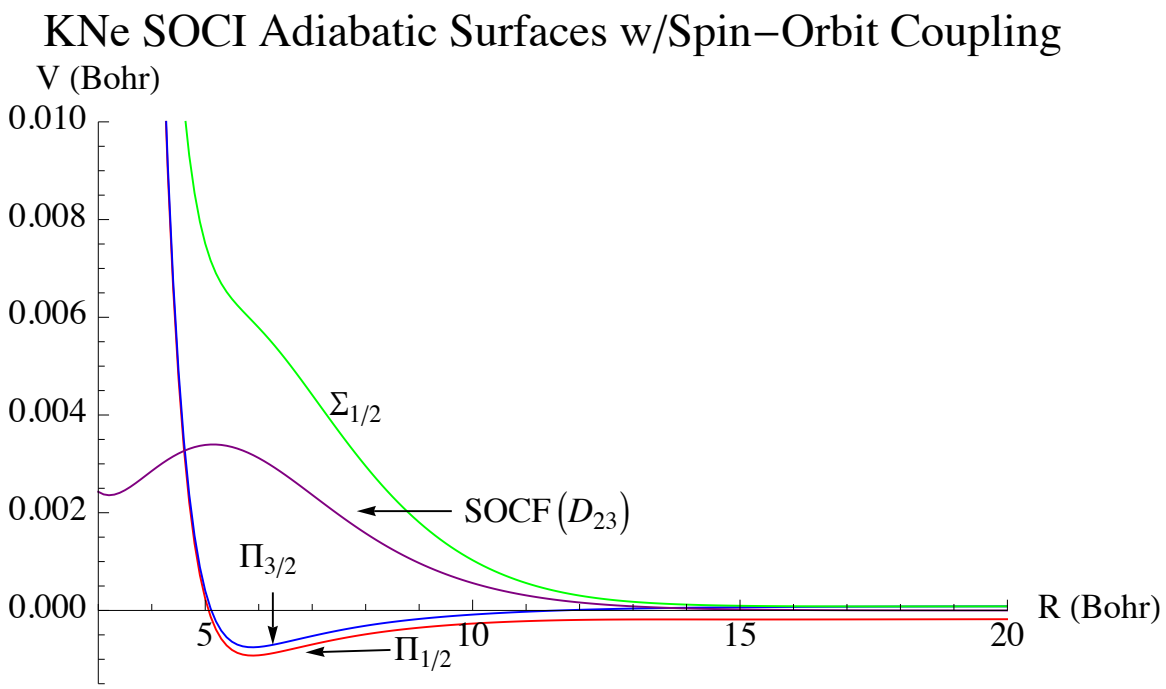

Figure 99. KNe Spin-Orbit CI Adiabatic PES w/Spin-Orbit Coupling.

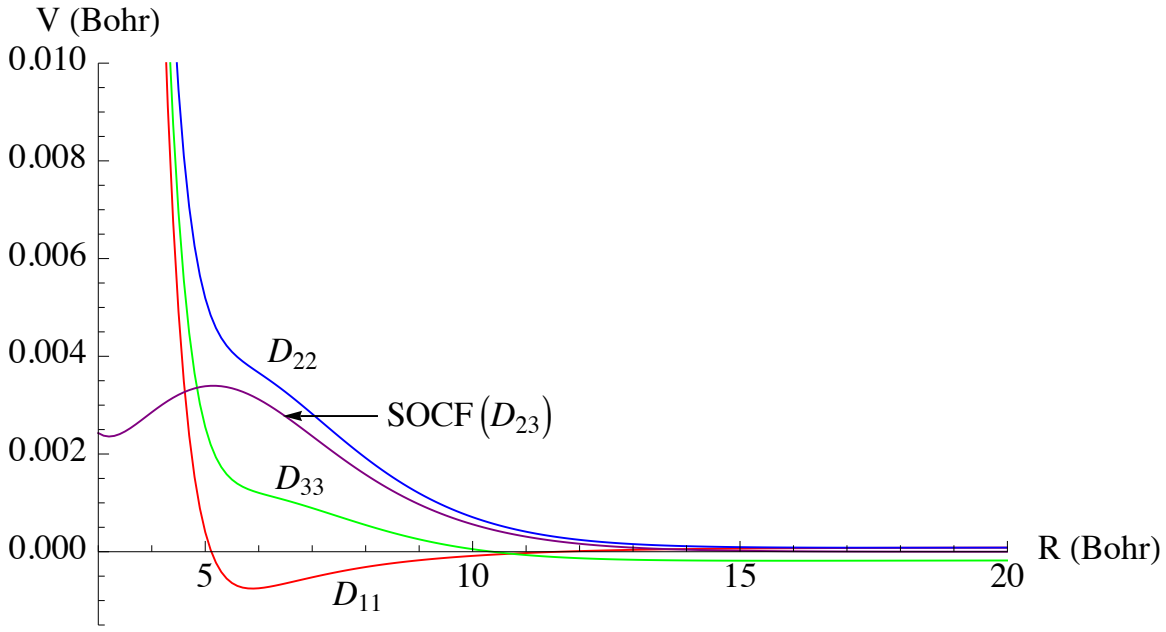

Figure 100. KNe Spin-Orbit CI Diabatic PES w/Spin-Orbit Coupling.

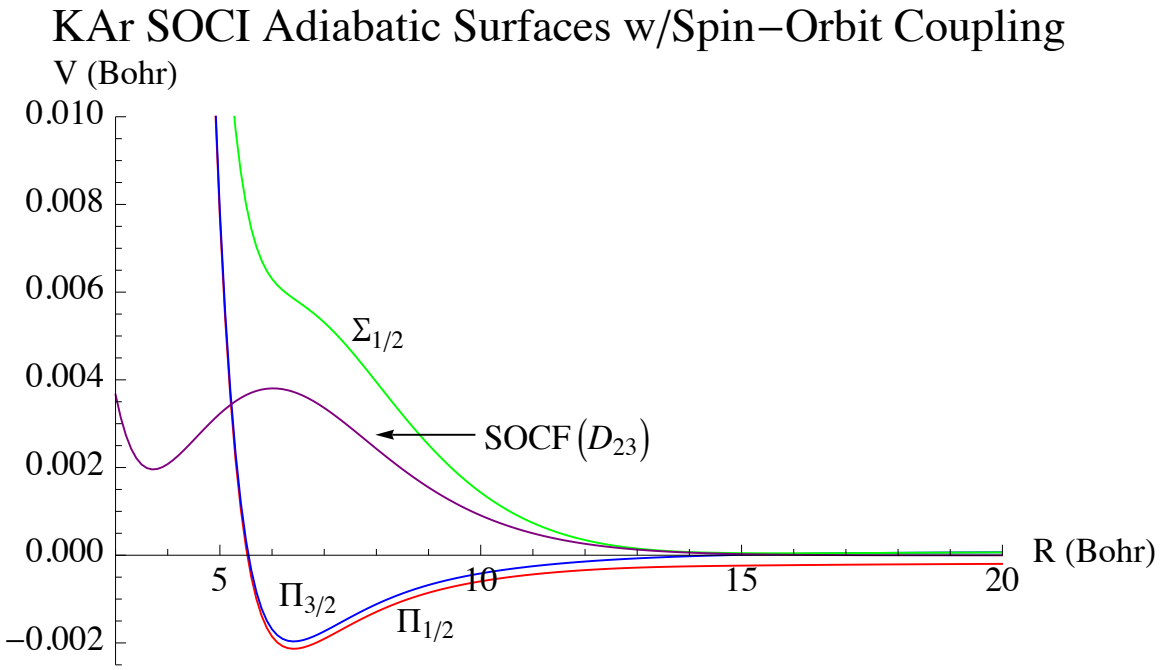

Figure 101. KAr Spin-Orbit CI Adiabatic PES w/Spin-Orbit Coupling.

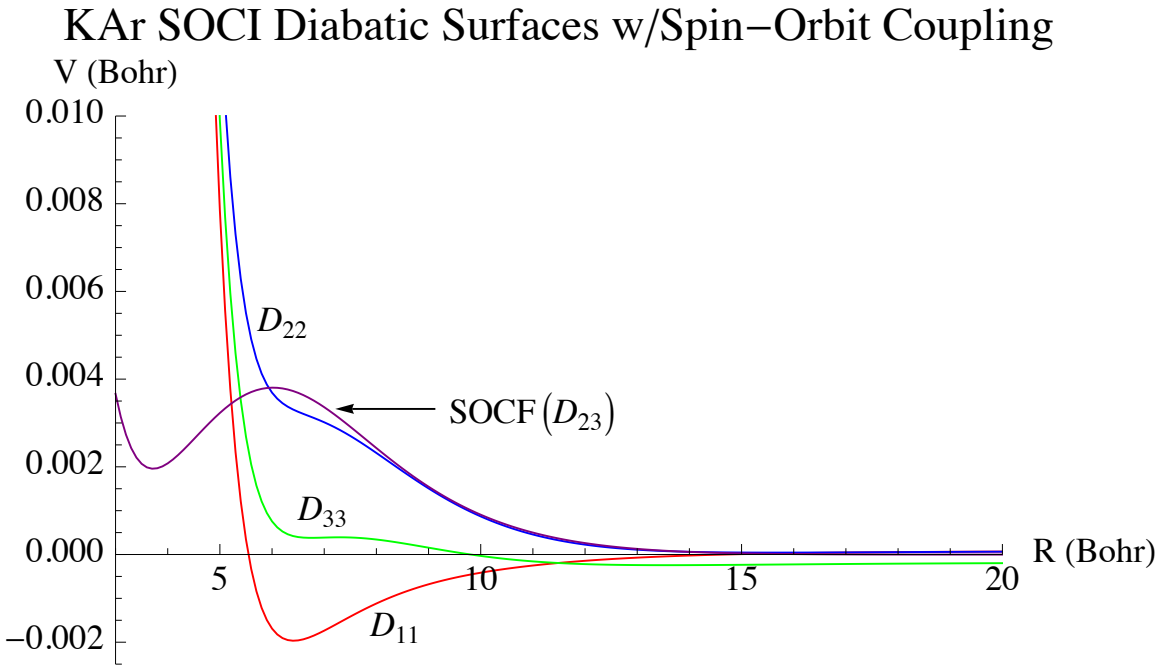

Figure 102. KAr Spin-Orbit CI Diabatic PES w/Spin-Orbit Coupling.

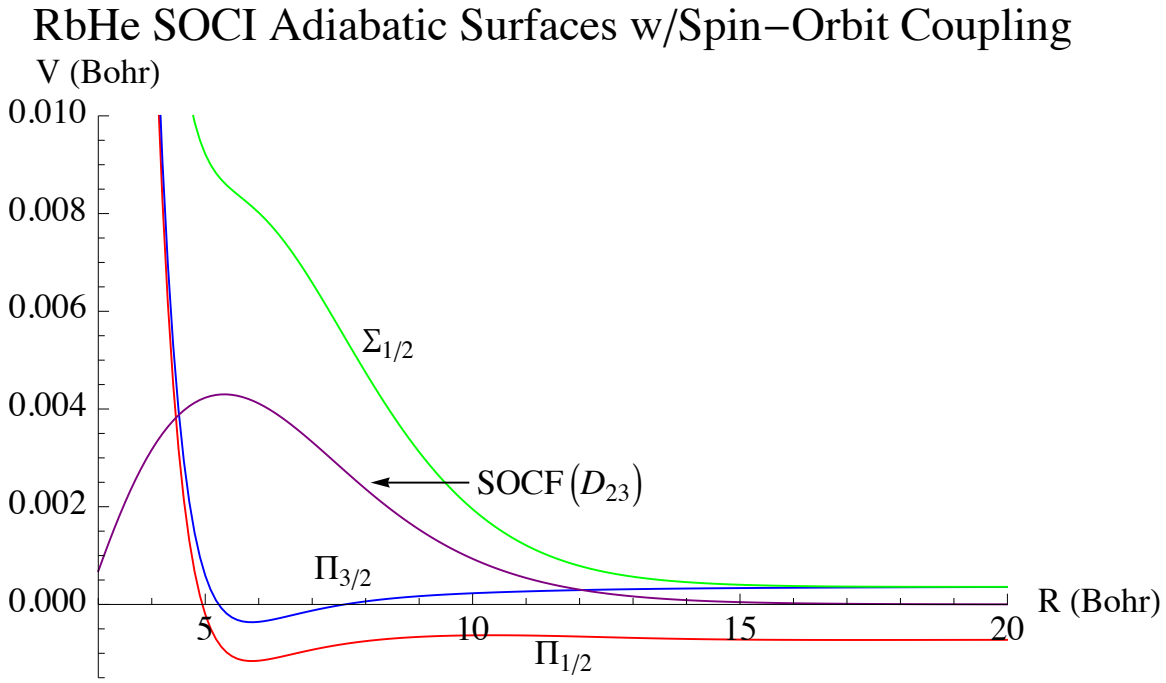

Figure 103. RbHe Spin-Orbit CI Adiabatic PES w/Spin-Orbit Coupling.

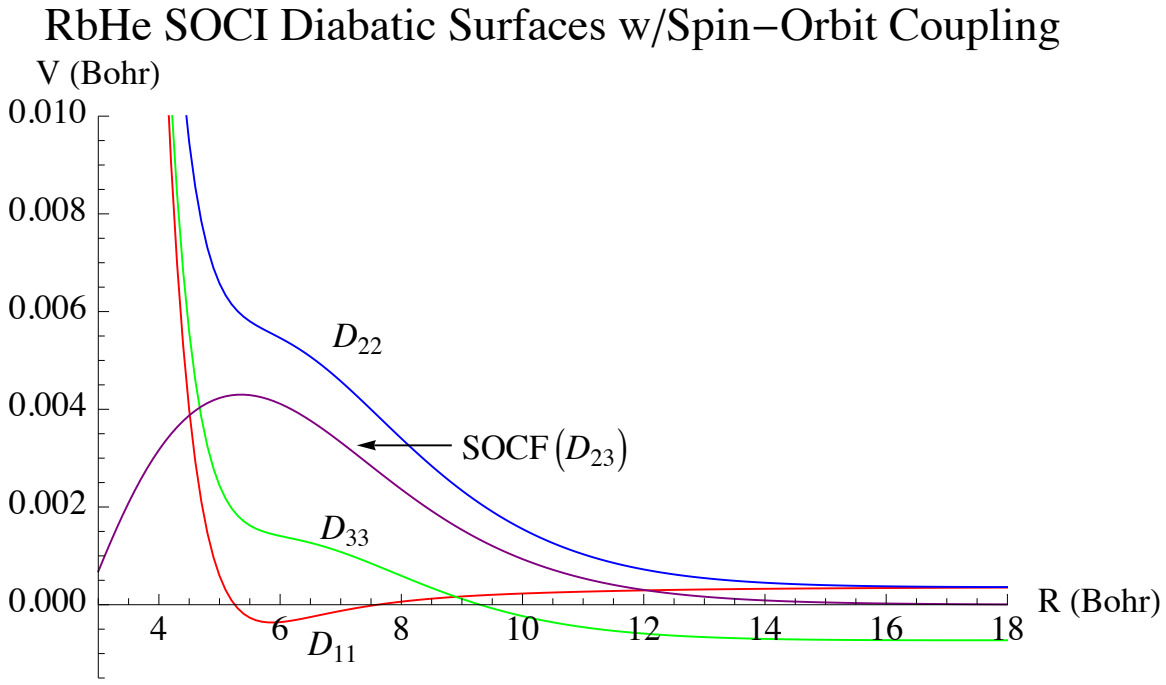

Figure 104. RbHe Spin-Orbit CI Diabatic PES w/Spin-Orbit Coupling.

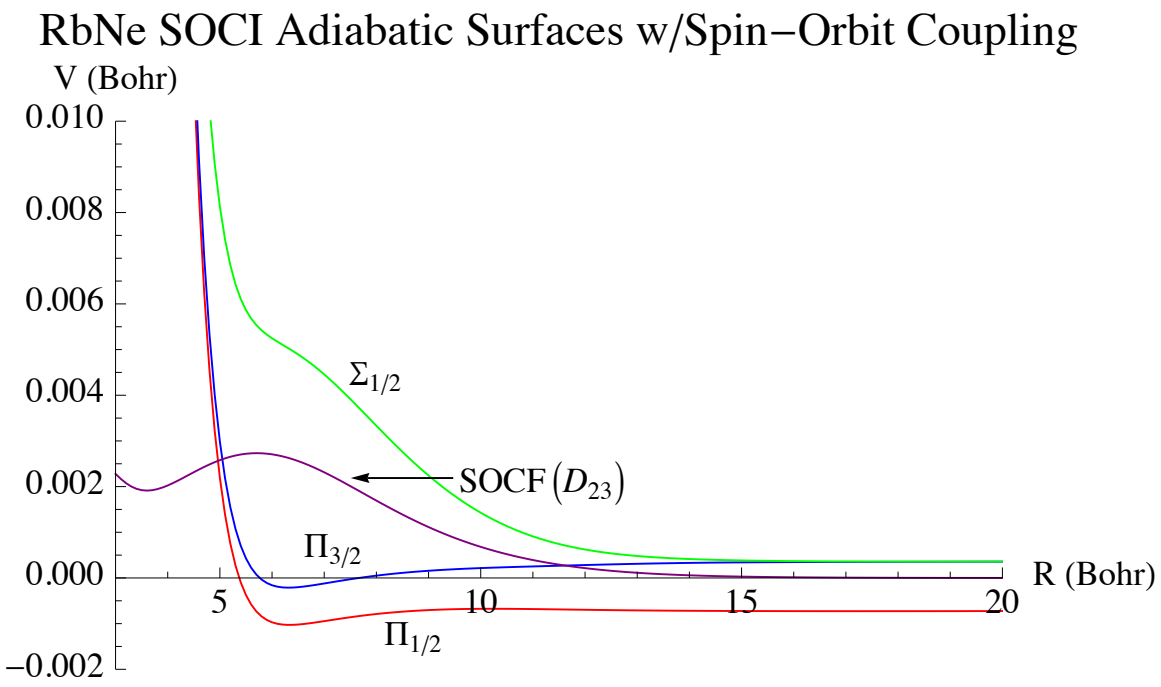

Figure 105. RbNe Spin-Orbit CI Adiabatic PES w/Spin-Orbit Coupling.

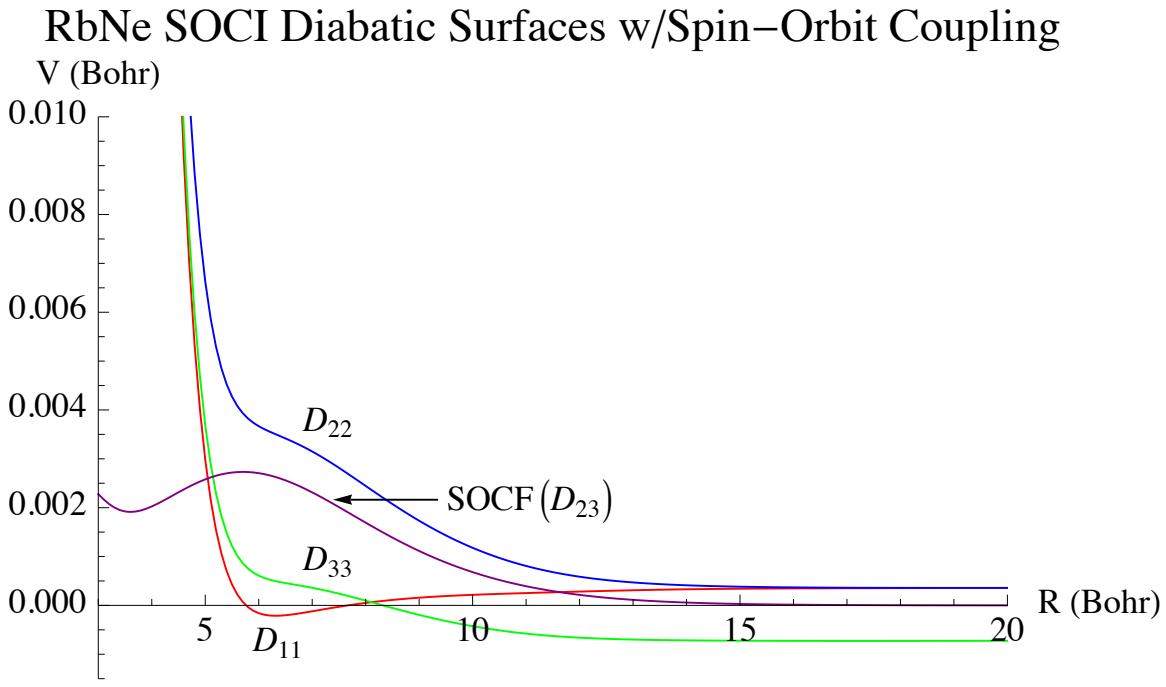

Figure 106. RbNe Spin-Orbit CI Diabatic PES w/Spin-Orbit Coupling.

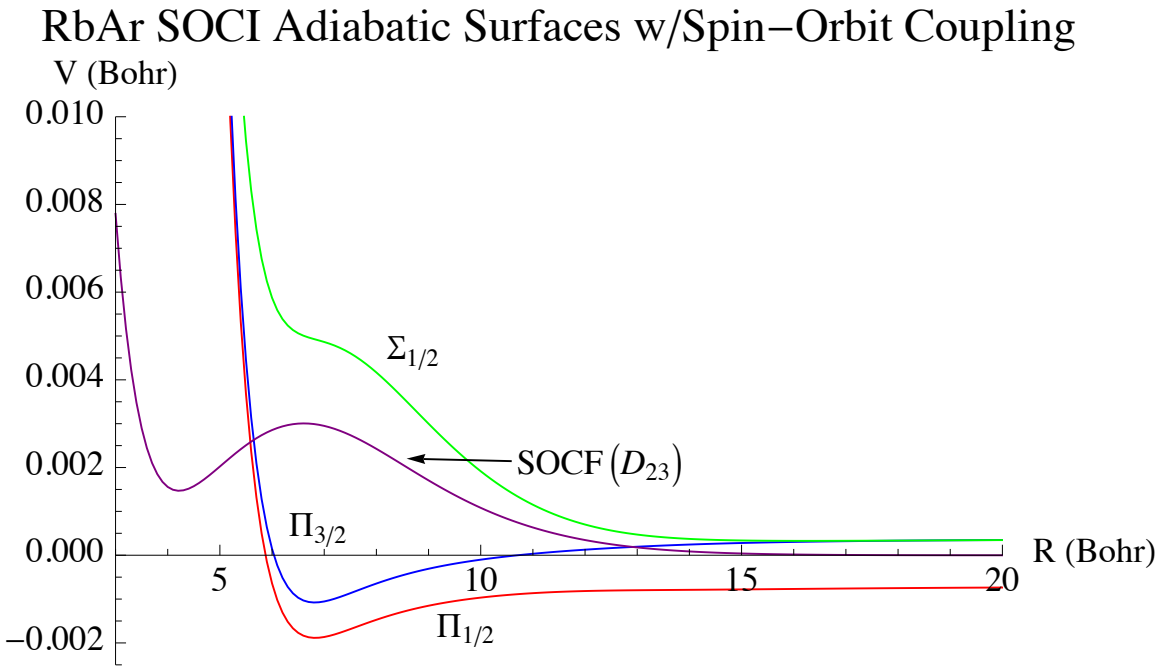

Figure 107. RbAr Spin-Orbit CI Adiabatic PES w/Spin-Orbit Coupling.

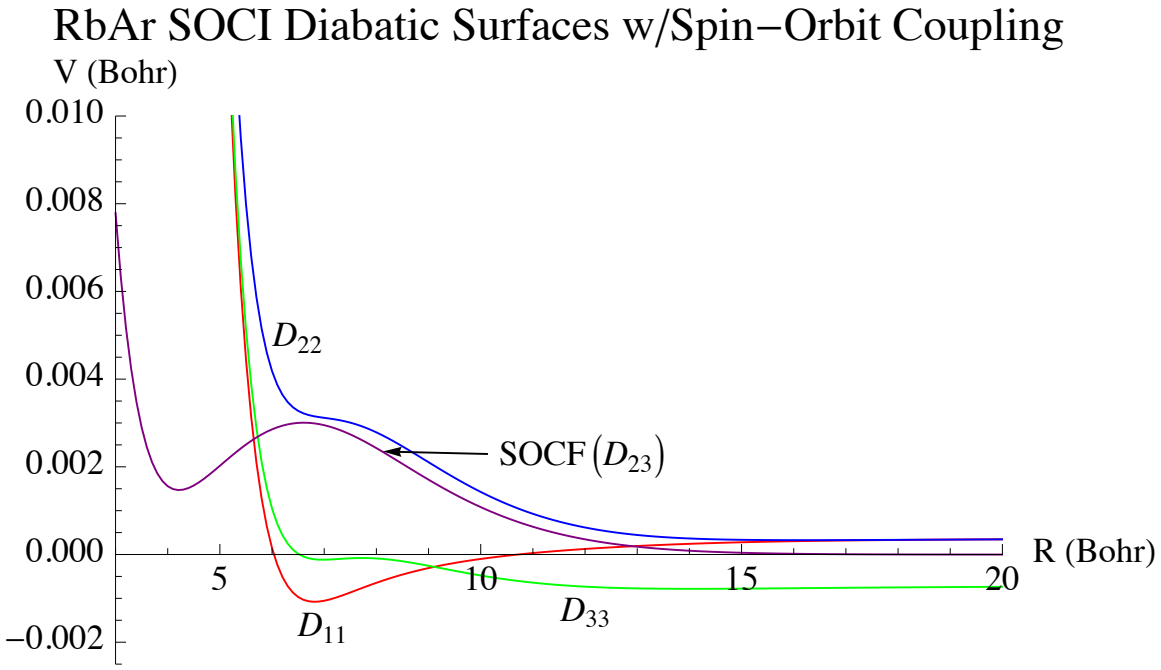

Figure 108. RbAr Spin-Orbit CI Diabatic PES w/Spin-Orbit Coupling.

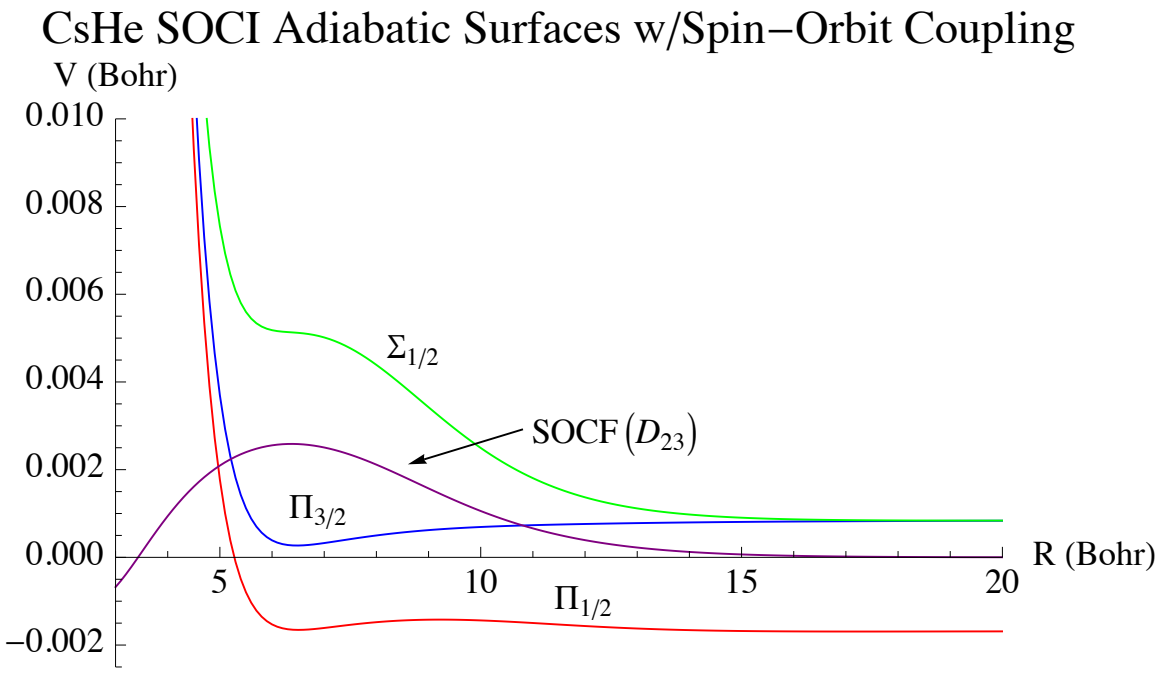

Figure 109. CsHe Spin-Orbit CI Adiabatic PES w/Spin-Orbit Coupling.

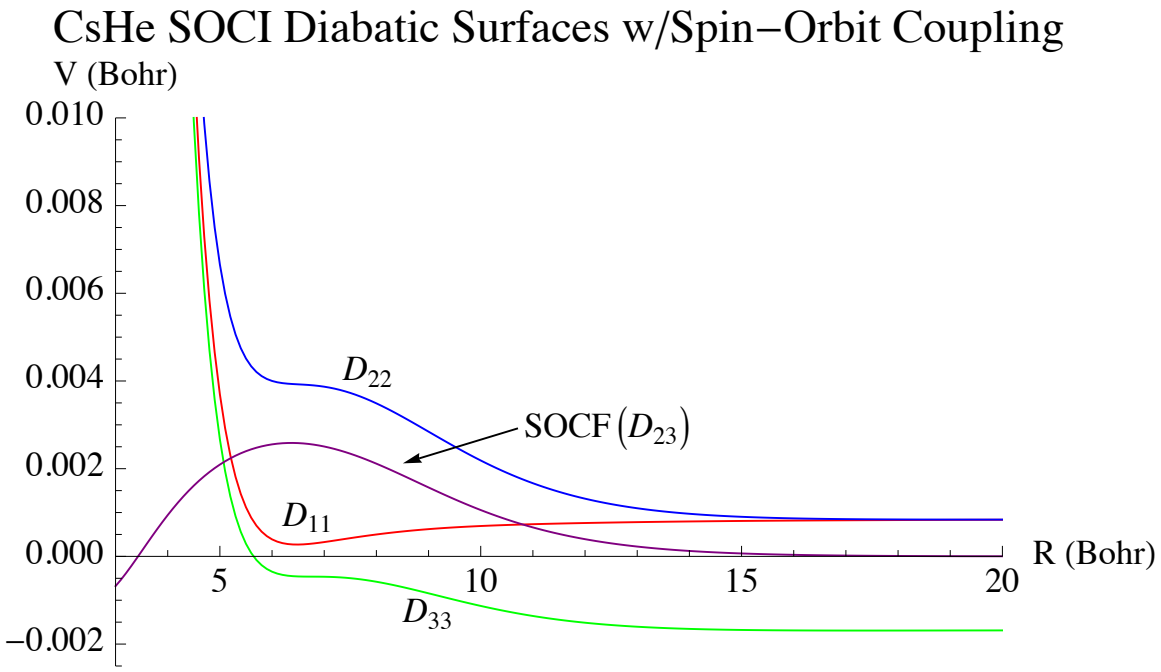

Figure 110. CsHe Spin-Orbit CI Diabatic PES w/Spin-Orbit Coupling.

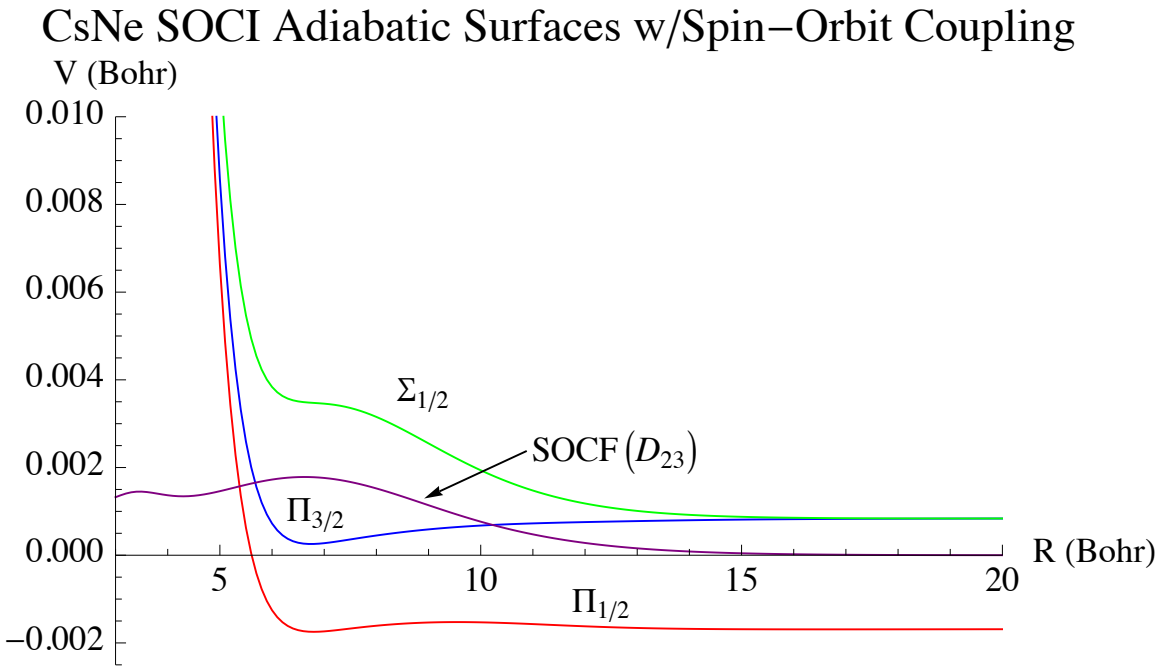

Figure 111. CsNe Spin-Orbit CI Adiabatic PES w/Spin-Orbit Coupling.

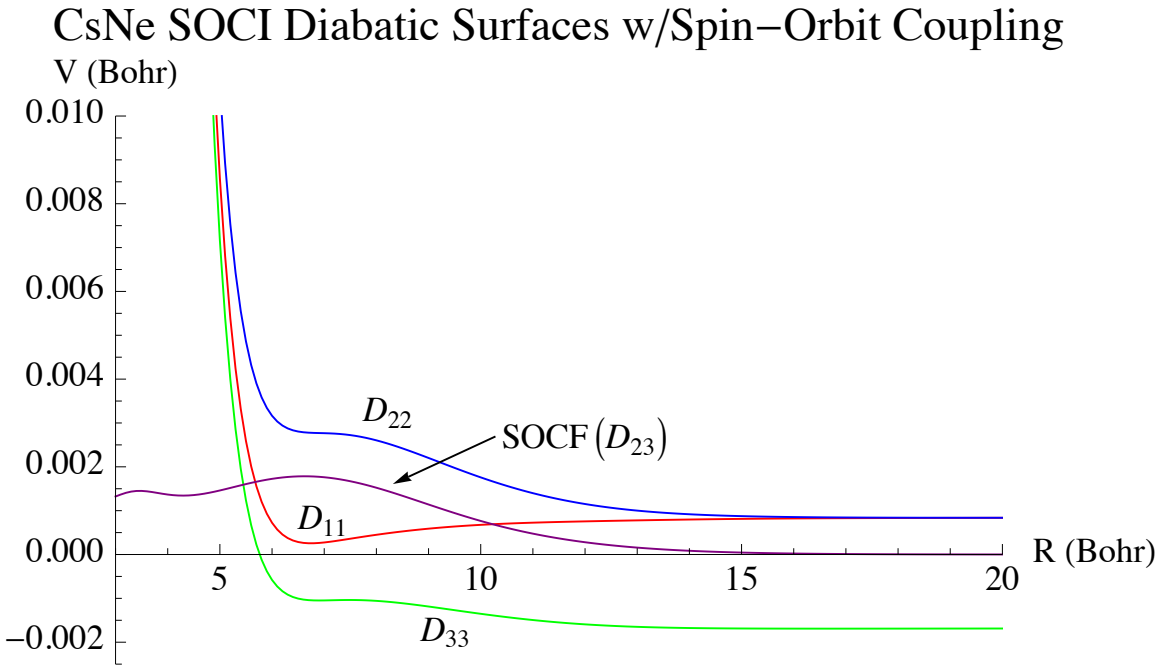

Figure 112. CsNe Spin-Orbit CI Diabatic PES w/Spin-Orbit Coupling.

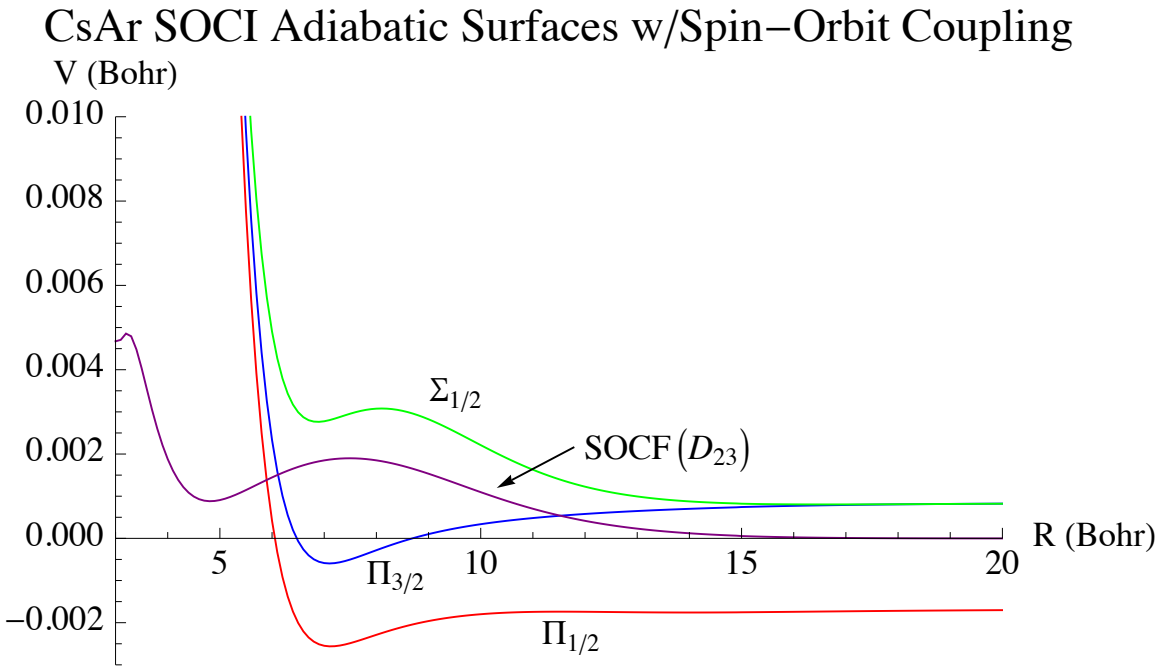

Figure 113. CsAr Spin-Orbit CI Adiabatic PES w/Spin-Orbit Coupling.

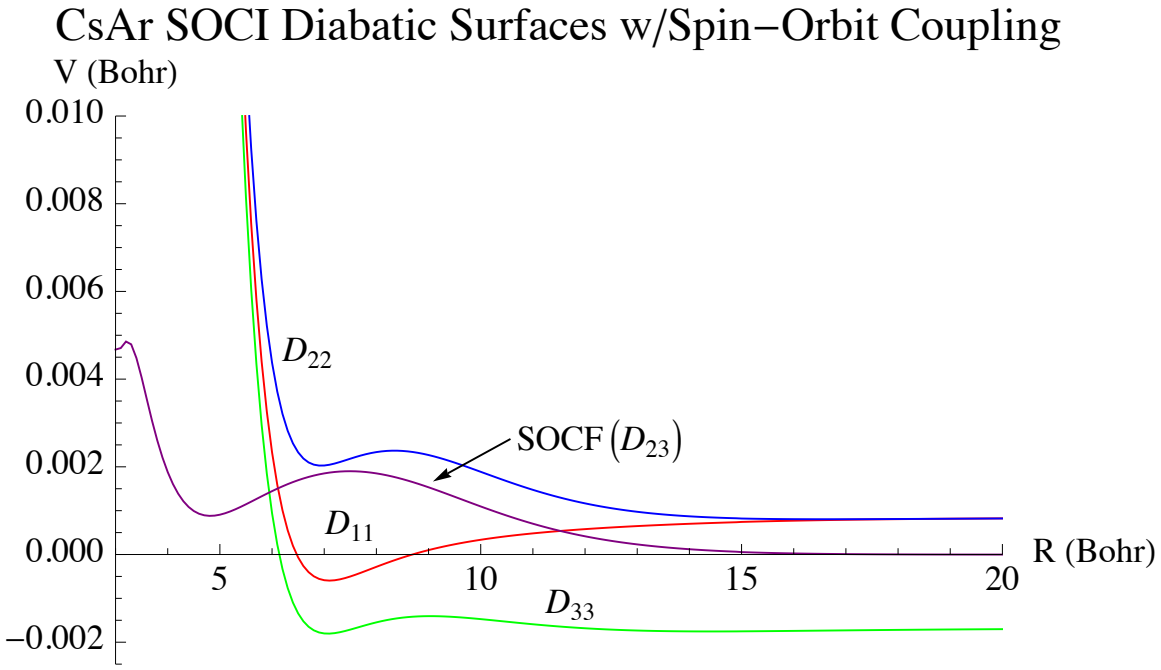

Figure 114. CsAr Spin-Orbit CI Diabatic PES w/Spin-Orbit Coupling.

Appendix C. Non Spin-Orbit CI PES

This appendix displays the M+Ng non spin-orbit configuration interaction potential energy surfaces along with the spin-orbit parameter $a(R)$.

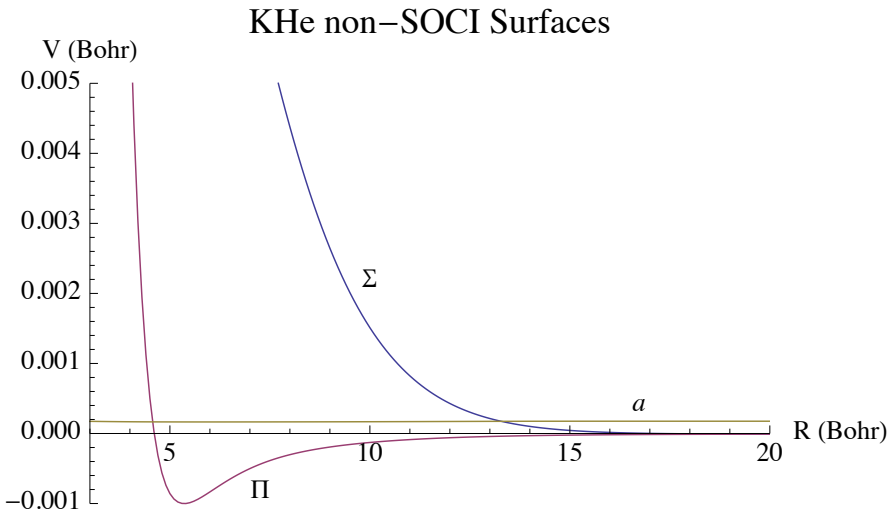

Figure 115. KHe Non Spin-Orbit CI PES w/ Spin-Orbit Parameter $a(R)$.

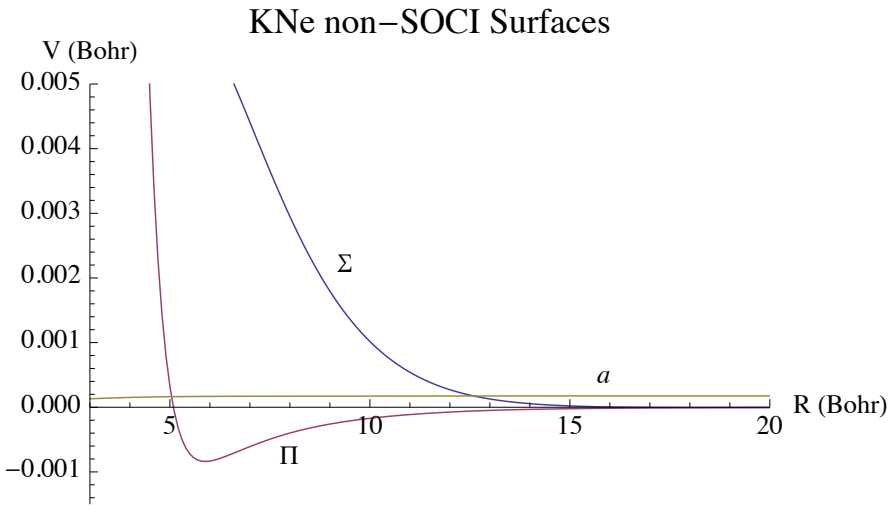

Figure 116. KNe Non Spin-Orbit CI PES w/ Spin-Orbit Parameter $a(R)$.

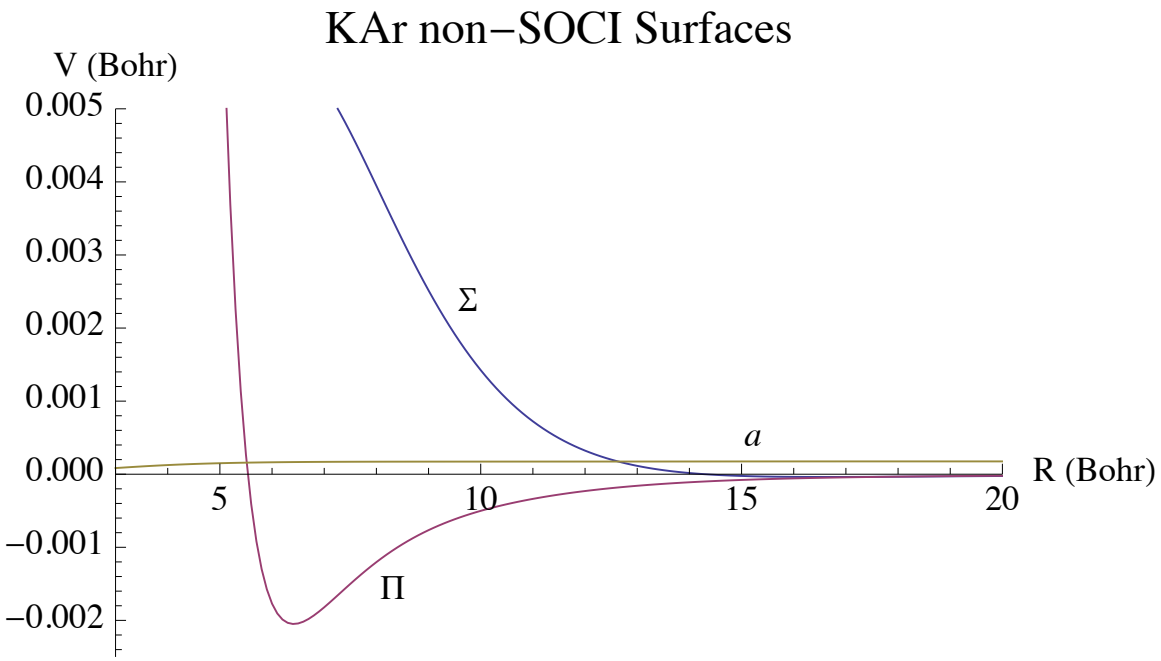

Figure 117. KAr Non Spin-Orbit CI PES w/ Spin-Orbit Parameter $a(R)$.

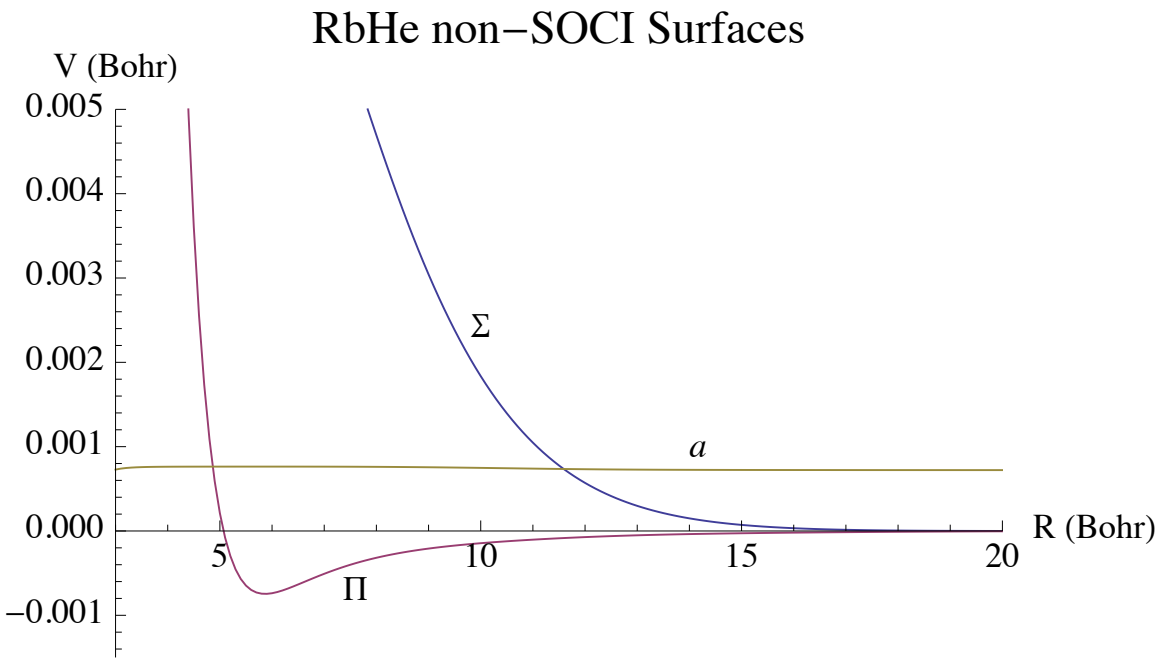

Figure 118. RbHe Non Spin-Orbit CI PES w/ Spin-Orbit Parameter $a(R)$.

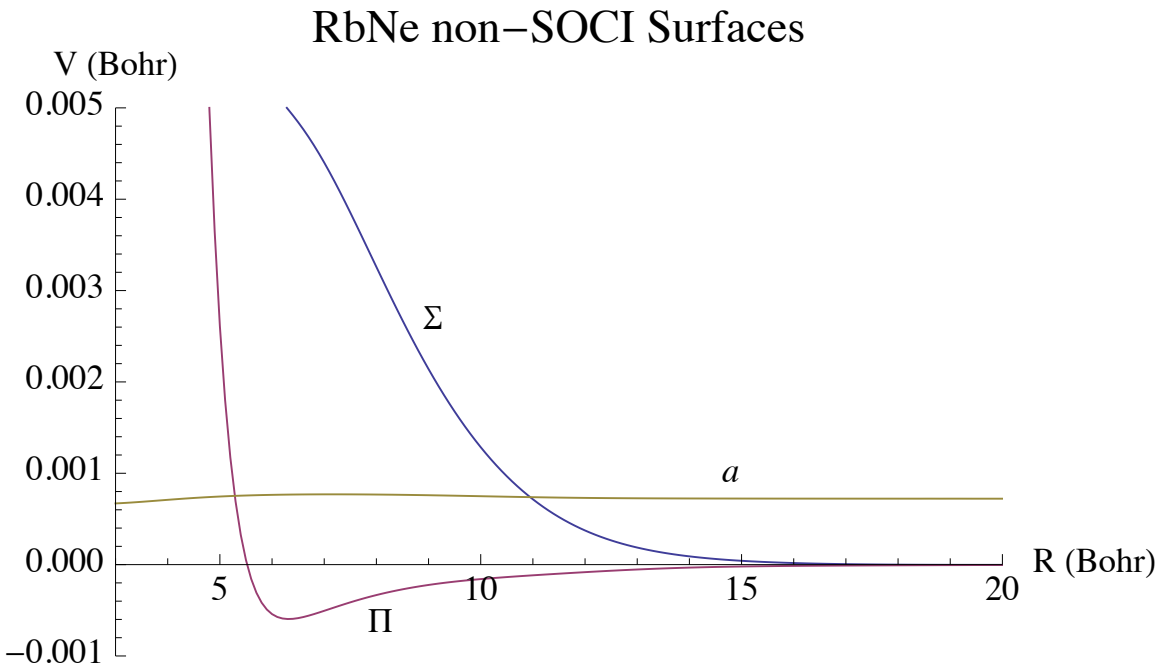

Figure 119. RbNe Non Spin-Orbit CI PES w/ Spin-Orbit Parameter $a(R)$.

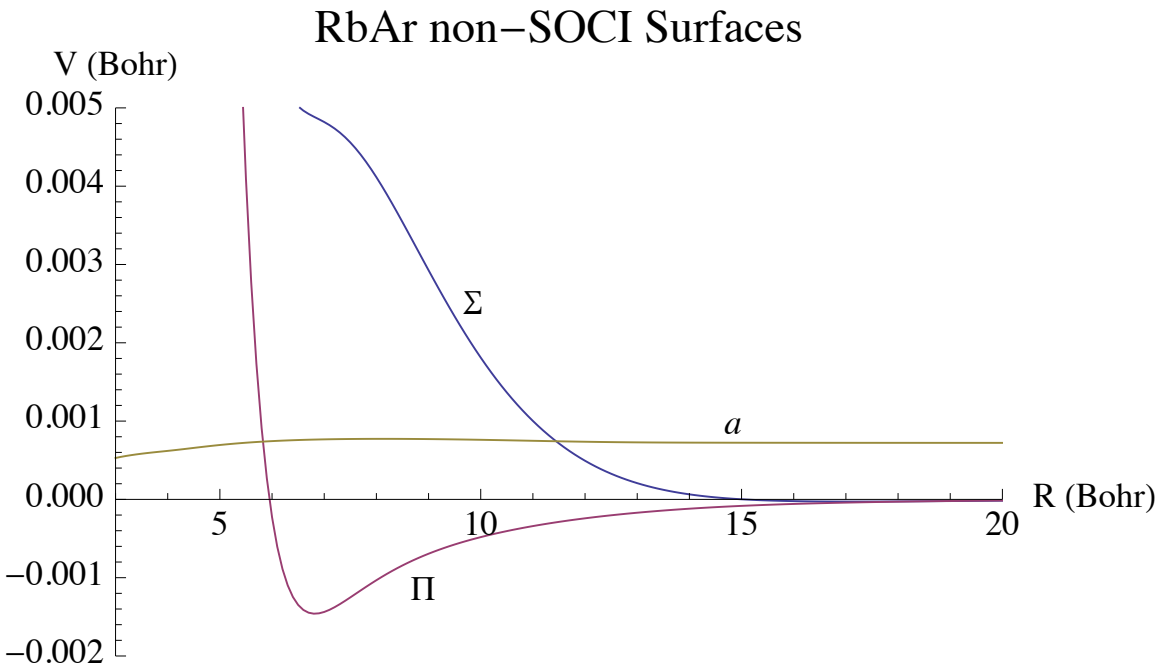

Figure 120. RbAr Non Spin-Orbit CI PES w/ Spin-Orbit Parameter $a(R)$.

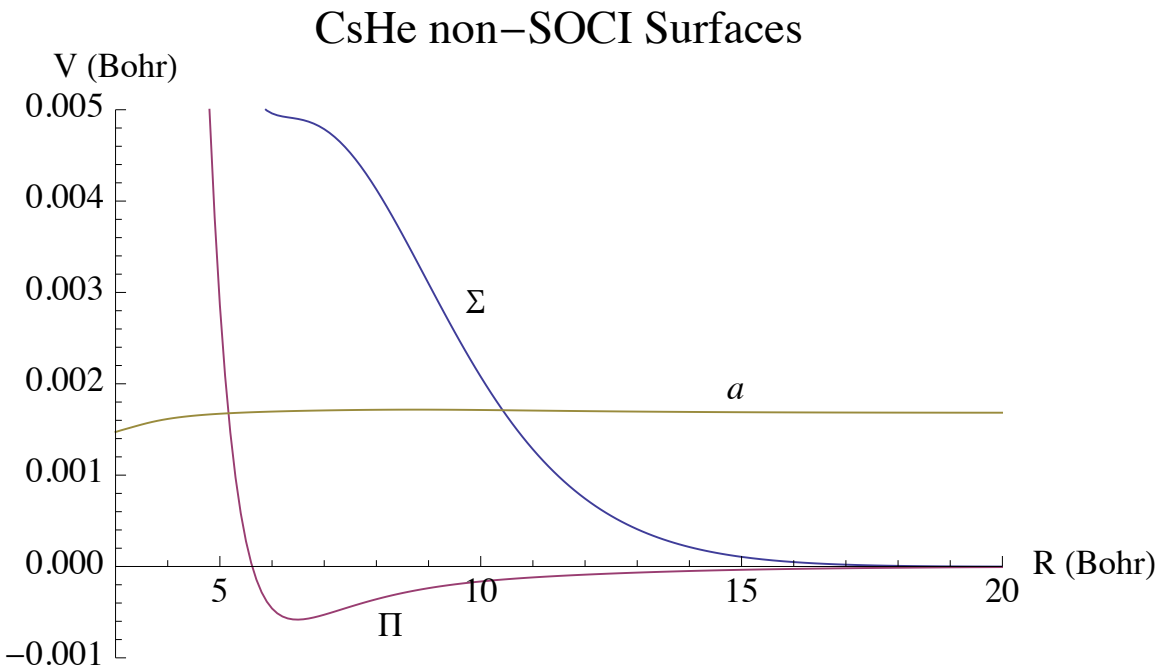

Figure 121. CsHe Non Spin-Orbit CI PES w/ Spin-Orbit Parameter $a(R)$.

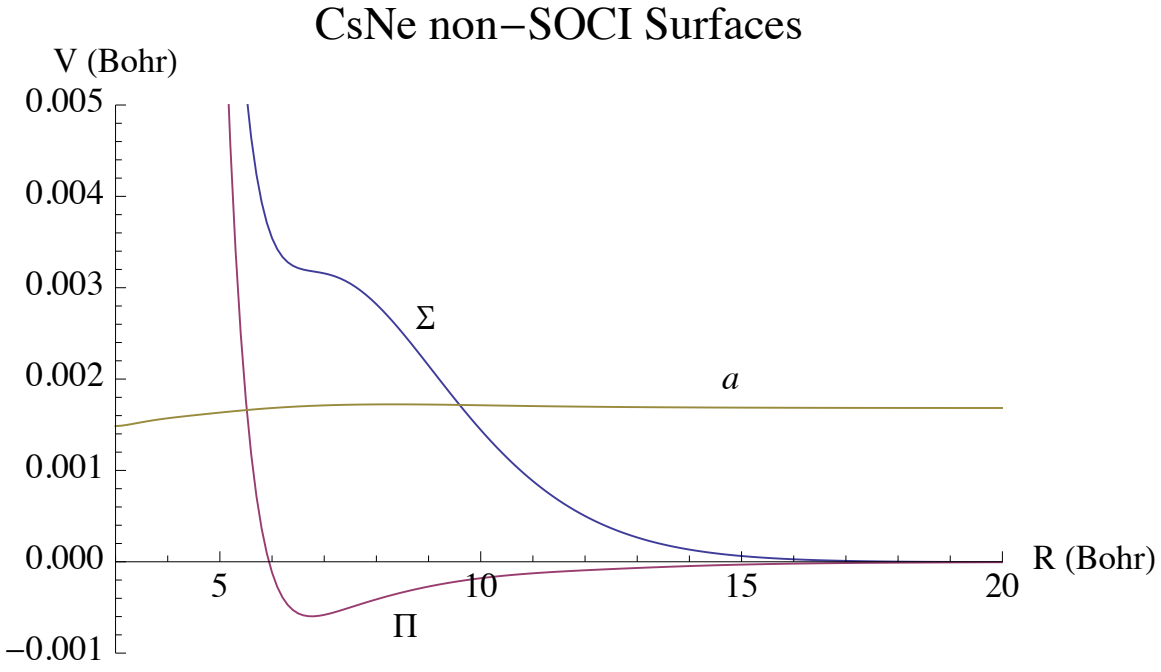

Figure 122. CsNe Non Spin-Orbit CI PES w/ Spin-Orbit Parameter $a(R)$.

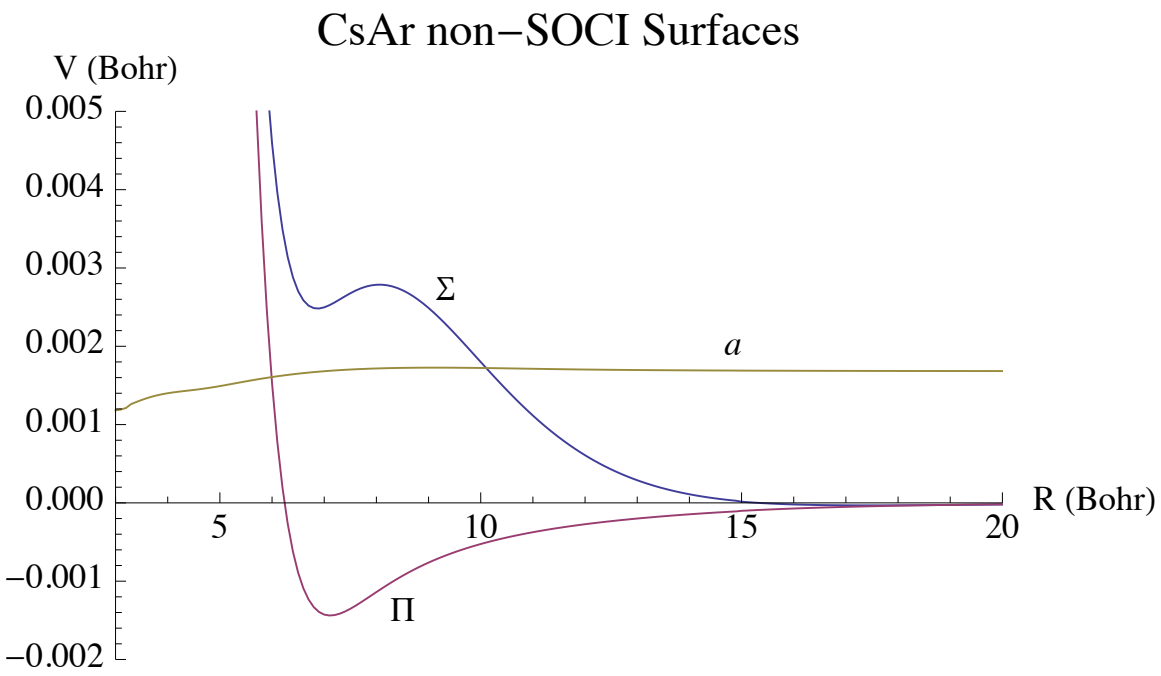

Figure 123. CsAr Non Spin-Orbit CI PES w/ Spin-Orbit Parameter $a(R)$.

Appendix D. Radial Derivative Coupling Term Predictions

This appendix displays the predicted mixing angle and derivative coupling term for the M+Ng systems derived from the non spin-orbit configuration interaction potential energy surfaces.

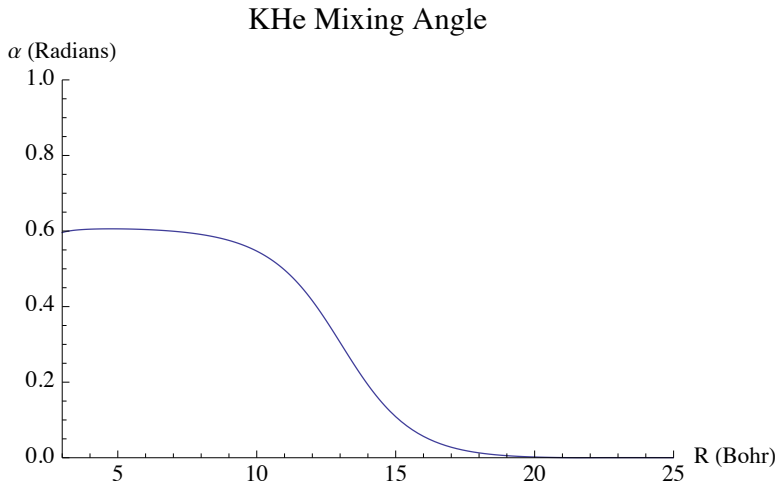

Figure 124. KHe Mixing Angle.

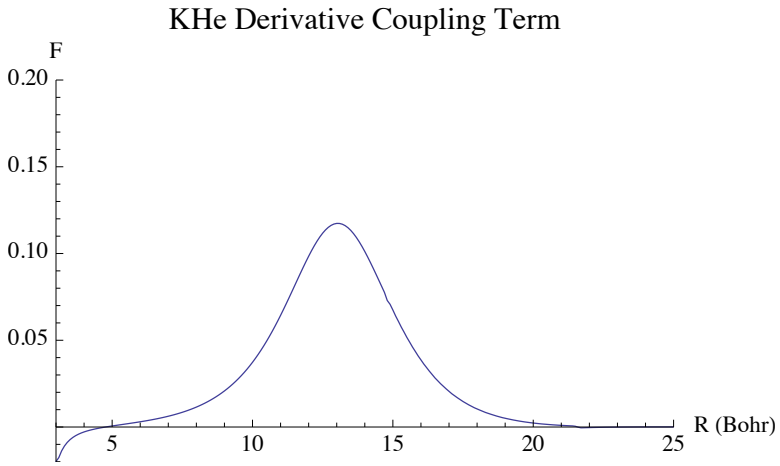

Figure 125. KHe Radial Derivative Coupling Term.

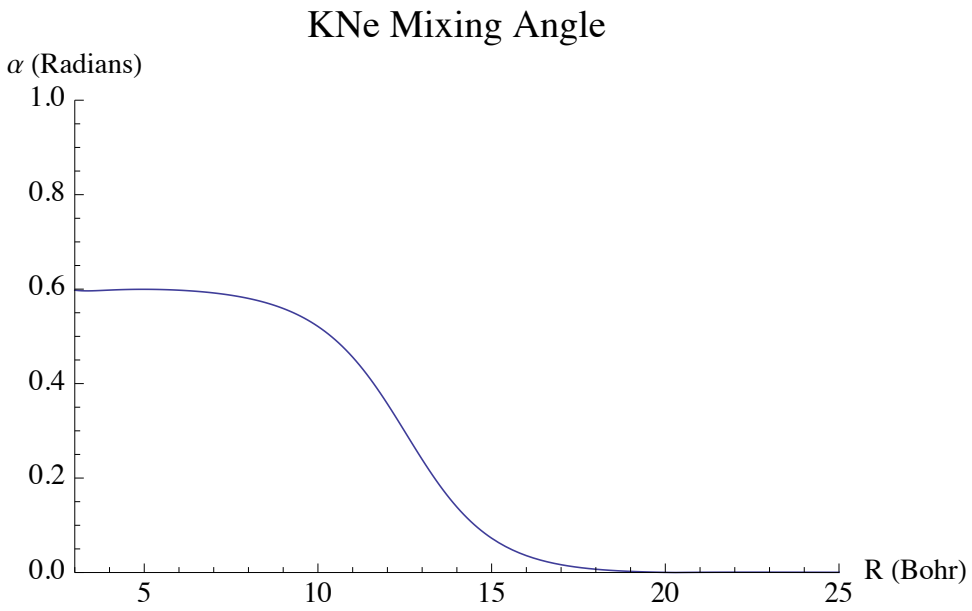

Figure 126. KNe Mixing Angle.

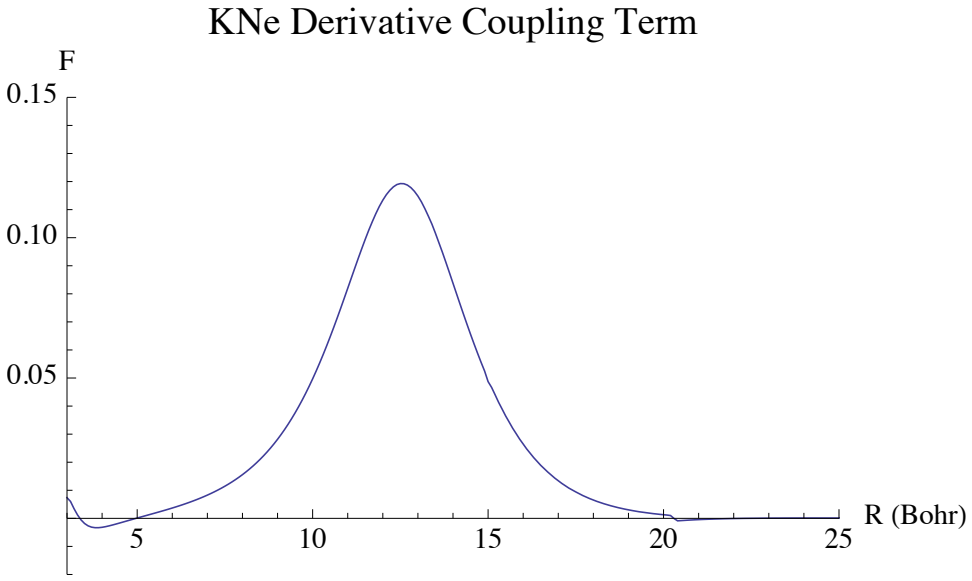

Figure 127. KNe Radial Derivative Coupling Term.

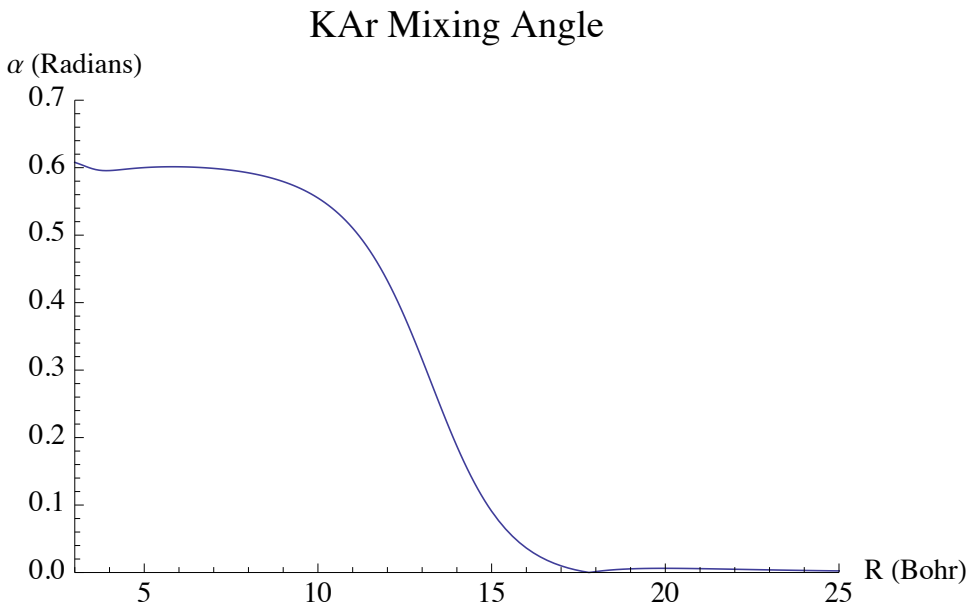

Figure 128. KAr Mixing Angle.

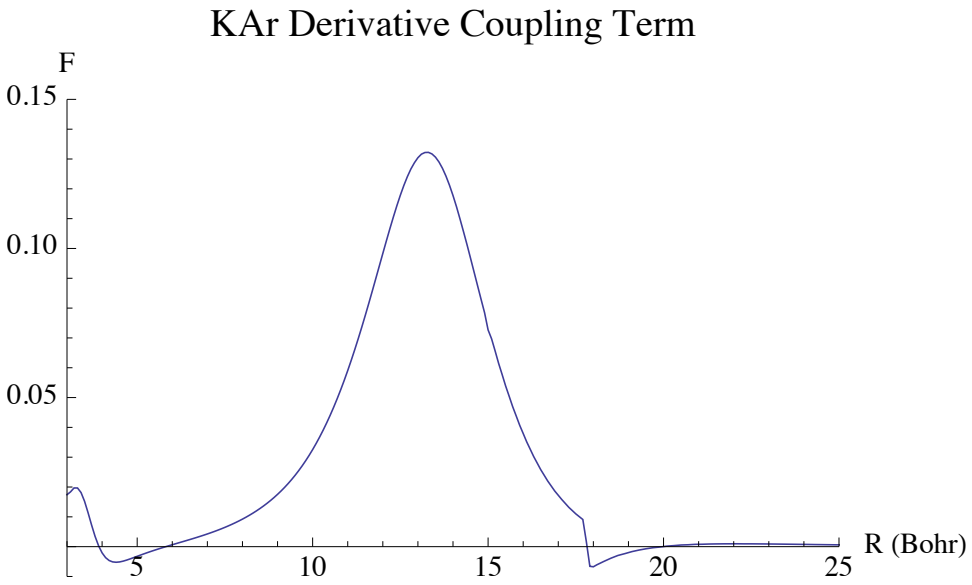

Figure 129. KAr Radial Derivative Coupling Term.

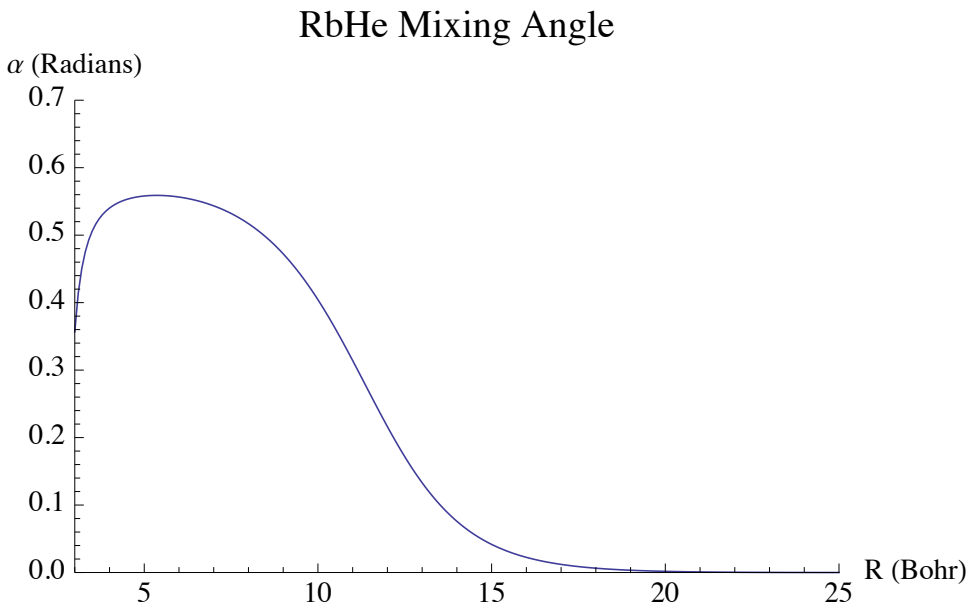

Figure 130. RbHe Mixing Angle.

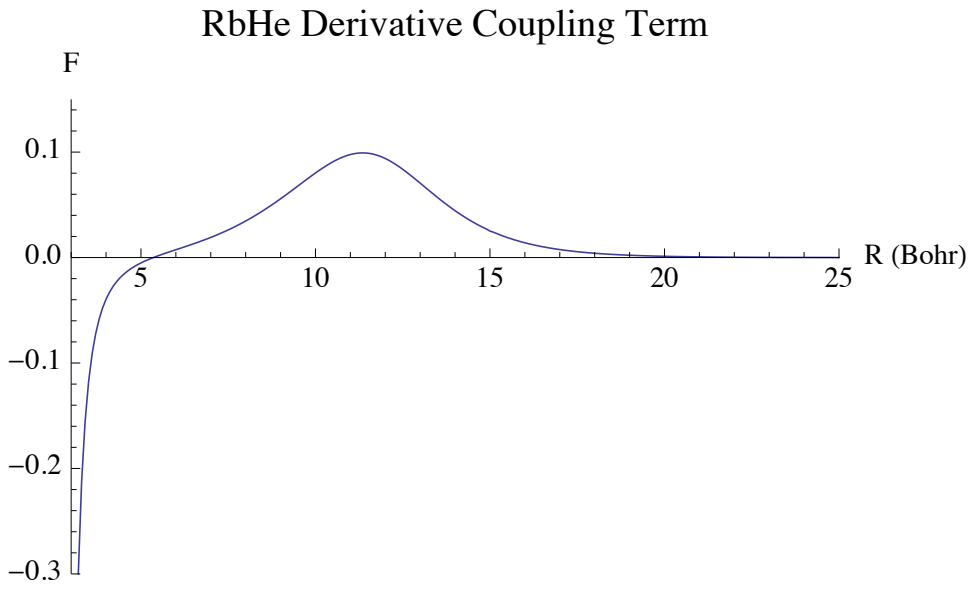

Figure 131. RbHe Radial Derivative Coupling Term.

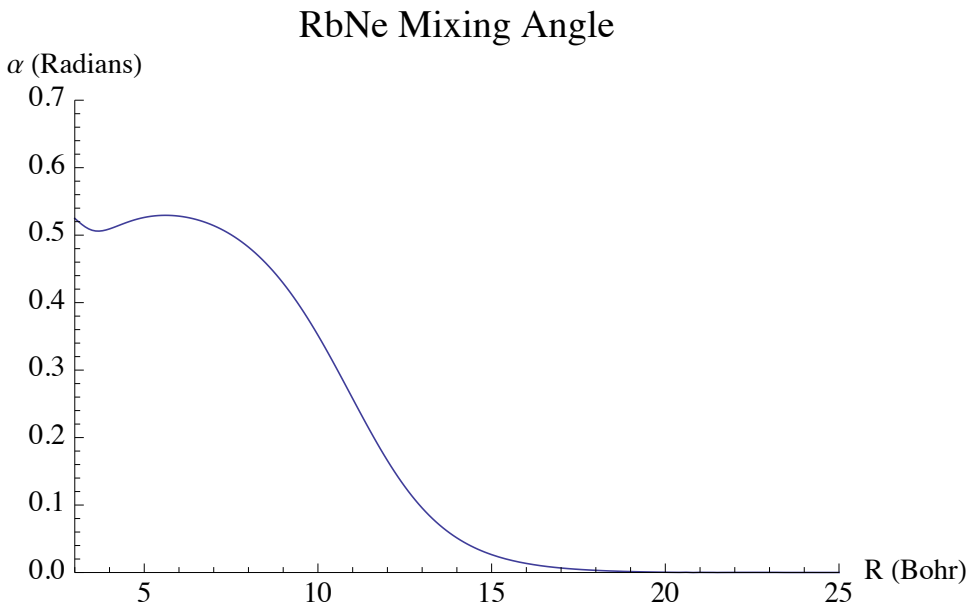

Figure 132. RbNe Mixing Angle.

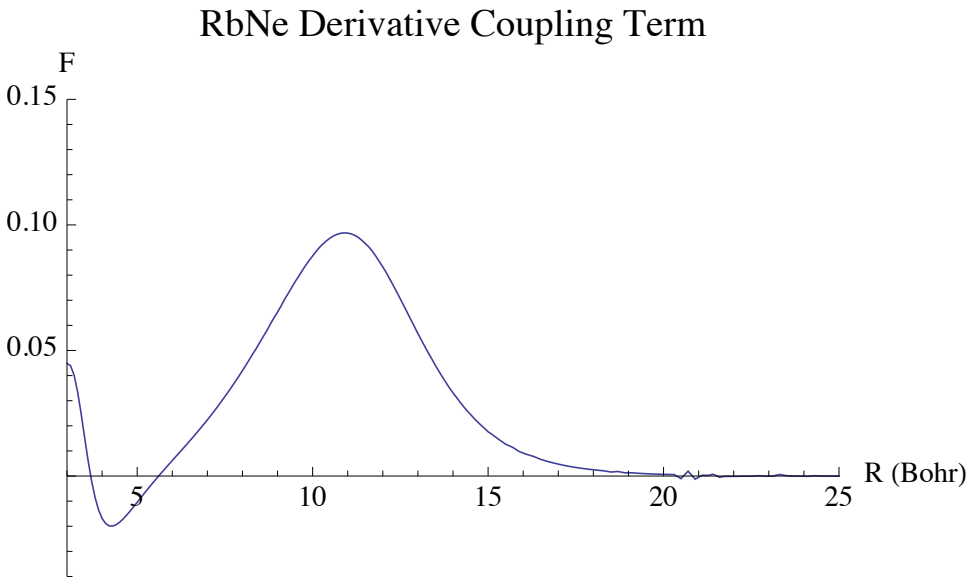

Figure 133. RbNe Radial Derivative Coupling Term.

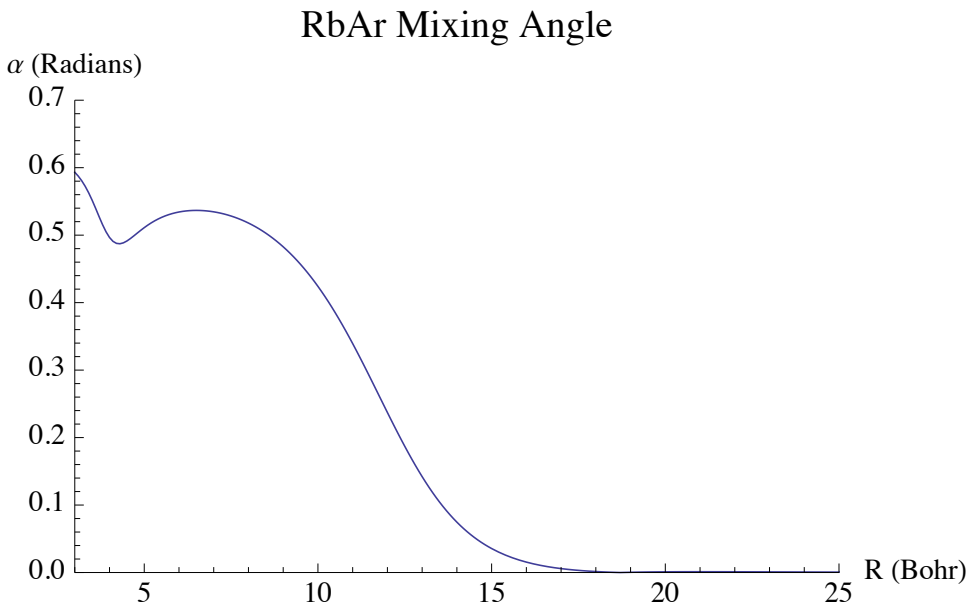

Figure 134. RbAr Mixing Angle.

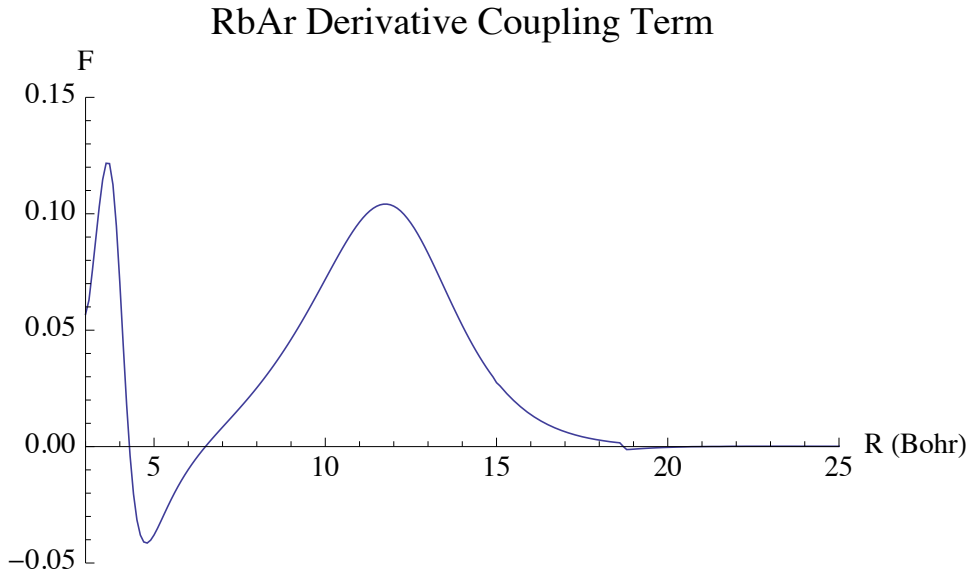

Figure 135. RbAr Radial Derivative Coupling Term.

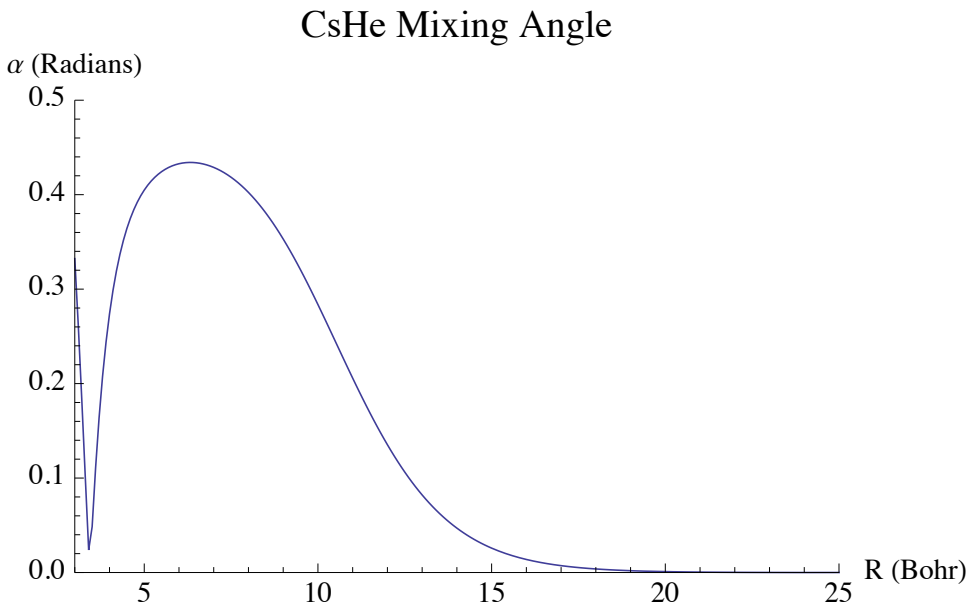

Figure 136. CsHe Mixing Angle.

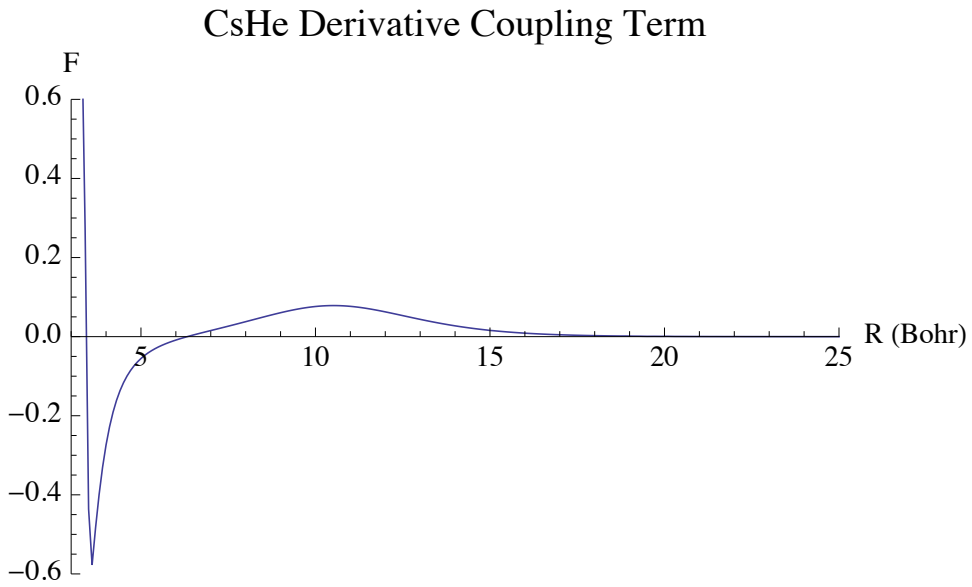

Figure 137. CsHe Radial Derivative Coupling Term.

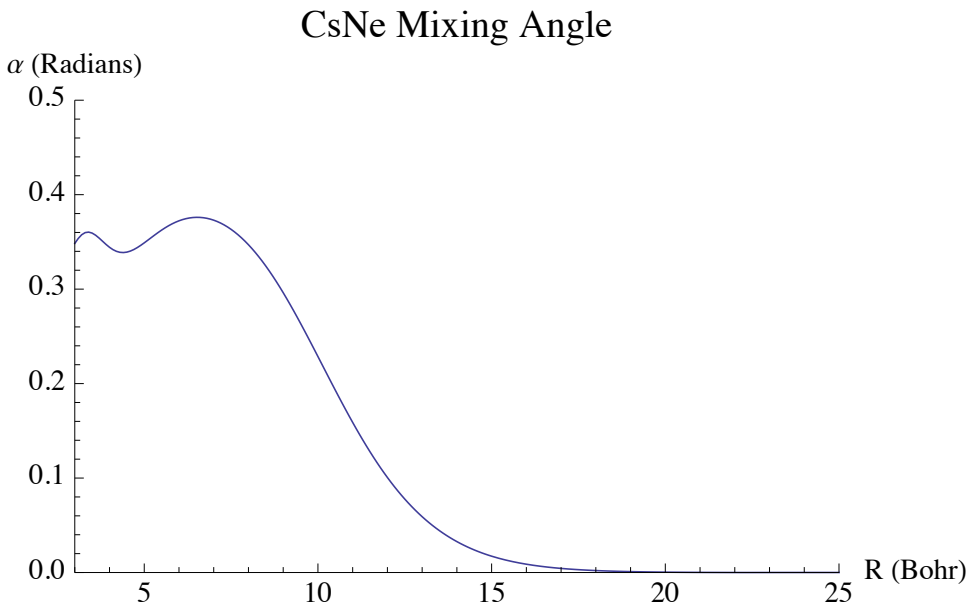

Figure 138. CsNe Mixing Angle.

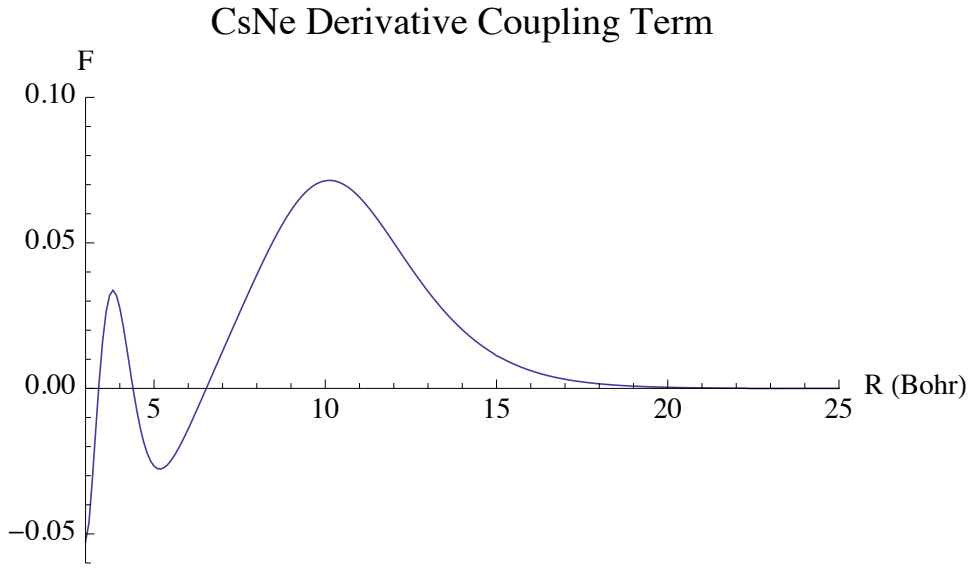

Figure 139. CsNe Radial Derivative Coupling Term.

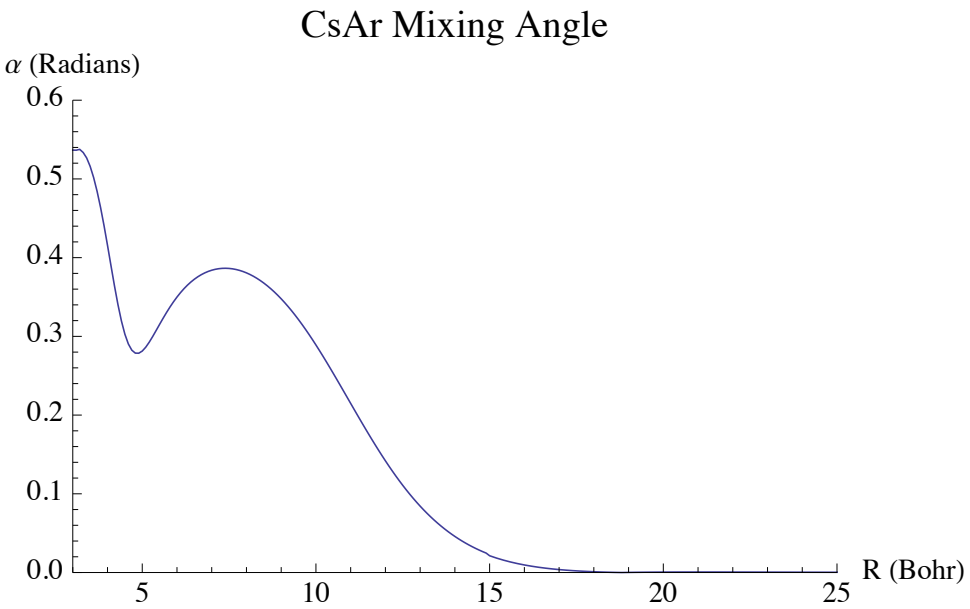

Figure 140. CsAr Mixing Angle.

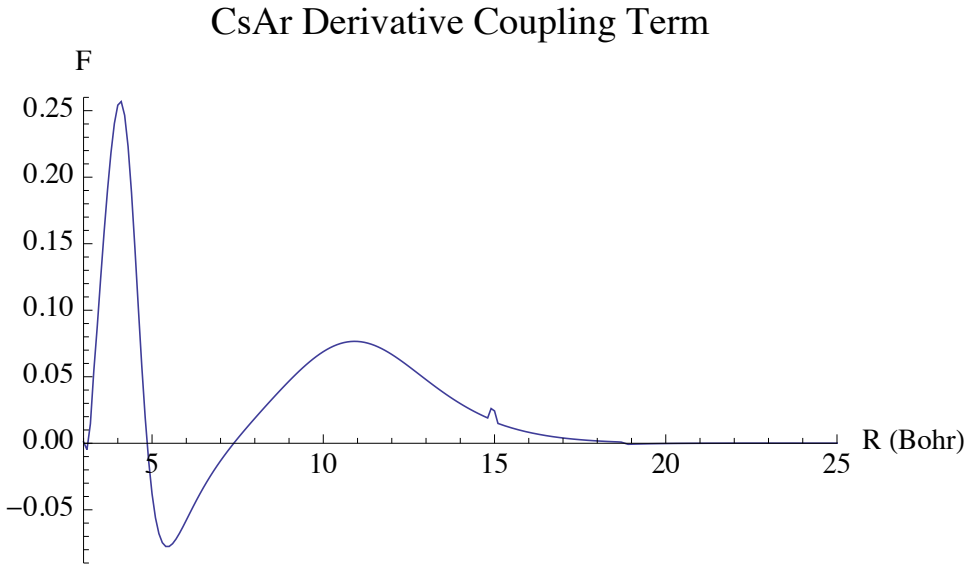

Figure 141. CsAr Radial Derivative Coupling Term.

Appendix E. State to State Detailed Balance

The principle of microscopic reversibility states that in a reversible reaction the mechanism in one direction is exactly the reverse of the mechanism in the other direction[43]. A consequence of this principle is that the $\widehat{\mathbf{S}}$-Matrix is symmetric and so the following equation is valid:

$$|S^{\gamma',\gamma}(E)|^2 = |S^{\gamma,\gamma'}(E)|^2 \tag{244}$$

where γ, γ' represent different channels. Recalling the equation for the BO state to state cross section the following equivalence holds in light of microscopic reversibility:

$$\begin{aligned}\sigma^{\gamma',\gamma}(E) &= \frac{\pi}{k^2_{\gamma'}}\sum_J (2J+1)|S^{\gamma',\gamma}(E)|^2 \\ &= \frac{\pi}{k^2_{\gamma'}}\sum_J (2J+1)|S^{\gamma,\gamma'}(E)|^2\end{aligned} \tag{245}$$

The numerator on the right hand side of Equation (245) can be replaced by $k^2_\gamma \sigma^{\gamma,\gamma'}(E)$. An equivalence now exists between the cross section in one direction and the cross section in the reverse direction.

$$\sigma^{\gamma',\gamma}(E) = \frac{k^2_\gamma}{k^2_{\gamma'}}\sigma^{\gamma,\gamma'}(E) \tag{246}$$

Noting that

$$\begin{aligned}k^2_\gamma &= \frac{2\mu_\gamma}{\hbar^2}(E - E_\gamma) \\ k^2_{\gamma'} &= \frac{2\mu_{\gamma'}}{\hbar^2}(E - E_{\gamma'})\end{aligned} \tag{247}$$

and that the reduced mass does not change between channels, $\mu_{\gamma'} = \mu_{\gamma}$, we now have an equation that captures state to state detailed balance:

$$\frac{\sigma^{\gamma',\gamma}(E)}{\sigma^{\gamma,\gamma'}(E)} = \frac{E - E_{\gamma}}{E - E_{\gamma'}} \tag{248}$$

As another confidence check that our time-dependent solution converged the ratio of the $|1/2, -1/2\rangle \leftrightarrows |1/2, 1/2\rangle$ and $|3/2, 3/2\rangle \leftrightarrows |1/2, 1/2\rangle$ cross section were compared against detailed balance. The results are plotted below.

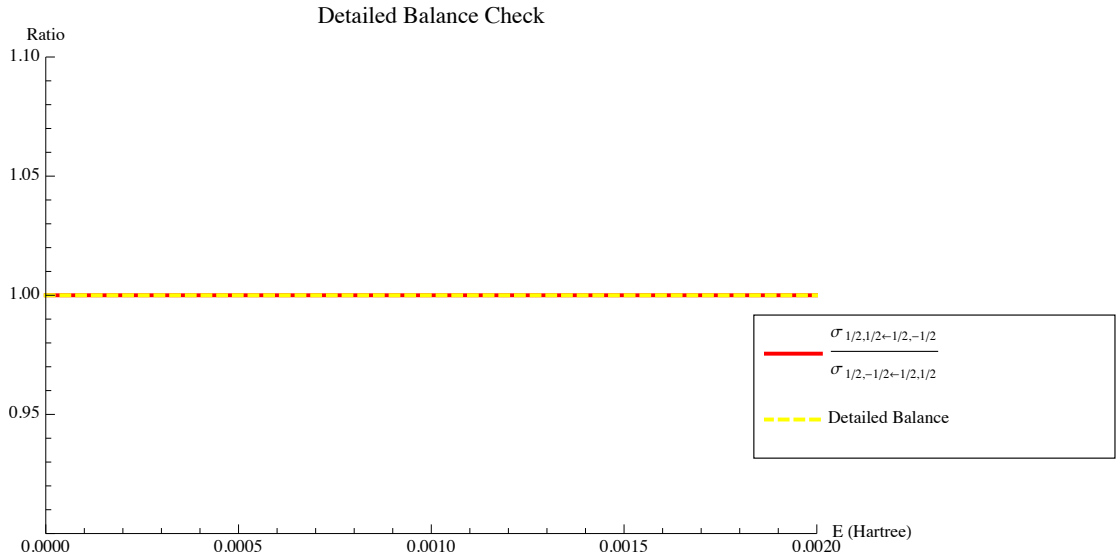

Figure 142. $|1/2, -1/2\rangle \leftrightarrows |1/2, 1/2\rangle$ **detailed balance check.**

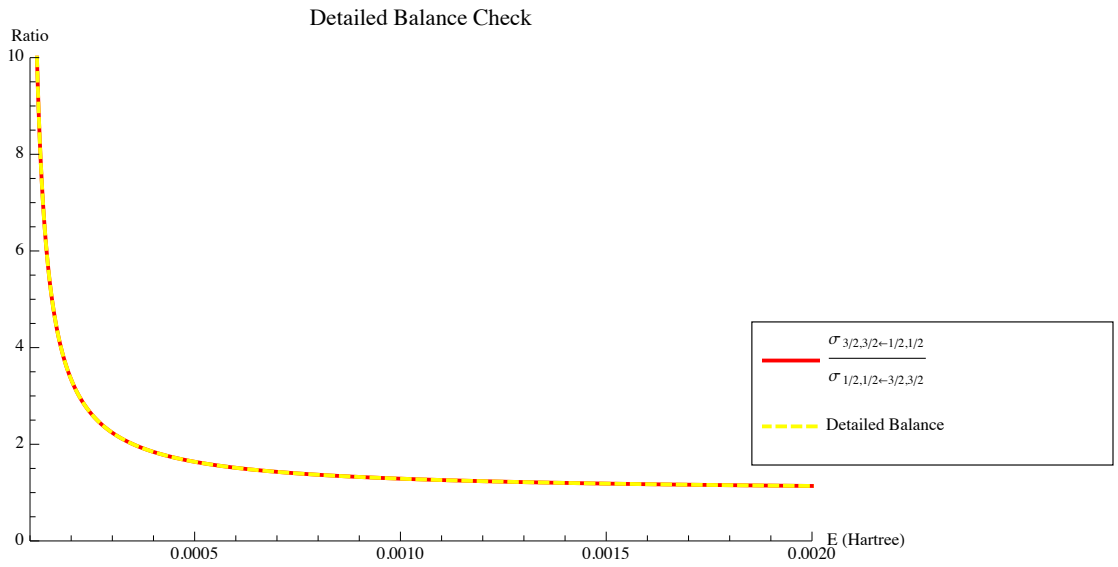

Figure 143. $|3/2, 3/2\rangle \leftrightarrows |1/2, 1/2\rangle$ **detailed balance check.**

Bibliography

[1] Alexander, Millard H., Tadeusz Orlikowski, and John E. Straub. "Theoretical study of intramultiplet transitions in collisions of atoms in ^3P electronic states with structureless targets: Ca(^3P)+He". *Physical Review A*, 28(1):73–82, 1983.

[2] Alvarellos, José and Horia Metiu. "The evolution of the wave function in a curve crossing problem computed by a fast Fourier transform method". *J. Chem. Phys.*, 88(8):4957–4966, 1988.

[3] Baer, Michael. "Introduction to the theory of electronic non-adiabatic coupling terms in molecular systems". *Physics Reports*, 358(2):75–142, 2002.

[4] Bandrauk, A. D. and H. Shen. "Improved exponential split operator method for solving the time-dependent Schrodinger equation". *Chem. Phys. Lett.*, 176(5):428–432, 1991.

[5] Beach, Raymond J., William F. Krupke, V. Keith Kanz, Stephen A. Payne, Mark A. Dubinskii, and Larry D. Merkle. "Resonance transition 795-nm rubidium laser". *Optics Letters*, 28(23):2336–2338, 2003.

[6] Beahn, T. J., W. J. Condell, and H. I. Mandelberg. "Excitation-Transfer Collisions between Rubidium and Helium Atoms". *Physical Review*, 141(1):83–87, 1966.

[7] Belcher, Lachlan. *Gradients and Non-Adiabatic Derivative Coupling Terms for Spin-Orbit Wavefunctions*. Ph.D. dissertation, Air Force Institute of Technology, 2011.

[8] Blank, L, D. E. Weeks, and G. S. Kedziora. "M+Ng Potential Energy Surfaces: M = K, Rb, and Cs and Ng = He, Ne, Ar". *in preparation*, 2011.

[9] Boggy, R. and F. A. Franz. "Cross section for $J, m_j \rightarrow J', m_{j'}$ transitions within the 4^2P states of potassium induced collisions with He, Ne, and Kr". *Physical Review A*, 25(4):1887–1899, 1982.

[10] Campbell, J. *Proc Lond Math Soc*, 28:381–390, 1897.

[11] Ciurylo, J. and L. Krause. "$4^2P_{1/2} \leftrightarrow 4^2P_{3/2}$ Mixing in potassium induced in collisions with noble gas atoms". *J. Quant. Spectrosc. Radiat. Transfer*, 28(6):457–461, 1982.

[12] Cohen-Tannoudji, et al. Claude. *Quantum Mechanics, volume 1*. Wiley-Interscience, New York, NY, 2005.

[13] Cooley, James W. and John W. Tukey. "An algorithm for the machine calculation of complex Fourier series". *Mathematics of Computation*, 19(90):297–301, 1965.

[14] Dashevskaya, E. I., E. E. Nikitin, and A. I. Reznikov. "Theory of Collisionally Induced Intramultiplet Mixing in Excited Alkali Atoms". *The Journal of Chemical Physics*, 53(3):1175–1180, 1970.

[15] Davidson, E.R. and D.W. SIlver. *Chem. Phys. Lett.*, 52:403, 1977.

[16] Delos, John B. "Theory of electronic transitions in slow atomic collisions". *Reviews of Modern Physics*, 53(2):287–358, 1981.

[17] Drake, Dordon W.F. *Spinger Handbook of Atomic, Molecular, and Optical Physics*. Springer, New York, NY, 2006.

[18] Ehrenreich, T., B. Zhdanov, T. Takekoshi, S.P. Phipps, and R.J. Knize. "Diode pumped caesium laser". *Electronics Letters*, 41(7), 2005.

[19] Gallagher, Alan. "Rubidium and Cesium Excitation Transfer in Nearly Adiabatic Collision with Inert Gases". *Physical Review*, 172(1):88–96, 1968.

[20] Gilmore, R. "Baker-Campbell-Hausdorff Formulas". *J. Math. Phys.*, 15:2090–2092, 1974.

[21] Grosser, J. "Angular Momentum Coupling in Atom-Atom Collisions". *Z. Phys. D*, 3(1):39–58, 1986.

[22] Jordan, J. A. and P. A. Franken. "Collision-Induced Mixing in the First Excited States of Sodium and Potassium". *Physical Review*, 142(1):20–25, 1965.

[23] Kolos, W. and L. Wolniewicz. "Nonadiabatic Theory for Diatomic Molecules and Its Application to the Hydrogen Molecule". *Reviews of Modern Physics*, 35(3):473–483, 1963.

[24] Konefal, Z. "Observation of collision induced processes in rubidium-ethane vapour". *Optics Communications*, 164:95–105, 1999.

[25] Krause, L. "Collisional Excitation Transfer Between the $^2P_{1/2}$ and $^2P_{3/2}$ Levels in Alkali Atoms". *Applied Optics*, 5(9):1375–1382, 1966.

[26] Krupke, William F., Raymond J. Beach, V. Keith Kanz, and Stephen A. Payne. "Resonance transition 795-nm rubidium laser". *Optics Letters*, 28(23):2336–2338, 2003.

[27] McQuarrie, Donald A. and John D. Simon. *Physical Chemistry A Molecular Approach*. University Science Books, Sausalito, CA, 1997.

[28] Mead, C. Alden and Donald G. Truhlar. "Conditions for the definition of a strictly diabatic electronic basis for molecular systems". *J. Chem. Phys.*, 77(12):6090–6098, 1982.

[29] Messiah, Albert. *Quantum Mechanics*. Dover Publications, Mineola, NY, 1999.

[30] Mies, F. H. "Molecular Theory of Atomic Collisions: Fine-Structure Transitions". *Physical Review A*, 7(3):942–957, 1972.

[31] Naylor, Arch W. and George R. Sell. *Linear Operator Theory in Engineering and Science*. Springer Science + Business Media, LLC, New York, NY, 1982.

[32] Nikitin, E. E. "Nonadiabatic Transitions between Fine-Structure Components of Alkali Atoms upon Collision with Intert-Gas Atoms". *J. Chem. Phys*, 43(2):744–749, 1964.

[33] Pack, Russel T. and Joseph O. Hirschfelder. "Separation of Rotational Coordinates from the N-Electron Diatomic Schrodinger Equation". *J. Chem. Phys.*, 49(9):4009–4020, 1968.

[34] Press, William H., Brian P. Flannery, Saul A. Teukolsky, and William T. Vetterling. *Numerical Recipes in C The Are of Scientific Computing*. Press Syndicate of the University of Cambridge, New York, NY, 1988.

[35] Sansonetti, J.E., W.C. Martic, and S.L. Young (2005). "Handbook of Basic Atomic Spectroscopic Data (version 1.1.2)". `http://physics.nist.gov/Handbook` [2010, October 5].

[36] Shankar, Ramamurti. *Principles of Quantum Mechanics (2nd Ed.)*. Kluwer Academic/Plenum Publishers, New York, NY, 1994.

[37] Sharma, A., N.D. Bhaskar, Y.Q. Lu, and W. Happer. "Continuous-wave mirrorless lasing in optically pumped atomic Cs and Rb vapors". *Appl. Phys. Lett.*, 39(3):209–211, 1981.

[38] Smith, F.T. "Diabatic and Adiabatic Representations for Atomic Collision Problems". *Physical Review*, 179(1):111–123, 1969.

[39] Swarztrauber, Paul and Richard Valent. "FFTPACK5". http://www.cisl.ucar.edu/css/software/fftpack5/index.html, 1990.

[40] Szabo, Attila and Neil S. Ostlund. *Modern Quantum Chemistry: Introduction to Advanced Electronic Structure Theory*. Dover Publications, Mineola, NY, 1996.

[41] Tannor, David J. and David E. Weeks. "Wave packet correlation function formulation of scattering theory: The quantum analog of classical S-matrix theory". *J. Chem. Phys.*, 98(5):3884–3893, 1992.

[42] Taylor, John R. *Scattering Theory: The Quantum Theory of Nonrelativistic Collisions*. Robert E. Krieger Publishing Company, Inc., Malabar, FL, 1972.

[43] Tolman, R. C. *The Principles of Statistical Mechanics*. Oxford University Press, London, UK, 1938.

[44] yih Tsaur, Gin and Jyhpyng Wang. "Constructing Green functions of the Schrodinger equation by elementary transformations". *Am. J. Phys.*, 74(7):600–606, 2006.

[45] Vleck, J. H. Van. "The Coupling of Angular Momentum Vectors in Molecules". *Reviews of Modern Physics*, 23(3):213–227, 1951.

[46] Weeks, David E. and David J. Tannor. "A time-dependent formulation of the scattering matrix using Moller operators". *Chemical Physics Letters*, 207(4):301–308, 1993.

[47] Worth, Graham A. and Lorenz Cederbaum. "BEYOND BORN-OPPENHEIMER: Molecular Dynamics Through a Conical Intersection". *Annu. Rev. Phys. Chem.*, 55:127–158, 2004.

[48] Zweiback, J. and W. F. Krupke. "28W average power hydrocarbon-free rubidium diode pumped alkali laser". *Optics Express*, 18(2):1444–1449, 2010.

REPORT DOCUMENTATION PAGE

Form Approved
OMB No. 074-0188

1. REPORT DATE *(DD-MM-YYYY)*	2. REPORT TYPE	3. DATES COVERED *(From – To)*
15-09-2011	Doctoral Dissertation	Sep 2008 – Sep 2011

4. TITLE AND SUBTITLE
Non-Adiabatic Atomic Transitions: Computational Cross Section Calculations of Alkali Metal-Noble Gas Collisions

5a. CONTRACT NUMBER

5b. GRANT NUMBER

5c. PROGRAM ELEMENT NUMBER

6. AUTHOR(S)
Lewis II, Charlton D., Capt, USAF

5d. PROJECT NUMBER

5e. TASK NUMBER

5f. WORK UNIT NUMBER

7. PERFORMING ORGANIZATION NAME(S) AND ADDRESS(ES)
Air Force Institute of Technology
Graduate School of Engineering and Management (AFIT/EN)
2950 Hobson Way
WPAFB OH 45433-7765

8. PERFORMING ORGANIZATION REPORT NUMBER
AFIT/DS/ENP/11-S04

9. SPONSORING/MONITORING AGENCY NAME(S) AND ADDRESS(ES)
High-Energy Laser Joint Technology Office
801 University Blvd SE
Ste 209
Albuquerque, NM 87106 505-248-8208; Harro.Ackermann@jto.hpc.mil

10. SPONSOR/MONITOR'S ACRONYM(S)
HEL JTO

11. SPONSOR/MONITOR'S REPORT NUMBER(S)

12. DISTRIBUTION/AVAILABILITY STATEMENT
DISTRIBUTION STATEMENT A
APPROVED FOR PUBLIC RELEASE; DISTRIBUTION UNLIMITED

13. SUPPLEMENTARY NOTES

14. ABSTRACT

Diode Pumped Alkali Lasers operate by exciting a gaseous cell of alkali metal to its $P_{3/2}$ excited energy state. A noble gas, present in the cell, collisionally de-excites the alkali metal to its $P_{1/2}$ state. The alkali atoms then relax to their $S_{1/2}$ ground state by emitting photons. The non-radiative de-excitation due to inert gas atoms represents an interesting juncture for DPALs operation. This process must be faster than the radiative relaxation back to the $S_{1/2}$ state for lasing to occur. The rate of non-radiative de-excitation is related to the collisional cross section and the cross section is related to the S-Matrix.

A time-dependent algorithm, the Channel Packet Method, was implemented to predict S-Matrix elements for alkali metal - noble gas (MNg) collisions. The S-Matrix contains the close-coupled Hamiltonian of the MNg system in body-fixed coordinates represented in the P-Manifold of states. There were two major state-to-state coupling phenomena responsible for intramultiplet mixing: spin-orbit and Coriolis.

A total of nine collisions were computationally simulated between Potassium, Rubidium, and Cesium and the noble gases Helium, Neon, and Argon. Temperature averaged cross-sections were calculated for the $P_{1/2}$ to $P_{3/2}$ transition and compared to experiment.

15. SUBJECT TERMS
Non-Adiabatic Collisions, Intramultiplet Mixing, Alkali Metal-Noble Gas Cross Section, Radial and Coriolis Coupling, DPAL

16. SECURITY CLASSIFICATION OF:			17. LIMITATION OF ABSTRACT	18. NUMBER OF PAGES	19a. NAME OF RESPONSIBLE PERSON
a. REPORT	b. ABSTRACT	c. THIS PAGE			David E. Weeks, AFIT/ENP
U	U	U	UU	268	19b. TELEPHONE NUMBER *(Include area code)* (937) 255 3636 ext 4561 david.weeks@afit.edu

Standard Form 298 (Rev. 8-98)
Prescribed by ANSI Std. Z39-18